EFFECT OF LOCAL CRYSTAL ORIENTATIONS ON THE ADIABATIC SHEARING AND CRACKING IN THE FORMATION OF SEGMENTED TI-6AL-4V CHIPS FROM TURNING

By

Jiawei Lu

A DISSERTATION

Submitted to
Michigan State University
in partial fulfillment of the requirements
for the degree of

Materials Science and Engineering– Doctor of Philosophy

2023

ABSTRACT

The Ti-6Al-4V (Ti64) alloy has been widely used as a light-weight structural material due to its excellent corrosion resistance and high strength even at elevated temperatures. However, the poor machinability of Ti64, leading to higher costs, has severely limited its application. The formation of segmented chips rather than smooth continuous chips, caused by the intrinsic low thermal conductivity of Ti64, is of great interest and significance for investigation.

Ti64 bars with various microstructures, namely mill-annealed (MIL), elongated (ELO), solution treated and aged (STA), and lamellar (LAM), were machined at 61, 91, and 122 m/min. The chips were collected, and their microstructures were characterized by scanning electron microscopy (SEM) and electron backscattered diffraction (EBSD). The morphology of these chips was also measured, and observations of the smooth and segmented sides were also made and compared.

For STA chips, nano-indentation and EBSD were used to investigate local shear strain phenomena. An existing continuum model based upon material constants and mechanical properties was used for shear band width prediction at various cutting speeds and the predicted values were compared with the measured values and discussed. In addition, a model based on the morphology of the segmented chips was adopted to calculate the homogeneous shear strains in the segments and catastrophic shear strains within the shear bands. Representative examples of chips were characterized by EBSD and analyzed using the stress tensor obtained from finite element numerical simulation. Finally, the chips were annealed at 500, 600 and 650 ℃ to investigate their response to annealing, revealing effects of the chip deformation history. For LAM, a few EBSD scans were also carried out to show the correlation between chip morphology and local orientations.

Overall, the work presented in this study demonstrates an approach to investigating the

formation of segmented chips and the severe deformation during turning. It can be further applied to the chips obtained from other machining methods and to identify effects of higher cutting speeds.

ACKNOWLEDGEMENTS

I would like to thank Dr. Bieler, my primary advisor, for the invaluable opportunities to work on this project, to visit IMDEA for research, and to present my work in many conferences and peer-reviewed journals. His expertise, enthusiasm, and constructive feedback have helped me overcome the obstacles in my research career and greatly contributed to the completion of this dissertation. I will always keep in mind his motivation and attitude, and pass it on as I keep on my research career.

Next, I would like to express my gratitude to Dr. Kwon, as well as Dr. Khawarizmi, who carried out the turning experiments and helped me with finite elements analysis using Deform 2D. In addition, many research results in this paper have been discussed with Dr. Kwon and Dr. Khawarizmi during our weekly meetings. Their insights and expertise have been instrumental in shaping the direction and scope of this work.

I would also like to thank the rest of my committee members, Dr. Guo and Dr. Eisenlohr, as well as professors from metal group, Dr. Crimp, Dr. Boehlert, for their valuable suggestions and guidance in my qualifying and comprehensive exams, and their efforts on responsible conduct of research.

Besides my committee members, I would also like to express my gratitude to Dr. Jon Molina-Aldareguia and Dr. Miguel Monclús for their help with nano-indentation experiments and suggestions on analysis of the results.

Last but not least, I would like to thank my colleagues, Dr. Per Askeland, Dr. Zhuowen Zhao, Genzhi Hu and many other graduate students from metal group for their kindly suggestions, as well as my family and friends Yining He, Dr. Shengyuan Bai, Dr. Quinn Sun, Dr. Danqi Qu, Haining Du, Tianhong Ying, Dr. Zinan Wang and many others for their support and care throughout my endeavors.

The present work was supported by the U.S. National Science Foundation (NSF) (NO. 1727525), and the Talent Attraction program of the Comunidad de Madrid (reference 2016-T3/IND-1600).

TABLE OF CONTENTS

CHAPTER 1 INTRODUCTION

Titanium was discovered in 1791 by the British reverend, mineralogist, and chemist William Gregor. He found it while examining magnetic sand from a river in Cornwall, England, and isolated a substance called "ilmenite" by removing the iron with a magnet and treating the sand with hydrochloric acid. He named the impure oxide of the new element "mechanite" after the location. Around the same time, the Berlin chemist Martin Heinrich Klaproth also isolated titanium oxide from a Hungarian mineral known as "rutile". Klaproth named it after the titans, who were children of Uranos and Gaia in Greek mythology, as they were similarly imprisoned in the earth's crust like the hard-to-extract ore[1].

It wasn't until over 100 years later that Matthew Albert Hunter from Rensselaer Polytechnic Institute in Troy, N.Y. was able to isolate the metal in 1910 by heating titanium tetrachloride (TiCl4) with sodium in a steel bomb. The father of the titanium industry is Wilhelm Justin Kroll from Luxembourg, who in 1932 produced significant quantities of titanium by combining TiCl4 with calcium. When World War II began, Kroll fled to the United States and demonstrated at the U.S. Bureau of Mines that titanium could be extracted commercially by reducing TiCl4 using magnesium instead of calcium. This method, known as the "Kroll process", is still widely used today.[1].

The initial applications of titanium alloys have been in aerospace industries like aero-engine and airframe manufacture, due to their excellent properties, mainly high specific strength and excellent corrosion resistance [1]. Over the past few decades, titanium and its alloys have been experiencing extensive development in industrial applications, such as petroleum refining, surgical implantation, nuclear waste storage, chemical and food processing, automotive, and marine applications [2], [3]. Among all the titanium alloys, Ti-6Al-4V is most commonly adopted in the above mentioned applications, which accounts for around 45-60% of the titanium products in practical use [2], [3].

1.1 Representative microstructures of Ti-6Al-4V alloy

For Ti64, the α-β phase transformation temperature is ~995℃ [12, 13]. The α phase is transformed to the β phase when heated above 995℃. The idealized orientation relationship between α and β unit cells of Ti64 are shown in Fig. 1.1. However, the lattice parameters of α and β don't match perfectly and thus strains are necessary when phase transformation takes place. As indicated in Fig. 1.2, an expansion of ~10% along $[2\bar{1}\bar{1}0]_{\alpha}$, a contraction of ~10% along $[01\bar{1}0]_{\alpha}$ and a contraction of ~1% along $[0001]_{\alpha}$ are required to become $[100]_{\beta}$, $[01\bar{1}]_{\beta}$, and$[0\bar{1}1]_{\beta}$, respectively. As a result of this imperfect matching, one of the $< 111 >_{\beta}$ directions need to be rotated by ~5° to align itself with one of the $< 2\bar{1}\bar{1}0 >_{\alpha}$ directions, leading to 6 possible β variants when transformed from one α grain, as illustrated in Fig. 1.2. Therefore, the misorientation between each two of these 6 β variants can be either 10°, 50°, 60° and 70°.

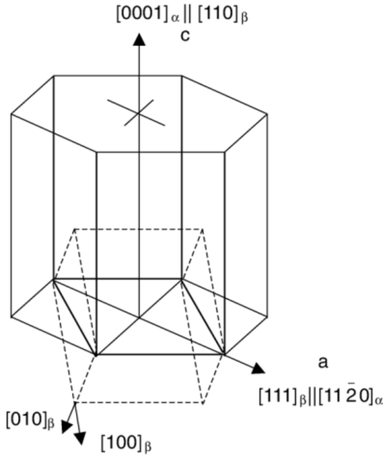

Figure 1.1 Idealized orientation relationship between α and β crystal structures [12].

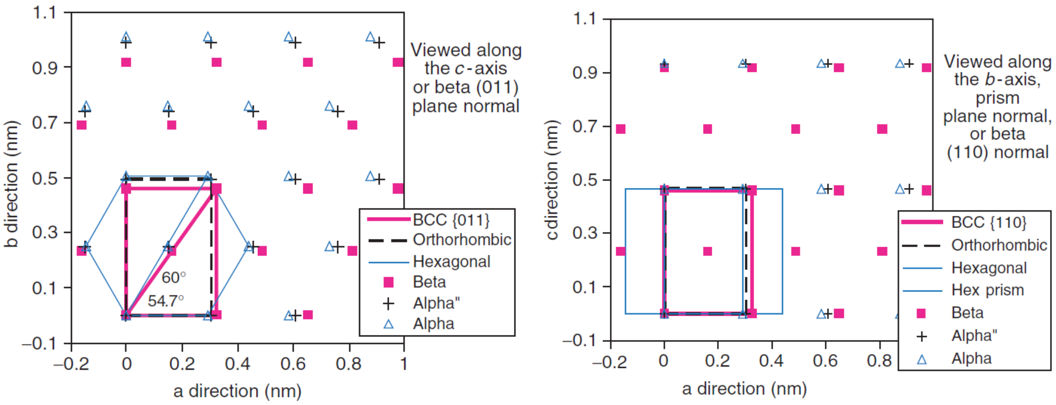

Figure 1.2 Atomic positions of α and β crystal structures are close so phase transformation is easy to take place [4].

When the β phase is transformed to α upon cooling, one $< 2\bar{1}\bar{1}0 >_{\alpha}$ direction is parallel to one of the two $< 111 >_{\beta}$ directions on one of the $\{110\}$ planes. Since there are six different $\{110\}$ planes within a β crystal, the c-axis of a daughter α crystal has six directions as well, and each direction has two variants which can be rotated about the c-axis by ~10° from each other.

In general, the aluminum equivalent and molybdenum equivalent equations (in wt.%) are adopted to describe the degree of stability of the α and β phases. Aluminum is one of the most important alloying elements due to its potent solid solution strengthening effect on the α phase [5]. Also, the addition of aluminum can reduce the density of titanium alloys. Molybdenum and vanadium can also solid solution strengthen the β phase and are two of the most popular β-stabilizing additives [6]

As a result, titanium alloys can be classified based on the phases present in their microstructure, due to the addition of different alloying elements. α alloys are consisting of mainly α phase while the alloys with the presence of a small amount of β phase are termed near-α alloys. Commercially pure (CP) titanium alloy is a typical α alloy. CP titanium is usually graded by oxygen and iron content. Compared with the β alloys, CP titanium is usually preferred for superior creep resistance and high-temperature applications [7]. On the other hand, α alloys have reduced ductility and poor forgeability and a two-orders-of-magnitude lower diffusion rate. Typical near-α alloys include Ti-3Al-2.5V, Ti-8Al-1Mo-1V, and Ti-6Al-2Sn-4Zr-2Mo, which are mainly used at temperatures between 400-520°C [7]. When the alloys have a mixture of both α and β phases, the alloys are classified as α+β alloys. Most common α+β alloys include Ti-6Al-4V, Ti-6Al-2Sn-4Zr-6Mo, Ti-6Al-2Sn. The microstructure and properties of α+β alloys can be controlled by heat treatment at temperatures between 315-400°C. If the alloys show the microstructure of mainly β phase at room temperature, the alloys are called β alloys [8]. Representative β alloys are Ti-15V-3Cr-3Al-3Sn, Ti-15Mo-2.7Nb-3Al-0.2Si, Ti-3Al-8V-6Cr-4Mo-4Zr and Ti-10V-2Fe-3Al [7].

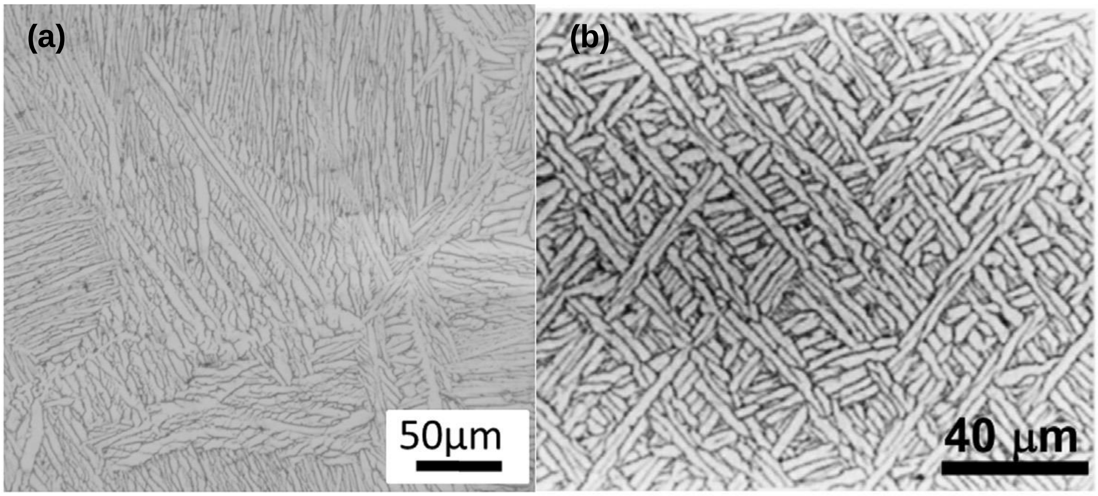

Figure 1.3 (a) Solution treated and furnace cooled Ti64 at 0.42°C s^{-1} from 1100°C×10 min [9];(b) Cooled from the β phase field at more than 1°C s^{-1} [10].

β-annealing requires heating the alloy into the β phase field (~1100°C) for a certain time, then followed by furnace cooling or air cooling or even quenching for different purposes. Usually, the β-annealing results in coarse prior β grains so the annealing temperature and time should be kept to the minimum. Matsumoto et. al [9] heated Ti64 to1100°C for10 min and then furnace cooled at the speed of 0.42°C s^{-1} and the resulting microstructure had coarse lamellar α+β phases (Fig. 1.3 (a), showing white α phase and black β phase). This is because α-laths nucleated at the grain boundaries of prior-β grains and grew inward as large α-colonies. However, when increasing the cooling rate, a basket-weave α+β phase microstructure (Fig. 1.3 (b)) was formed [10] with finer and shorter α-laths with increasing cooling rate. An increased driving force led to the nucleation and growth of α-laths at both prior-β grains boundaries and boundaries between the newly formed α-laths. Both reasons led to the formation of the microstructure as shown in Fig. 1.3 (b).

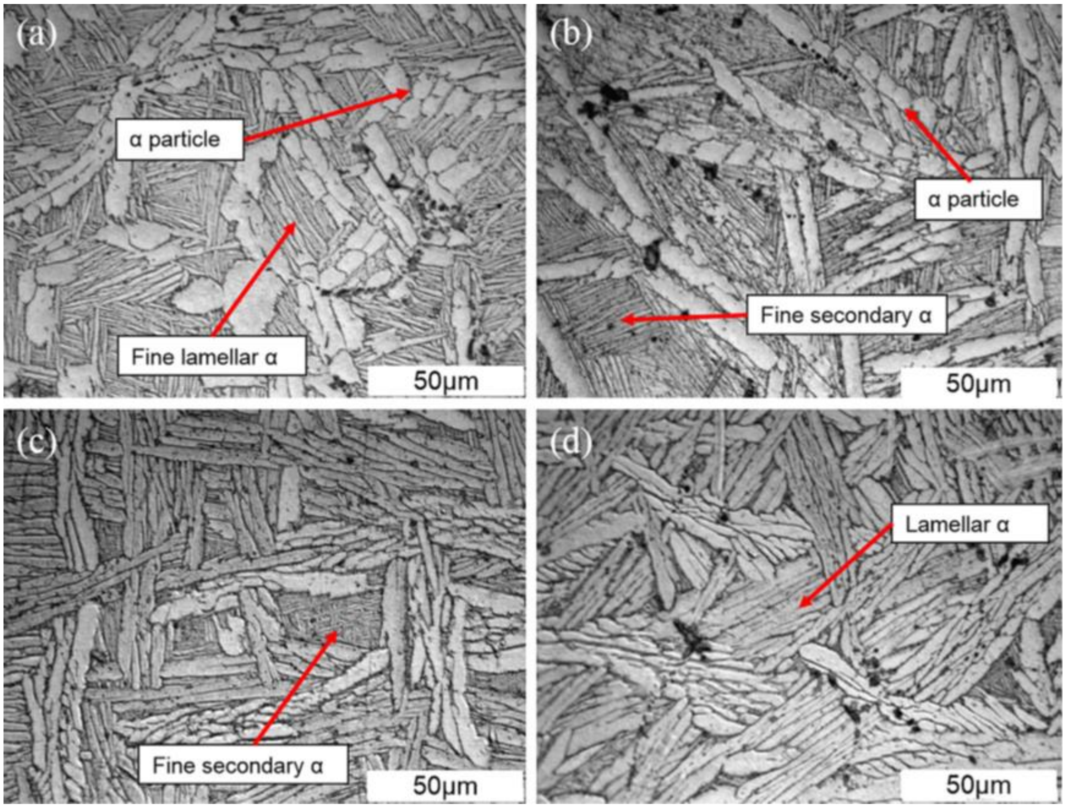

Figure 1.4 Optical micrographs of the microstructure isothermally held at (a) 970℃, (b) 950℃; (c) 930℃; and (d) 900℃ for 30 min [11].

Zhang et al. [11] investigated the effect of thermal history on the microstructure evolution of Ti64 during solidification. Typical α-Widmanstätten colonies were formed when cooling directly from 1700℃. To further study the special microstructure at 950℃, the microstructures at 970℃, 930℃, and 900 ℃ were investigated. The microstructure at 970℃ (Fig. 1.4 (a)) consisted of primary α particles and secondary α lamellar structure, which is referred to as bimodal microstructure. The tendency of α breakdown (forming small primary α grains) was higher at 970℃ than at 950℃. When the temperature decreased to 930℃ (Fig. 1.4 (c)), the microstructure was coarse α lamellae scattered with small fine lamellar colonies. The microstructure obtained at 900°C was mainly coarse α lamellae, as shown in Fig. 1.4 (d).

The average width for primary α lamellae (i.e. α that forms from during the isothermal hold below the β transus) decreased from 9 μm to 3 μm with decreasing temperature from 970°C to 900°C. The growth of the primary α was dominated by the diffusion mechanism when the specimens were isothermally held, resulting in coarser primary α with increasing temperature. Another feature was that the volume fraction of primary α decreased with increasing isothermal holding temperature. This is because the driving force for the nucleation and further transformation of primary α at 970°C was weaker than at 900 °C. The primary α was coarser and had a higher tendency of breakdown with increasing holding temperature. The breakdown of primary α can be ascribed to Ostwald ripening and boundary splitting mechanisms during isothermal holding. When the temperature was below the β transus, the primary lamellar α nucleated at the grain boundaries or at the interior of the grains. The subsequent isothermal holding led to the coarsening of the primary lamellar α by diffusion mechanism. EDS results showed that the vanadium concentration increased in the retained β grains, leading to a lower phase transformation temperature. The grain boundaries of primary α provided nucleation sites and inhibited the growth of secondary lamellar α.

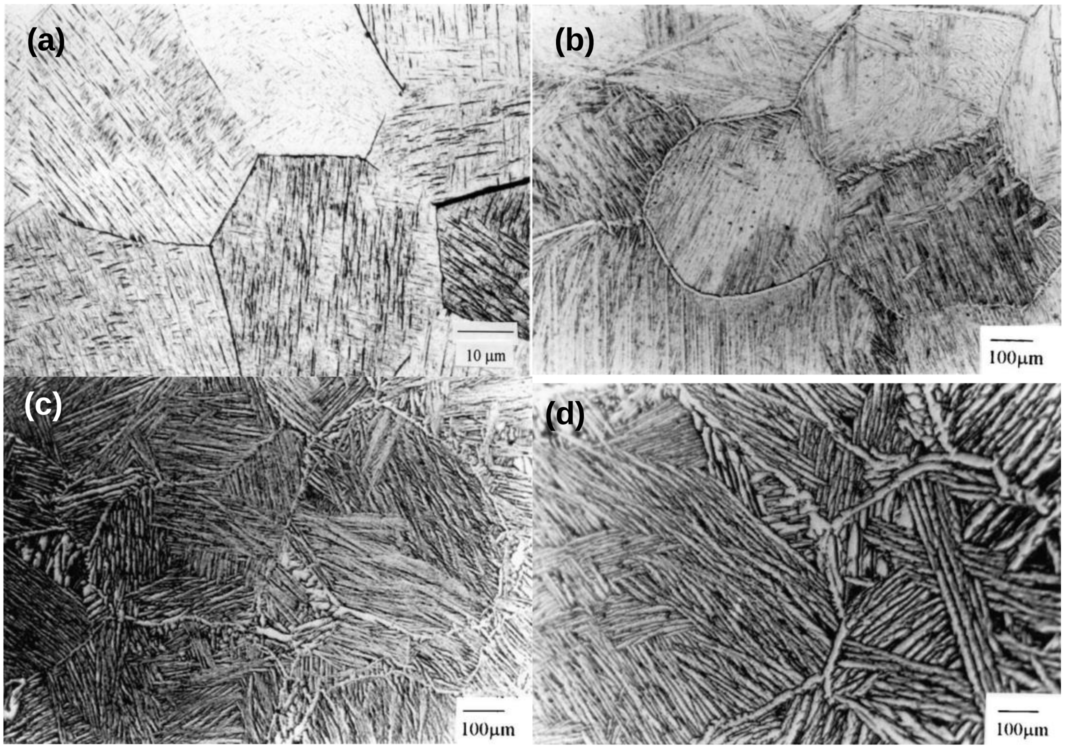

Figure 1.5 Microstructures of Ti64 when cooling from 1100 °C at the cooling rate of (a)5.1°Cs^{-1}; (b)3.4 °Cs^{-1}; (c) 0.81 °Cs^{-1}; (d)0.23 °Cs^{-1} [12].

Gil et al. [12] conducted experiments on the microstructure and mechanical properties of Ti64 at different cooling rates. As can be seen from Fig. 1.5, martensite was formed when the cooling rate was 5.1°Cs^{-1}. The thickness of α-Widmanstätten plates increased with decreasing cooling rate (~4μm at 3.4°Cs^{-1} and ~8μm at 0.23°Cs^{-1}). The high diffusivity at low cooling rate allowed the atoms to move faster so that the α-Widmanstätten plate was thicker. The increase of β grain size can lower the starting β to α transformation. The β phases with a grain size of 600 μm had a ~250°C lower starting transformation temperature than those with a grain size of 100 μm. The mechanical properties for a lamellar microstructure are mainly determined by prior β grain size, the size of the α+β lamellae, thickness of α lamellae, and the morphology of the interlamellar interface (β phase) [13]. Refined prior β grains and thinner α lamellae can result\ in a higher tensile strength, which can also explain the higher strength for the Widmanstätten microstructures.

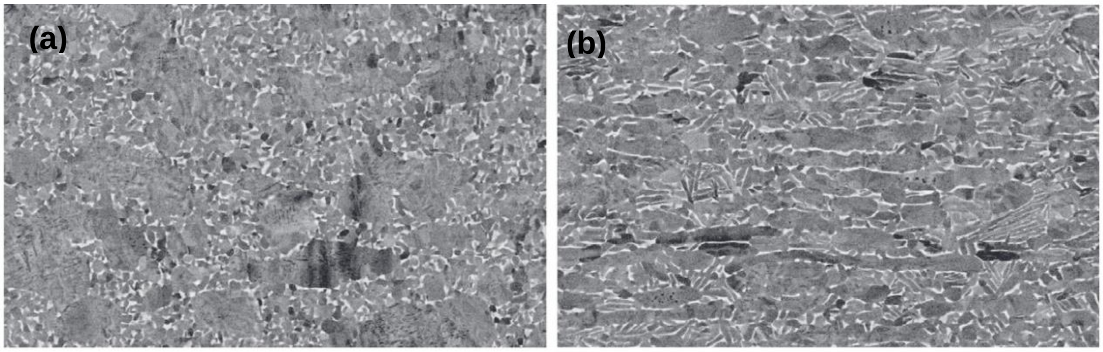

Figure 1.6 Backscattered electron (BSE) images of the microstructure of mill-annealed Ti64 (a) in-plane view (b) cross-section view[14].

Mill annealing for Ti64 is usually carried out in the temperature range of 700-800℃ for 1-4 h, followed by air cooling. The main purpose of mill annealing is to retain the wrought-state microstructure. Mulay et al. [14] compared the microstructure and mechanical properties of Ti64 manufactured by direct metal laser melting (DMLM) and mill annealing. The in-plane Backscattered electron (BSE) image (Fig. 1.6) shows globular α grains (dark phase) with the β phase (bright phase) decorating the grain boundaries. The cross-section view exhibited elongated α grains and β grains were located along the grain boundaries. The compressive yield strength of mill annealed Ti64 (1059 MPa) was comparable to that of the DMLM sample (1066 MPa).

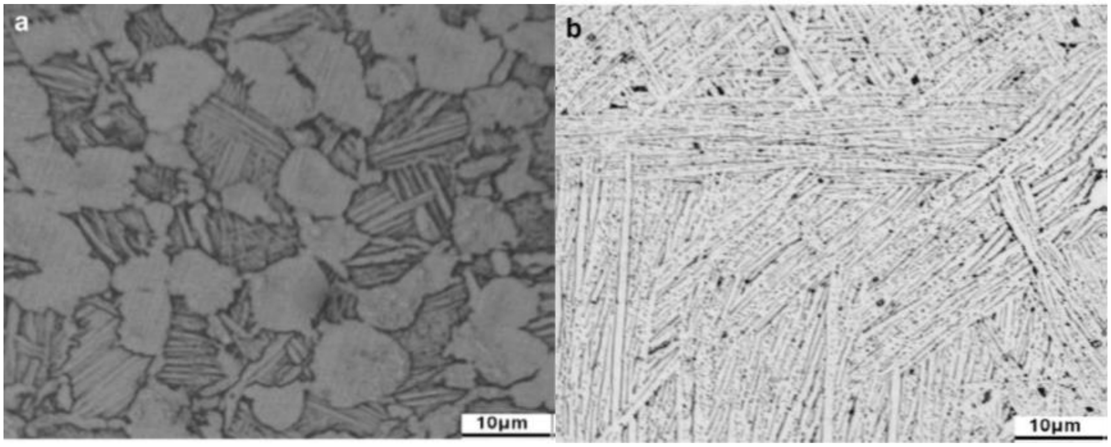

Figure 1.7 (a) bimodal; and (b) lamellar microstructure of Ti64 alloy [15].

Recrystallization annealing is heating the alloy into the upper end of α+β field (~950℃) for up to 2 h, followed by furnace cooling. After annealing, the α and β phases are both essentially dislocation free [10]. Liu et al. [15] obtained two different microstructures by annealing at 950℃ for 1 h, followed by air cooling, and annealing at 1020℃ for 1 h, followed by air cooling, respectively. Fig. 1.7 (a) exhibits the bimodal microstructure when annealed at 950℃ and Fig. 1.7 (b) shows the lamellar microstructure when annealed at 1020℃. The bimodal microstructure consists of primary α phase and lamellar α+β phase while the lamellar microstructure is mainly lamellar α+β phase.

Meyer et al. [16] investigated the quasi-static and dynamic compressive tests and impact tests of Ti64 with different microstructures (as shown in Fig. 1.8) obtained by different heat treatments. The bimodal microstructure (Fig. 1.8 (b)) exhibited a higher yield stress than coarse lamellar microstructure (Fig. 1.8 (a)), which was 1040 MPa and 960 MPa, respectively. The coarse-grained martensite microstructure (Fig. 1.8 (c)) and the globular primary α microstructure (Fig. 1.8 (d)) exhibited even higher yield strengths (1120 MPa and 1170 MPa, respectively).

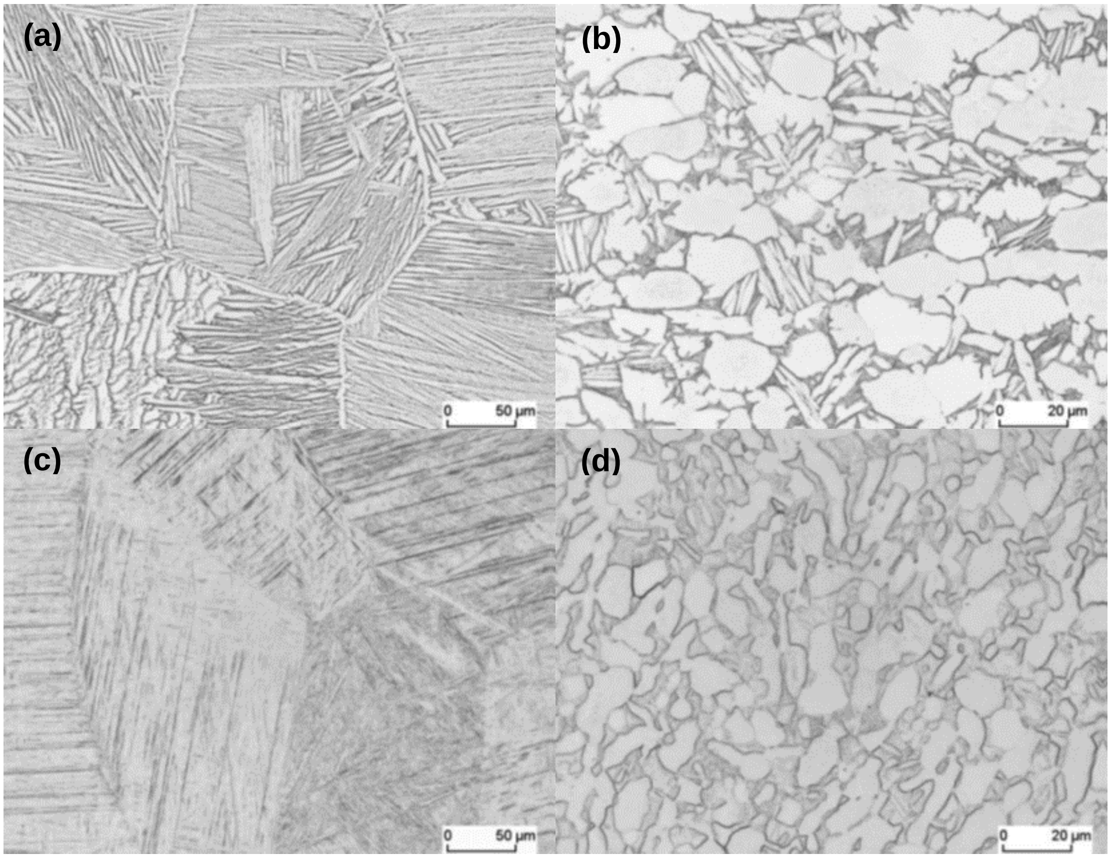

Figure 1.8 Optical microstructures of Ti64(a) annealed at 1065℃, furnace cooling; (b) annealed at 955℃ and furnace cooling; (c) annealed at 1065℃ and water quenching; (d) annealed at 900℃, water quenching and aged at 600℃ [16].

On the other hand, the specific energy consumption of the bimodal microstructure (310 J/cm^3) was much higher than those of the other three (coarse lamellar: 125 J/cm^3, coarse-grained martensite: 120 J/cm^3, and globular primary α: 260 J/cm^3), indicating a better deformability among these four microstructures. This may be ascribed to the residual-stress-free state after annealing at 955℃ and followed by furnace cooling.

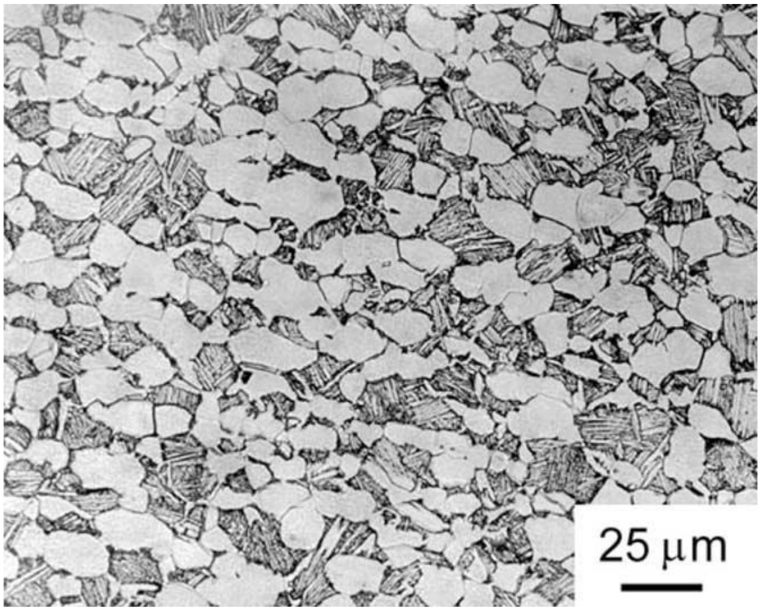

Figure 1.9 Optical micrograph of the bimodal Ti64 microstructure showing primary α and lamellar α+β structure [17], similar to that after recrystallization annealing.

A typical duplex annealing for Ti64 includes 870-950°C for 0.2-1.0 h, followed by air cooling, and 680-730°C for 2-4 h, again followed by air cooling [10]. The first stage of annealing controls the fraction and morphology of α phase while the second stage allows the precipitation of acicular secondary α phase in the metastable β phase. The Ti64 alloy was solution-treated 925°C for 1 h, fan air cooled and then stabilized at 700°C for 2 h by Nalla et al. [17]. As can be seen from Fig. 1.9, the microstructure after duplex annealing consists of equiaxed primary α and lamellar α+β, similar to that after recrystallization annealing.

1.2 Improvements of cutting tools and other approaches

Titanium is not actually a rare substance as it ranks as the ninth most plentiful element and the fourth most abundant structural metal in the Earth's crust exceeded only by aluminum, iron, and magnesium. Unfortunately, it is seldom found in high concentrations and never found in a pure state [1]. However, the poor machinability of Ti and its alloys, which leads to high costs of finished parts, has severely limited their applications [18]. The poor machinability of Ti alloys arises from their extremely low thermal conductivity (~7.5 W/Km [2]). Also, the phase transformation from α to β may occur at high cutting speeds [19], which can be detrimental to the cutting tool since the β phase is much more chemically active, with 4-5 orders of magnitude faster diffusivity [8].

Machinability has not been accurately defined but it should at least take the following aspects into account: tool life, removal rate of work materials, cutting force, surface finish and chip shape [20]. Tool life is the machining time by which a fresh tool can work before a specified amount of tool wear is obtained [21]. To be specific, tool life when machining titanium can be defined as the machining time by which a fresh tool can work before the flank wear reaches a specified amount. If the experiments are carried out at the same cutting speed, the cutting length can be utilized instead of the machining time in some cases. However, titanium and its alloys are notoriously known for its poor machinability (low machining efficiency and severe tool wear), which can be attributed to their extremely low thermal conductivity and high hardening rate [2], [20]–[22].

There have been many attempts to improve the tool life in different ways. Nabhani [23] used cubic boron nitride (CBN) and polycrystalline diamond (PCD) inserts as cutting tools for titanium alloys. The higher critical temperature at which adhesion and welding started to develop indicated that PCD (760°C) and CBN (900°C) coated inserts had higher cratering wear resistance than the bare carbide tool (740°C). Schrock *et al.* [19] investigated the crater wear condition of both PCD and carbide inserts at different cutting speeds. For PCD inserts, the rake face wear was uneven, fractured and rough, indicating attrition at 61 m/min. A smooth crater developed at 122 m/min, showing a diffusion/dissolution wear mechanism. For carbide inserts, the rake face showed smooth craters at both cutting speeds. Amin et al. [3] investigated the effectiveness of uncoated WC-Co and PCD inserts in end milling of Ti64 alloy. The results show that average surface toughness produced by PCD inserts is lower than that produced by carbide inserts. As can be seen from Fig. 1.10, total volume of metal removal per tool life for PCD insert is much larger than that for carbide inserts over a much higher cutting speed range. At the cutting speed of 120 and 160 m/min, the volume of metal removal of PCD inserts is almost 3 times as large as that of carbide inserts. The applicable cutting speed for uncoated carbide should be 40 m/min while for PCD tool it should be 120 m/min.

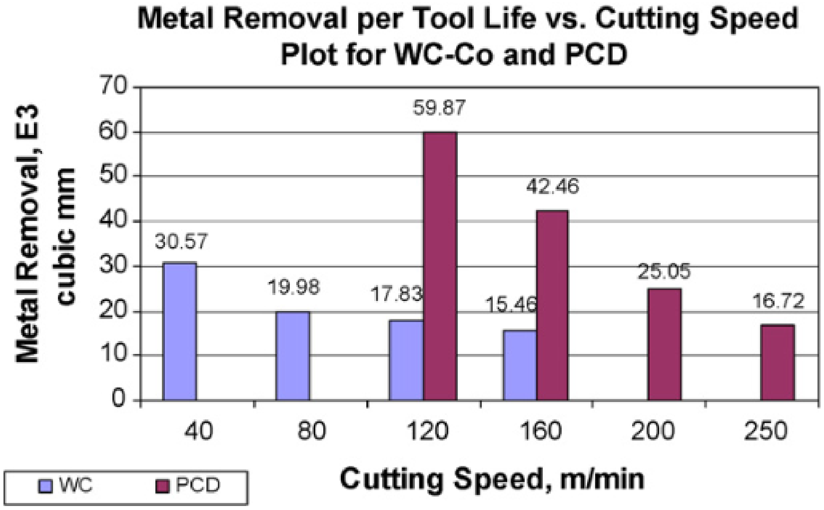

Figure 1.10 Total volume of metal removed per tool life shows the coated PCD tool has superior ability of cutting titanium alloys, compared with the tungsten carbide insert [3].

Three PCD tools made of different diamond grain sizes (CTB002 (2µm), CTB010 (10µm) and CTM302 (2-30µm)) were examined by turning experiments [24]. The flank wear of tools CTB002 and CTB010 developed steadily as indicated by the linearly increasing tangential force and the maximum width of flank wear (VBs). For CTM 302, large-scale fracture happened at the beginning of the cutting and the fracture at the tip restricted the development of flank wear. On the rake faces, scattered adhesion layers were found on the rake faces of the tools CTB002 and CTB010. An intact adhesion layer was preserved on the rake face of the tool CTM302. In addition to the elements from PCD inserts (Co) and workpiece material (Ti), oxygen was found on the tool rake faces due to the oxidation of the adhered titanium alloy. Plus, the oxygen content was related to the cutting temperature at the tool/chip interface.

Since the coated tools are costly but not as effective as expected in improving the wear resistance in dry machining process, other clean and sustainable cutting approaches have drawn the attention. Many researchers [25]–[33]turned to the minimum quantity lubrication (MQL) approach, which consumes very small amount of fluids (typically 20-150mL/hr [34]). Compared with conventional flooding method, which obviously is a non-clean cutting approach, even with the clean and sustainable dry cutting, MQL is cost-efficient and guarantees the safety for both environment and the worker. Wang et al. [32] machined Ti-6Al-4 V alloy using various turning approaches such as dry, wet cooling, MQL cooling. It can be concluded that coefficient of friction under MQL turning at higher cutting speed was much lower than dry turning and flood cooling, and ultimately resulted in enhanced lubrication at the tool-chip contact surface. In contrast with the dry cutting condition, temperature and the consequent tool wear is significantly decreased using MQL strategy [35]. Some other researchers [36]–[38], [39, p. 2], [40]–[42] adopted cryogenic cooling approach, using liquid nitrogen (LN2) or CO2-snow to lower the high temperature caused by cutting in order to extend the tool life. Compared to dry and flood machining, both flank wear and rake wear were reduced during cryogenic machining at 150 m/min. In addition, the cutting forces decreased by 15% and 44% at 100 m/min and 150 m/min, respectively [37]. Nevertheless, the consumption of LN2 can add considerably to the total machining cost [38]. However, both cutting strategies still lead to segmented chips.

1.3 Formation of segmented chips

Since the coatings are not so cost-effective in extending tool life, a better understanding of the formation of segmented chips might be the key to improving the machinability of Ti64. In previous research work, the thermo-plastic instability took place when the critical cutting speed of 0.15 m/s (9 m/min) was exceeded [43], [44]. Also, the shear bands started to show up when the chip load (the cutting speed times the feed rate) is around 0.004 m^2/min [43], [45]. Ye et al. [46] validated that the transition of the flow pattern from continuously serrated to discontinuously segmented almost always occurs when the input energy is equal to or greater than the total energy dissipation during the whole shear band relaxation process.

There have been two theories concerning the formation of the segmented Ti chips obtained from machining. One possibility is the propagation and growth of cracks from the outer surface of the chips [43], [47]. The other one attributes segmented chip formation to adiabatic shear bands caused by localized shear deformation resulting from the predominance of thermal softening over strain hardening [48], which is also frequently referred to as a thermoplastic instability. According to Vyas and Shaw [47], a shear crack will initiate at the free surface at point D in Fig. 1.11, where the shear stress is maximal, and will proceed downward along the shear plane toward the tool tip (point O). Initially, the crack will be continuous across the width of the chip, which is called a gross crack, but will become discontinuous as higher crack arresting normal stresses are encountered. These disconnected localized cracks are called microcracks.

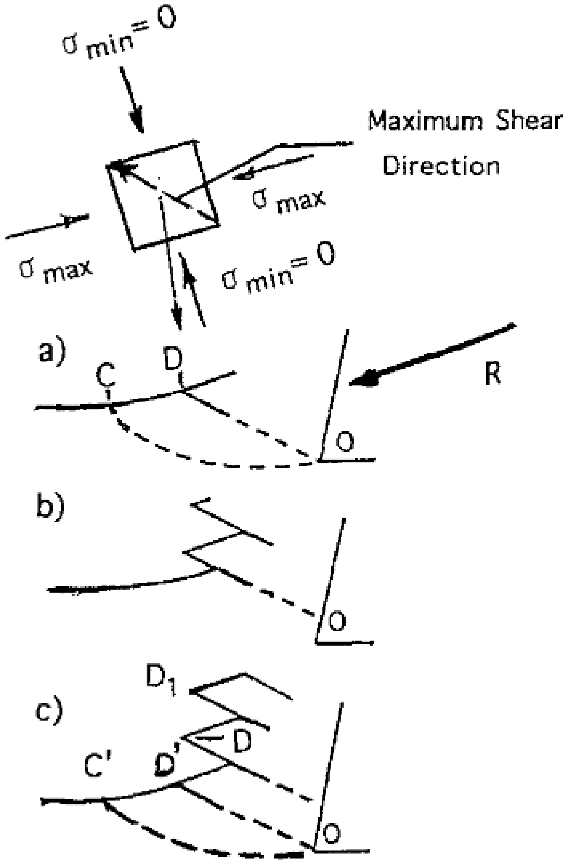

Figure 1.11 mechanism of saw tooth formation due to the crack propagation along the maximal shear direction [47].

Continuum isotropic models for segmented chips have been developed, where the width of the shear band can be calculated based upon the model developed by Molinari et al. [22], [49]:

$$t = \frac{12\sqrt{2m}\cos\,(\theta - \omega)kT_r}{at_0 V cos\theta}$$

where θ is the shear angle, ω is the tool rake angle (0° in this study), m and a are non-dimensional strain hardening and thermal softening coefficients of the material, k is the thermal conductivity, T_r is room temperature, t_0 is the shear flow resistance and V is the cutting speed. The non-dimensional thermal softening parameter a can be calculated based on [22], [50]:

$$a = \frac{\alpha\kappa_0}{\rho c} \times (b\dot{\varepsilon}_0)^m$$

where κ_0 is the yield strength, ρ is the density, c is the specific heat capacity, $\dot{\varepsilon}_0$ is the reference strain rate and b is a physical constant of the material. The parameters used for the calculation can be obtained in [22]. Ye et al. [51] proposed the concept of shear band evolution degree and that the evolution degree is the ratio of current shear displacement to the critical shear displacement. When the evolution degree is less than 1, the shear band is not fully mature, and this will influence the shear band spacing as a result of the shear stress in the shear band. Once the shear displacement reaches the critical value of 1, the shear stress in the shear band vanishes [51] and the shear band stops growing in width because the propagation process of shear bands is stress-controlled [52]. From orthogonal cutting experiments, Ye *et al.* determined that the evolution degree can be worked out from the fluctuation of the cutting force:

$$X = 1 - \frac{F_{min}}{F_{max}}$$

Liu et al. [22] investigated the milled Ti64 chips and shear band widths at 250 m/min and 500 m/min were measured to be 5.8 and 5.9 μm, respectively. According to the model, the shear band width is inversely proportional to the cutting speed, thus the shear band width at 250 m/min should be twice that at 500 m/min. On the other hand, the evolution degree at 250 m/min was calculated to be half of that at 500 m/min. Finally, these two cutting speeds resulted in similar as-measured shear band widths at 250 and 500 m/min.

In general, the homogeneous shear strain γ_{seg} between shear bands is given by [53]–[55]:

$$\gamma_{seg} = \frac{1}{\lambda_h sin\phi_{seg}} \sqrt{{\lambda_h}^2 - \frac{2\lambda_h \cos\left(\rho_{seg}\right)}{\sin\left(\phi_{seg} + \rho_{seg}\right)} + \frac{1}{sin^2(\phi_{seg} + \rho_{seg})}}$$

where ϕ_{seg} is the direction of the localized shear, ρ_{seg} is the complementary angle of ϕ_{seg}. λ_h is the chip compression ratio that can be obtained by the ratio of the deformed chip thickness, h_c, and the undeformed chip thickness, h, or the ratio of cutting speed, v_c, and chip flow speed, v_{ch}, as illustrated in Fig. 1.12:

$$\lambda_h = \frac{h_c}{h} = \frac{v_c}{v_{ch}}$$

The catastrophic shear strain, γ_c, and the strain in the shear band, γ_{sb}, are:

$$\gamma_c = \frac{p_{sb}}{\delta_{sb}}$$

$$\gamma_{sb} = \gamma_{seg} + \gamma_c$$

where p_{sb} is the shear displacement (referred to as "shear band projection" in their context [55]) and δ_{sb} is the shear band width. This model provides the means to investigate the correlation between the shear strain and the chip morphology and potentially better understanding for the formation of segmented chips. Results of these models can be compared with the criteria that adiabatic instability happens when the slope of true stress-true strain curve becomes zero [56], [57].

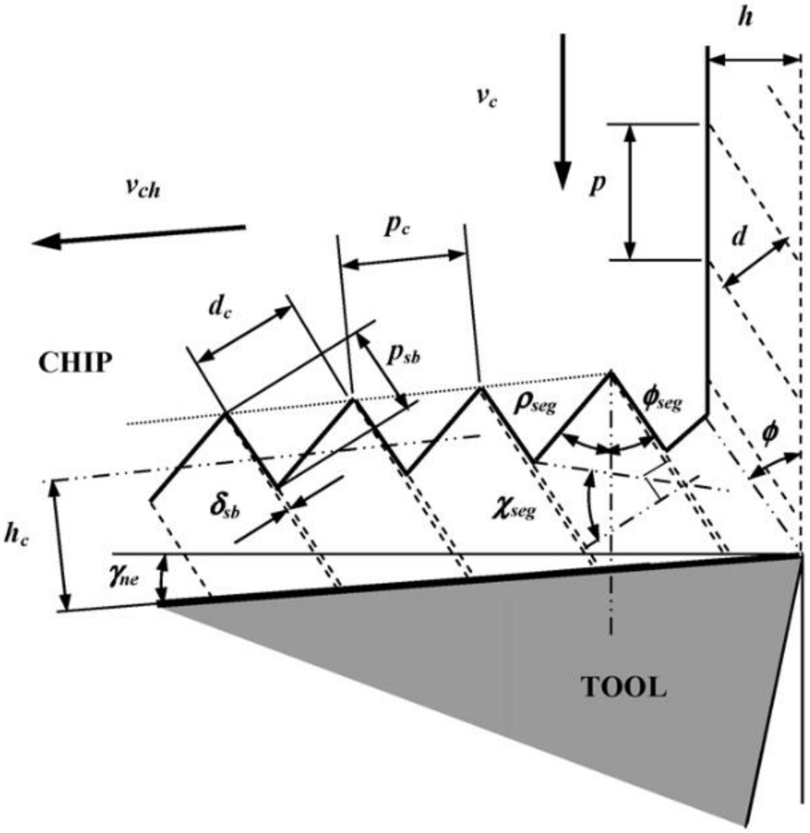

Figure 1.12 Shear strain calculation based upon the chip segment geometry [55].

When investigating the formation of segmented chips, finite element (FE) simulation is a powerful and useful methodology that has been widely adopted in modeling of the machining process [58]. The modeling procedure is a challenging task using even the most advanced software since the machining process is under severe deformation condition such as high strain, high strain rate, high stress and high temperature. Therefore, most of the published research work was performed under the assumption of orthogonal cutting, the simplest configuration of machining. The main issues in FE simulation of machining operations are:

1. To provide accurate material constitutive and damage models, over a wide range of strains (0.1-10), strain rates (10^5-10^6 s^{-1}), and temperatures (800-900°C or even higher when machining hard-to-cut materials) (material nonlinearity).

2. To define mechanical and thermal contacts at the tool-chip and tool-workpiece interfaces correctly.

3. To overcome the severe element distortion due to chip formation (geometric nonlinearity).

4. To calculate both temperatures and displacements simultaneously in a highly nonlinear, coupled thermomechanical dynamic process.

The tool is mostly considered as a rigid body due to its high stiffness compared with the workpiece [59], [60]. Al-Zkeri et al.[61] compared the results obtained using rigid and elastic tools. The simulation started with a rigid tool model to minimize the simulation time. After reaching steady state cutting temperature and forces, the tool was switched to an elastic body and the elastic tool stresses were computed. The results showed that the stress in the elastic tool model is only 2% lower than the rigid body model, attesting the validity of the FE modeling with the assumption of considering the tool as a rigid part.

Only a portion of the workpiece is modeled as a planar rectangle (2D simulation) with a relatively short length compared to the actual workpiece, for simplicity. the plane strain condition was usually assumed in orthogonal turning tests when the uncut chip thickness (feed) was much smaller (5-10 times) than the width of cut.

The equations of motion for 2D cutting problems are as following [62]:

$$\frac{\partial \sigma_{xx}}{\partial x} + \frac{\partial \sigma_{xy}}{\partial y} + \rho b_x = \rho \frac{\partial^2 u_x}{\partial t^2}$$

$$\frac{\partial \sigma_{yx}}{\partial x} + \frac{\partial \sigma_{yy}}{\partial y} + \rho b_y = \rho \frac{\partial^2 u_y}{\partial t^2}$$

where σ is the Cauchy stress, ρ is density, b is the body force, t is time, u is the material displacement, and $x - y$ is the reference coordinate system.

Heat transfer during the machining process is governed by the energy equation as following

[63]:

$$\rho c\left(\frac{\partial T}{\partial t}+V_x\frac{\partial T}{\partial x}+V_y\frac{\partial T}{\partial y}\right)=k\left(\frac{\partial^2 T}{\partial x^2}+\frac{\partial^2 T}{\partial y^2}\right)+\dot{Q}_g$$

where c and k are specific heat capacity and thermal conductivity, V_x and V_y are the material velocities in the x and y directions. Also, $\dot{Q}_g$ is the sum of heat generations from two sources during machining: plastic work in the primary and secondary deformation zones and frictional work on the tool-chip interface. The heat generation equation is [63]:

$$\dot{Q}_g=\eta_P\dot{W}_P+\eta_F\dot{W}_F=\eta_P(\sigma\dot{\varepsilon}_P)+\eta_F(\tau V_{ch})$$

where η_P and η_F are the fraction of plastic work converted to heat and the fraction of friction work converted to heat. $\dot{W}_P$ and $\dot{W}_F$ are in turn the rate of plastic work per unit material volume and the rate of frictional work per unit contact area. σ, $\dot{\varepsilon}_P$, τ and V_{ch} are flow stress, effective plastic strain rate, frictional shear stress at the tool-chip interface, and chip velocity along the tool-chip interface, respectively.

The conduction heat transfer between the chip and tool:

$$\dot{Q}=h_{int}(T_{ch}-T_t)$$

where h_{int} is the thermal conductance coefficient between chip and tool, T_{ch} and T_t are the temperatures of chip and tool, respectively.

Similarly, convection heat transfer between the chip and the surrounding ambient is:

$$\dot{Q}=h(T_{ch}-T_a)$$

where h is the convection heat transfer coefficient between the chip surface and the ambient, T_{ch} and T_a are the temperatures of chip and ambient, respectively.

It has been well recognized that the material model in the FE simulation of machining process cannot be identified using quasi-static tests, due to the fact that the material undergoes high strain,

strain rate, and temperature during cutting process. Therefore, alternative techniques such as high-speed compression tests, impact tests, and split pressure Hopkinson bar (SPHB) tests have been extensively used in determining material constitutive and damage models in FE simulation. The commonly used material constitutive models include: Johnson-Cook [64], Power law, Zerilli-Armstrong [65], Usei-Maekawa-Shirakashi [66], Oxley [67], Marusich [68], among which Johnson-Cook is the most commonly adopted one:

$$\sigma = (A + B\varepsilon^n)\left(1 + Cln\frac{\dot{\varepsilon}}{\dot{\varepsilon}_0}\right)[1 - (\frac{T - T_r}{T_m - T_r})^m]$$

where σ is the equivalent flow stress, ε is the equivalent plastic strain, $\dot{\varepsilon}$ is the equivalent plastic strain rate, $\dot{\varepsilon}_0$ is the reference equivalent plastic strain rate, T is the workpiece temperature, T_m is the material melting temperature, T_r is the room temperature. Different values of the material constants (A, B, n, m) for Ti64 based upon researchers' experimental work [69]–[72] can be found in [73].

Among all the friction models, the constant Coulomb friction coefficient at the entire tool-chip interface shear friction model is most commonly used [58], the friction factor is defined as following:

$$m = \frac{\tau}{\tau_Y}$$

Where τ is the frictional shear stress and τ_Y is the work material shear flow stress.

There have been many other attempts [74]–[79] to obtain good agreement between the experimental and simulation results in terms of the cutting forces and chip morphologies, by modifying and comparing the constitutive models. Calamaz et al. [78] carried out numerical analysis of chip formation and shear localization in the cutting process of Ti64 alloy, using a modified Johnson-Cook model. The result showed that the best agreement was obtained when using a high friction coefficient of 2, together with the introduced strain softening parameter a of 0.11. Ducobu et al. [79] investigated three different models for simulations:

First model: Lagrangian with Johnson–Cook law (LJC), taking only crack propagation into account.

Second model: Arbitrary Lagrangian Eulerian (ALE) with TANH law (ALETHAN), taking only strain softening into account.

Third model: Lagrangian with TANH law (LTANH), taking both crack propagation and strain softening into account.

As shown in Fig. 1.13, The first model leads to many highly deformed elements, but no apparent serrated chips can be observed. This is mainly due to the unavailability of continuous remeshing in Abaqus/ Explicit v6.8. The second model produces a chip with small teeth. In contrast, the third model produces a saw-toothed chip with a morphology that is observed in the experimental results [80].

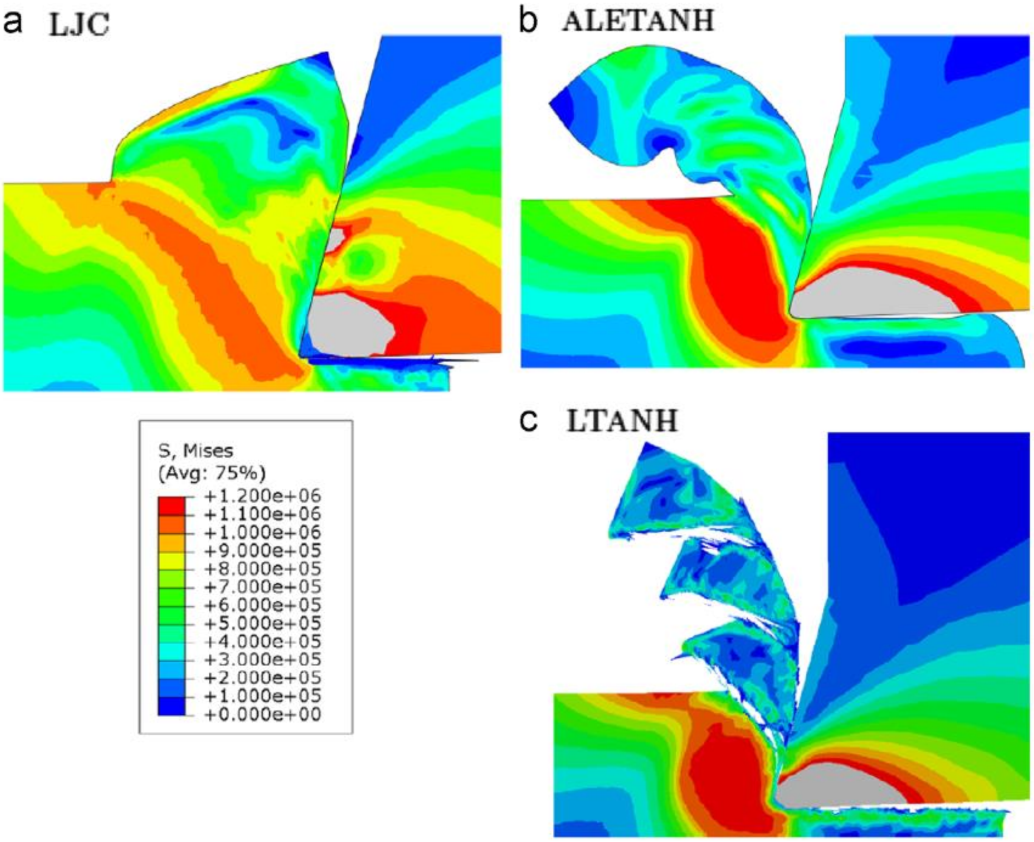

Figure 1.13 Von Mises stress contours during chip formation using different material models LTANH model shows the appearance of cracks [79].

Zang et al. [81] made attempts to explain the segmented chip formation mechanism with FE simulation. The results showed that the temperature of adiabatic shear zone is obviously higher than the surrounding segments. At each cutting speed, a crack was observed right next to the adjacent shear band (Fig. 1.14). Both the crack length and the segmented degree of the chips increased with increasing cutting speed. Indeed, the primary shear zone initiates around the tool tip and propagates toward the free surface, and then the crack initiates from the free surface of the chip. A similar conclusion has been made in the paper by Molinari et al. [74]. In their investigation of adiabatic shear band formation in cutting Ti64 alloy, it has been found that the shear bands are generated at the tool tip and propagate towards the chip free surface. Shear bands grow within the chip formation region as the chip flows away from the workpiece. As shown in Fig. 1.15, the shear band has no time to reach the free surface of the chip, as the shear band propagation time is longer than the shear band convection time. As a result, the shear bands are not fully developed.

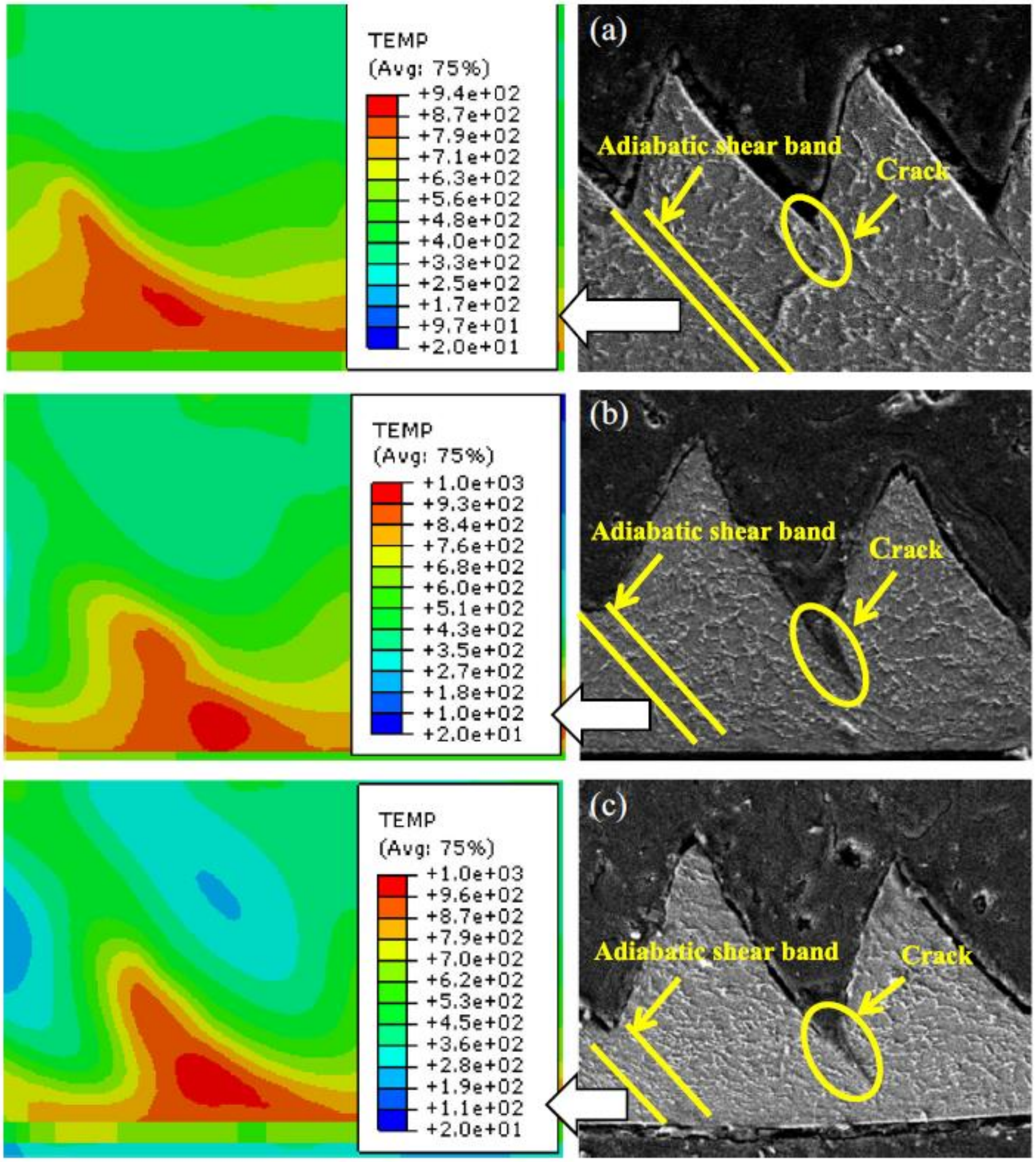

Figure 1.14 Micrographs of serrated chips and the temperature profiles of simulated adiabatic shear bands for Ti- 6Al-4V (a) 80, (b) 120, and (c) 160 m/ min [81]. The temperature within the adiabatic shear band shows the shear band is triggered by the secondary shear zone.

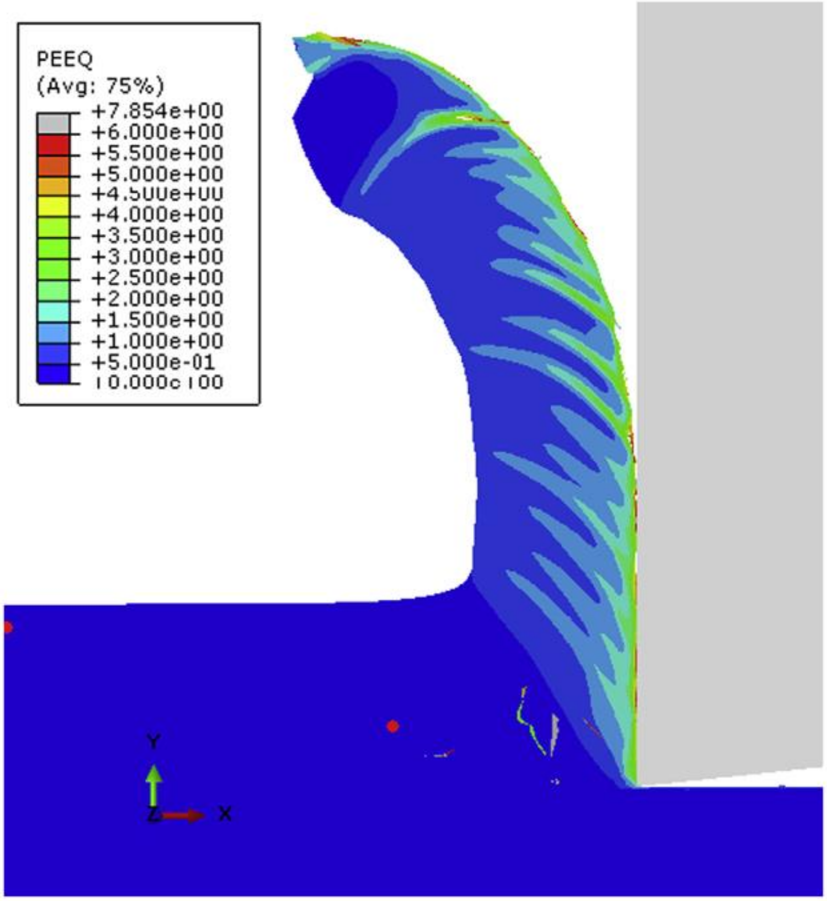

Figure 1.15 Chip morphology and strain isoclines at the cutting speed of 350 m/s with the feed of 0.1 mm [74]. The strain field indicates how the adiabatic shear band originates from the secondary shear zone.

Sima et al. [73] conducted serrated chip formation simulation of the Ti64 alloy using constitutive models with non-temperature-dependent parameters (Model 1), with temperature-dependent parameters (Model 2), and with temperature-dependent parameters and strain softening (Model 3), all of which are based upon J-C constitutive model. Predictions using Model 3 resulted in the closest matches to the experimental forces and cutting and thrust forces for the other two uncut chip thickness conditions. According to Model 3, effective shear strain in the shear bands is much higher than that in the chip segments (Fig. 1.16). However, their results showed that effective shear stress within the primary shear zone is much higher (Fig. 1.17), which is contrary to the thermo-plastic instability hypothesis.

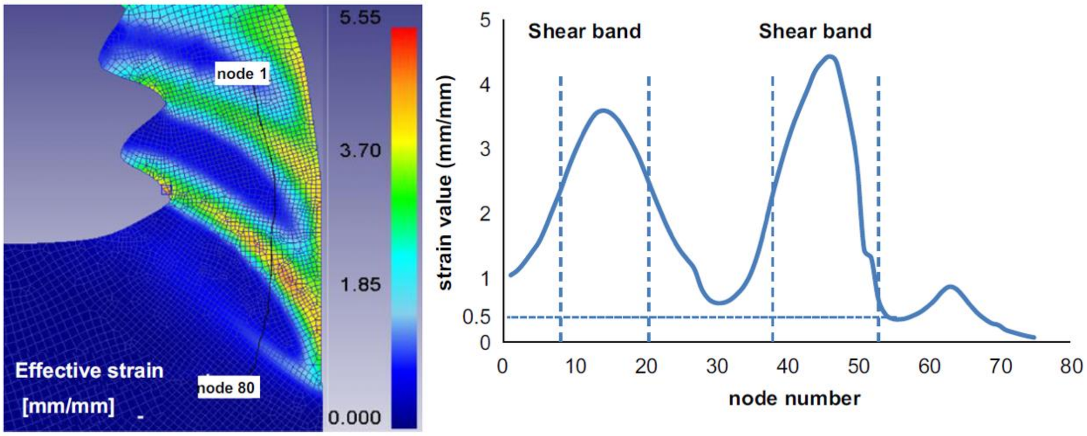

Figure 1.16 Effective strain values along a path into the segmented chip with adiabatic shearing [73]

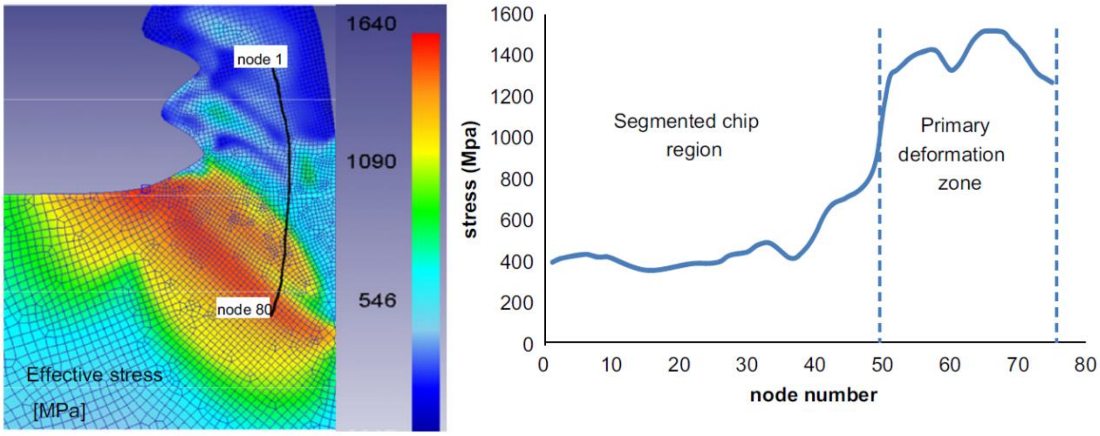

Figure 1.17 Effective stress values along a path into the segmented chips [73].

Many papers [2], [22], [46], [82] have revealed that the transition of chip morphology from continuous chips at a cutting speed as low as 0.05 m/s, to more or less regular serrated with localized shearing and possible presence of cracks at the cutting speed from 1 - ~40 m/s, and discontinuous chips at very high cutting speeds. In addition, the chip morphology is also dependent on the depth of cut [83], initial microstructure of the workpiece [84], and even the wear condition of the cutting tool [85], [86].

Only one paper published in 2022 focused on the effect of initial orientations of workpiece on the formation of segmented chips, to the author’s best knowledge. The effect of both initial texture and strain hardening on the formation of Ti64 chips in orthogonal cutting has been investigated by Palaniappan et al. [87]. The texture modification was induced by cold-rolling Ti64 plates with thickness reductions of 30%, 40%, 45% and 47%. A gradual transition from heterogeneous to homogeneous deformation has been observed in optical images of the chips machined from Ti64 plates with increasing thickness reduction (Fig. 1.18). The initial texture of the plate influenced the ease of deformation in intense shear bands leading to crack formation, while strain hardening determined the stress increment required to reach a value for fracture to initiate at the free surface of chip. Prism slip turned out to have the highest Schmid factor in the annealed as-received Ti64 plate with respect to the shear direction in the primary shear plane. In addition, among all the slip systems, prism <a> slip has the lowest CRSS and thus it is easy for severe shear deformation to take place in annealed as-received material. In contrast, basal <a> slip has highest Schmid factor in the cold-rolled Ti64 plates [87]. However, the Schmid factors are calculated based upon the general texture, not the local grain orientations. Also, the investigation basically attributed the formation of segmented chips to the preferred slip systems depending on the texture detected.

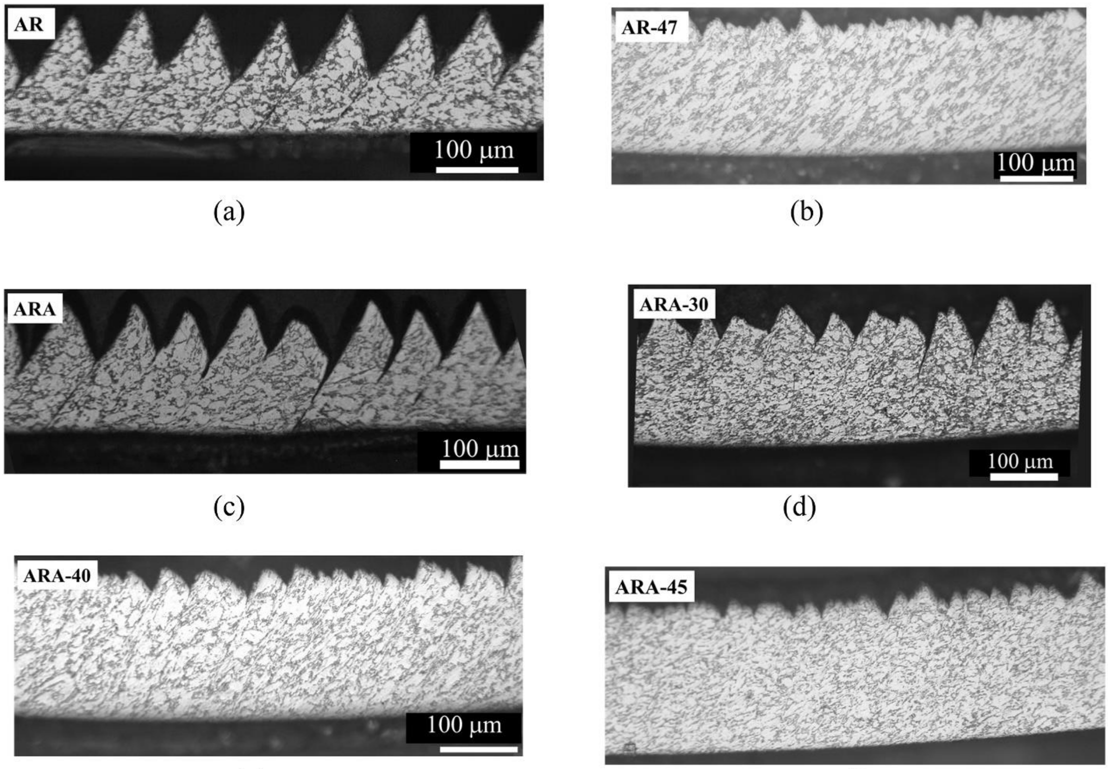

(a) (b) (c) (d) (e) (f)

Figure 1.18 Optical micrographs of chips machined from plates subjected to different thermo-mechanical processing conditions: as-received(AR), as-received material annealed and cold-rolled (ARA) and the number indicates the cold rolling reduction percentage [87].

1.4 Shear bands in other severe deformation process

Adiabatic shear deformation is used to describe the localization of plastic flow that occurs in many metals and alloys when they are deformed at high strain rates to large plastic strains, for instance, in high speed torsion and compression, ballistic impact, machining and explosive fragmentation [88]. It is usually manifested as zones of intense shear deformation and/or microstructural modification of the original material, up to hundreds of microns wide, interspersed between regions of lesser and relatively homogeneous deformation. Adiabatic shear has been interpreted theoretically in several ways. Flow localization in shear is attributed to the destabilizing effect of the thermal softening which can outweigh the effects of strain and strain rate hardening in a deforming region when the local rate of heat generation resulting from the plastic flow exceeds the rate of dissipation into the surrounding material. By assuming negligible stain rate sensitivity, and that the onset of shear localization coincides with the maximum in the local shear stress-shear strain curve, the susceptibility of metals to adiabatic shear banding can be easily predicted. The observations of the frequent occurrence of shear bands in aluminum, titanium, uranium, and steels during the ballistic impact is in accord with these predictions. Adiabatic shear banding is an important deformation mode and the shear zones later become sites for eventual failure of the material. Once intense shear localization has commenced, steep strain, strain rate and temperature gradients are generated perpendicular to the plane of localization and change with time. These parameters and the evolution of the shear bands have not been well understood, but material properties definitely play an important role in determining the final widths and structures of these shear bands.

Shear bands in metals and alloys can be classified as either transformed or deformed, on the basis of their metallographic appearances. The transformed shear bands refer to those with a permanent change in microstructure, whereas deformed shear bands are manifested as zones of intense shear deformation consisting of the original microstructure. The temperature rise in the transformed shear bands is thus supposed to be higher than the deformed one. In steels, the transformed shear band is generally martensitic, and the shear deformation is sufficiently localized. Shear bands in $\alpha+\beta$ titanium alloys exhibit broadly similar behavior. This implies that the transformed shear band is associated primarily with phase transformation in the shear band, and hence restricting the number of alloy systems in which it can form. The resistance to adiabatic shear deformation of different alloys was evaluated via critical strain and relative critical strain rate to form shear zones of comparable width and plotted in Fig. 1.19. It can be seen that metals with low thermal diffusivity and low resistance to adiabatic shear localization are more susceptible to the formation of transformed shear band. CP Ti, Ti64 and 4130 steel tend to form transformed shear bands, while 1020steel and aluminum alloys tend to form deformed shear bands. Pure copper and pure aluminum rarely form discrete shear bands, but rather zones of diffuse shear. Low thermal diffusivity may cause the local temperature to rise rapidly at an early stage of deformation, to exceed the transus temperature, or even perhaps to melt the shear band material under extreme conditions. The phase transformation may be achieved by the rapid diffusion of various atomic species at elevated temperatures within a very short time (typically up to tens of microseconds). For instance, it is noteworthy that in pure titanium the self-diffusion coefficient of pure α jumps from 10^{-12} to 10^{-9} $cm^{-2}s^{-1}$ for β at the transformation temperature.

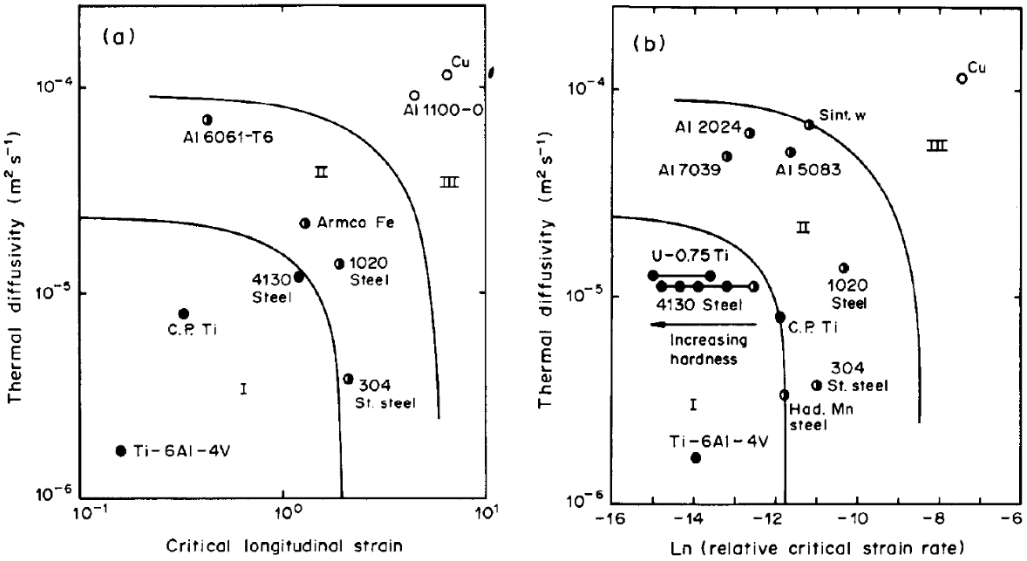

Figure 1.19 Thermal diffusivity at room temperature of different metals plotted against their resistance to adiabatic shear localization (note different logarithmic scales in (a) and (b)). Solid symbols: metals tend to form transformed shear bands (region I); half-open symbols: metals tend to form deformed shear bands (region II); open symbols: metals do not tend to form discrete shear bands (region III) [88].

The adiabatic shear bands of AM50 and Ti64 alloys in the shear compression tests were investigated by Rittel et al. [89]. The true stress and strain curves show three stages in the shear compression process (Fig. 1.20). Stage 1 extends from $\varepsilon = 0$ to $\varepsilon(\sigma_{peak})$. In this stage, plastic deformation is uniform, without localization. The temperature increases modestly with increasing strain. The measured temperature rise is always less than the calculated rise, indicating that some of the energy is stored in the material. Stage 2 spans from the strain at peak stress to the strain at which the measured and calculated thermal curves intersect. In this stage the stress is decreasing, and the measured temperature exceeds the calculated limit past the intersection point. The deformation is not strictly homogeneous, but not yet fully localized either. Generally, the measured temperature below the calculated value, indicating that the underlying assumption of strain homogeneity is still valid to some extent for temperature rise estimation. Stage 3 starts when the calculated temperature is lower than the measured one, showing that all of the mechanical energy transforms into heat. The intersection point of the two temperature curves indicates the onset of the intense localization corresponding to the ASB. The true stress- strain curve no longer represents the real status of the deforming gauge as a result of shear localization and thermal softening is dominant in this stage. Elongated dimples are seen on the fracture surface of Ti64 alloy while extensive wear features are observed for AM50.

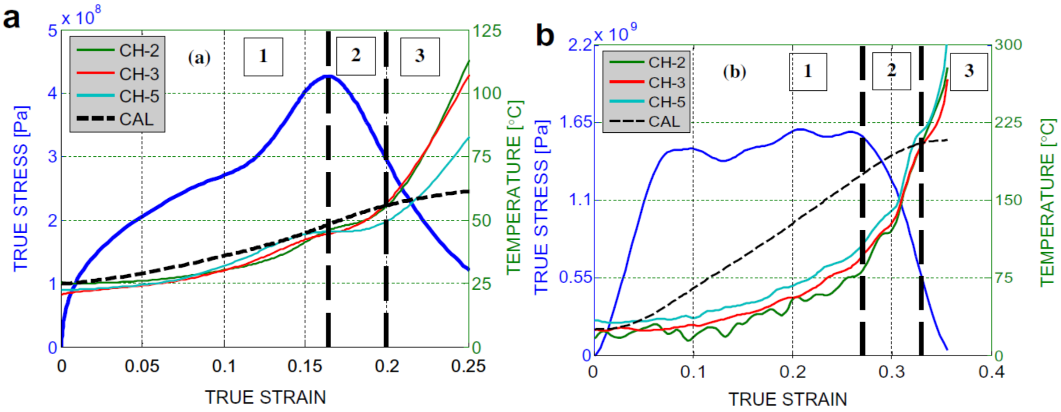

Figure 1.20 Typical stress and temperature vs. strain for (a) AM50 and (b) Ti6Al4V alloys for a strain rate is around 3000s^{-1}. The temperature is measured at three locations and recorded channels 2, 3, and 5, and compared with calculated value (dashed line) [89].

The evolution of multiple adiabatic shear bands of commercially pure titanium and Ti-6Al-4V alloy in a thick-walled implosion experiment is investigated by Xue et al. [52]. The sample was sandwiched between a copper driver tube and a copper stopper tube and is collapsed inward during the test at a strain rate of ~$10^4 s^{-1}$. The shear bands nucleated at the internal surface of the specimens and construct a periodic distribution at an early stage. The thickness of the shear band varied with respect to the distance from its tip. The largest shear band thickness in CP Ti is approximately 10 µm. It is observed that a number of microstructure changes could and did occur within the shear bands, including dynamic recovery and recrystallization, phase transformation and even amorphization, depending on the temperature that can be reached within the shear band. The presence of fine equiaxed subgrains within the shear band, with an average diameter of 0.2 µm provided direct evidence for dynamic recrystallization. The deformation time is lower by orders of magnitude than that required for diffusion. Thus, a rotational recrystallization mechanism by Derby [90] in the classification of dynamic recrystallization, was proposed for the shear bands. In their study, bifurcation (Fig. 1.21) of shear bands is geometrically necessary due to the spiral trajectory of the bands, starting on the internal surface. Similar bifurcation features have been observed in other research [15], [91]. The propagation mechanism of shear bands is a rotation mechanism as illustrated in Fig. 1.22 [92]. Fig. 18 shows the nucleation, growth, elongation and rotation, and the coalescence of the voids within the shear bands. Similar phenomena (Fig. 1.23) are also observed in the SHPB compression tests [15].

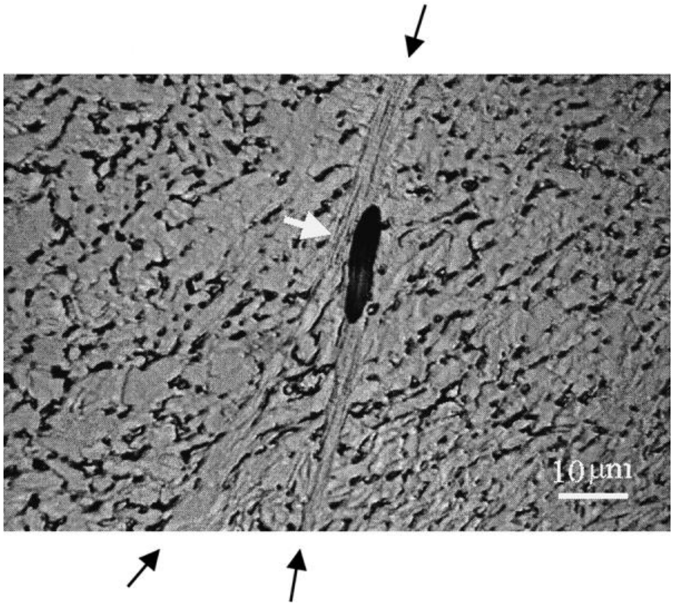

Figure 1.21 Shear band bifurcation and induced damage in Ti– 6Al–4V alloy [52].

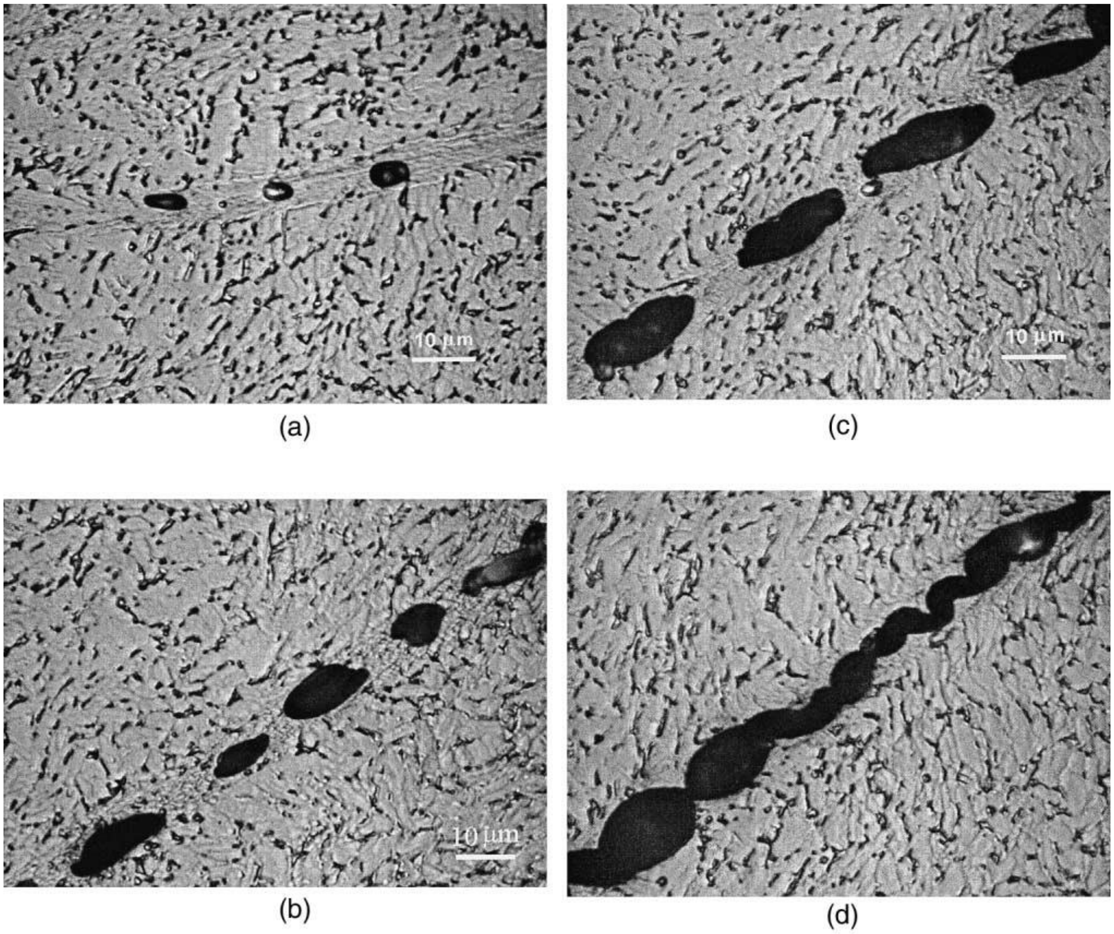

Figure 1.22 Void nucleation and growth inside a shear band in Ti–6Al-4V alloy: (a) nucleation of voids within a shear band; (b) growth of voids; (c) elongation and rotation of voids; (d) coalescence [52].

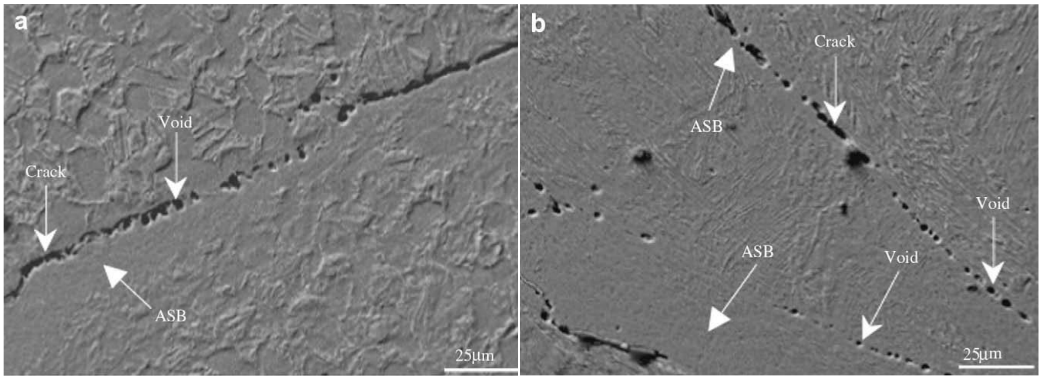

Figure 1.23 The nucleation, growth, and coalescence of micro-voids in the interfaces between ASBs and matrix bulk [15].

Adiabatic shear bands are usually studied by the method of ballistic impact tests. Meyers et al. [92] investigated the microstructure of the adiabatic shear band in commercially pure titanium in the ballistic impact test. A CP Ti plate with a thickness of 12.5 mm, was impacted by a cylindrical steel projectile with a diameter of 3 mm at the velocity of 600 m/s. The penetration into the target was about 6 mm. ~15 shear bands were observed on the section along the axis of projectile. The widths of the bands varied between 1 and 10 microns. Regions away from the shear bands, but close to the impact surface show abundant twinning. In the boundary between the shear band and matrix, very small grains and well-defined grain boundaries within the shear bands can be observed. The selected area diffraction (SAD) pattern of the matrix shows HCP reflections from one crystal ($[1\bar{1}01]$ zone axis), while the SAD pattern of the shear band shows a discontinuous HCP ring, indicating multiple small grains. The micro-grain morphology doesn't change significantly from the center of the band toward the matrix, indicating that the material did not melt. Solidification would most probably produce columnar grains in the vicinity of the shear band-matrix interface. The grain size ranges from 0.05 to 0.3 microns. The dislocation density in the micro-grains is in general not very high. It seems to be somewhat higher in larger grains. Parallel and regularly spaced Moire fringes indicate that no dislocations exist in small grains.

To better understand the deformation behavior of pure titanium, an adiabatic stress-strain curve was developed. The interpolation of the isothermal stress-strain curves was made by assuming a linear stress strain response at all temps for the tests conducted by Conrad et al. [93], and discussed by Meyers [92]. Low strain-rate data was used due to the unavailability of high strain-rate date. The temperature computation was finished after a shear strain increment of 0.1. In each increment, the area under the stress strain curve was computed and the energy was fully converted to the temperature increase by using the temperature-dependent heat capacity. Catastrophic shear will occur at a plastically deforming location within a material when the slope of the true stress-true strain function becomes zero [57] and is in accordance with the result by Meyers et al. [92]. From Fig. 1.24, the instability sets in at $\gamma = 1$ at a temperature of approximately 350 °C. The critical shear strain predicted by Culver et al. [94] was 1.2-1.4, which is surprisingly close to what was obtained in this study. In some metals, the shear strain within a shear band has been found to reach values of even more than 500. For the Ti64 tested under similar conditions, a shear strain of 5 was found.

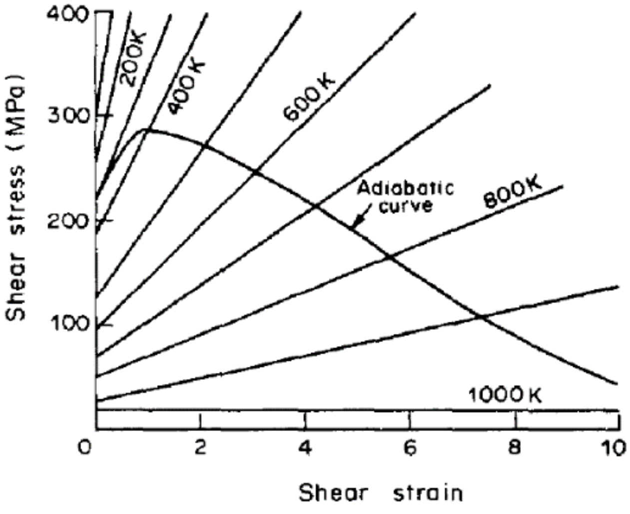

Figure 1.24 Isothermal (straight lines) shear stress-strain response of commercially pure titanium between 100 and 1000 K; adiabatic shear stress-strain curve showing maximum at $\gamma = 1$ [92].

A micromechanical mechanism for the propagation of shear bands has been proposed (as illustrated in Fig. 1.25), although any proposed mechanism for the formation and propagation of the shear bands is speculatory at this point. The temperature rise and thermal softening within the bands were caused by the adiabaticity. As the plastic deformation continued, the band region underwent dynamic recrystallization, leading to the grain size reduction. An equilibrium temperature was achieved at which deformation took place primarily by micrograin boundary sliding. This mechanism is also favored by creep and super-plasticity at high temperature. It is noteworthy that the central part of the micrograin won't undergo significant plastic deformation and the deformation within the shear band will take place without deforming the grains to the same extent as the global strain. The shear band width could be constant due to the rotations of the micrograins. Also, the dislocations whose generation and motion is the shear mechanism can be annealed out at such high temperature.

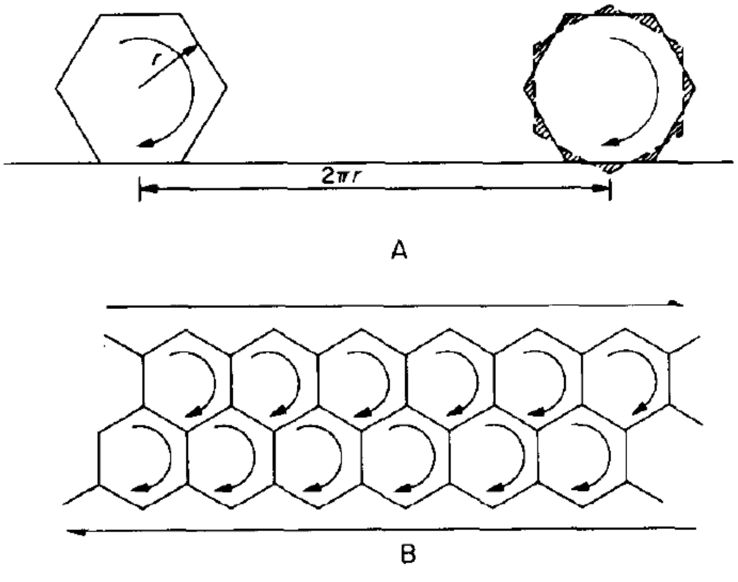

Figure 1.25 Proposed mechanism for shear band propagation involving micrograin rotation and sliding of micrograin boundaries. (A) Microngrain rotating by 2π and translating by 2πr in process; hatching indicates regions in which substantial plastic deformation has to take place. (B) Array of rotating micograins producing translation of upper part of band with respect to lower part [92].

1.5 Critical assessment of understanding of adiabatic shear in Ti64 cutting

Although many attempts have been made over the past decades regarding machining Ti64 alloy, there is still lack of understanding of the formation of the segmented chips. Relevant questions include:

1) Which mechanism is dominant when forming the segmented chips, cracking or adiabatic shearing?
2) How to estimate the homogeneous shear strain and the catastrophic shear strain and how does the cutting speed affect them?
3) What is the correlation between the shear strains and the two mechanisms of segmented chip formation?
4) Does the microstructure and local crystal orientation influence the morphology of the segmented chips? If so, how do they influence and what crystal orientation is beneficial for the formation of adiabatic shear?
5) Is there direct evidence of the α → β phase transformation during cutting?

Thus, the aim of the present study is to further investigate the formation of segmented chips from the perspective of materials science, based upon the local stress tensor revealed by FE simulation and local orientations characterized by electron backscattered diffraction (EBSD).

In the present dissertation, stress tensor obtained from finite element numerical simulation will be adopted for Schmid factor analysis and compared with the simplified plane strain compression assumption. Detailed information on the constitutive model and material constants, as well as other experimental methodologies will be introduced in Chapter 2. Chapter 3 contains the initial microstructures of solution treated and aged (STA), mill annealed (MIL), elongated (ELO) and lamellar (LAM) grade Ti64. Preliminary observations of the chips obtained from cutting these four grades are introduced in Chapter 4. In Chapter 5, the model that predicts the shear band width and another model that calculates both the homogeneous shear and catastrophic shear in the chips, are introduced and adopted to compare the effect of cutting speeds on the formation of segmented STA chips. More cases are incorporated, analyzed, and discussed in detail in Chapter 6, in order to reveal the rationale behind the nucleation of cracks and adiabatic shear band. Annealing of STA chips at 500, 600 and 650 ℃ were carried out to examine how the deformation microstructure responds to heat treatment as a forensic means to infer the state of the deformed chip, and the results are discussed in Chapter 7.

CHAPTER 2 METHODOLOGY

2.1. Turning experiments

The chips used in this study were obtained from dry turning experiments performed on a solution-treated and aged (STA) Ti64 bar with a diameter of 12.7 cm and a length of 64.8 cm, obtained from Rolled Alloys Inc. Fig. 2.1 shows three schematic views of the turning experiment where the observed cross section of the chip is illustrated in Fig. 2.1 (c). The original as-received bar microstructure was characterized on the surface perpendicular to the radial direction, which is the same material orientation that is viewed on the chip. The bar was turned at cutting speeds of 1, 1.5, and 2 m/s (61, 91, and 122 m/min), respectively, where 1 m/s is a typical industrial cutting speed. The 1.2 mm depth of cut and 0.127mm/rev feed rate were kept constant for all turning experiments. The cutting tools were uncoated H13A grade tungsten carbide (WC) tool from Sandvik Coromant© with 6% cobalt binder, 0° rake angle, and 15° leading angle. Additional information about the tool, cutting geometry, and the turning machine are available in [84].

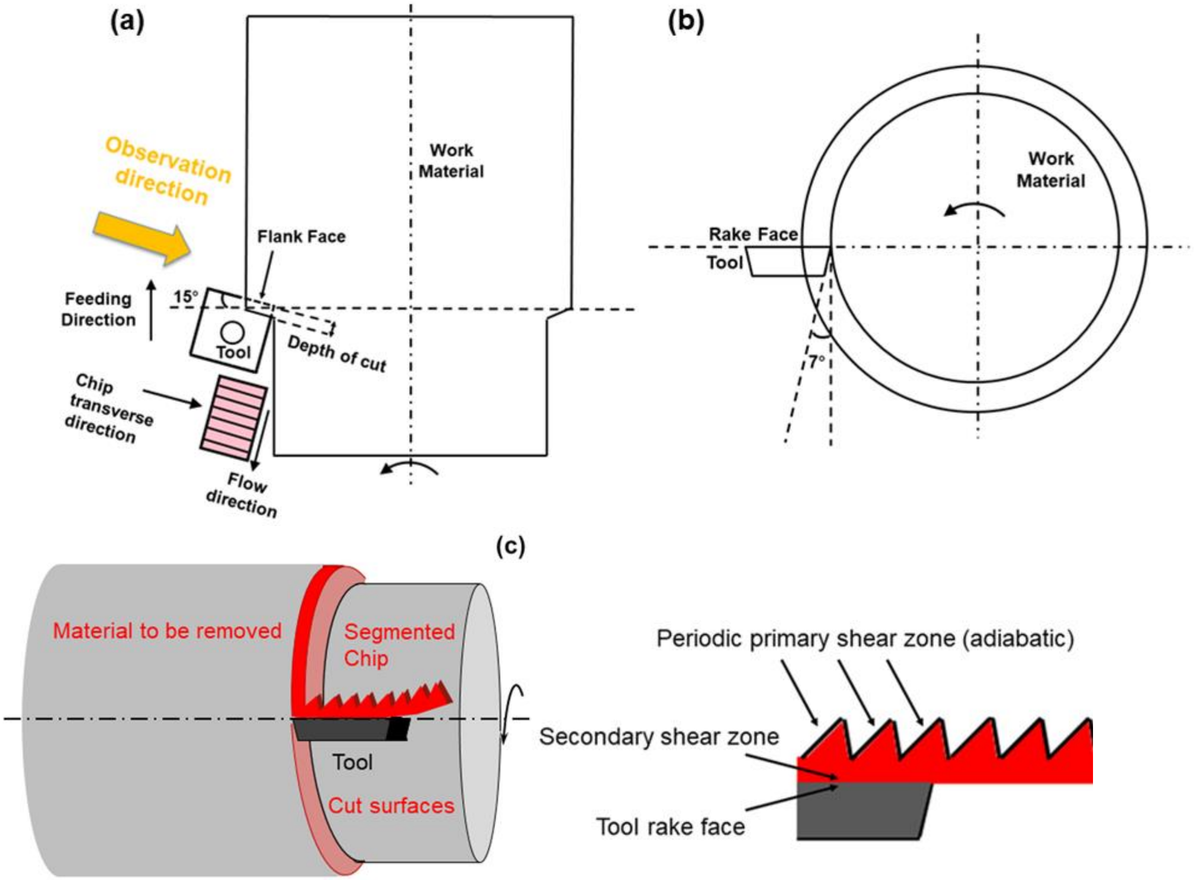

Figure 2.1 Geometry of the turning experiment (a) top view; (b) side view along the turning axis; (c) view from the bar radial direction, which is close to the observation direction of the segmented chips [95].

2.2. Mounting the chips

Since the chips were curved in a three-dimensional way, a steel supporting clip was used to hold the chips so that the intended cross section could be polished after mounting them in conductive Bakelite using a hot press. The stainless-steel clip also provided the means to maintain a stiff load path between nano-indenter and the base platen in the nanoindentation machine. After mounting, the chips were ground using 400 to 2000 grade SiC papers until a thickness reduction of ~ 0.8 mm to observe the middle of the chip since the stress state on the two sides and in the middle are quite different (as discussed in Chapter 3). The samples were then polished using OPS (Oxide Polishing Suspension) 0.8 μm Colloidal Silica for 2-3 h to achieve mirror-like surfaces.

2.3. Nanoindentation arrays

A Hysitron TI 950 Triboindenter equipped with a Berkovich indenter was used for the nanoindentation arrays on as-received material, 1 m/s and 2 m/s chips. A matrix of 400 (20 × 20) indents covering an area of 30 μm × 30 μm was used with a spacing of 1.5 μm. Nanoindentation measurement arrays were obtained using the high-speed mode of the instrument, with loading-holding-unloading times of 0.1-0.1-0.1 s and a maximum load of 3000 μN, resulting in penetration depths in the range of 100–150 nm. Hardness and reduced modulus were derived using the Oliver and Pharr method [96].

2.4. SEM and EBSD characterization

The microstructure of the as-received material and chips obtained after cutting at 1 m/s and 2 m/s were observed using a Tescan Mira or an Orsay Holding scanning electron microscope (SEM) with an accelerating voltage of 25 keV, working distance of 15 mm, under the backscattered electron (BSE) detector. Orientation mapping of both the as-received material and the chips was investigated using an Ametek (TSL) orientation imaging microscopy (OIM) system on the TescanMira, or using an hkl system (Oxford Instruments) on the Orsay Holding SEM with a step size of 0.25 μm. Analysis and cleanup of EBSD data (including one iteration of neighbor confidence index (CI) correlation followed by grain CI standardization clean-up) was conducted using OIM Analysis software v.8.5.0. The method for identifying the width of shear bands is based upon discontinuities in the shapes of deformed α_p grains that were sheared. The shear band width is determined to be the distance between the parallel lines where the shape of the equiaxed α_p grains become severely elongated, as illustrated schematically in Fig. 2.2.

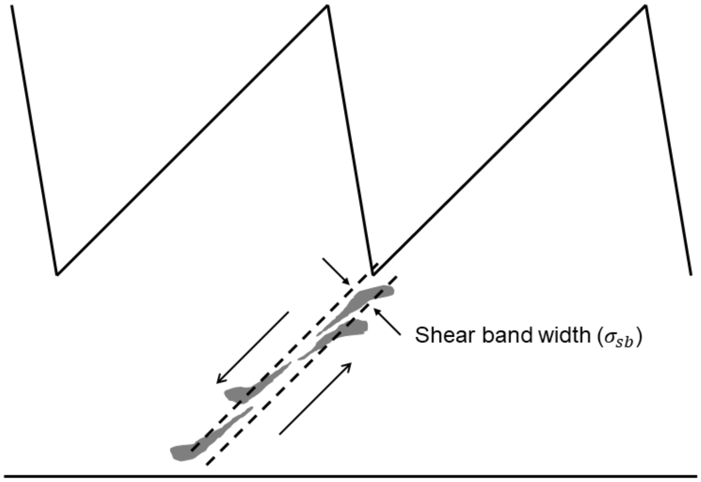

Figure 2.2 Schematic illustration showing shear band width determination. The distance between discontinuities in the shape of globular α_p grains is used to define the shear band width (σ_{sb}). The shear band usually contains multiple highly sheared α_p grains [95].

2.5 Finite element analysis

To estimate the interaction between the tool and the work material, a 2-D FEA numerical simulation of the Ti64-STA machining was performed using DEFORM-2D v.11.2 commercial software [97]. The numerical model was based on a plane strain orthogonal cutting geometry that approximates turning using a Lagrangian approach that allows continuous remeshing in the highly deformed chip. The tool was modeled as a mechanically rigid body but with a meaningful thermal conductivity to allow the temperature to rise during cutting. A heat transfer coefficient of 20 kW/°C was used to allow fast heat conduction from workpiece into the tool, all initially at 20°C. The initial mesh had 6043 elements for the workpiece and 2477 elements for the tool. A 5 µm mesh size was used in the workpiece close to the cutting zone with a constant shear friction coefficient of 0.9 between the tool and workpiece. There are two approaches utilized to simulate the formation of segmented chips [73], by using damage or material failure models [98]–[100], or by using modified material models with temperature-dependent flow softening based adiabatic shearing [75], [101]. In the present work, the isotropic Cockroft-Latham model damage criterion value was adjusted to a value of 2000 to make the chip segmentation size closer to experimental values. The morphology of the simulated chip is consistent with the actual chips. More detailed information can be seen in [97].

2.6 IPF maps and pole figures

(110) and $(1\bar{1}0)$inverse pole figure (IPF) maps can also be used to visualize the soft and hard orientations better with respect to the shear direction. However, rotations about the $< 0001 >$,$< 10\overline{10} >$ and $< 11\bar{2}0 >$ by any degrees will still exhibit red, blue and green colors. This is the intrinsic problem with IPF maps and as a result no choice is perfect. The (001) IPF maps, most commonly referred to as the normal direction IPF maps, are widely used. In the present study, the normal IPF maps are used consistently.

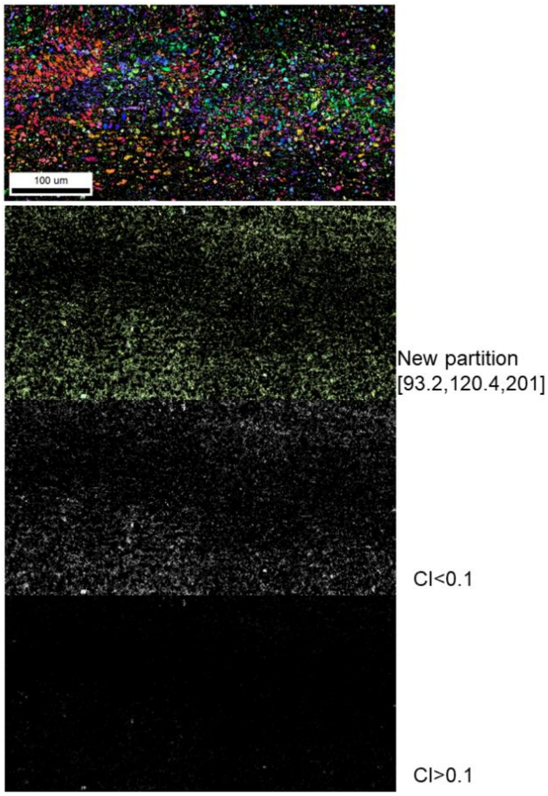

Figure 2.3 Confidence index (CI) distribution of the selected orientation (Eulers=[93.2, 120.4, 201]) shows that CI>0.1 can eliminate a number of noise from the scan.

The normal IPF mapping of the as-received Ti-4Al-6V bar is shown in Fig. 2.3. The pole figures of the scan show a pronounced peak with the Euler angles of [93.2, 120.4, 201]. A partition of this orientation has been made to further analyze this corresponding peak on the pole figure. The CI distribution map showed that most of these data points have CI<0.1. This indicates that these are the noise points that contribute to the majority of this peak. So CI>0.1 is crucial for omitting the noise points. For the as-received material, both the α_p and β_t (α laths in β_t) can be indexed and the criterion to distinguish the two microconstituents in a course scan is their image quality (IQ) value. Presumably α_p has higher IQ values than β_t. As can be seen in Fig. 2.4, the pole figures of these two microconstituents look similar and β_t has made slightly higher contributions to the micro-texture. It is interesting to note that the transformed β has a strong orientation relationship with the primary α. It is important to make this clear since no information of β_t in the chips can be collected in deformed chips, probably due to the severe deformation in the material. In summary, the pole figures are plotted with CI>0.1 and IQ > 50%.

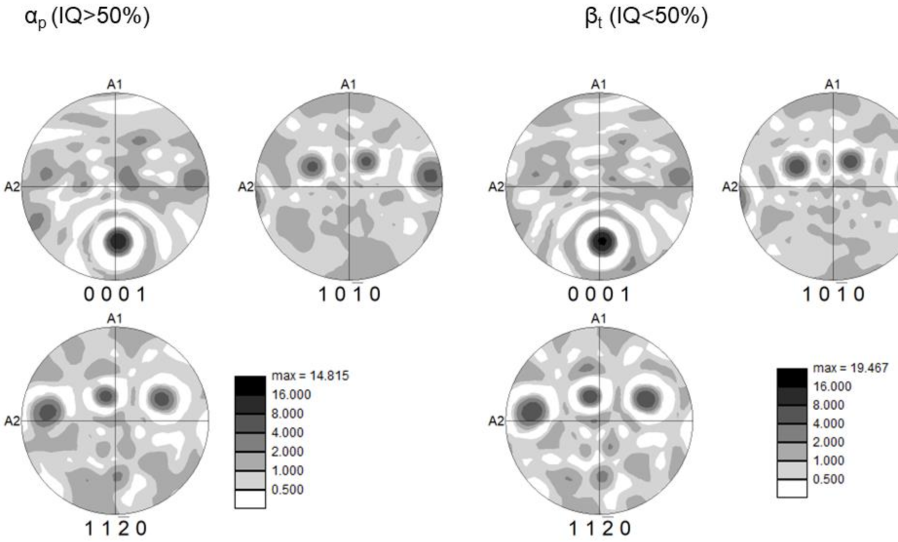

Figure 2.4 The pole figures based upon the contributions of α_p and β_t microconstituents show that β_t contribute a little more to the peak intensity than α_p.

2.7 Rotation of stress tensor from FE simulation

To apply the stress tensors from the FE simulation to the crystal orientations for Schmid factor calculation purpose, they have to be rotated between the two coordinate systems. The stress tensors obtained from the simulation results are in the coordinate system with x-axis pointing down and y-axis pointing to the right. They need to be rotated when calculating the Schmid factors in the coordinate system with x-axis pointing up and y-axis pointing to the left. The rotation matrix is determined to be:

$$R = \begin{bmatrix} cos\pi & -sin\pi & 0 \\ sin\pi & cos\pi & 0 \\ 0 & 0 & 1 \end{bmatrix} = \begin{bmatrix} -1 & 0 & 0 \\ 0 & -1 & 0 \\ 0 & 0 & 1 \end{bmatrix}$$

Taking the stress tensor at point #5 for example, the stress tensor in the EBSD coordinates is determined to be:

$$\sigma'_{P5} = R * \begin{bmatrix} 303 & -279 & 0 \\ -279 & 45 & 0 \\ 0 & 0 & 174 \end{bmatrix} * R' = \begin{bmatrix} 303 & -279 & 0 \\ -279 & 45 & 0 \\ 0 & 0 & 174 \end{bmatrix} = \sigma_{P5}$$

This indicates that the stress tensor stays in the same form as in the cutting simulation setting, because the stress tensor is symmetric. The illustration of the three principal stresses (in chapter 5) also reveals the symmetry of the stress tensor so that the rotation about z-axis by 180° doesn’t change the stress tensor.

CHAPTER 3 UNDEFORMED MICROSTRUCTURES OF THE AS-RECEIVED BARS

The microstructures and micro-textures of the four as-received Ti64 bars were first investigated in order to provide the basis for comparing the chips from the various grades. Observations of the segmented surface, smooth surface and the cross-section of the various chips will be presented in the next chapter.

3.1 Microstructure and textures

Four 4 different grades of Ti-6Al-4V alloy bars were studied, namely solution treated and aged (STA), mill annealed (MIL), elongated (ELO) and lamellar (LAM). The representative microstructures of the STA, MIL, ELO and LAM Ti64 alloys are shown in Fig. 3.1. The STA alloy in Fig 3.1 (a,e) has the typical bimodal microstructure, consisting of ~50 vol. % primary α_p (darker grains), and ~50 vol. % transformed β_t, which is also referred to as lamellar $\alpha+\beta$ regions (brighter regions) [84]. The MIL grade alloy in Fig. 3.1 (b,f) exhibits equiaxed dark α grains with white β phases on the grain boundaries. In contrast, elongated α grains with β phases on the grain boundaries are present in ELO grade in Fig. 3.1 (c,g). The images of the LAM grade in Fig. 3.1 (d,h) have fine β lamellae (straight white lines) and large prior β grain size.

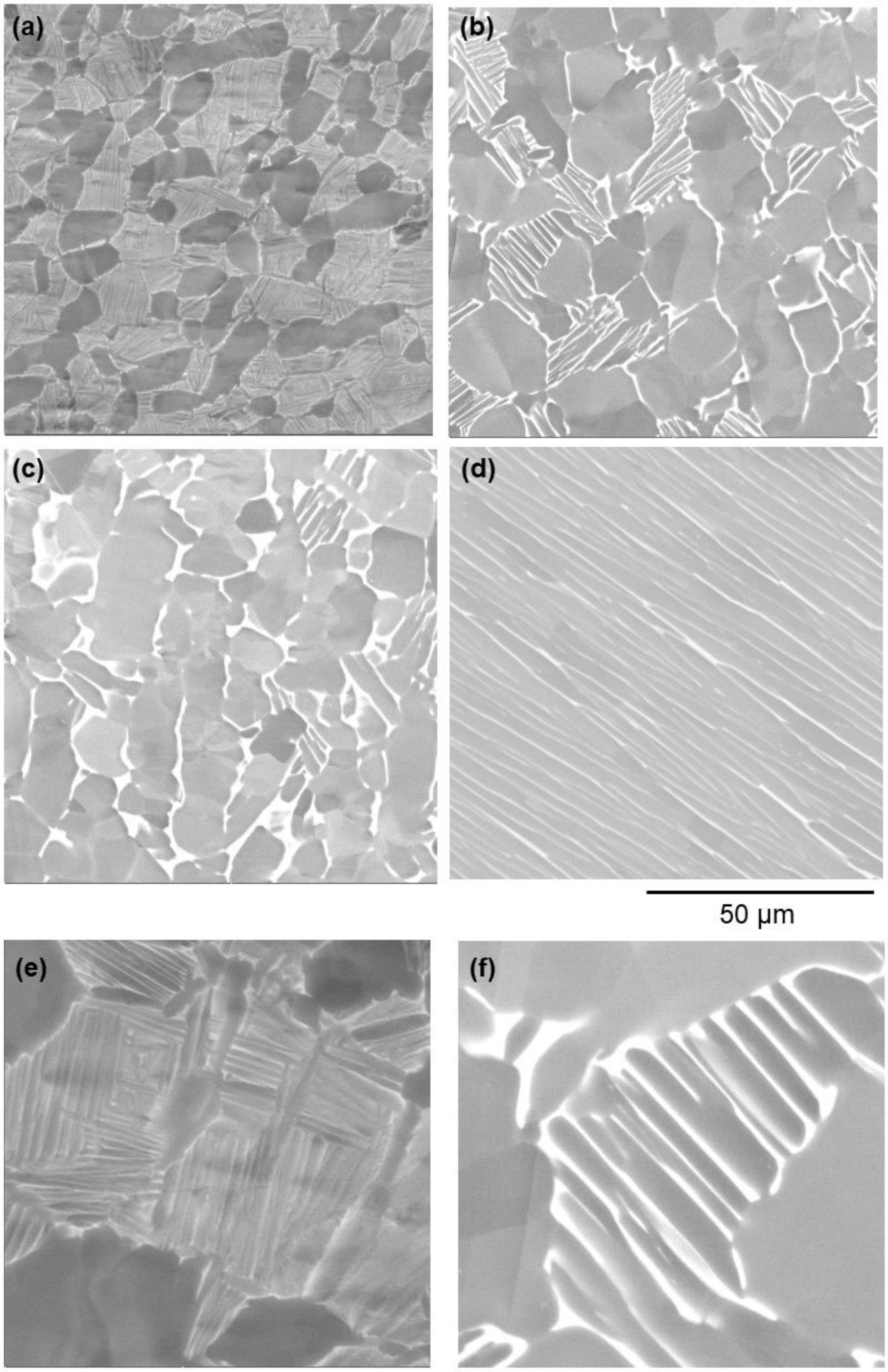

Figure 3.1 Representative microstructure of (a) solution treated and aged (STA); (b) mill annealed (MIL); (c) elongated (ELO), (d) lamellar (LAM) Ti-6Al-4V ;(e)(f)(g)(h) show the microstructures at a higher magnification. The images at two magnifications share the same scale bar, respectively.

Figure 3.1 (cont'd)

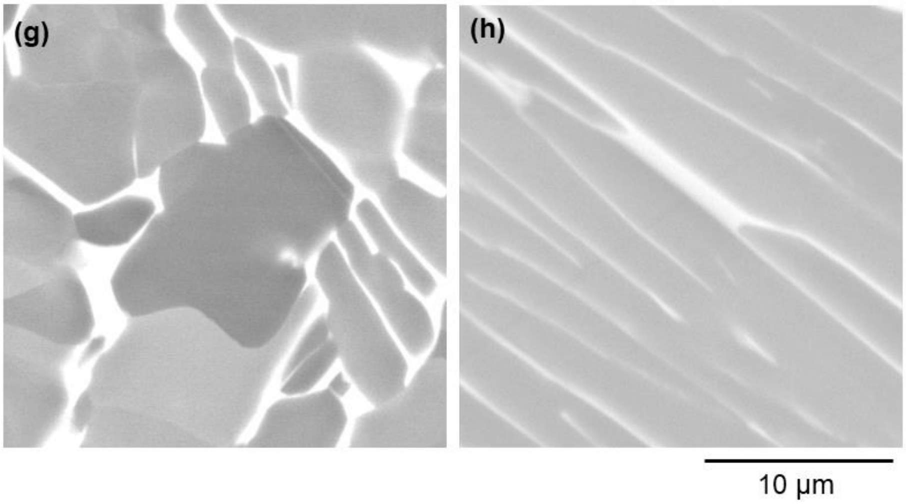

Fine EBSD scans of STA, MIL and ELO alloys can be seen in Fig. 3.2. In general, the β phase in all three alloys cannot be indexed by OIM. In the STA alloy, the secondary α phase in the lamellar regions can be indexed. Lamellar regions may be composed of multiple colonies with various orientations. For the LAM alloy, the size of colonies showing the same orientation is much larger compared to the other three grades, as shown in Fig. 3.3. The prior β grain size can be greater than 1 mm and this leads to a significantly different chip morphology as described in Chapter 4.

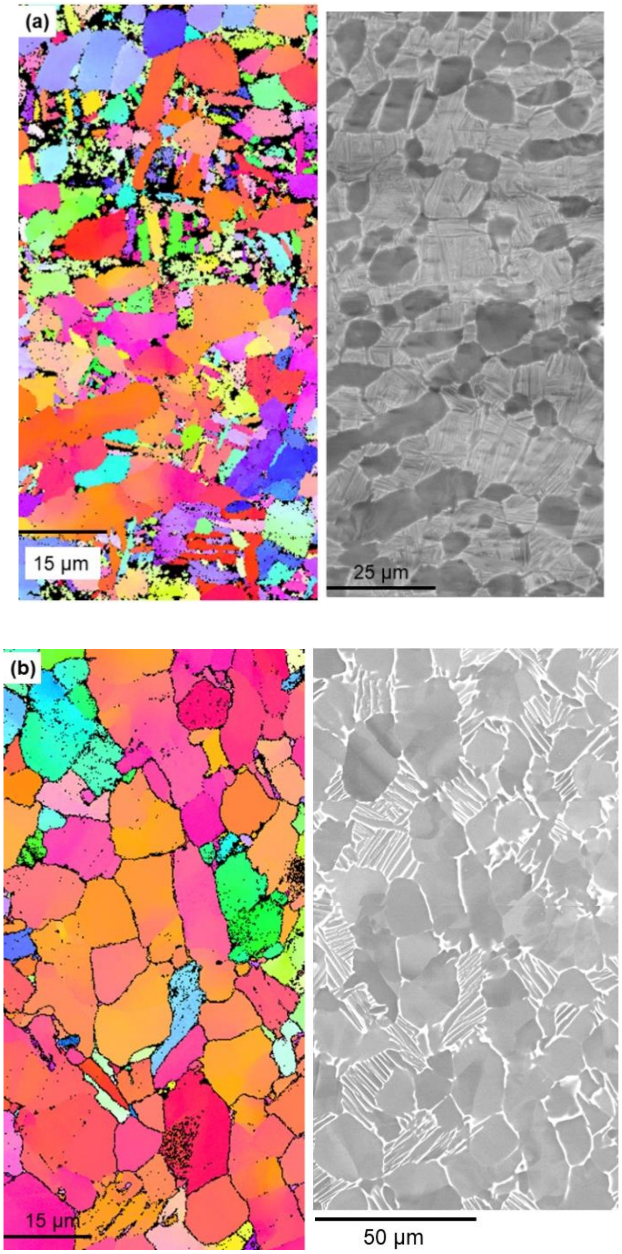

Figure 3.2 Electron backscattered diffraction (EBSD) normal direction inverse pole figure (IPF) mapping of (a) STA; (b) MIL; (c) ELO Ti64 alloy.

Figure 3.2 (cont’d)

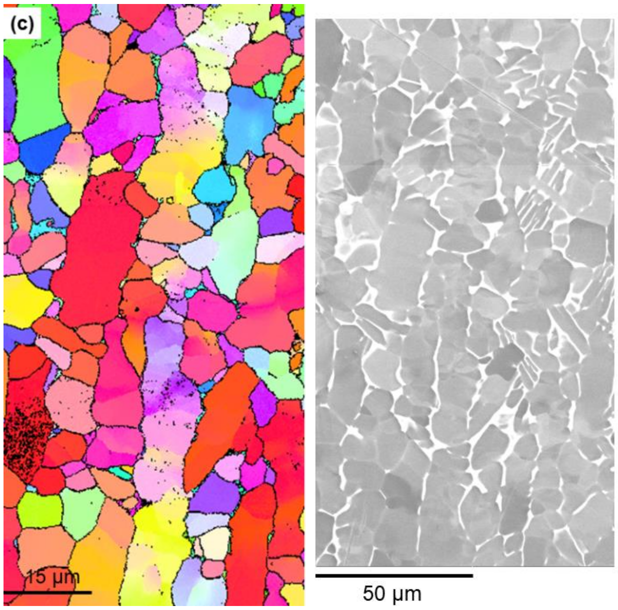

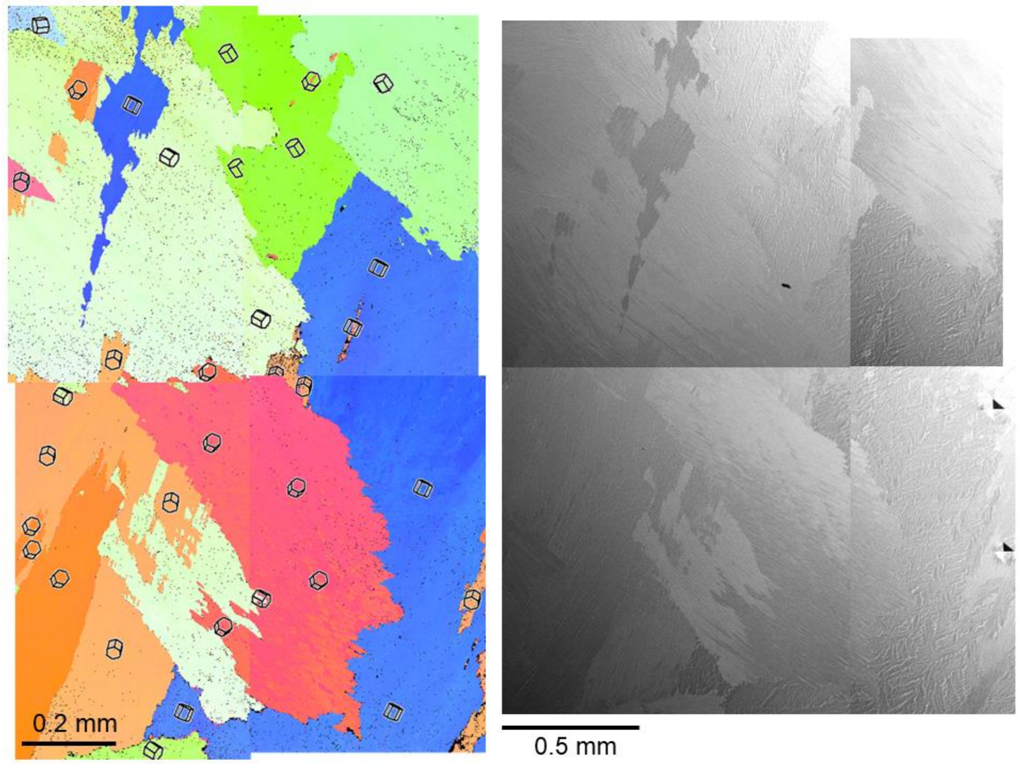

Figure 3.3 EBSD normal direction IPF mapping and BSE image of lamellar (LAM) Ti64 alloy. The grain size of LAM alloy is huge compared to STA, MIL and ELO grades.

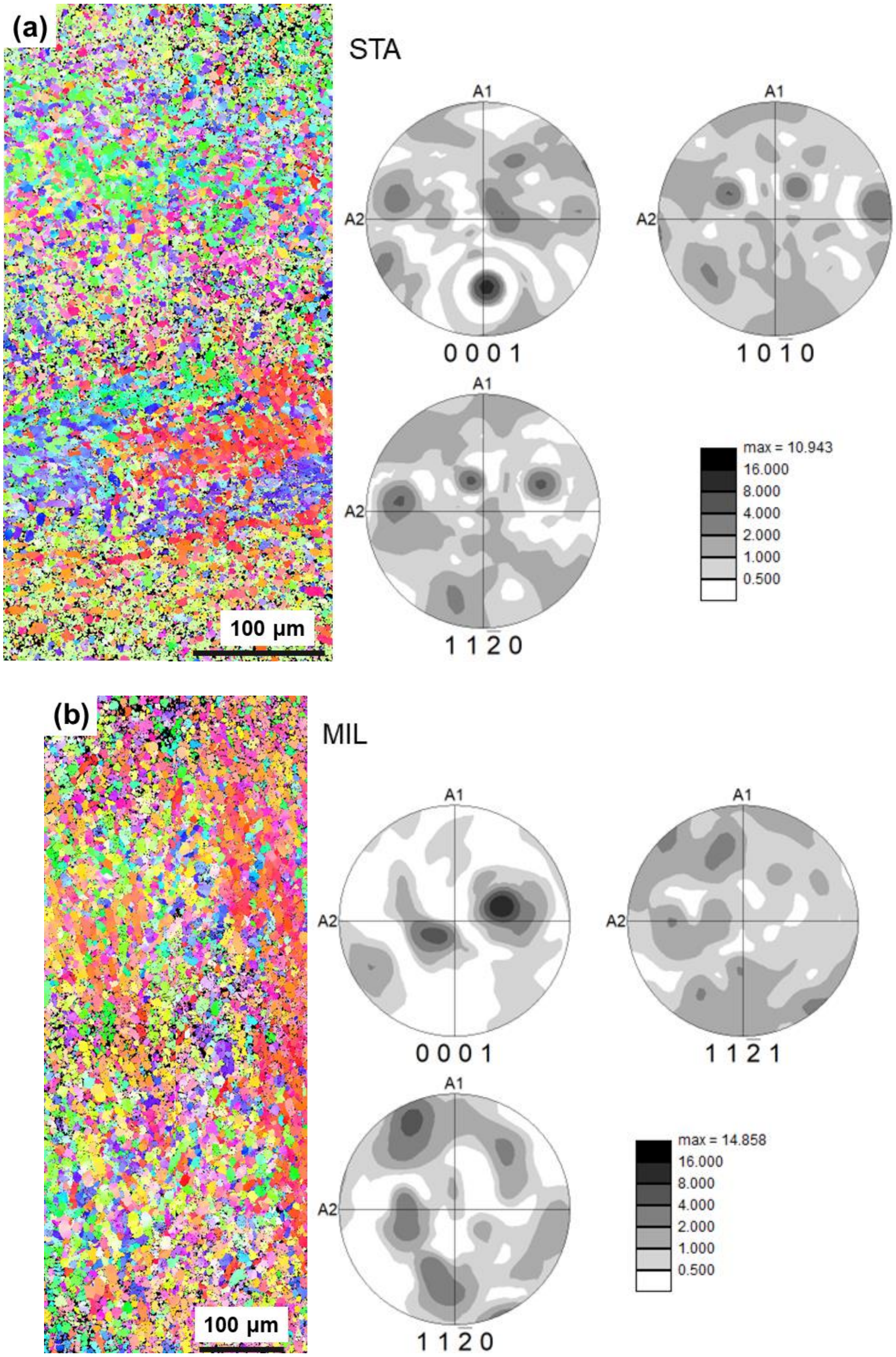

Figure 3.4 EBSD normal direction inverse pole mapping and corresponding pole figures that show the macro-texture of (a) STA; (b) MIL; (c) ELO Ti64 alloy.

Figure 3.4 (cont’d)

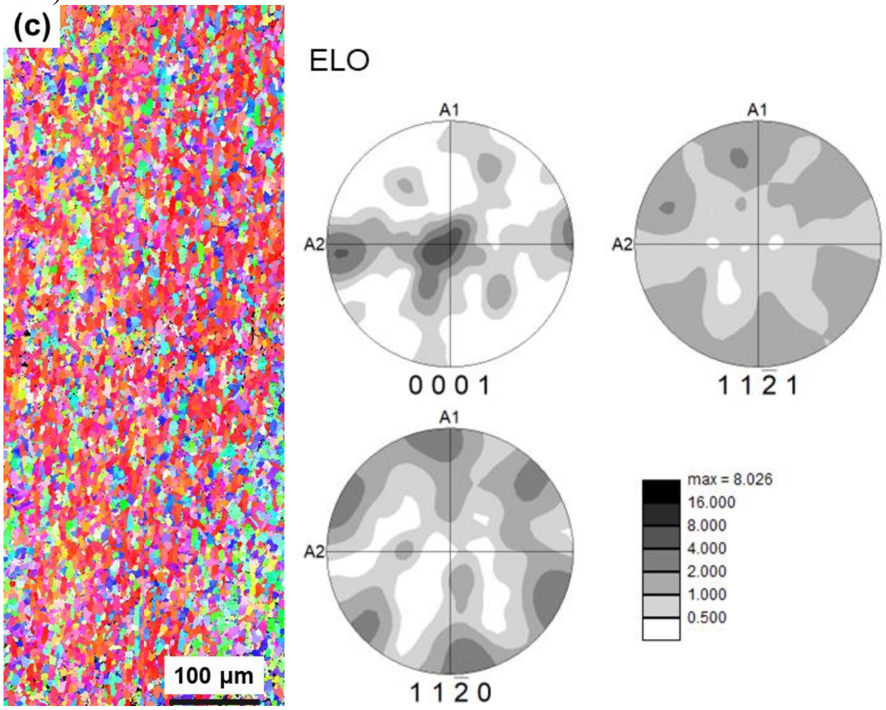

There are many orientations in the STA alloy where each cluster of grains has a similar orientation leading to the presence of micro-texture. For instance, the two clusters with green color located in the upper mid and mid part, the red and blue clusters in the lower mid parts of the IPF color map in Fig. 3.4. These clusters are the reason for the appearance of many peaks on the pole figures. In the MIL-grade alloy, the right margin of the IPF map shows red-colored orientation and the left margin shows green-colored orientations, which explains the presence of three dominant (001) components on the pole figure. The IPF map of ELO alloy shows an overall red-colored orientation, with non-red-colored orientation appearing on the lower right part. The pole figure exhibits a strong basal texture as a result. As described in later chapters, the micro-textureed regions have a strong impact on the machinability of the alloy and the formation of each segment.

3.2 Conclusions

The undeformed microstructures of STA, MIL, ELO and LAM grade Ti64 alloys were investigated. LAM grade has a very large grain size compared to the other three grades and it will affect the formation of segmented chips.

CHAPTER 4 AS-CUT STA, MIL, ELO AND LAM CHIPS

In this chapter, the chips obtained from solution treated and aged (STA), mill annealed (MIL), elongated (ELO), and fully lamellar (LAM) grade Ti-6Al-4V bars are investigated. The initial microstructures of these alloys have been discussed in Chapter 3. Images of the serrations, chip-tool contact surface, and the segmented surface of these chips are compared. In addition, EBSD scans of the LAM chips showed pronounced effect of the initial orientation on the morphology of LAM chips. The favorable slip systems are discussed based upon the maximal Schmid factor calculation under the plane strain compression boundary condition. EBSD and nano-indentation analysis of STA chips reveal the low strain hardening rate of titanium. Portions of this chapter describing the STA microstructure are adapted from a published paper[1].

4.1 As-received STA chips from stable cutting stage

4.1.1 Cross-section observation

The chip morphologies at various scales with the cutting speeds of 1, 1.5 and 2 m/s are shown in Fig. 4.1 The 1 m/s chips were much more curled than the 1.5 and 2 m/s chips. The mounted chips were ground to the approximate middle of the chip for cross-section observation (removed ~0.8 mm). Unlike chips machined at 1.5 and 2 m/s, the micro-morphologies of chips cut at 1 m/s show a number of undeveloped serrations, which can be considered as a transition from continuous to serrated chips [22], [37], [83], [96], [102] (serrations and oscillating load occurs above 0.15 m/s). According to Wan et al. [103], the chips obtained from turning at the cutting speed of 30.2 m/s showed only incipient separation of segments. In the present work, the segments/teeth at 1m/s is much more developed compared with their observation but still less developed than 1.5 and 2

---

[1] Effect of Cutting speed on Shear Band Formation and Chip Morphology of Ti-6Al-4V alloy using Nanoindentation and EBSD Mapping, Jiawei Lu, Ryan Khawarizmi, Miguel Monclús, Jon Molina-Aldareguia, Patrick Kwon, Thomas R. Bieler, *Materials Science and Engineering A* 862 (2023) 144372, DOI: 10.1016/j.msea.2022.144372.

m/s. The microstructure of the chips show that the shear bands in the primary shear zone were oriented about 45° from the chip flow direction.

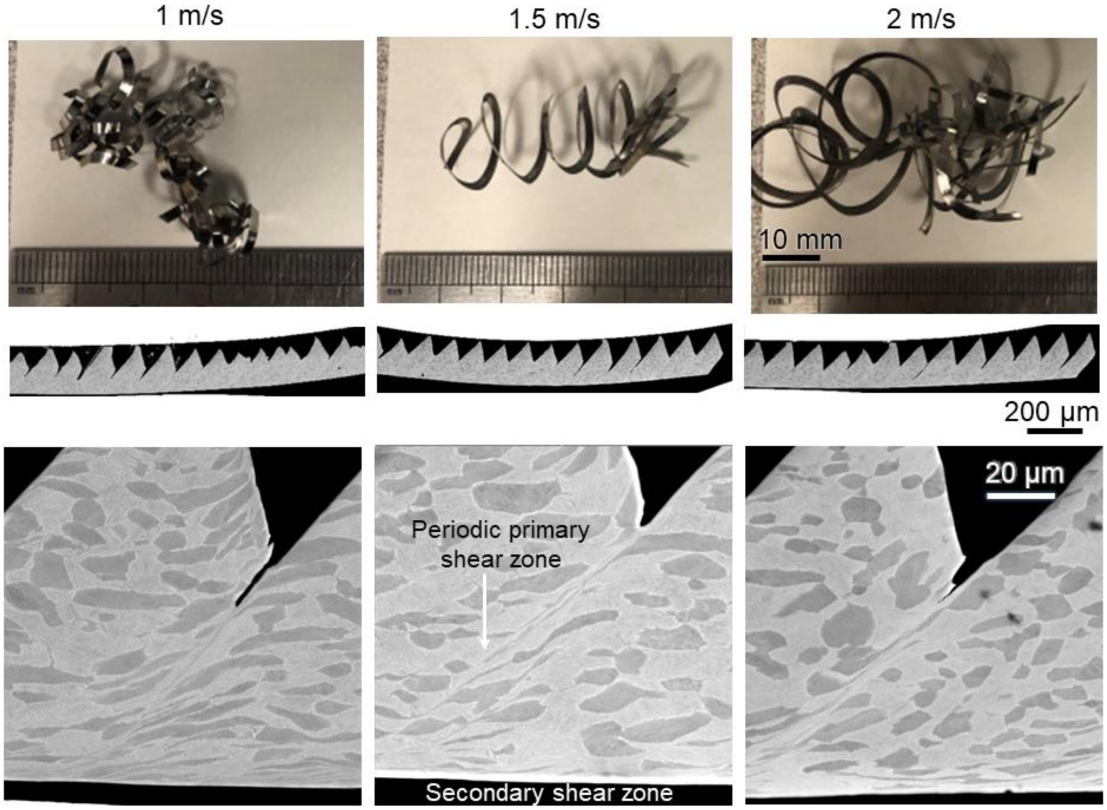

Figure 4.1 The 1 m/s chip is more curled than 1.5 and 2 m/s chips and the serrations resulting from the primary shear zones between serrations are more regularly spaced at higher cutting speeds.

The parameters characterizing the morphology of the chips include: peak height h_p, valley height h_v, and the distance between two neighboring shear bands S. These lead to the definitions of segmentation degree,

$$G_s = \frac{h_p - h_v}{h_p} \tag{1}$$

shear angle,

$$\theta = \frac{\pi}{2} - \theta' \tag{2}$$

where θ' is the angle between the smooth surface of the chip and the direction of primary shear zone [83], the equivalent thickness,

$$t_e = \frac{h_p + h_v}{2} \tag{3}$$

and the segmentation frequency,

$$f = \frac{V_c}{s} \tag{4}$$

From ~70 measurements of segmented chips, all parameters are compared in Fig. 4.2. A slight increase occurred in peak height, equivalent thickness, and shear band spacing from 1 to 2 m/s with a corresponding decrease in the valley height. The shear angle was nearly the same at each speed (42.8°, 43.4°, 43.1°, respectively), which agreed with the observation that the dependence between shear angle and cutting speed in orthogonal cutting is weak at high cutting speeds [49], [104]. The segmentation degree increased significantly from 0.34 at 1 m/s to 0.45 at 1.5 m/s, and further to 0.48 at 2 m/s, indicating that the chip was more segmented with increasing cutting speed. For all of these metrics, the spread of the standard deviation for all three speeds overlap. The frequency of segmentation went up in proportion to the cutting speed, but the frequency at 2 m/s was less than twice that at 1m/s, consistent with an increase in shear band spacing at higher cutting speed.

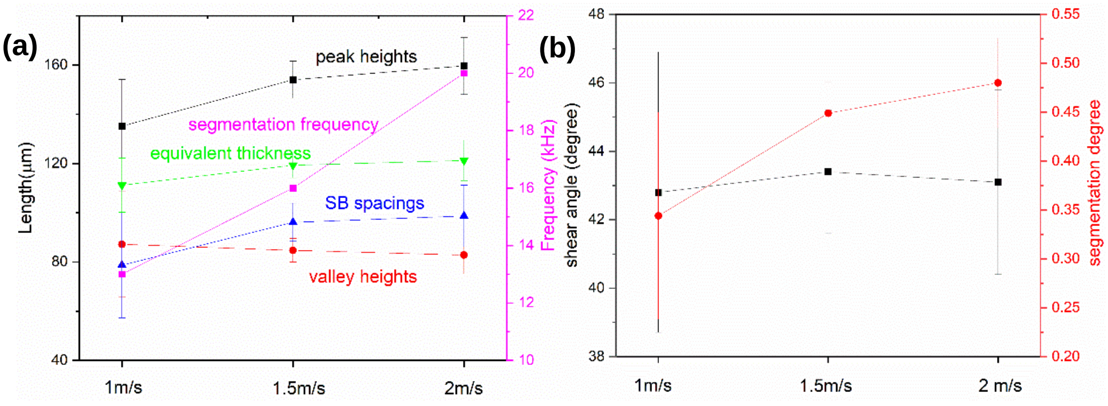

Figure 4.2 Chip segmentation metrics following definitions in [83] vary slightly with increasing cutting speed, with spreads that overlap.

4.1.2 Segmented surface observation

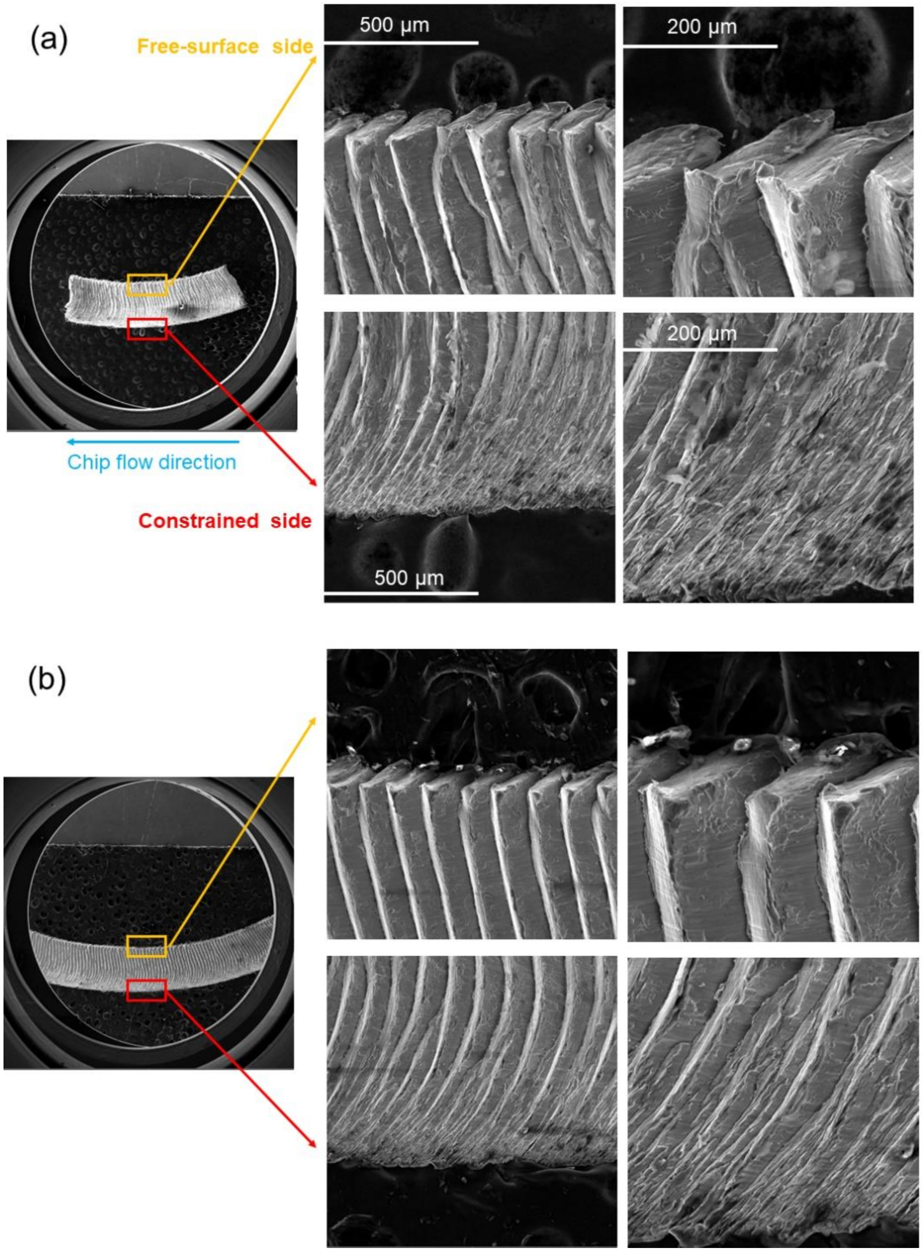

Figure 4.3 segmented surface of the chips obtained at the cutting speed of (a) 1 m/s; (b) 1.5 m/s; (c) 2 m/s. Top and bottom sides are non-symmetric.

Figure 4.3(cont'd)

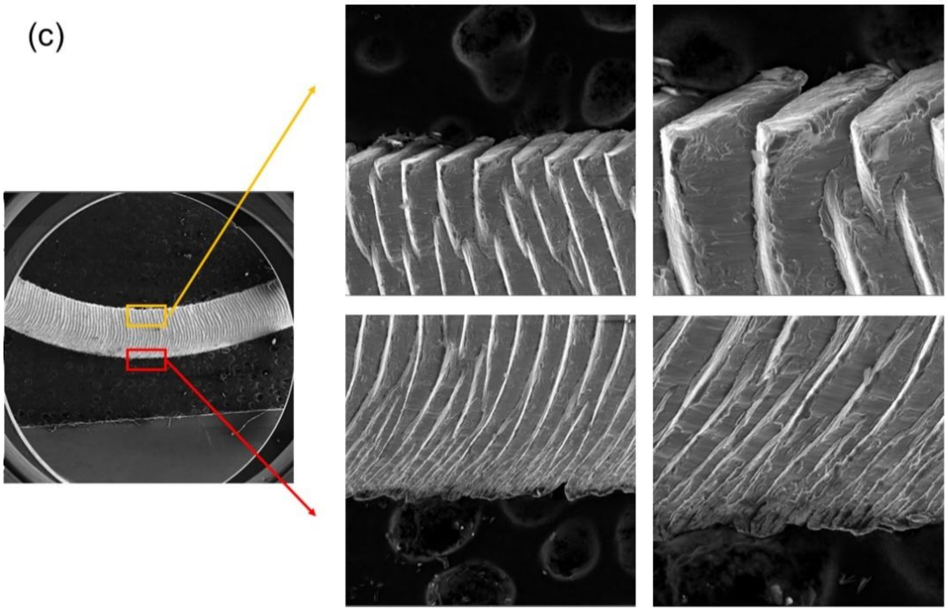

The segmented surface of the chips at 1, 1.5 and 2 m/s are shown in Fig. 4.3. It is interesting to note that the two edges (top and bottom) of the chips are non-symmetric, at all cutting speeds. The top side is rectangular shaped with a certain amount of height while the bottom side is cut from the workpiece with the height of zero, which indicates that the formation of segmented chips initiates from the free-surface side, not the constrained side. This is consistent with the proposal of Vyas and Shaw [47] that the segmented chip is formed due to the initiation of cracks on the free surface of the chip. The chip flow direction on this figure is from right to left as shown by the cyan arrow. This asymmetry is the reason that the cross-section of the chip in the present work is observed in the middle of the chip (removal of ~0.8mm).

4.1.3 Smooth surface observation

The smooth side observations before polishing are shown in Fig. 4.4. At all cutting speeds, there are grooves on the tool-chip contact surface. In addition, it shows that there is not much material removed from tool-chip contact surface on the 1m/s chip surface while many particles have been pulled out at 2 m/s, leaving the scar-like features on the surface, and potentially these particles form the adhesion layer on the crater surface of the cutting tool. The histograms of both teeth spacings and scars are investigated and plotted on Fig. 4.5. The results in Table 4.1 show that the peak of teeth spacing coincides with the peak of scar spacing, especially at 2 m/s, same for the histogram itself. This indicates that material being pulled out on the chip-tool contact surface is highly correlated to the formation of the primary shear zone. A possible explanation for this correlation is the occurrence of α to β phase transformation in the primary shear zone due to higher temperature increase at the cutting speed of 2 m/s. β phase is much softer and stickier than α and thus large chunks of material is adhered to cutting tool. This hypothesis is supported by the observation in Fig. 4.8.

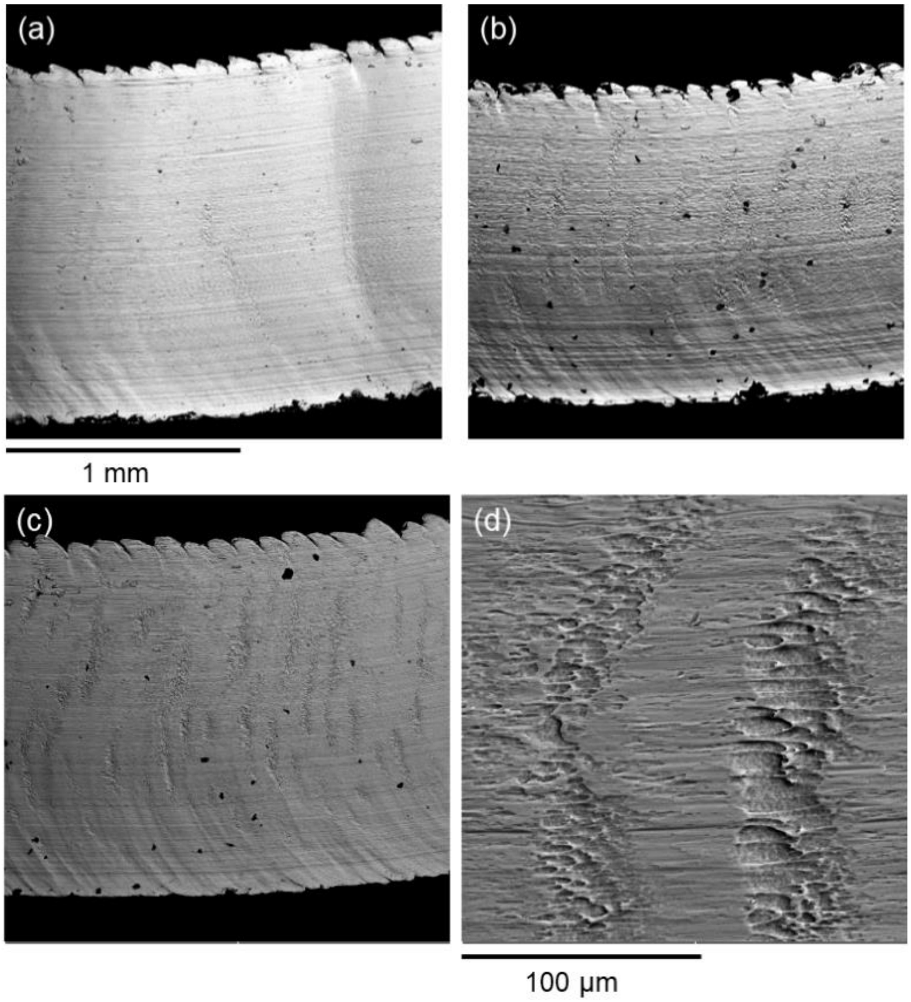

Figure 4.4 morphology of the smooth side of the chips before polishing, magnification of 100X (a) 1m/s; (b)1.5 m/s; (c) 2 m/s and (d) magnification of 500X, 2 m/s.

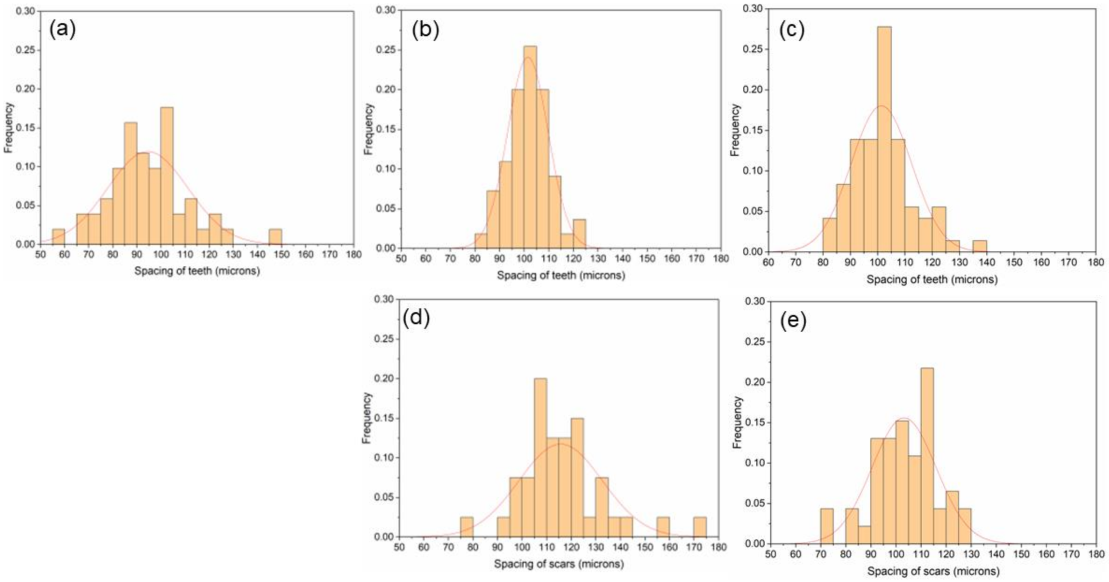

Figure 4.5 the histograms of teeth spacing and scar spacings at the cutting speed of (a) 1 m/s; (b)(d) 1.5 m/s; (c)(e) 2 m/s.

Table 4.1 peak spacing of the teeth and scars showing the stick slip is highly related to the formation of PSZ

	1 m/s	1.5 m/s	2 m/s
Peak of teeth spacing (μm)	95	102	102
Peak of scar spacing (μm)	N/A	115	103

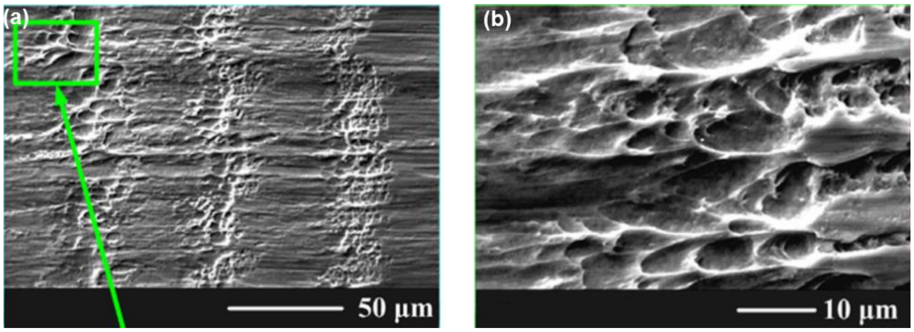

Figure 4.6 Tool-chip contact surfaces at different cutting speeds from [46].

Similar smooth side observation is reported in the work by Ye et al. [46] (Fig. 4.6). When the cutting speed is as low as 0.05 m/s, the tool-chip contact surface is quite smooth. At the cutting speed of 7.8 m/s, the removal of material can be seen in Fig. 4.6 (a). The features in the green box are considered as elongated dimples. The regularly distributed dimple structure on the tool-chip contact surface is related to the periodical shear banding inside the PSZ because their spacings are in accordance. Also, the periodic dimples indicate that the chip movement on the tool rake face is stick slip in nature. At cutting speeds of about 69 m/s, local melting occured at the PSZ root on the rake face. This can be inferred from the formation of fully melted shear bands to render fully discontinuous chips as further increasing the cutting speed.

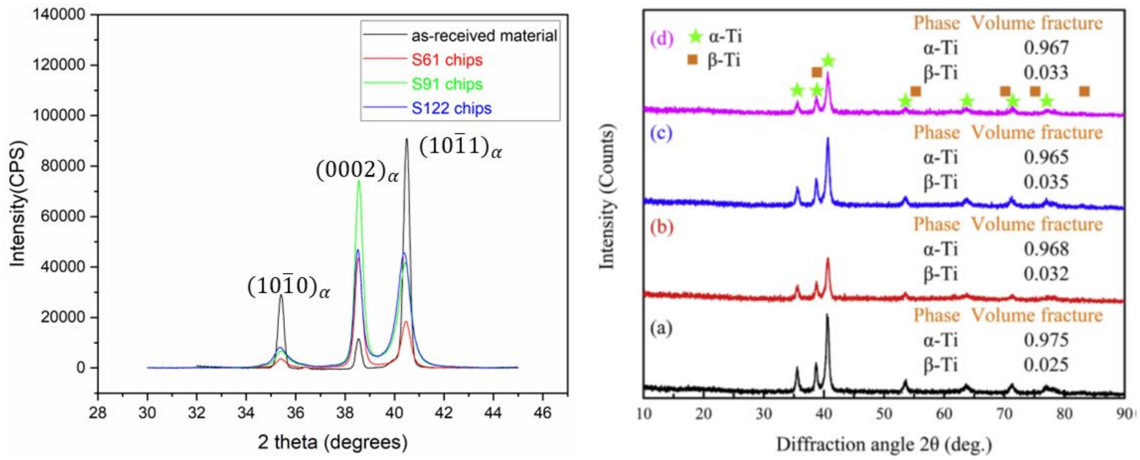

Figure 4.7 Left figure: phase determination on the smooth surface of the 1 m/s, 1.5 m/s and 2 m/s chips. Right figure: Phase analysis of micro-chips formed in micro-milling the (a) first, (b)second, (c) third, and (d) fourth micro-slot [86].

The XRD results on the smooth side of the chips in our investigation (Fig. 4.7 left image) failed to show the presence of β phase. However, XRD results on the milling chips by Wang et al. [86] did attest the appearance of β phase. In addition, the volume fraction of β phase increased slightly with increasing cutting time. The smooth surface after slight polishing without any grinding can be seen in Fig. 4.8. The samples were prepared by only polishing without grinding in order to see the microstructure as close to the tool-chip contact face as possible. The PSZ lines are more pronounced at 2 m/s compared to 1.5 m/s, but they can be barely seen at 1 m/s. Within these PSZ lines, more β phase (white color) can be seen with increasing cutting speed. The volume fraction of β phase on the tool-chip contact face is determined by ImageJ. The result show that β volume fraction increased from 50% (as-received), to 60% at 1m/s, 62% at 1.5 m/s and further to 68% at 2 m/s, as listed in Table 4.2. This provides direct evidence for the phase transformation at higher cutting speed (2m/s). The TEM selected area diffraction results of the chip obtained from turning at 59.6 m/s [103] can also support the phase transformation hypothesis. The diffraction pattern shows the presence of both α and β phases in the ASB [103]. When the cutting speed increases to 126.6 m/min, multi electron diffraction ring pattern appeared, which indicated nanocrystalline in ASB [103].

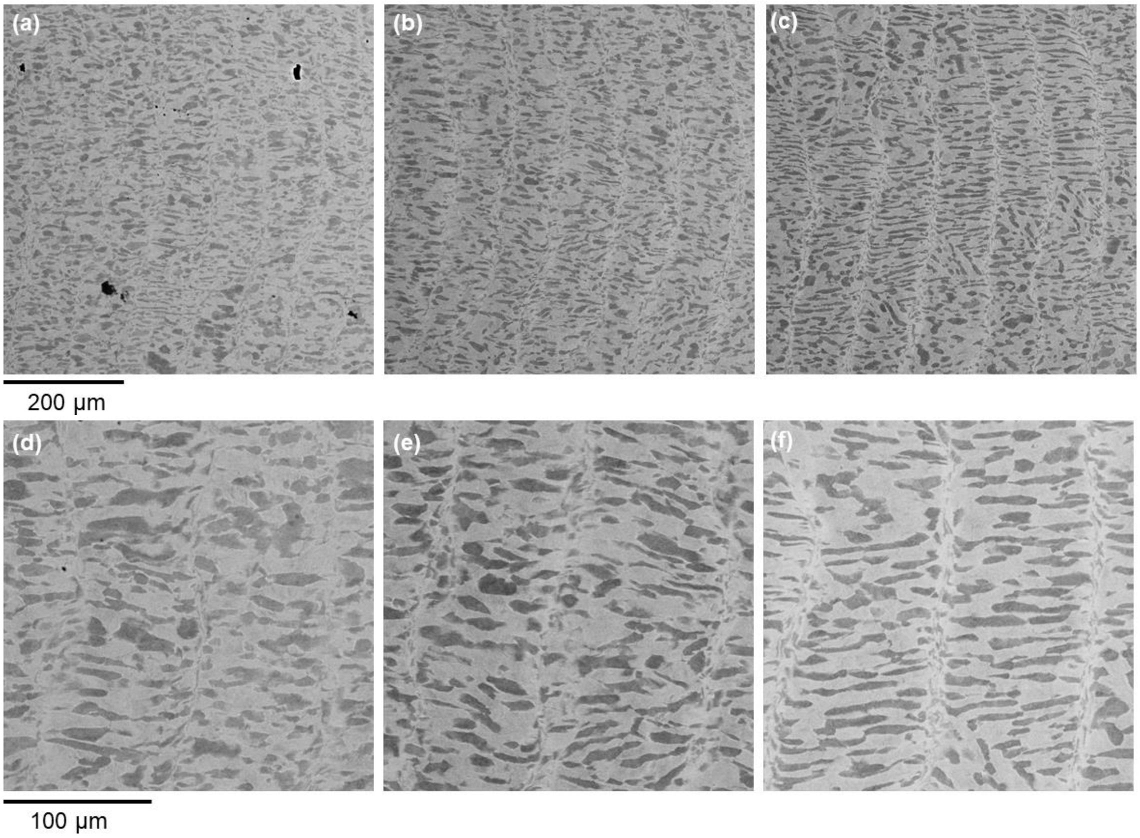

Figure 4.8 microstructure of the smooth side of the chips after slight polishing without grinding: (a)(d): 1 m/s; (b)(e)1.5 m/s; (c)(f): 2 m/s.

Table 4.2 β volume fraction increased with increasing cutting speed

	As-received	1 m/s	1.5 m/s	2 m/s
β volume fraction	50%	60%	62%	68%

4.1.4 The chip morphology at the beginning and end of cutting phase

At the beginning phase of cutting (Fig. 4.9), the chips at all cutting speeds show similar features as those obtained from the stable stage. 1 m/s chips still show less developed segments and the saw-teeth were more developed with increasing cutting speed. However, near the end phase of cutting (Fig. 4.10), the chip morphologies are so distinctive from both the beginning and steady stages. At 1 and 1.5 m/s, the segmented surface of the chips was no longer smooth, indicating more unstable deformation occurring at the end of cutting due to excess tool wear. The chips at 1 m/s show further transgranular crack propagation from the crack tip formed during the cutting, probably resulting from the increased vibration and chatter at the end of cutting. For the 1.5 m/s chip, the valley height is much larger than those obtained at the beginning and steady stages, while it is the opposite case in 2 m/s chips. In addition, there seems to be more shearing on the prior turned side of the chip. This might be the result of tool with excess wear cannot remove the as much material as in the previous stage, most likely due to the build-up edge and adhesion layer.

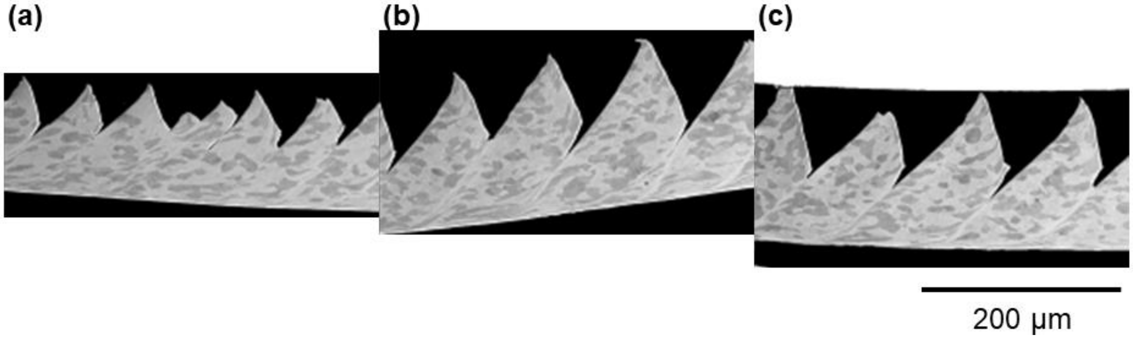

Figure 4.9 Morphologies of the chips obtained at the beginning stage of turning: (a) 1 m/s; (b) 1.5 m/s; (c) 2 m/s.

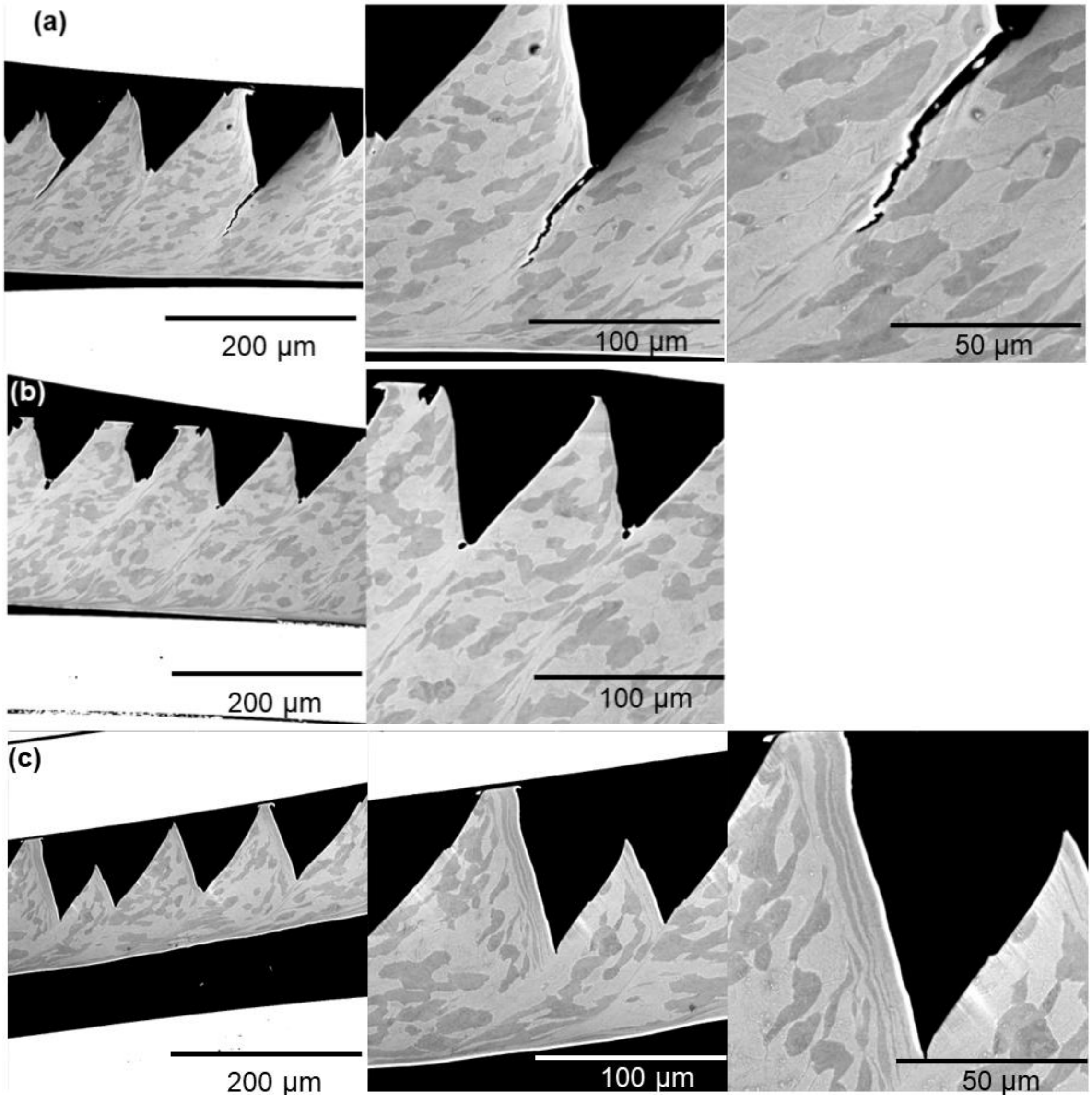

Figure 4.10 Morphologies of the chips obtained at the end stage of turning at various magnifications: (a) 1 m/s; (b) 1.5 m/s; (c) 2 m/s.

4.1.5 Nano-indentation analysis

As mentioned in as-received workpieces part, though the EBSD software was set to identify both α_p and β_t orientations, most of the pixels in the β_t (lamellar α+β regions) were identified as α phase in the EBSD map (Fig. 4.11 (b)) because the β laths are so thin and account for only ~3-8 vol. % of the alloy [105], [106]. As a result, BSE image as shown in Fig. 4.11 (a) is necessary to distinguish α_p and β_t regions. On the hardness map, α_p grains can be seen clearly as they exhibit consistently higher hardness the β_t (lamellar α+β) regions. The orientations of α_p grains and their corresponding hardness values are plotted on the inverse pole figure in Fig. 4.11 (d). The hardness of α_p grains are highly dependent on their orientations. For instance, grain #16 had the highest hardness value (6.65 GPa) among the 18 grains, while grains #1, 5, 7 and 8 (4.89, 4.9, 5.22, 5.22 GPa, respectively) were much softer due to their softer orientations, as shown in Fig. 4.11. Grains with similar orientations had very similar hardness values (e.g. Grain #3, 4, 6).

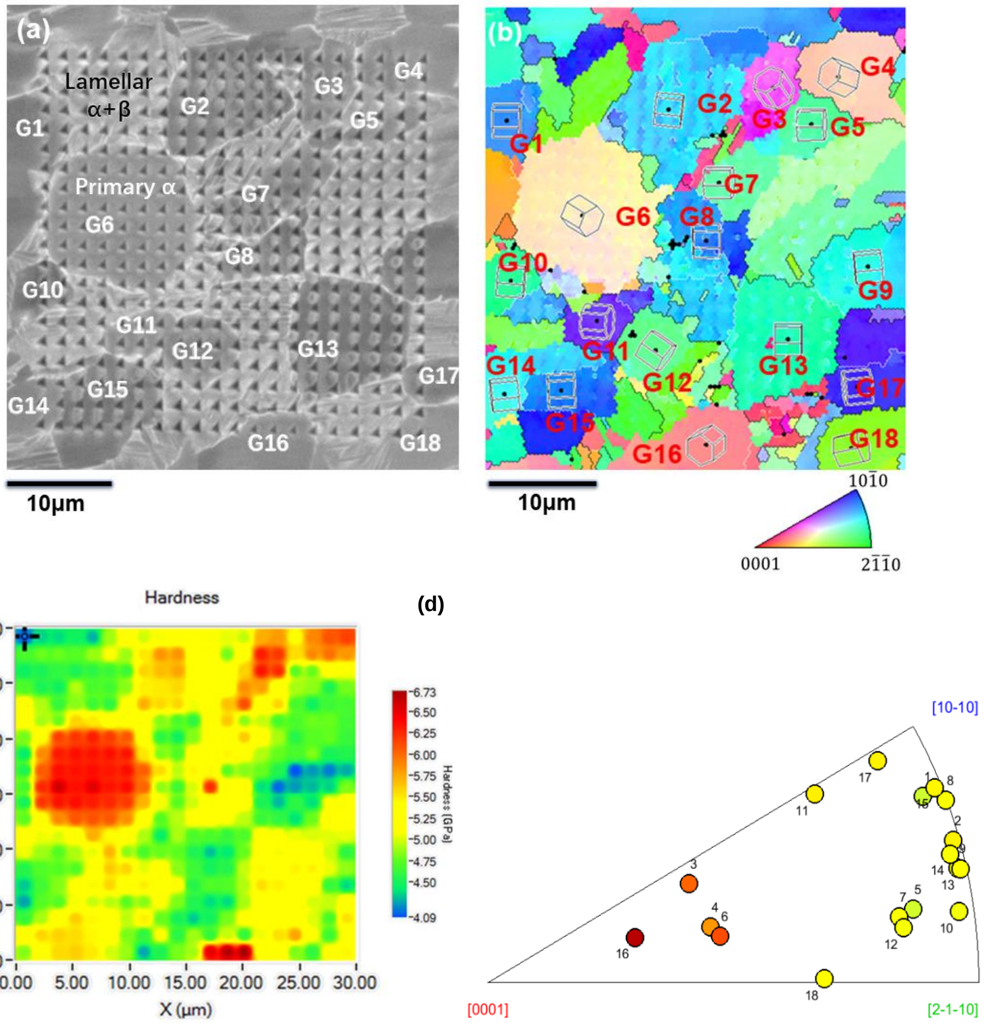

Figure 4.11 (a) Backscattered electron (BSE) image after nano-indentation of the as-received Ti-6Al-4V; (b) corresponding electron backscattered diffraction (EBSD) normal direction inverse pole figure (IPF) mapping; (c) corresponding hardness map; and (d) inverse pole figure (IPF) shows that the hardness depends on the primary α grain orientation (same color scale as the hardness map).

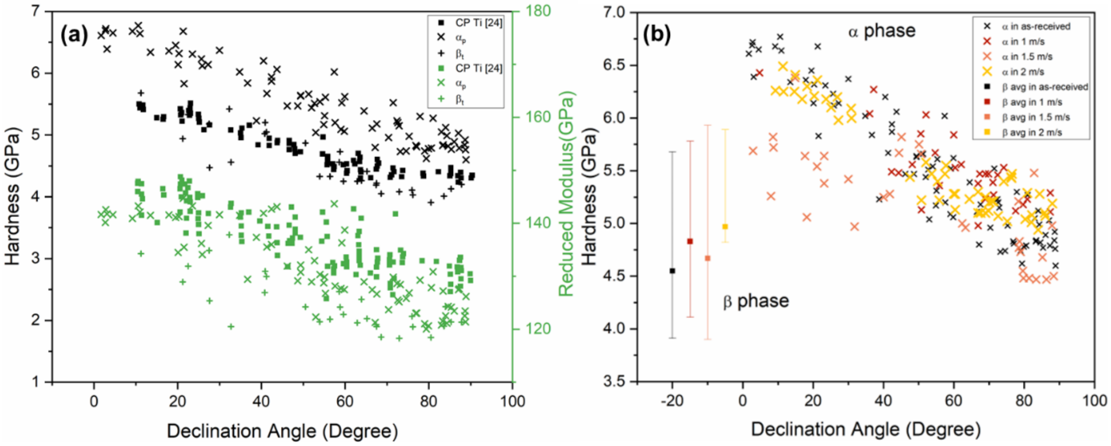

Figure 4.12 (a) The hardness and reduced modulus of the αp in as-received STA Ti64 and commercial pure (CP) Ti data from literature [107] decrease with declination angle; (b) The cutting speed of 1.5 m/s shows lower hardness at low declination angles than 1 and 2 m/s.

Table 4.3 Maximum, minimum and average hardness values of α_p / β_t phase, the (Max-Min)/Avg ratio shows hardness variation of β phase is larger than α phase

Material	**Phase**	**Max (GPa)**	**Min (GPa)**	**Avg (GPa)**	**(Max-Min) (GPa)**	**(Max-Min)/Avg**
CP Ti [24]	**α**	5.51	4.24	4.77	1.27	0.27
	β	N/A	N/A	N/A	N/A	N/A
Ti-6Al-4V As-received	**α_p**	6.77	4.60	5.52	2.17	0.39
	β_t	5.68	3.91	4.55	1.77	0.39
Ti-6Al-4V 1m/s	**α_p**	6.43	4.98	5.51	1.45	0.26
	β_t	5.78	4.12	4.83	1.66	**0.34**
Ti-6Al-4V 1.5m/s	**α_p**	6.38	4.47	5.20	1.91	0.37
	β_t	5.94	3.90	4.68	2.04	**0.44**
Ti-6Al-4V 2m/s	**α_p**	6.49	4.94	5.52	1.55	0.28
	β_t	5.89	3.82	4.97	2.07	**0.42**

The hardness of the α_p grains in as-received Ti64 bar was highly dependent on the c-axis direction as indicated in Fig. 4.12. The reduced elastic modulus followed a similar decreasing trend with increasing declination angles between the c-axis of α_p grain and the indenter direction. The highest hardness of 6.72 GPa was obtained when the declination angle was ~2.8°. A similar trend in commercial purity (CP) Ti was also reported by Britton et al. [107], but its hardness is about 20% lower (square symbols in Fig. 4.12 (a)). This differs from the observations of Han et al. [106] , where no relationship between hardness and orientation was apparent, but that material shows significant orientation gradients and sub-grain boundaries in the α_p grains and the β_t had an acicular shape suggesting that a high cooling rate was used. The systematically higher hardness in the present work is mainly due to the solid solution strengthening effect of aluminum in α_p grains. Also, the present measurements show that the β_t has a similar hardness as CP Ti but is not as hard as the α_p component in the Ti64 microstructure, indicating the lack of Al solid solution strengthening in the dominant α fraction of the β_t, and/or the presence of the softer β phase. The reduced modulus of the α_p is slightly lower than CP Ti, but the β_t component is about 10% more compliant, as BCC β Ti has a lower stiffness [108]. Average values in Table 4.3 show that the hardness of β_t is consistently lower than the α_p phase, and bold values show that the variation in the hardness of β_t is larger than that of α_p. These measurements show that the properties of titanium are very anisotropic, which is important for interpreting the detailed analysis of chip geometry in the following sections.

4.2 MIL chips

The cross-section of MIL chips are shown in Fig. 4.13. These serrations are more regularly spaced and fully developed with increasing cutting speed. The primary shear zone has the appearance of a lamellar microstructure, unlike the STA chips. Like the STA chips, a small number of shear bands are bifurcated in the 1.5 m/s chip. The chip-tool contact surface is illustrated in Fig. 4.14. Some of the black spots on these images are the voids and the others are particles on the surface. In addition to the fine grooves aligned with the chip flow direction, there are more scar-like features with higher cutting speeds. In Fig. 4.15, the upper part of the image is the outward facing edge of the chip, while the lower part of the image is the constrained edge of the chip next to the workpiece, which shows bent and more evenly spaced finer surface ridges. The top and bottom edges of the chips are non-symmetric. The top side has geometric features with a consistent height while the bottom side is pulled away from the workpiece. These features indicate that the formation of segmented chips initiates from the free-surface side, not the constrained side. This is consistent with the proposal of Vyas and Shaw [47] that the segmented chip is formed due to the initiation of cracks on the free surface of the chip. The chip flow direction on this figure is from right to left as shown by the cyan arrow. To avoid complications from the asymmetry, the cross-sections of chips in the present work are observed in the middle of the chip (removed ~0.8mm).

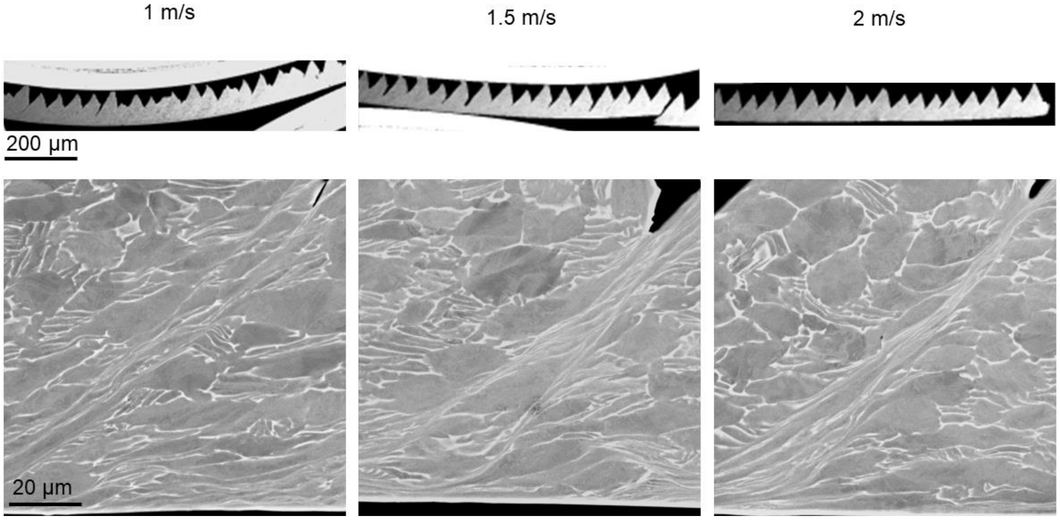

Figure 4.13 MIL chips at 1, 1.5 and 2 m/s. Periodic primary shear zone and secondary shear zone can be seen clearly and the serrations at higher cutting speed are more regularly spaced.

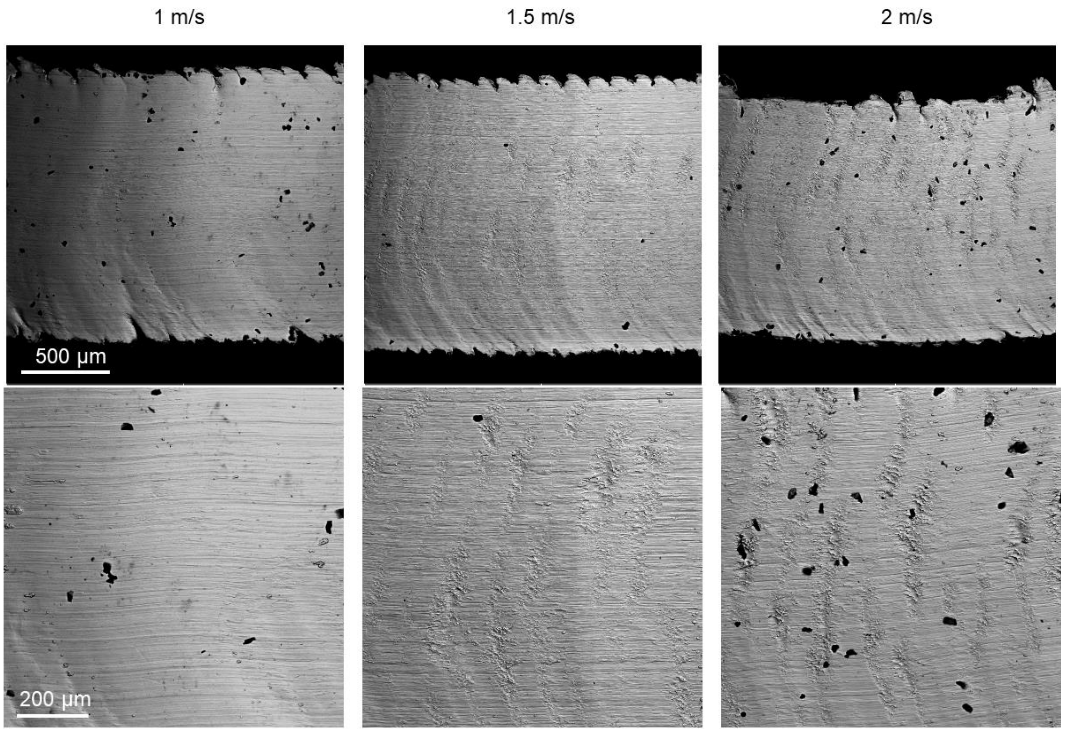

Figure 4.14 Smooth side of the MIL chips at low and high magnifications before sectioning and polishing. In addition to the grooves, the number of scar-like features increased with cutting speed.

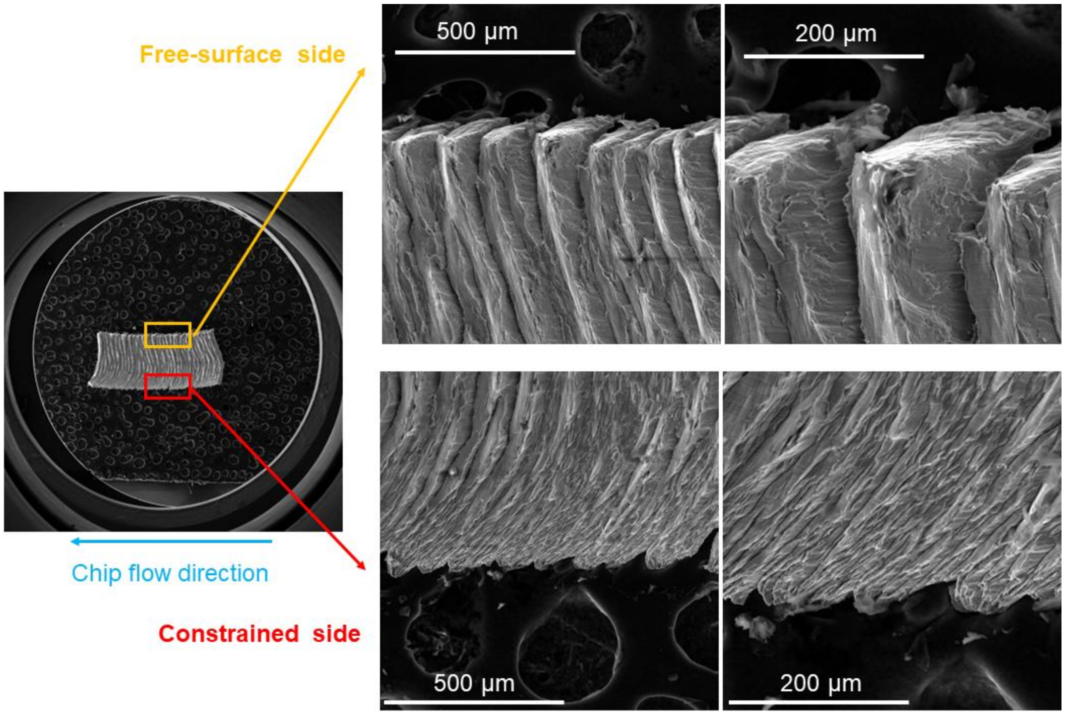

Figure 4.15 Representative images of the segmented side of MIL chips. The top and bottom sides show asymmetric features.

4.3 ELO chips

The cross-section of ELO chips, as shown in Fig. 4.16, shows similar features as the MIL chips. The serrations become more and more pronounced and regularly spaced with increasing cutting speed. The initial microstructure of the ELO chips consists of equiaxed alpha grains and beta phase on the grain boundaries of alpha. Similar to the MIL chip, the primary shear zone appears to have more of the lighter beta phase. At the 2 m/s cutting speed, the microstructure appears similar to STA grade. The chip-tool contact surface at all cutting speeds also shows groove and scar-like features at the 2 m/s cutting speed (Fig. 4.17). The segmented side of the chip is also very similar to the MIL chip (Fig. 4.18).

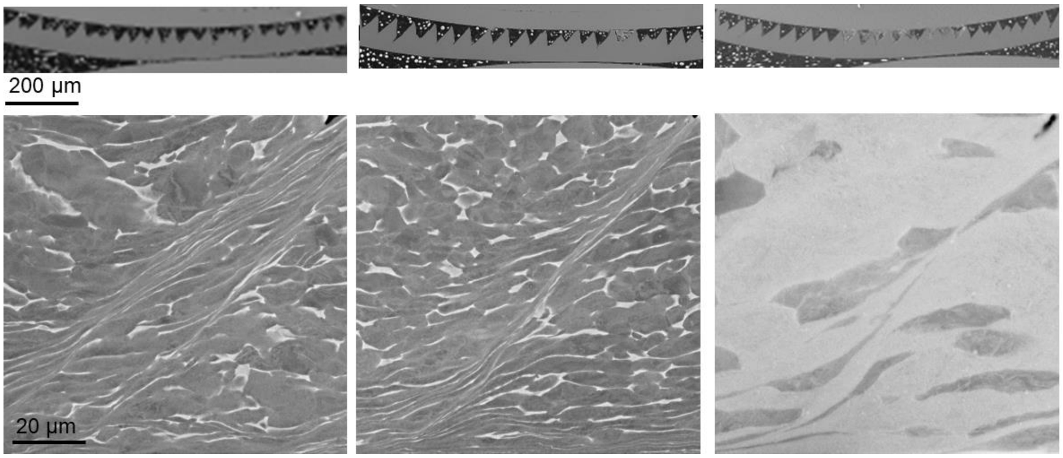

Figure 4.16 ELO chips at 1, 1.5 and 2 m/s. Periodic primary shear zone and secondary shear zone can be seen clearly and the serrations at higher cutting speed are more regularly spaced.

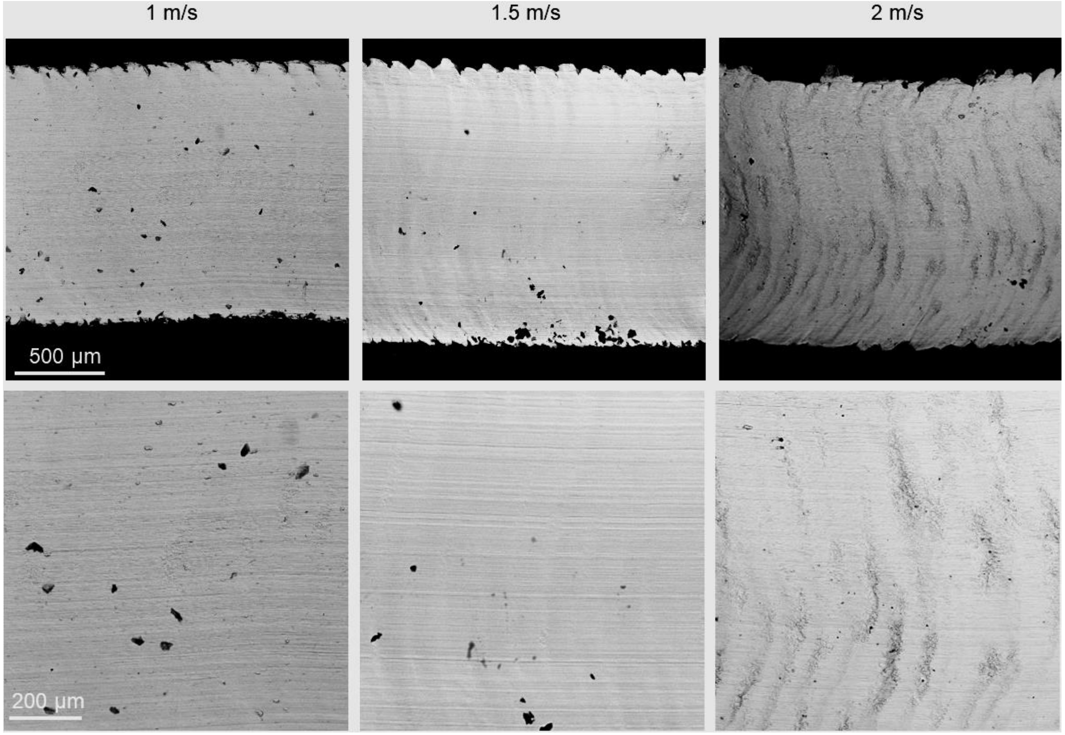

Figure 4.17 Smooth side of the ELO chips before polishing at low and high magnifications. More scar-like features are apparent at higher cutting speeds in addition to the grooves.

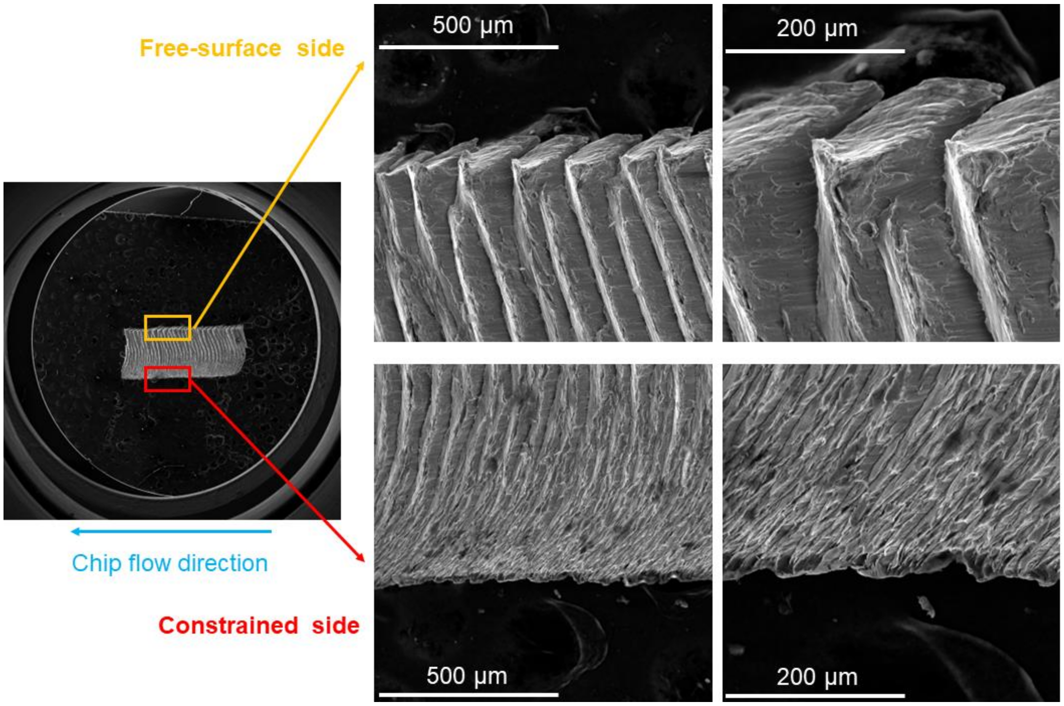

Figure 4.18 Representative images of the segmented side of MIL chips. The top and bottom sides show asymmetric features.

4.4 LAM chips

4.4.1 Morphology of LAM chips

In general, the morphology of the LAM chips at all three cutting speeds exhibited more variability compared with the MIL, ELO and STA chips. In contrast to the other three grade chips, the variability of serrations in the LAM chip increased significantly with increasing cutting speed, as shown in Fig. 4.19. For the two smaller serrations, the primary shear zone can be clearly seen, which is composed of the lamellar microstructure. In contrast, no obvious primary shear zone can be observed in the huge serration in Fig. 4.19. The substantial variability can also be seen even on the chip-tool contact surface (Fig. 4.20). There is a large amount of damage on both the top and bottom side of the chip as shown in Fig. 4.20. For the LAM chips at all three cutting speeds, the groove feature is still obvious and visible, but the scar-like feature is not as pronounced as with chips of the other grades. The damage can also be seen from the segmented side of the chip as shown in Fig. 4.21 This observation is consistent with the flank wear results by Nguyen et al. [84]. The flank wear of insert for LAM grade machining is substantial especially at 91 and 122 m/min.

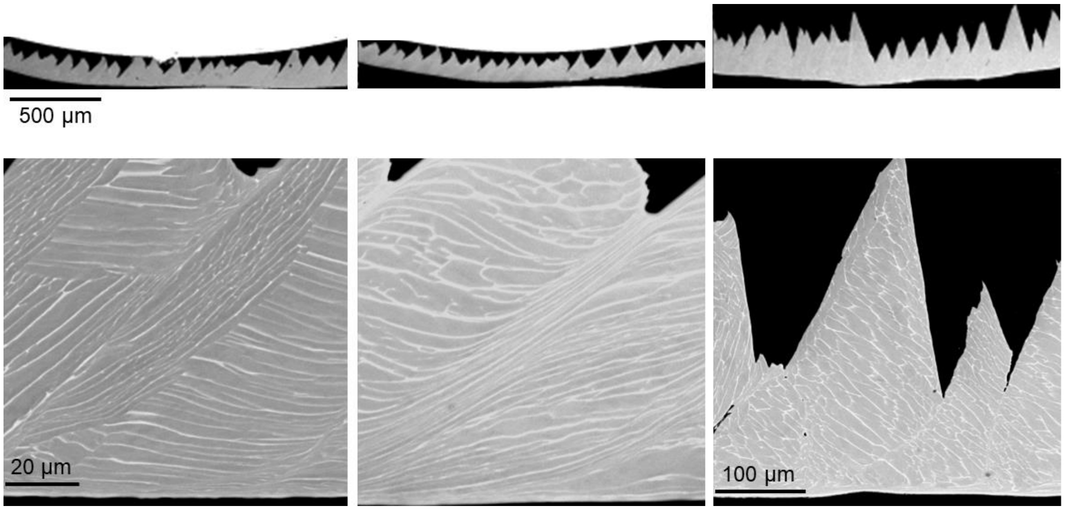

Figure 4.19 LAM chips at 1, 1.5 and 2 m/s. Periodic primary shear zone and secondary shear zone can be seen clearly and the serrations at higher cutting speed show more variability.

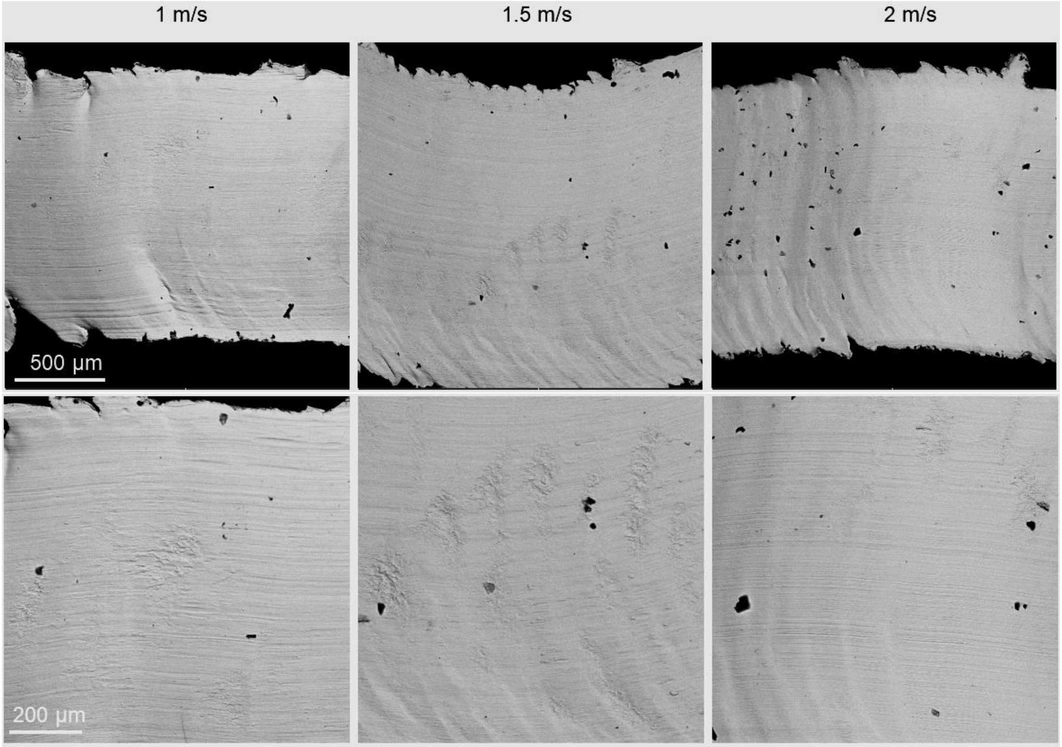

Figure 4.20 Smooth side of the LAM chips before polishing at low and high magnifications. There are more scar-like features visible at higher cutting speeds in addition to the grooves.

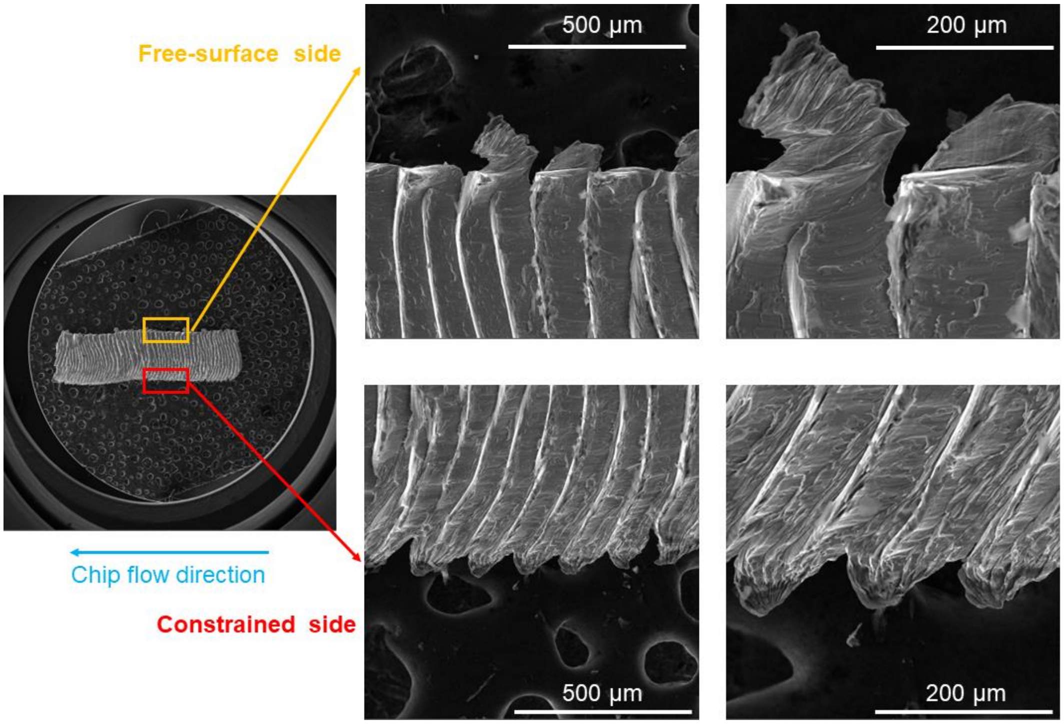

Figure 4.21 Representative images of the segmented side of LAM chips. Top and bottom sides show asymmetric features.

4.4.2 EBSD scans of LAM chips

The variability of the chip morphology is highly dependent on the initial orientation of the lamellar colony. In Fig. 4.22, the serrations with an average segmented degree of 0.49 show blue orientations (Morphology I). Basal <a> slip is favored with the maximal Schmid factor of 0.62 under the plane strain condition. The light green orientation of neighboring lamellar colony favors pyramidal <c+a> slip with the maximal Schmid factor of 0.56, but <c+a> slip has a 3-times higher CRSS than the basal <a> slip. In addition, the Schmid factor of basal <a> slip is even higher than the Pyramidal <c+a> slip. It is likely that the blue orientation colony experienced more deformation compared with the light green colony.

The second type of morphology with an average segmented degree of 0.59 is correlated with green orientations (Fig. 4.23). Also, there are uneven lamellar widths in the microstructure compared with the first type. Pyramidal <a> slip is favored with the maximal Schmid factor of 0.53 under the plane strain compression boundary condition. The red orientation of another lamellar colony favors pyramidal <a> slip with an even higher maximal Schmid factor of 0.61. It can be inferred that the green orientation is highly favored by pyramidal <a> clip. Compared with the serrations with blue orientations, the adiabatic shear bands are very narrow, and evident by a slightly lighter shade of gray, and where beta laths terminate at the ASB on the BSE image. Also, the average segmented degree of the green orientations is a little bit higher than that of the blue orientations.

The serrations are exaggerated (Morphology III) in Fig. 4.24, where the average segmented degree is 0.7, compared with 0.49 for Morphology I and 0.59 for Morphology II. Similar to Morphology II, the adiabatic shear band is very narrow, and in one location, perpendicular to the smooth surface of the SSZ. Schmid factor calculations show that the preferred slip system for the golden orientation is the pyramidal <c+a> slip with the maximal Schmid factor of 0.54. The magenta color with a slightly different orientation may be the result of large regions of cooperative deformation during the cutting, which is different from other orientations of the lamellae colonies. Pyramidal <c+a> slip has the highest CRSS among all of the hexagonal Ti slip systems, so the resistance to deformation from the cutting force in Morphology III is the highest. As a result, , the cutting force fluctuation for forming ASBs is large when cutting LAM chips, especially at the cutting speed of 2 m/s. This is consistent with the large variability in chip morphologies at all cutting speeds indicated in Fig. 4.19. The effect of initial grain orientation on the morphology of the chips is pronounced for LAM grade since the grain (lamellar colony) size of LAM is huge compared with STA, MIL, ELO grades (Nguyen et al. [84] showed that the LAM sample had the largest colony size of 743 μm and STA and MIL samples with lamellar colonies each had a similar lamellar colony size of around 20 μm). The large lamellar colonies with hard orientations (golden colored) account for the exaggerated serrations, and those with soft orientations (blue and green colored) lead to the smaller serrations.

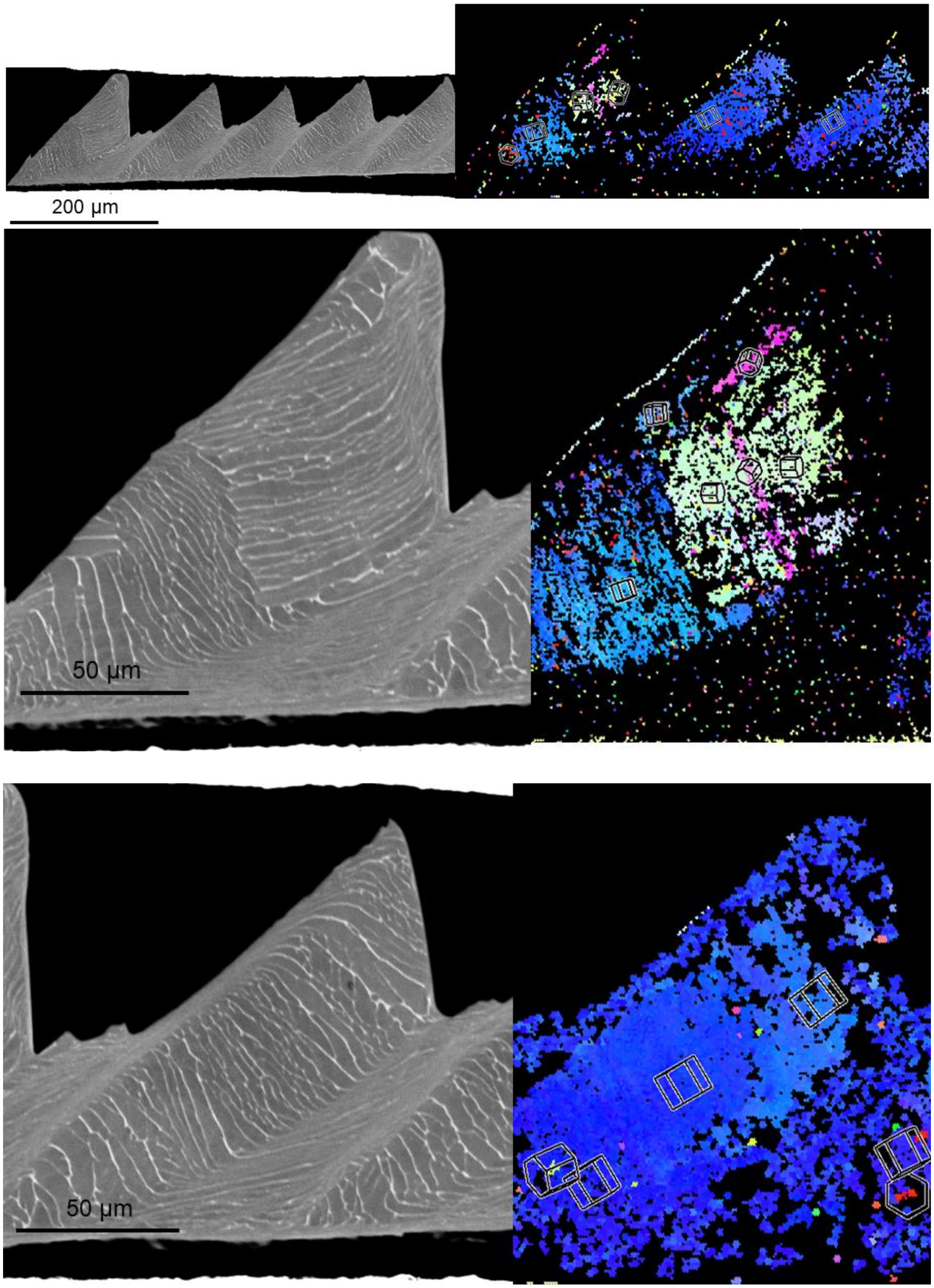

Figure 4.22 Morphology I with the average segmented degree of 0.49 showing maximal Schmid factor value of 0.62 (basal <a> slip) under the plane strain condition.

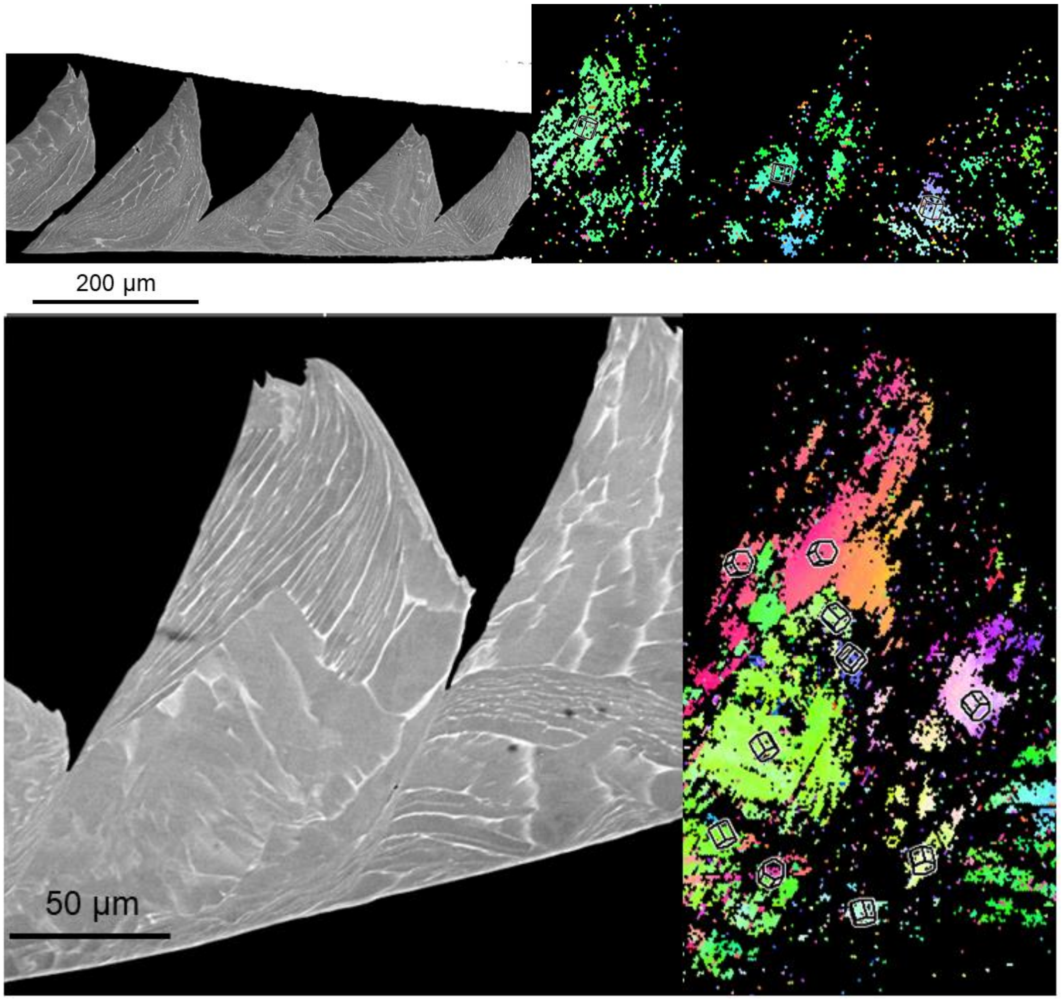

Figure 4.23 Morphology II with the average segmented degree of 0.59 showing maximal Schmid factor value of 0.53 (pyramidal <a> slip) under the plane strain condition.

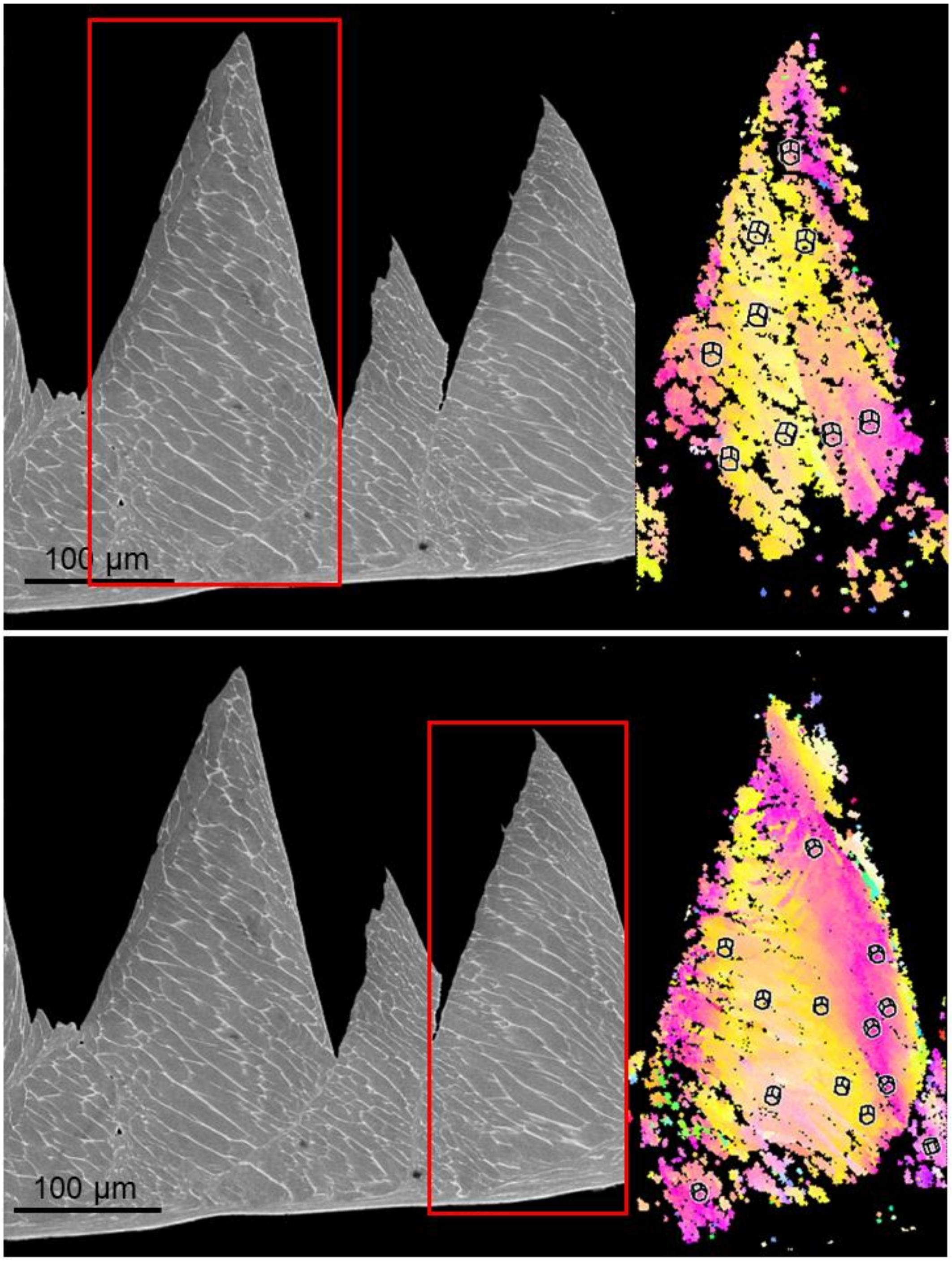

Figure 4.24 Morphology III with the average segmented degree of 0.7 showing maximal Schmid factor value of 0.54 (pyramidal <c+a> slip) under the plane strain condition.

4.5 Conclusion

1. The chips cut at 1, 1.5 and 2 m/s all show segmented morphology. With increasing cutting speed, there is a slight increase in peak height, equivalent thickness, and shear band spacing, together

with a slight decrease in valley height. The shear angle remained stable around 43 °. The chips are more and more segmented with increasing cutting speed since the segmented degree increased significantly.

2. The constrained side of the chip is more homogeneous while the free surface side is apparent segmented. At the cutting speed of 1 m/s, the tool-chip contact surface of the chip is smooth and scar-like features are more apparent with increasing cutting speed, which may account for the formation of adhesion layer on the tool rake face.

3. The hardness of both α_p and β_t in Ti64 alloy was highly dependent on its orientation both before and after machining, ranging from 4.5 and 3.9 GPa (c-axis perpendicular to indenter direction) to 6.7 and 5.7 GPa (c-axis parallel to indenter direction), respectively, and the hardness of α_p was consistently higher than that of β_t. The modulus shows the same trend; The hardness of α_p after machining was close to those before machining, indicating that a balance of strain hardening and thermal recovery took place during deformation.

4. The images of the tool-chip contact surface provide evidence of phase transformation during the cutting process.

5. The chip morphologies at the beginning phase are similar to the chip morphologies from the steady stage. At the ending phase of cutting, the chips at 1 m/s showed further transgranular crack propagation from the crack tip formed during the cutting. For the 1.5 m/s chip, the valley height is much larger than those obtained at the beginning and steady stages, while it is the opposite case in 2 m/s chips.

6. The scar-like features on the smooth side of the chips are more pronounced with increasing cutting speed for all grades. The morphology of the chips show higher variability with increasing cutting speed, especially the LAM grade.

7. The initial microstructure has a substantial impact on the morphology of the segmented chips. The LAM grade shows exaggerated serrations and obvious variability due to the huge prior β grains and α colonies. The morphology of MIL and ELO chips were similar to the STA chips and show more uniform geometry.

8. For the LAM chips, the orientations that favor basal <a> lead to the segmented chips with the lowest segmented degree and a diffuse shear band, while orientations that pyramidal <c+a> resulted in the segmented chips with the highest segmented degree and an extremely narrow shear band.

CHAPTER 5 SHEAR BAND WIDTH PREDICTION AND SHEAR STRAIN ESTIMATION IN STA CHIPS

In order to check the variability of the crack depth along the chip width, the fracture surfaces were investigated when a chip was bent in the way shown in Fig. 5.1 (a). Ideally, there will be a straight valley line, as indicated in Fig. 5.1 (b). However, the valley line throughout the chip width is not a perfect straight line, as can be seen from Fig. 5.1 (c). Fig. 5.1 (d) and (e) shows the counterparts of the fracture surfaces, with the detailed features labeled on both surfaces. In Fig. 5.1 (d), there are scoring marks all over the region above the valley line, which corresponds to the tool-chip contact surface observation in Chapter 4. A large amount of shearing features can be seen in Fig. 5.1 (e) and similar features can be seen right below the valley line in Fig. 5.1 (d), showing evidence that the crack propagates past the valley. In contrast to the relatively straight valley line in Fig. 5.1 (d), the shear crack length in Fig. 5.1 (e) varies dramatically throughout the chip width. For instance, it can be seen from Fig. 5.1 (e) that the crack propagation stops at point A, B and C, leading to a large variation in the crack length. This variability of crack propagation may be directly related to the local stress state and surrounding orientations. It also reveals that the morphology of a particular position on the chip is highly dependent on the depth of the cross-section observation plane, which depends on slip behavior in the local crystal orientations. Hence, investigations of crystal orientations in cross sections will reveal which slip systems are more likely and affected crack growth at each location, and correlation between the formation of crack and the local orientations is sought[2].

The chip morphology becomes more uniform and regularly spaced with increasing cutting

---

[2] This chapter is adapted from a published paper, Effect of Cutting speed on Shear Band Formation and Chip Morphology of Ti-6Al-4V alloy using Nanoindentation and EBSD Mapping, Jiawei Lu, Ryan Khawarizmi, Miguel Monclús, Jon Molina-Aldareguia, Patrick Kwon, Thomas R. Bieler, *Materials Science and Engineering A* 862 (2023) 144372, DOI: 10.1016/j.msea.2022.144372.

speed. As a result, 2 m/s chips are investigated first to try to reveal the correlation between the formation of cracks and the local orientations. In contrast, 1 m/s chips exhibited large variability in chip morphology, homogeneous shear strain, and crack length. It would be a good idea to check whether the correlation still makes sense in the cases where there are more variations. Finally, the intermediate cutting speed was also investigated.

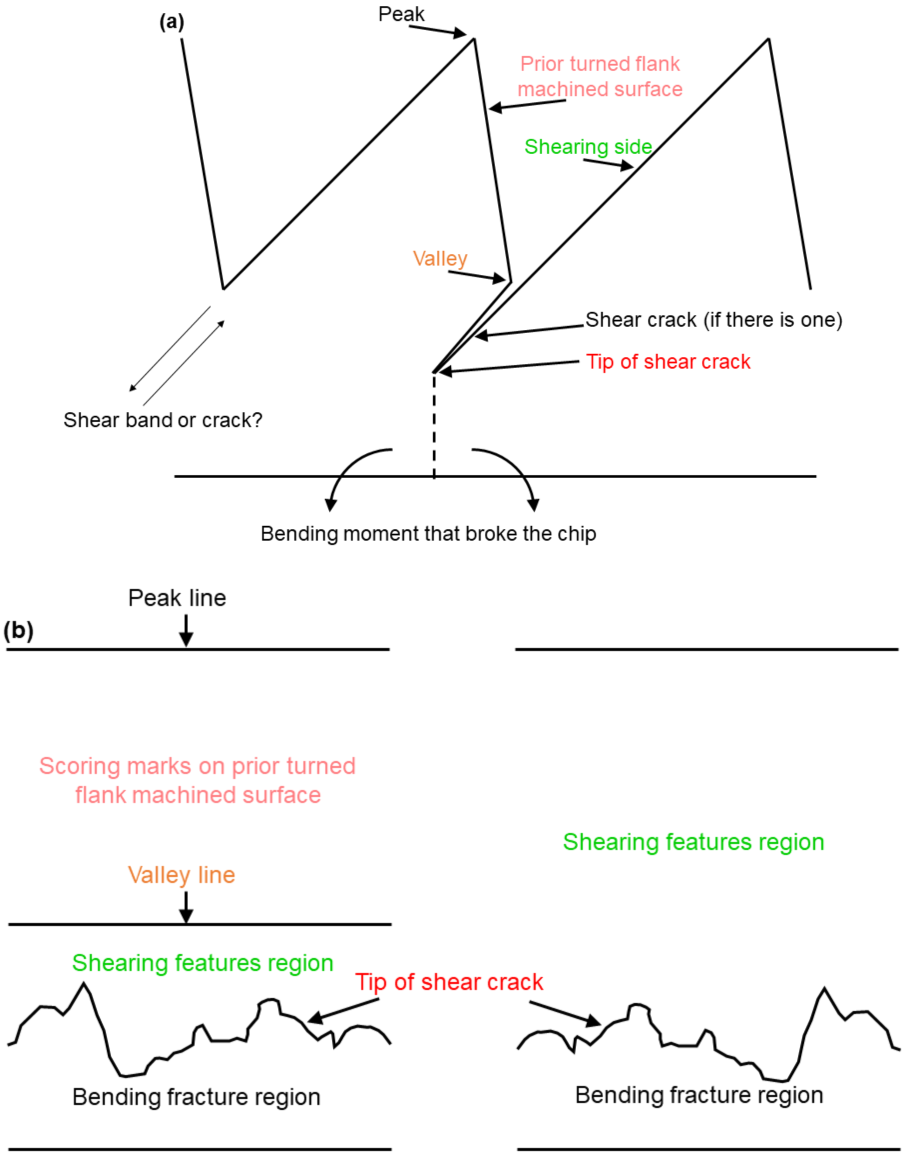

Figure 5.1 (a) Illustration of bending a chip; (b) schematic plot of the fracture surface; (c) the fracture surface tilted at low mag; (d) and (e) the corresponding fracture surfaces on both sides, (d) is the prior turned flank surface and (e) is the shearing side.

Figure 5.1 (cont'd)

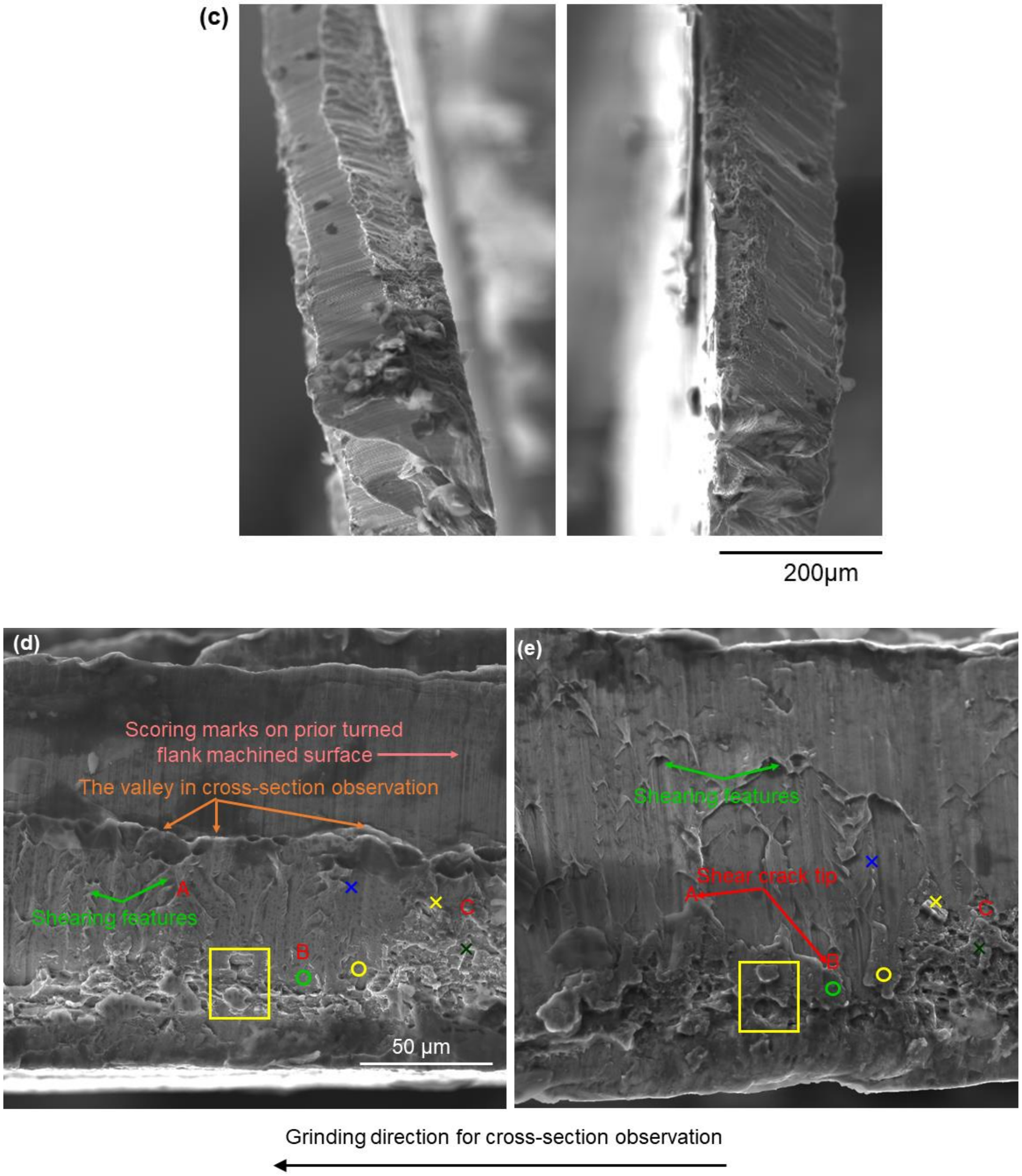

In this chapter, a model that predicts the shear band width, as well as the model that calculates both the catastrophic shear strain within the ASB and the homogeneous shear strain in the segments, are introduced and adopted. The teeth where nanoindentations were tested on were selected and discussed. This methodology will be applied to tens of teeth at each cutting speed in the next chapter to provide a statistical perspective.

5.1 Shear band width calculation

During the cutting process, the homogeneous shear strain rate is related to the shear angle θ, tool rake angle ω (0° in this study), cutting speed V_c, and the spacing perpendicular to the shear band S [51], [109]:

$$\dot{\gamma} = \frac{V_c cos\omega}{2\times\frac{\sqrt{2}}{2}\times S\times cos(\theta-\omega)} \tag{5}$$

The shear strain rates were calculated to be ~13,000, 16,000, and 20,000 s^{-1} at cutting speeds of 1, 1.5 and 2 m/s, respectively. Thimm et al. determined the shear strain rate in linear orthogonal cutting at a range of cutting speeds between 1.33 and 2 m/s (the strain rate decreased with increasing depth of cut) with a rake angle of 0 ° and a depth of cut of 0.1 and 0.2 mm using digital image correlation (DIC) [110], resulting in a range of ~14,000 and 28,000 s^{-1}. The calculated results in the present work agreed with their measurements since feed rate in the present turning experiment was 0.127 mm/rev, which is between 0.1 and 0.2 mm/rev in Thimm's orthogonal cutting [110].

The width of the shear band can be calculated based upon the model developed by Molinari et al. [22], [49]:

$$t = \frac{12\sqrt{2m}\cos(\theta-\omega)kT_r}{at_0 V cos\theta} \tag{6}$$

where θ is the shear angle, ω is the tool rake angle (0° in this study), m and a are non-dimensional strain hardening and thermal softening coefficients of the material, k is the thermal conductivity, T_r is room temperature, t_0 is the shear flow resistance and V is the cutting speed. The non-dimensional parameter a can be calculated using [22], [50]:

$$a = \frac{\alpha\kappa_0}{\rho c} \times (b\dot{\varepsilon}_0)^m \tag{7}$$

where κ_0 is the yield strength, ρ is the density, c is the specific heat capac`ity, $\dot{\varepsilon}_0$ is the reference strain rate and b is a physical constant of the material. The parameters used for the calculation are from Liu et al. [22]. In addition, a shear flow resistance of 950 MPa and yield strength of 1050 MPa at the reference strain rate of 14000 s^{-1} at room temperature was adopted [111], since the strain rate was determined to be between 10000 and 20000 s^{-1} when the cutting speed was at 1.33 and 2 m/s in linear orthogonal cutting experiments in [110]. The shear flow stress is nearly the same for shear strain rates from 1×10^4 to 5×10^4 s^{-1} in split Hopkinson pressure bar (SHPB) tests [112].

The predicted shear band widths based upon equation (6) are 10.5, 7 and 5.2 μm at the cutting speeds of 1, 1.5 and 2 m/s. However, the measured shear band widths from BSE images are ~1.3 μm at 1 and 1.5 m/s, and ~2μm at 2 m/s, which are 1/10-1/4 of the model predictions. For the segmentations that formed a crack rather than a distinct shear band, the width of the shear band near the end (tip) of the crack is used for the calculation in 4.2.

The measurements show discrepancies between inverse proportionality between shear band width and cutting speed, which is the fundamental basis for this model. One reason for the six-ten times thinner shear band width measurements may come from using the shear flow resistance and yield strength from a lamellar Ti64 microstructure while experimentally, a bi-modal microstructure was used, which has higher yield strength and hardness [113]. Also, material constants such as thermal conductivity, specific heat capacity, strain hardening and thermal softening coefficients can vary at elevated temperatures [70], but these are not likely to account for the factor of 4 to 10 reduction in shear band width. As the flow softening commonly observed in hot working results from microstructural evolution [113], a microstructural instability could also facilitate reaching high enough temperatures for transformation to β, which would cause an even more concentrated shear instability. It is possible that adiabatic heating causes transformation to β, and because the β phase is much softer, the shear band would become even more localized and could account for the small observed shear band widths (the model does not consider a phase transformation to a softer structure).

In addition to the microstructure change, the shear band width also depends on its degree of evolution [36, 42]. The evolution degree is the ratio of current shear displacement to the critical shear displacement. When the evolution degree is less than 1, the shear band is not fully mature and this will influence the shear band spacing as a result of the shear stress in the shear band. Once the shear displacement reaches the critical value of 1, the shear stress in the shear band vanishes [51] and the shear band stops growing in width because the propagation process of shear bands is stress-controlled [52]. From orthogonal cutting experiments, Ye et al. [51] determined that the evolution degree can be worked out from the fluctuation of the cutting force, showing that the degree of shear band evolution increased gradually with increasing initial shear strain rate in the primary shear zone. A study of the milling Ti64 showed shear band widths at 250 m/min and 500 m/min to be 5.8 and 5.9 μm, respectively. The evolution degree at 250 m/min was half of that at 500 m/min. According to the model, the shear band width is inversely proportional to the cutting speed. These two opposing aspects resulted in similar as-measured shear band widths at 250 and 500 m/min. In the present study, the evolution degrees are calculated in Table 5.1 and the shear bands width values are listed in Table 5.2. By taking the evolution degree into account, predicted shear band widths are 6.2, 2.9 and 1.6μm which is much closer to the average as-measured widths of 1.3, 1.3 and 2μm at 1, 1.5, and 2 m/s,respectively, but this does not account for the opposite trend in width from the observations, nor the variability in chip geometry observed in the chips. According to the full width half max (FWHM) method, the shear band widths from the simulated results (Fig. 5.2) are consistently around 15 μm, which does not agree with the as-measured or the predicted values. As mentioned in Chapter 2, the mesh size of the simulation is 5 μm and this may account for the large shear band width result since no features below 5 μm can be obtained using such mesh size. In Chapter 5, there is a pronounced variability in shear band width of chips cut at 1 m/s when a lot more cases are included, which is of interest and will be discussed. For 1.5 and 2 m/s chips, the shear band widths are consistently as narrow as 1-2 μm.

However, none of this research focused on the local orientation of the α_p grains. The model by Molinari et al. [22], [49] showed that the shear band is only affected by the cutting speed while the theory by Ye et al. [95] indicates that the evolution degree depends on the cutting speed. This may not be sufficient, if the heterogeneous deformation in titanium alloys is taken into account. In a thick-walled implosion test, the initiation of the shear bands was considered as a heterogeneous nucleation process by Xue et al. and the initiation sites may be located at favorably oriented grains or even defects [52]. This work shows that nucleation of shear bands requires a critical shear strain at a certain stress. Hence, finding the shear strain in a shear band is needed.

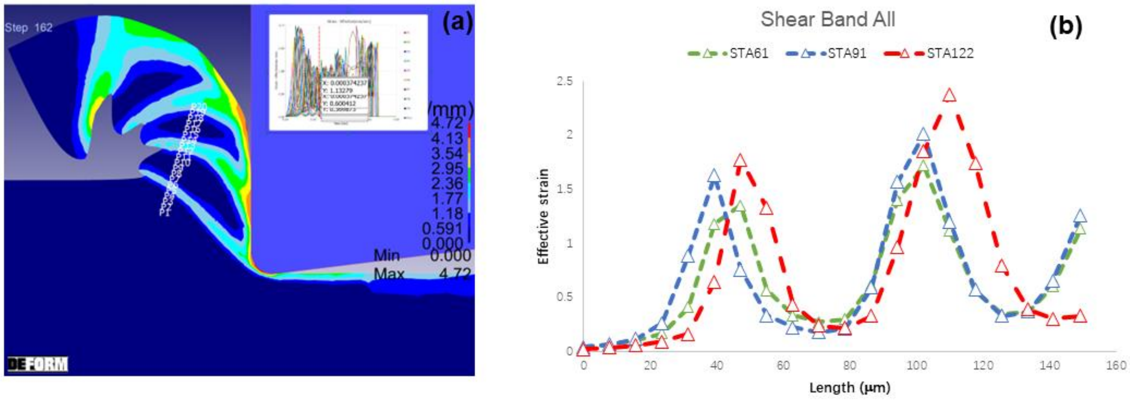

Figure 5.2 (a) Simulated chip morphology that shows consistent peak/valley heights and segment spacing with the experimental results; (b) effective strain distribution along the lines in (a), for shear band width estimation.

Table 5.1 Evolution degree (X) calculated by cutting forces

	F_{max} (N/mm)	F_{min}(N/mm)	$X=1-F_{min}/F_{max}$
1m/s	487.9	202.7	0.59
1.5 m/s	443.7	262.7	0.41
2 m/s	400.4	278.0	0.31

Table 5.2 The shear band width comparison of Molinari model, as-measured, and FE simulation

	1 m/s	1.5 m/s	2 m/s
Molinari model [22], [49]	10.5 µm	7 µm	5.2 µm
Modified by evolution degree (X) [95]	6.2 µm	2.9 µm	1.6 µm
As-measured	1.3 µm	1.3 µm	2 µm
FE simulation (FWHM)	15.8 µm	15.8 µm	15.7 µm

5.2 Shear strain calculation

The shear bands in serrated chips are widely separated, so the homogeneous shear and localized catastrophic shear strains can be calculated from geometric considerations. In general, the homogeneous shear strain γ_{seg} between shear bands is given by [53]–[55]:

$$\gamma_{seg} = \frac{1}{\lambda_h sin\phi_{seg}}\sqrt{{\lambda_h}^2 - \frac{2\lambda_h \cos(\rho_{seg})}{\sin(\phi_{seg}+\rho_{seg})} + \frac{1}{sin^2(\phi_{seg}+\rho_{seg})}}, \tag{8}$$

where ϕ_{seg} is the direction of the localized shear, ρ_{seg} is the complementary angle of ϕ_{seg}. λ_h is the chip compression ratio that can be obtained by the ratio of the deformed chip thickness h_c and the undeformed chip thickness h, or the ratio of cutting speed v_c and chip flow speed v_{ch};

$$\lambda_h = \frac{h_c}{h} = \frac{v_c}{v_{ch}}, \tag{9}$$

The catastrophic shear strain γ_c and the strain in the shear band γ_{sb} are:

$$\gamma_c = \frac{p_{sb}}{\delta_{sb}} \tag{10}$$

$$\gamma_{sb} = \gamma_{seg} + \gamma_c \tag{11}$$

where p_{sb} is the shear band projection and δ_{sb} is the shear band width.

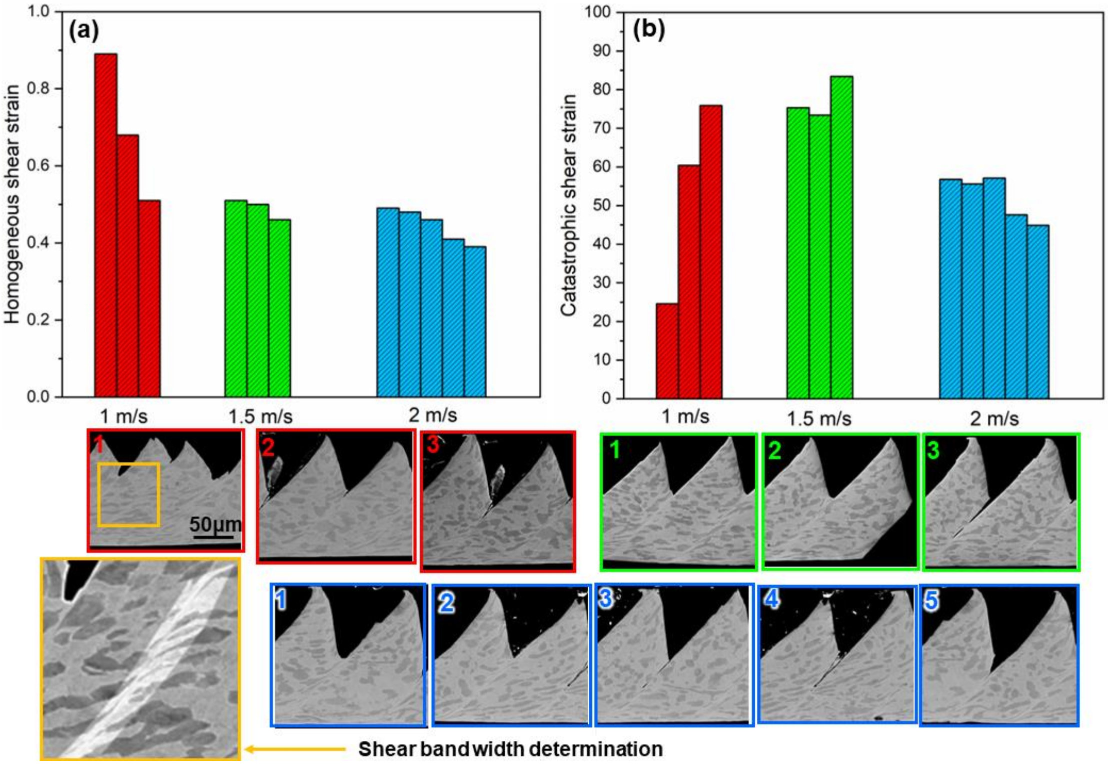

Figure 5.3 (a) Homogeneous shear strain calculated in each segment in an increasing order, (b) catastrophic shear strain calculated in each adiabatic shear band at three cutting speeds. The presence of crack is correlated with smaller homogeneous shear strain.

Shear strains were calculated from this model in several locations in 1, 1.5, and 2 m/s chips as shown in Fig. 5.3, where the homogeneous shear strain varied from ~0.4 to 0.9. There is a slight decrease from ~0.7 to ~0.4 with increasing cutting speed (excluding some special cases). This homogeneous shear strain is smaller than the homogeneous shear strain value of 1.15 from a single pass of equal channel angular extrusion (ECAE) process with a channel angle of 90° [114], due to the expansion in the width direction of the chip and the presence of shear bands. In contrast, the catastrophic shear in Fig. 5.3 (b) exhibited a decreasing trend from 60-75 at 1 m/s, to 40-60 at 2 m/s (which is much higher than the calculated shear strain (~28) in high speed cutting of a 30CrNi3MoV steel [115]). In the thick-walled cylinder implosion experiment, the shear strain in the shear band increased significantly from 4 to 41 and further to over 200 with increasing global shear strain, which can even generate melting [52]. The inaccuracy in calculating catastrophic shear strain lies in the determination of shear band width. The shear bands formed in the solution treated-quenched-aged Ti64 in the present study can be composed of both α_p and β_t, but only the sheared α_p grains can be identified in BSE images and EBSD maps. As a result, the measured shear band width might be slightly smaller.

At all three cutting speeds, the homogeneous shear strain decreased with increasing size of cracks. A possible explanation for the formation of crack is that the initiation of shear bands is strain controlled and also orientation dependent. When the homogeneous strain reached a critical value and the local orientations of αp grains were soft to form a potential shear band, a shear band would form and a strain instability developed. Consequently, shear stain between shear bands stopped due to the strain localization in the shear band. At some point, either micro-voids appeared and kept growing to coalescence, or a crack nucleated at the free surface. If the crack is formed from the free surface of the chip, as proposed by Vyas and Shaw [47], the shear strain between shear bands could be lower than that needed for an adiabatic shear band to form. This would be favored when the orientations of α_p grains where a crack forms (near the tip of an emerging tooth) are hard to deform. It is possible that some of the cracks formed from the free surface of the chip while others were the result of coalescence of voids within a shear band. As no stretched micro-void features were observed in the examples in the present study, it seems likely that the cracks initiated from the free surface of the chip, especially for the straight cracks (green #3, blue #4, #5).

A partially developed shear band is illustrated in the 1 m/s chip labelled as '1' in Fig. 5.3 (a), with the lowest catastrophic shear strain of 24.6, which is approximately one third of the shear strain values of 60.4 and 75.9 in the other two shear bands analyzed at the same cutting speed. From more detailed analysis below, the shear stress needed to deform this shear band is lower than the other two locations, leading to much less energy absorbed per unit volume during the cutting process, making this adiabatic shear band "less adiabatic". Also, the spacing between the shear bands at this location is ~30 μm, approximately one third of more typical spacings of ~80 μm where the shear strains are three times as large. In addition, the segmented degree at this location is only 0.19, much smaller than the other two locations (0.43 and 0.52), indicating that this chip morphology is closer to a continuous chip. The large morphology variation in the 1 m/s chips accounts for the large error bar shown in Fig. 4.2 in Chapter 4. These considerations suggest that the crystal orientations within this shear band are beneficial for the cutting process. As the energy input is more homogeneous in this part of the chip, the cutting tool will also experience a more uniform force.

5.3 Slip modes activated in the shear bands

In hexagonal metals, there are several dislocation slip and twinning systems with different critical resolved shear stresses (CRSS) that can be activated during the plastic deformation. The most easily activated systems are basal ⟨a⟩ slip, prismatic ⟨a⟩ slip, but pyramidal ⟨a⟩ slip (Burger's vector $\langle \mathrm{a} \rangle = \frac{1}{3}\langle 11\bar{2}0 \rangle$), as well as first- and second-order pyramidal slip with the Burger's vector $\langle \mathrm{c+a} \rangle = \frac{1}{3}\langle 11\bar{2}3 \rangle$ are activated to a lesser degree because they have higher CRSS values [105]. At room temperature, basal slip has a CRSS that is ~23% higher than prismatic slip, but this ratio is temperature dependent, and at elevated temperatures, basal and prism slip have CRSS values that are more similar [116]. Twinning has a CRSS that is higher than prism or basal slip, but not as high as the CRSS of 1st order ⟨c+a⟩ slip, which is ~2.6 times higher than prism ⟨a⟩ slip so that prismatic slip is easier to occur. The Schmid law indicates that a slip system can be activated if the resolved shear stress reaches or exceeds its CRSS. In machining conditions, the stress and strain rates are high, so it is likely that all slip system families are activated during deformation. 2nd order pyramidal ⟨c+a⟩ slip is seldom observed but it is discussed in investigations such as slip transfer [117], [118], and in a study on Ti64 texture evolution during the machining process that indicated that 2nd order pyramidal ⟨c+a⟩ slip made a large contribution to the 'C' shear texture. When a crystal orientation has a higher Schmid factor (SF) for a particular slip system, it is more likely to be activated. Therefore, SF analysis is widely used to predict the activation of deformation modes, but it is defined for uniaxial stress state [119], [120]. In the present discussion, 2nd order pyramidal ⟨c+a⟩ slip is not discussed further since the calculated Schmid factors of 2nd order ⟨c+a⟩ slip are generally similar to those of 1st order ⟨c+a⟩ slip, so both 1st and 2nd order ⟨c+a⟩ slip would have similar driving force in these high stress conditions.

The generalized Schmid factors[3] of α_p grains near the shear band are estimated under the assumption that these grains were deformed under the plane strain compression stress tensor $\begin{bmatrix} -1 & 0 & 0 \\ 0 & 1 & 0 \\ 0 & 0 & 0 \end{bmatrix}$. This tensor provides the maximum shear stress on two 45° planes in the material, rather than just the one that is relevant to the turning process. Based upon inspection of slip systems with high generalized Schmid factors, only those with slip planes close to the primary shear direction are considered.

The maximum Schmid factor of relevant basal ⟨a⟩, prism ⟨a⟩, pyramidal ⟨a⟩ and pyramidal ⟨c+a⟩ slip is labeled on each α_p grain in blue, red, green and orange, respectively, in Fig. 5.4 (a)

---

[3] The Schmid factor is defined for uniaxial deformation, which has a maximum value of 0.5. Extending this to a general stress tensor leads to a maximum generalized Schimd factor of $\sqrt{2}/2$, corresponding to simple shear.

and Fig. 5.5 (a) for two exemplary shear bands. In the 1 m/s chip in Fig. 5.4, the orientation of grain #11, a red grain orientation in the (001) inverse pole figure map in Fig. 5.4 (a), was highly favored with a Schmid factor of 0.7 for prism ⟨a⟩ slip (the c-axis is perpendicular to the page). The crystal rotated only about the c-axis as dislocation glide on prism planes would not change the orientation of the c-axis or the dominant slip mode. Basal ⟨a⟩ slip in Grain #10 has a Schmid factor of 0.61, which is also a facile slip system with a high Schmid factor. Clearly, most of the grains near the shear band were easily deformed by prism or basal slip. Hence, the shear stress in the shear band was low for two reasons: i) the high Schmid factors on facilitate slip systems enables activation of slip at a low resolved shear stress; ii) the CRSS of basal ⟨a⟩ and prism ⟨a⟩ slip is lowest among all the slip systems. Combined with the aforementioned small shear strain (24.6) in the shear band, the overall shear strain was spread out over a wider area, leading to less concentrated energy dissipation per unit volume than in other shear bands, which seems counterintuitive, given the ease of deformation. As a result of the more uniform strain, the temperature did not reach the level required for phase transformation to β.

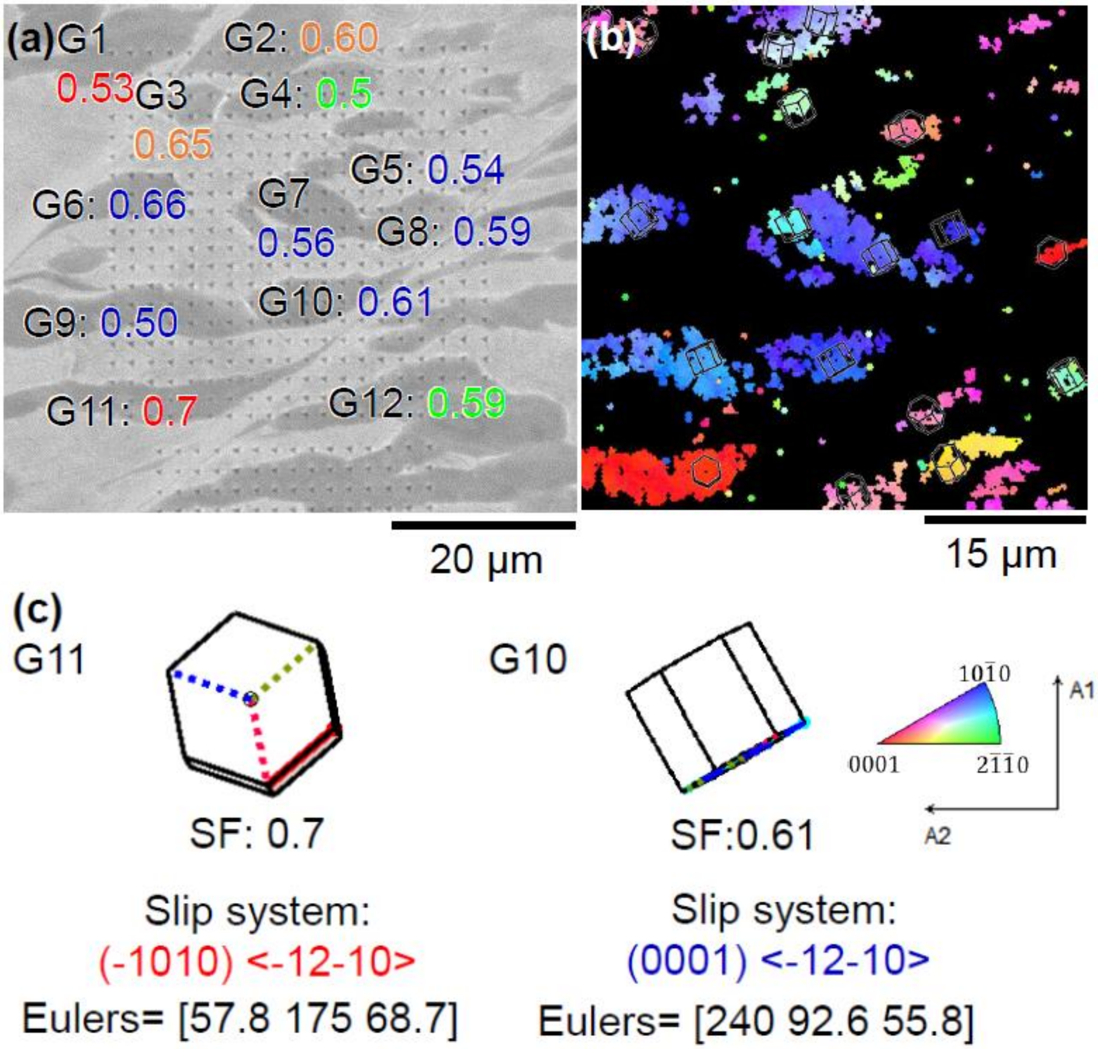

Figure 5.4 BSE image of the first location (less developed serration) in 1 m/s chip, with maximal SF labeled on each grain; (b) (001) IPF map. (c) dominant slip systems in Grains 11 and 10 are easily activated. Maximum Schmid factors (based upon plain strain compression) are labeled: blue: basal <a> slip; red: prism <a> slip; green: pyramidal <a> slip; orange: pyramidal <c+a> slip.

In the shear band in Fig. 5.5, the pyramidal ⟨a⟩ slip Schmid factor of grain #4 in Fig. 5.5 (a) was 0.52. With dislocation glide on the pyramidal plane, the initial orientation rotated to the new orientation of grain #4-2 in the shear band, making it more favored for basal ⟨a⟩ slip (SF: 0.63), resulting in texture-softening. Since the CRSS of pyramidal ⟨a⟩ slip was initially higher than basal <a> or prism <a> slip and the strain rate and the shear strain was high (31.06), the dissipated energy was much higher than it would have been at 1 m/s. With a higher stress leading to more dissipated strain energy, more adiabatic heating took place, making it more likely that a phase transformation from α to β may have occurred. Two possible transformed β variants (among the six possibilities) with the highest Schmid factors (0.69 in both cases) are illustrated in Fig. 5.5 (d), whose orientations were found based upon transforming the α_p grain #4-2 to its parent β orientation [121], [122]. Following deformation, cooling causes the β to transform back to α by the conventional orientation relationship: $\{110\}_\beta//(0001)_\alpha$ and $\langle 111\rangle_\beta//\langle 2\bar{1}\bar{1}0\rangle_\alpha$, which would result in orientations with the basal plane parallel to the shear band. While this is not obvious due to the high strains in the shear band, this is the subject of continuing investigations.

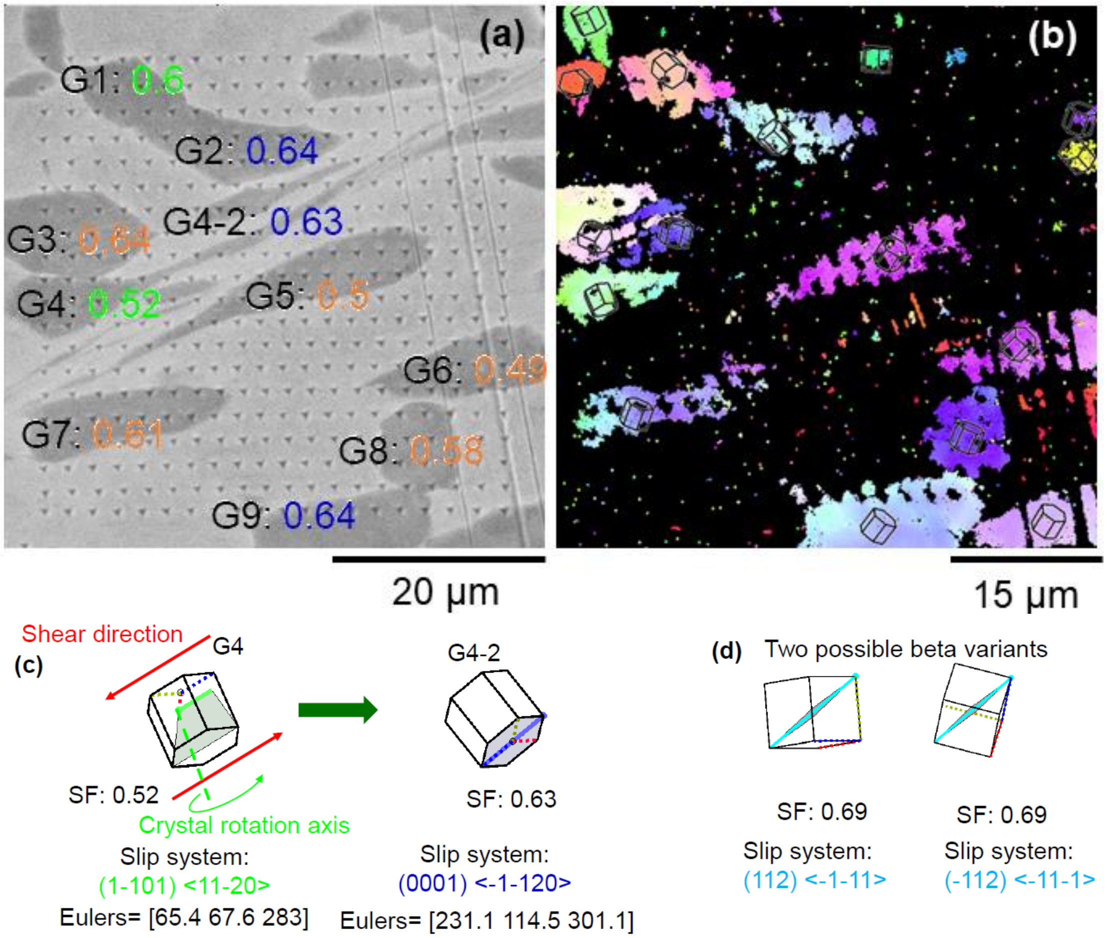

Figure 5.5 (a) BSE image of representative location in 2 m/s chip, with maximal SF labeled on each grain; (b) (001) IPF map. (c) the dominant slip system in grain 4 and shear band. (d) two possible beta variants based on G4-2 orientation. Maximal Schmid factors are labeled: blue: basal <a> slip; red: prism <a> slip; green: pyramidal <a> slip; orange: pyramidal <c+a> slip. (same coordinate system as in Fig.5.4).

Fig. 5.6 shows four additional cases of either cracks or shear bands that occurred at the cutting speed of 2 m/s. It has been reported that the nucleation, growth and coalescence of micro-voids will form the cracks within the shear band due to large shear strains [52]. In Fig 5.6. (c) and (d), it is interesting to see that the α_p grains in the vicinity of a potential shear band show large SF values in the 45° shear direction, yet cracks formed rather than shear bands. On the other hand, the calculated shear strains in these two cases are 0.46 and 0.41, respectively, smaller than those two with adiabatic shear bands (0.48 and 0.49). This suggests that the cracks may be formed by nucleation from the outer surface of the chip [43], [123] rather than due to the large shear strain within the shear band. The morphology of these two cracks is different from the cracks formed by the micro-voids as well. The cracks in Fig. 5.6 (c) and (d) show no evidence of coalescence of micro-voids. However, the crack in Fig. 5.6 (c) shows straight fracture feature and was blunt at the end, whose propagation mechanism is mode II (sliding mode), while a feature similar to the bifurcation of the shear band was observed in the crack in Fig. 5.6 (d). A systematic assessment of cracks vs. shear bands with respect to crystal orientation is the subject of further investigation (Chapter 6).

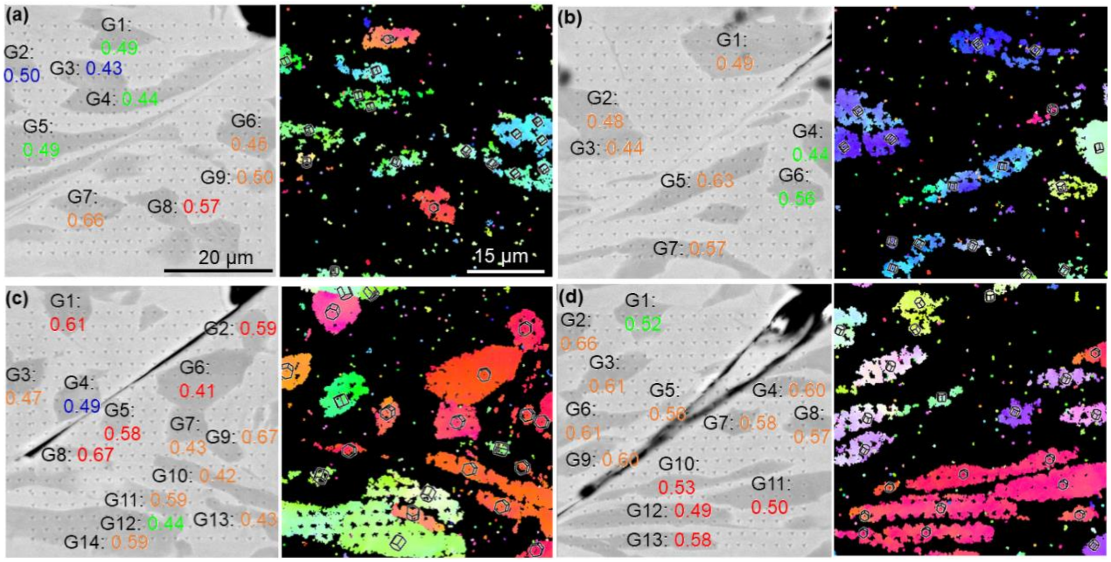

Figure 5.6 The chips cut at 2 m/s: (a) pure shear band; (b)both shear and crack; (c) crack that show straight features; (d) crack that show features like shear band bifurcation.

5.4 Conclusion

1. The as-measured shear band widths from BSE images are ~1.3 μm at 1 and 1.5 m/s, and ~2μm at 2 m/s, which are only 1/10 to 1/3 of the model predictions (12, 8, 6 μm, respectively). This substantial discrepancy can be explained by both the parameters utilized in this calculation model and the evolution degree. However, the essential reason is that this model considers the material to be homogeneous, which is not the reality in Ti64 alloy;

2. The homogeneous shear strains in the segments vary from ~0.4 to ~0.7, depending on local orientation and cutting speed. There is a slightly decreasing tendency in homogeneous shear strain with increasing cutting speed. In addition, there appears to be a correlation between the presence of crack and small homogeneous shear strain;

3. The slip systems activated within the shear band include prism <a>, pyramidal <a> and basal <a>. Prism <a> slip occurs with a lower stress in theory and a smaller catastrophic shear strain by calculation, and as a result the temperature rise is small and less likely to reach the β transus temperature. Also, the neighboring α_p grains in the segment, with soft orientations, exhibited large

homogeneous shear strain, which is beneficial to the cutting tool. In contrast, the deformation due to the activation of pyramidal <a> slip leads to higher stress and larger catastrophic shear strain. Thus, α to β phase transformation could have happened in this condition. It is also interesting to note that the orientation of this α_p grain was rotated slightly due to the deformation and became more favored by basal <a> slip.

CHAPTER 6 EFFECT OF LOCAL ORIENTATION AND CUTTING SPEED ON THE FORMATION OF SEGMENTED STA CHIPS

The crack variability and cases from a few chip locations in the previous chapter reveals the importance of the local crystal orientations. Both the nucleation of the crack near the chip free surface and the generation of adiabatic shear from the secondary shear zone are highly dependent on the local crystal orientations. In this chapter, tens of teeth are investigated using a systematic methodology introduced in Chapter 5, in order to reveal the rationale behind the formation of crack, adiabatic shear band or both in each tooth.

6.1 Chips at 2 m/s

6.1.1 Crack length, segment spacing and homogeneous shear strain distribution of 2 m/s chips

The chips cut at 2 m/s are illustrated in Fig. 6.1. As discussed in the previous chapter, all the teeth are fully developed compared to the 1 m/s chips. Among 32 locations investigated, only 7 exhbited pure shear band without crack (location # 2, 4, 10, 11, 24, 31, 32, as can be seen in Fig. 6.2). Generally speaking, the α_p grains within the shear bands do not exhibit a large aspect ratio, indicating a more uniform shear deformation compared with 1 m/s (this will be further discussed in Chapter 6.2). To explore correlations between geometric features such as crack length, spacing between shear bands, and homogeneous shear strain indicated by grain aspect ratios, these metrics are plotted with respect to position in Fig. 6.2. Segment spacings are in the range of 50 and 95 μm and exhibited a normal distribution (Fig. 6.3). Similarly, the homogeneous shear strains within the segments also followed a normal distribution and its range is between 0.4 and 0.7. In contrast, the distribution of crack lengths does not follow normal distribution, which means the occurrence of crack is not random but resulted from some reason. Most of the cracks are shorter than 45 μm, while only 4 cracks have a length of 60-100 µm. Fig. 6.4 shows a trend of decreasing crack length with increasing homogeneous shear strain. A possible explanation is that the adiabatic shear band in the primary shear zone is shear strain induced and shear stress controlled. When the homogeneous shear strain accumulates to a certain extent, the temperature increase will be large enough to trigger the thermo-plastic instability and an adiabatic shear band happens as a result. When the shear band is well developed, the crack, which is another way to form segmented chips, is suppressed. The segment spacing also tends to decrease with increasing homogeneous shear strain. The segment spacing is determined once the shear band is formed, and thus the spacing is smaller when the shear band is easier to form (larger homogeneous shear strain). This phenomenon should result in decreasing crack length with decreasing segment spacing.

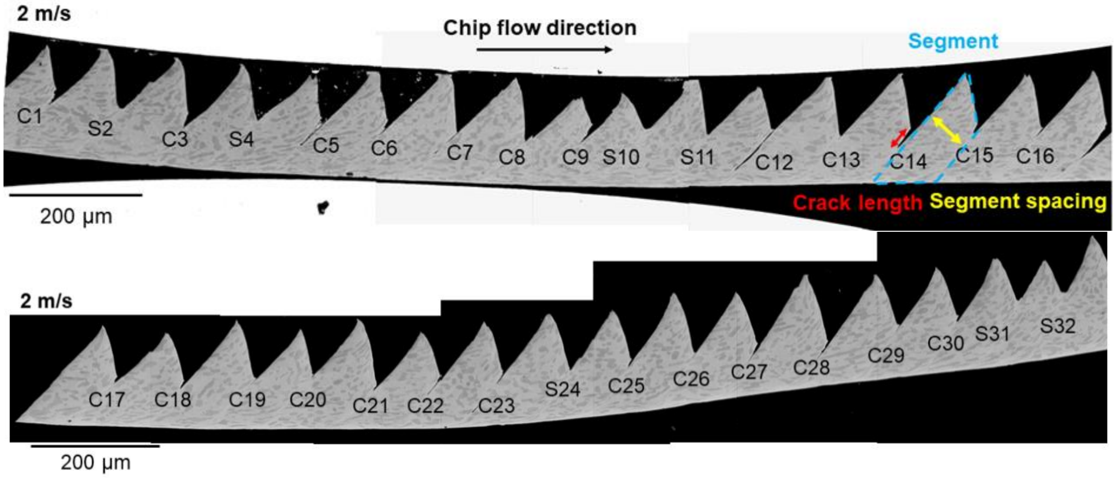

Figure 6.1 2m/s chips on which segment spacing, shear strain, and crack length are investigated (The locations are label with C or S which represents the presence of crack or only shear band.). Measurements of crack length, segment spacing, and homogeneous shear strain within the segment is illustrated.

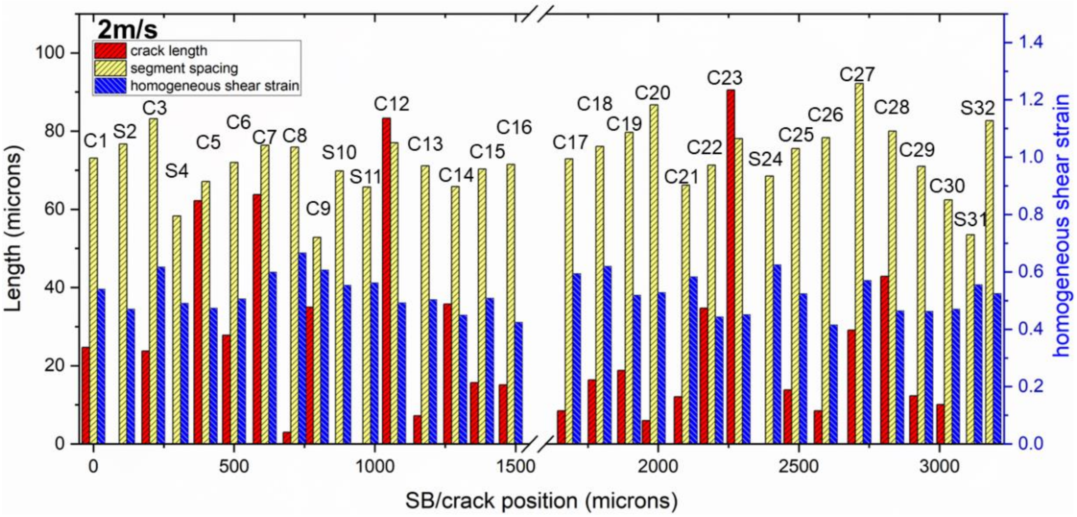

Figure 6.2 The distribution of crack length, segment spacing, and homogeneous shear strain within each segment, with respect to their actual locations at 2 m/s.

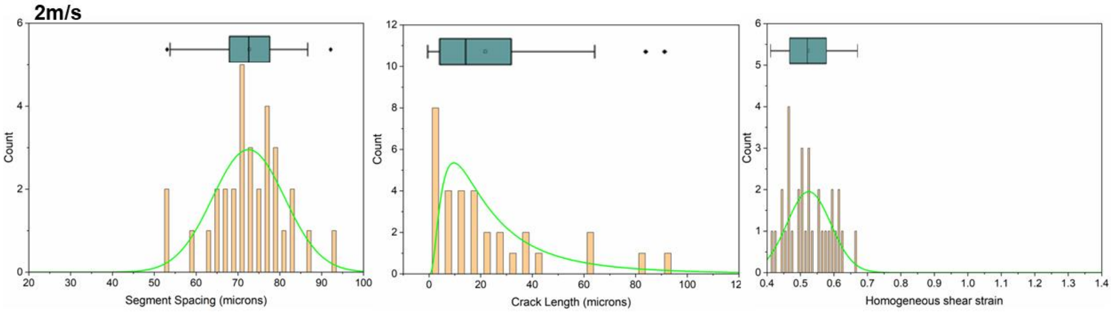

Figure 6.3 The histogram of crack length, segment spacing, and homogeneous shear strain within each segment.

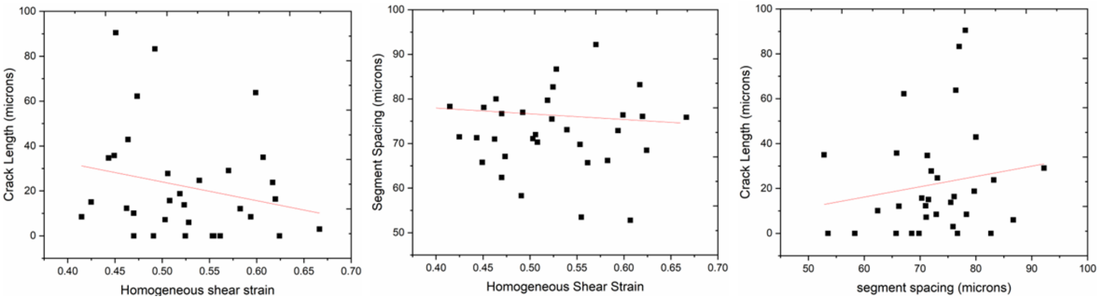

Figure 6.4 Correlation between crack length, segment spacing, and homogeneous shear strain within each segment.

6.1.2 Schmid factor analysis

To estimate what slip systems are likely to be active in a given shear band, the stress tensor is needed. A simulation was performed as part of this project, using a Johnson-Cook material model optimized to match the geometry of the observed chips by DEFORM 2D v.11.2 commercial software. The tool was modeled as a mechanically rigid body but with a meaningful thermal conductivity to allow the temperature to rise during cutting. A cutting length of 1 mm was used in the FE simulation to see multiple segments while minimizing the computation time. A value of 2000 for the Cockroft-Latham model damage criterion was used to make the chip segmentation size closer to experimental values. Detailed information of the Johnson-Cook constitution model, material constants of STA Ti64, shear friction coefficient and heat transfer coefficient of the tool, and other simulation parameters can be referred to in [97].

The simulation for chips cut at 2 m/s is shown in Fig. 6.5. The effective stress distribution shows an adiabatic shear band, within which the effective stress is much lower than that in the segment. As can be seen in Fig. 6.5, the stress tensors at 15 points were extracted from FE simulation by DEFORM 2D. Using the local stress tensors at location P5, generalized Schmid factors were computed for crystal orientations present in each segment in Fig 6.6.

The two prevailing theories concerning the formation of segmented chips are (i) propagation and growth of cracks from the outer surface of the chips [47] and (ii) adiabatic shear bands caused by localized shear deformation [48], respectively. According to the bending fracture surface observation in Fig. 5.1., and the correlation between the crack length and homogeneous shear strain, these two mechanisms are competing with each other in forming segmented chips, depending on the local crystal orientations. Orientations of the α_p grains near the tip of each tooth and the corresponding locations prior to shear on the other side of the shear band were identified using electron backscatter diffraction (EBSD). The stress tensor at point 5, the tip of teeth within the potential shear band (labeled on Fig. 6.5 (e)) is determined to be:

$$\sigma_{simulation} = \begin{bmatrix} 303.47 & -279.2 & 0 \\ -279.22 & 44.83 & 0 \\ 0 & 0 & 174.14 \end{bmatrix}.$$

Using this stress tensor and Schmid factors were computed and the slip systems with the top five values were recorded.

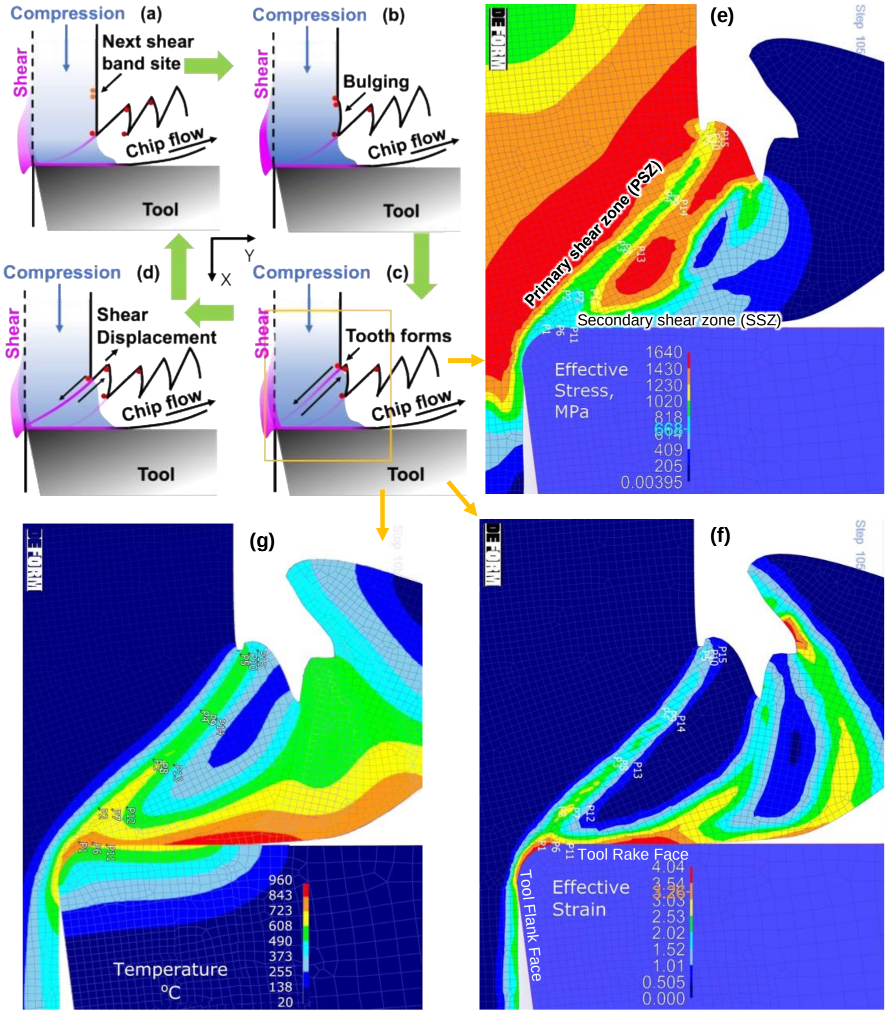

Figure 6.5 Illustration of 2-D segmented chip formation cycle (a-d) caused by localized shear, where the pair of red dots identify positions that were once adjacent prior to cutting. The blue and magenta shaded area represents the regions that are highly stressed. The effective stress (e), strain (f) and temperature (g) in the 2 m/s FEM simulation illustrate formation of a shear band at the time when a tooth emerges. The position labeled P15 was used to extract a local stress tensor [97].

On the other hand, the plane strain compression stress tensor used in Chapter 5, where the cracks tended to occur in segments with lower homogeneous shear strain, was also used to compare with the simulation result. This prior correlation is in agreement with the above discussion of Fig. 6.4, which is based upon a much larger sample size. It is reasonable to compare the stress tensor from the simulation and the plane strain stress tensor:

$$\sigma_{plane\ strain} = \begin{bmatrix} -300 & 0 & 0 \\ 0 & 300 & 0 \\ 0 & 0 & 0 \end{bmatrix}.$$

Since the shear only happens in one of the two 45° directions, the top three highest Schmid factors with slip in the direction observed will be used because those revealing the shearing in the other 45°direction did not actually occur. The results are shown in Fig. 6.7.

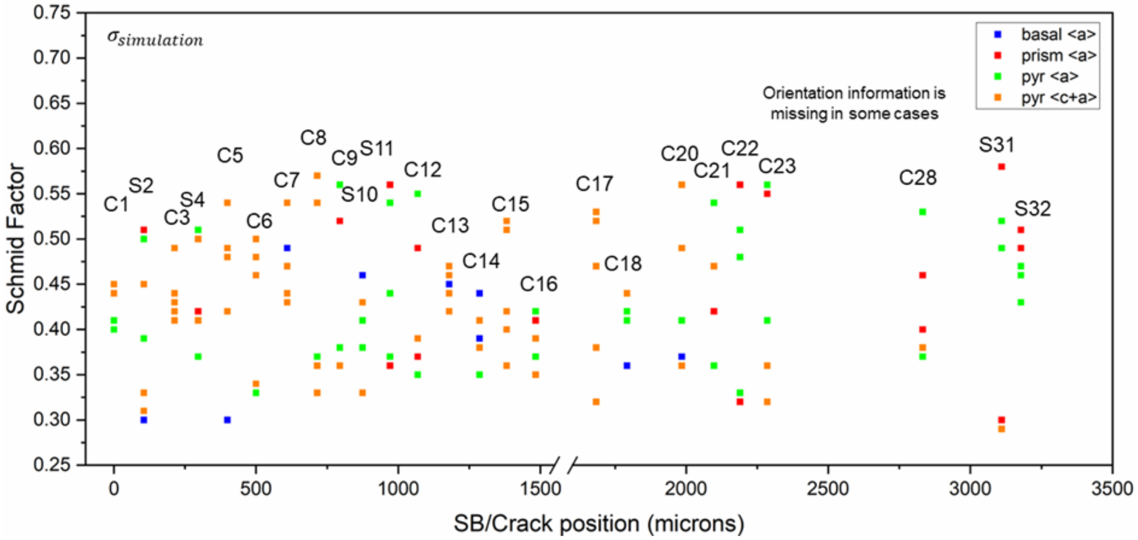

Figure 6.6 Top five Schmid factors calculated under the stress tensor from FE simulation ($\sigma_{simulation}$) show the presence of crack with pyramidal <c+a> slip activated.

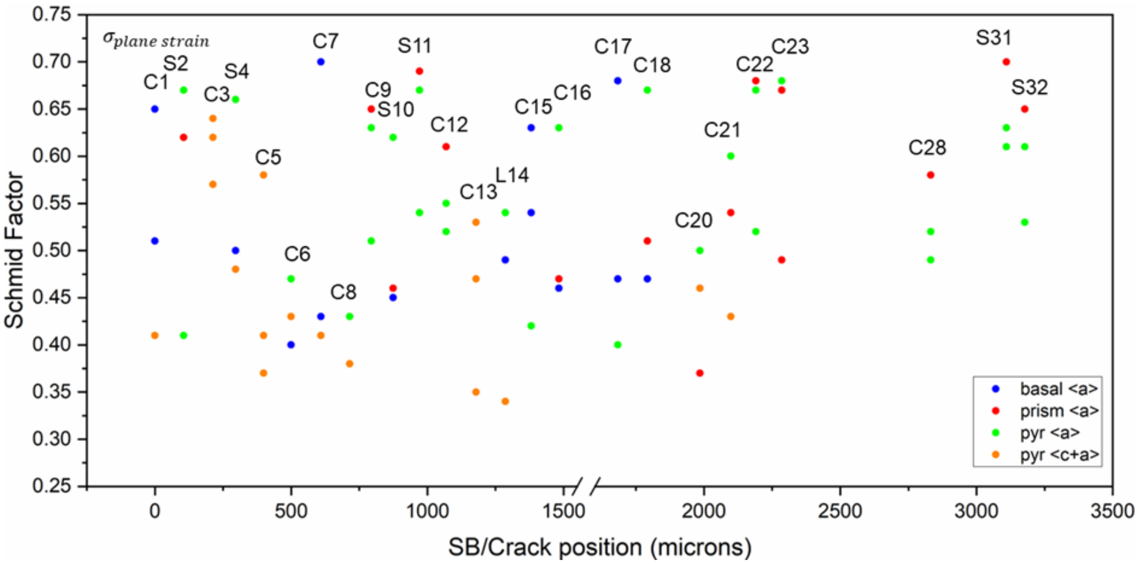

Figure 6.7 Top three Schmid factors calculated under the plane strain compression condition ($\sigma_{plane\ strain}$) show the activation of non <c+a> slip at all locations.

The Schmid factors calculated for dominant orientations described using the stress tensors from the FEM simulation are plotted in Fig. 6.6, for each characterized segment in the 2 m/s chip. About half of the segments show high Schmid factors for <a> slip, 4 for basal, 7 for prism, and 6 on pyramidal planes. All 6 segments without cracks are included in this set. There are 10 segments with much higher Schmid factors for pyramidal <c+a> slip, all of which are correlated with cracks. As is well-known, the CRSS of <c+a> slip systems are much higher than basal <a>, prism <a> and pyramidal <a>. Given the high strain rate sensitivity of stress at strain rates above about 100 s^{-1} [70], and the fact that different slip systems have different strain rate sensitivity [124] is likely that the stress state is saturated, and is high enough to activate significant <c+a> slip, though it may not account for the majority of strain. Given that the CRSS is at least 3 times higher for <c+a> slip the degree of <c+a> slip that occurred would generate at least 3 times as much heat for the same amount of strain as <a> slip. As a result, the thermal instability could be triggered at a lower strain than in conditions dominated by <a> slip, leading to the nucleation and growth of micro-voids and/or crack formation along the shear band. Another possibility is that the shear crack initiated at the free surface and kept propagating toward the tip of tool until a stress state or softer material at higher temperature that could arrest the crack was encountered. The variability in temperature based upon different amounts of work and adiabatic heating could account for variable crack depths.

The plane strain compression boundary condition leads to Schmid factors that are ~20% higher than those calculated using the FE simulation stress tensor (Fig. 6.7), and the Schmid factors for <a> slip systems were highly favored at all except 2 locations where <c+a> systems were favored. This differs significantly from the FE simulation stress tensor results. Only slip system Schmid factors where the slip plane was aligned with the shear bands were considered. Though both approaches may approximate what actually occurred, it is unclear whether a kinematic plane strain compression boundary condition is more descriptive than a stress-based condition from the simulation based upon isotropic properties. As it is reasonable that the stored elastic strain energy would be high in <c+a> slip systems, and higher stored energy would favor crack nucleation, the simulation stress states are probably more meaningful.

6.1.3 Representative cracks and shear bands in 2 m/s chips

Fig. 6.8 gives examples of the orientations favored by prism <a>, basal <a>, pyramidal <a>, pyramidal <c+a> slip and orientations that are resistant to deformation. In the order of from left to right, higher stress level is needed and decreasing likelihood of happening for these slip systems. According to the shear displacement, the grain near the valley to the left of the shear band/crack was adjacent to the one near the tooth. It is thus meaningful to compare their orientations and the orientations of other grain pairs that were adjacent prior to cutting.

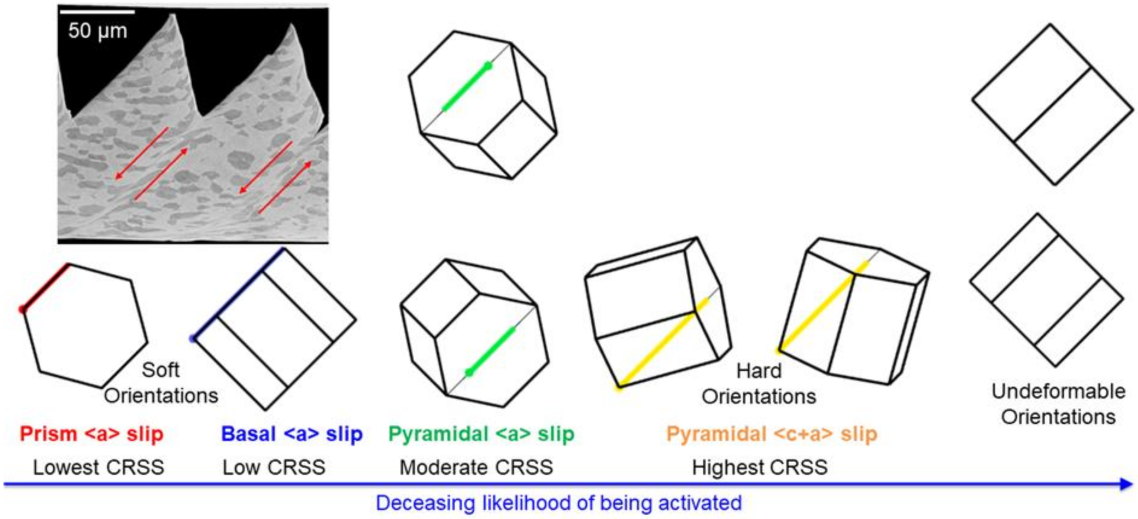

Figure 6.8 Crystal orientations with slip systems aligned with the plane of shear in order of likelihood of happening.

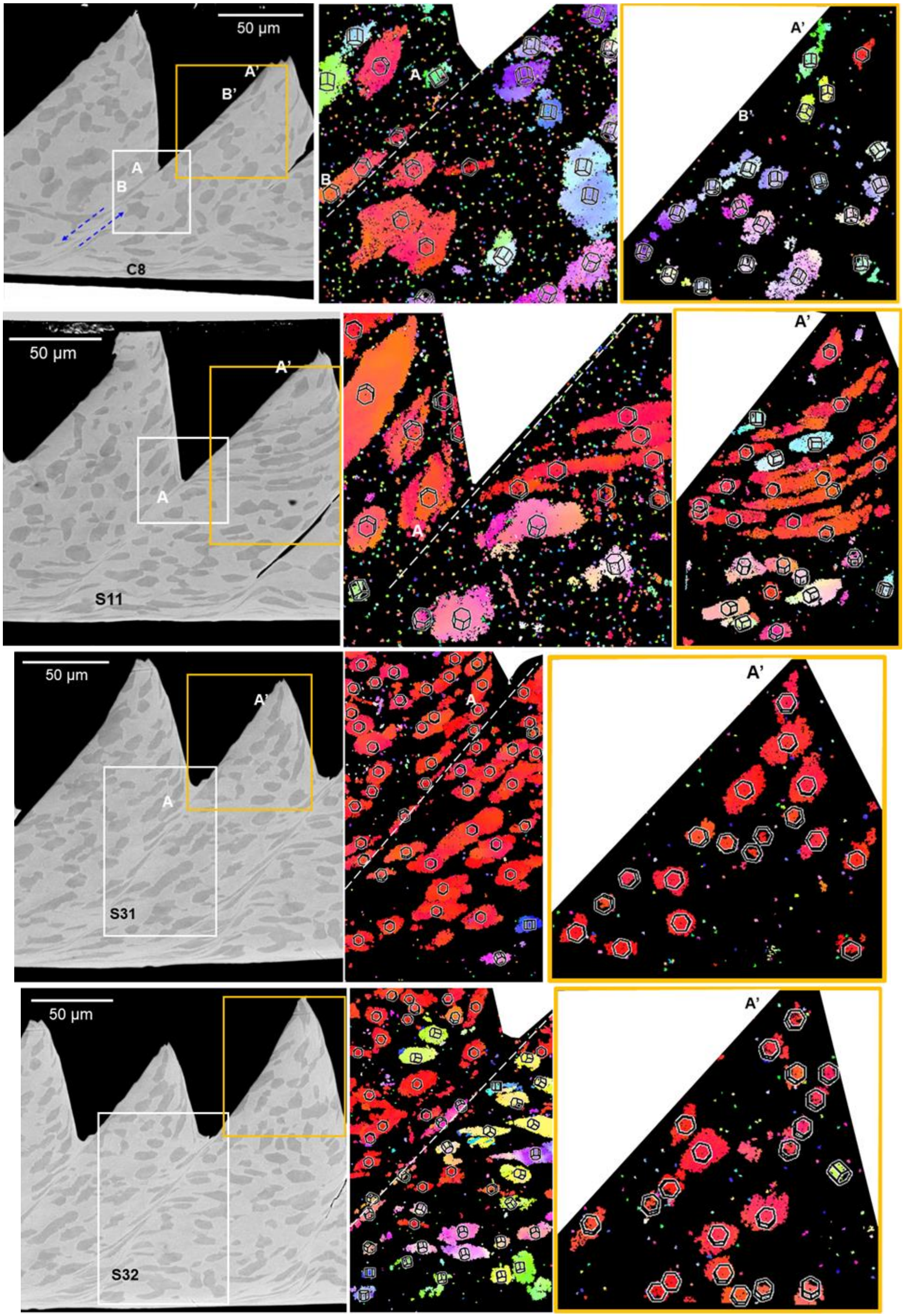

Figure 6.9 2 m/s chip segments with localized shear bands and elongated grains favoring prism <a> slip. Blue dashed arrows on the first SEM image illustrate the sense of shear. White dashed lines on EBSD maps indicate the center of the shear bands.

In Fig. 6.9, four examples of shear bands without cracks are illustrated. In C8, dashed arrows identify the location of the ASB in the map beneath the valley. C8 and S11 have narrower shear bands than S31 and S32. They share the characteristic that the α_p grains show a large amount of shear have the same red orientation that favors prism <a> slip systems. In C8, the α_p grain near the upper right peak has a hard-to-shear orientation (A') and the one near the valley (A) also has a green orientation but is relatively much easier to shear. Prior to cutting the two grains were located next to each other, and their orientations can be similar (due to the commonly seen micro-texture in Ti alloys) or very different. In this case, they have distinctively different orientations. This might give rise to the tiny crack that is right on top of the sheared α_p grain with red orientation. Since the easy-to-shear grain has made main contributions to the shear displacement required to form the segmented chip, the crack is trivial and may reflect the small green orientation. In addition, this case supports the proposal that the adiabatic shear band may originate from the secondary shear zone by Molinari et al. [74]. As can be seen in the EBSD scans in previous work [97], the elongated grain B has the same orientation as the grain below it that transitions from the secondary shear zone to the primary shear zone as half of it is sheared horizontally and the other half is sheared in the 45 ° direction. In the other three cases, a number of prism <a> favored red orientations were detected in the vicinity of the shear bands, for both the peaks and valleys. This makes good sense since the prism <a> slip is the easiest to activate slip system in hexagonal Ti alloys.

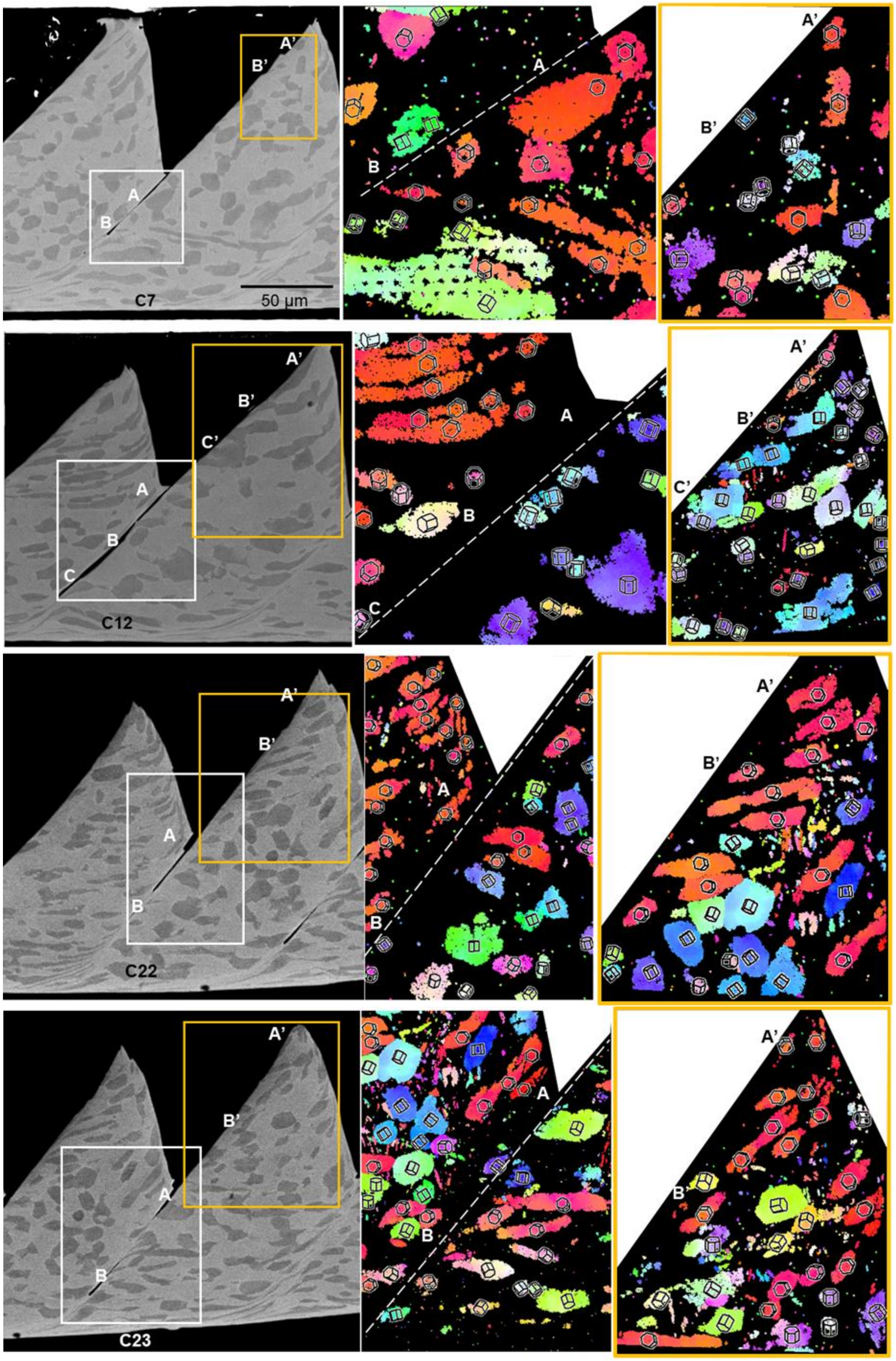

Figure 6.10 2 m/s chip segments with localized shear bands and elongated grains favoring prism <a> slip. Blue dashed arrows on the first SEM image illustrate the sense of shear. White dashed lines on EBSD maps indicate the center of the shear bands.

Fig. 6.10 provides four examples of long straight Mode II cracks. Looking at the orientations in the crucial regions where the upper right peak and the region to the left of the valley were adjacent prior to cutting, there are many α_p grains with red orientations that favor prism <a> slip near the shear bands, suggesting that prism orientations may be helpful but not sufficient to prevent cracking. In C7, the homogeneous shear strain in this segment is 0.6 (large enough to induce the adiabatic shear band at 2 m/s), but unlike uncracked ASBs, other crystal orientations above the valley side of C7 are present that may have prevented uniform deformation of red grains. If the long straight crack initiated at the tip of the tooth and propagated to the crack tip, then it was arrested at a ductile red grain that has a high aspect ratio to the right of crack tip, where the material was hotter and softer. At the tip of the tooth, orientations are red and blue, where the blue orientation is favorably oriented for basal slip, and this grain was originally opposite the nearly circular green grain (marked B and B'). As the green grain is a harder orientation that was initially adjacent to a soft "blue" basal orientation, a plastic strain incompatibility resulted, and the fracture surface ledge discontinuity is located here. Other α_p grains near this elongated α_p grain also have orientations favored by prism <a> slip, but they remained nearly equiaxed or globular. Two hypotheses could account for this: The first one is that the shear band initiated from hot and soft SSZ and propagated toward the cooler and stronger free surface of the chip, as proposed by Molinari et al. [74] based upon their simulation results. The temperature around the peak is much lower than the SSZ and the stress is much higher, making a crack is easier to nucleate. The second one is that localized shear deformation and crack propagation are two competing mechanisms during the formation of segment chips. One argument that supports the two competing mechanisms is the crack length. Vyas and Shaw [47] mentioned in their work that the crack length was controlled by the frequency of segmentation. The higher the frequency is, the shorter the crack length will be. The present work shows that the crack lengths are random at each speed and there is no obvious trend with increasing cutting speed, as either (frequency increases with increasing cutting speeds [125]). This supports the hypothesis that the formation of cracks is dependent on the local orientations and cracks are competing with and complementary with the ASBs in order to satisfy the shear displacement between the peak-valley pair to form segmented chips.

ASB C12 has some similar characteristics, as C7, as prism red regions at the tip of the tooth are also present on the upper valley side, but beneath that B' has soft orientation but B has hard orientations, resulting in incompatible strains on two sides. Further beneath B-B' pair, at locations C-C', the tooth has hard orientations that would also lead to incompatible strain on the two sides. Above the valley of C12, there are many red grains that are elongated horizontally, reflecting compression prior to forming the ASB/crack. In contrast, those below this cluster have very small amounts of deformation. This shows that the so-called homogeneous shear strain within the segment is not homogeneous across the segment. The rounded valley to the left of the crack suggests ductile deformation and formation of a smooth rather than notched peak, but the subsurface strain incompatibility may have triggered the crack beneath the softer tooth tip volume. This scenario is more exaggerated in in C22, where the volume of ductile red orientations is larger, but harder blue orientations are beneath the surface of the adiabatic shear band. However, in this case, there was no evidence of forming a smoother tooth, and instead, a wider crack opening took place, and this suggests that the crack nucleated deep beneath the surface. A similar set of features is present in C23, where a deep crack nucleation may have taken place due to harder orientations in the ASB regions. Furthermore, the calculated homogeneous shear strains in C22 and C23 are low, 0.44 and 0.45, which can account for the absence of adiabatic shear bands because the nucleation of adiabatic shear bands is strain induced and then the propagation of the shear bands is stress controlled [52].

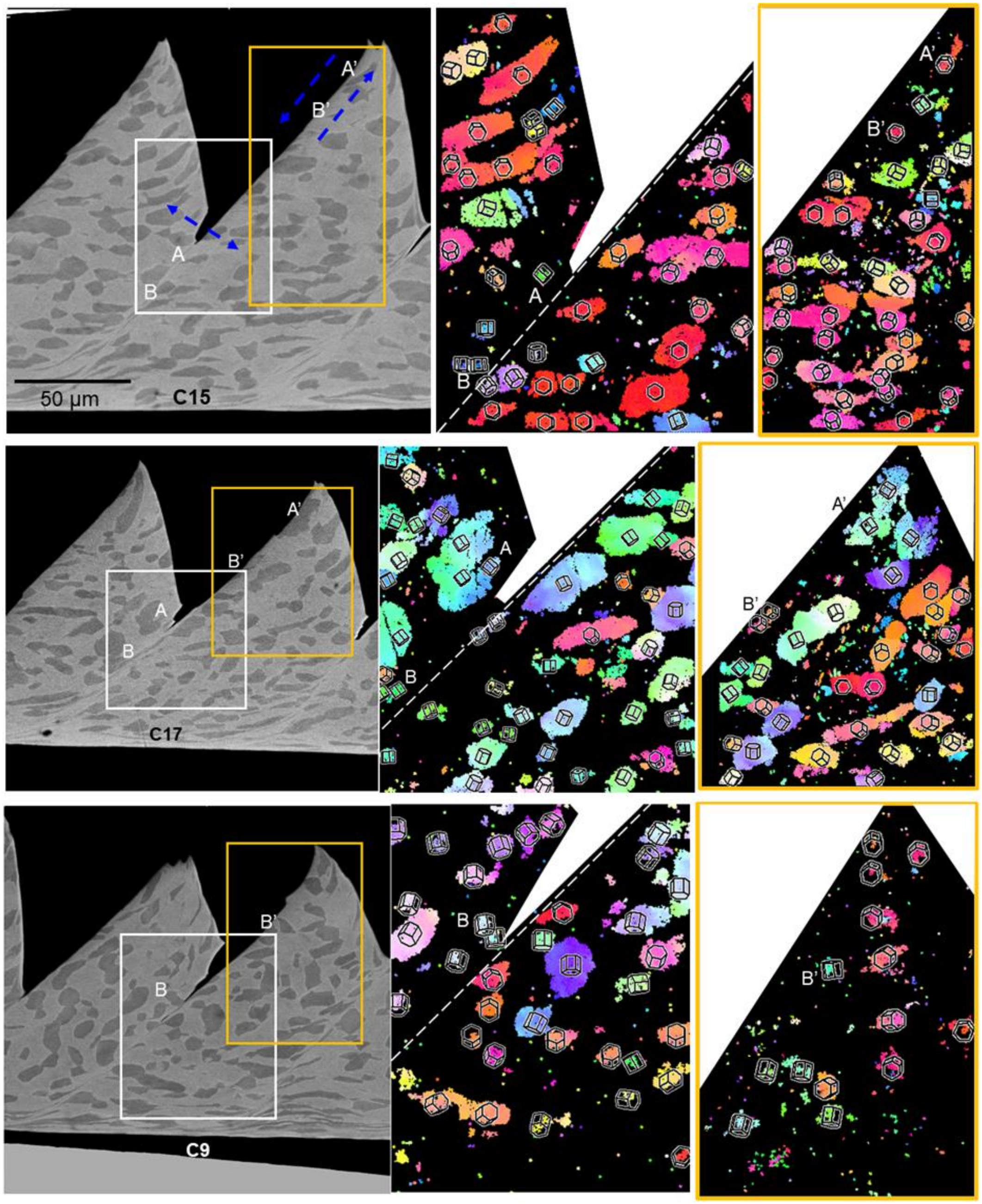

Figure 6.11 Wide-open cracks provide evidence of mode I propagation.

Figure 6.11 (cont'd)

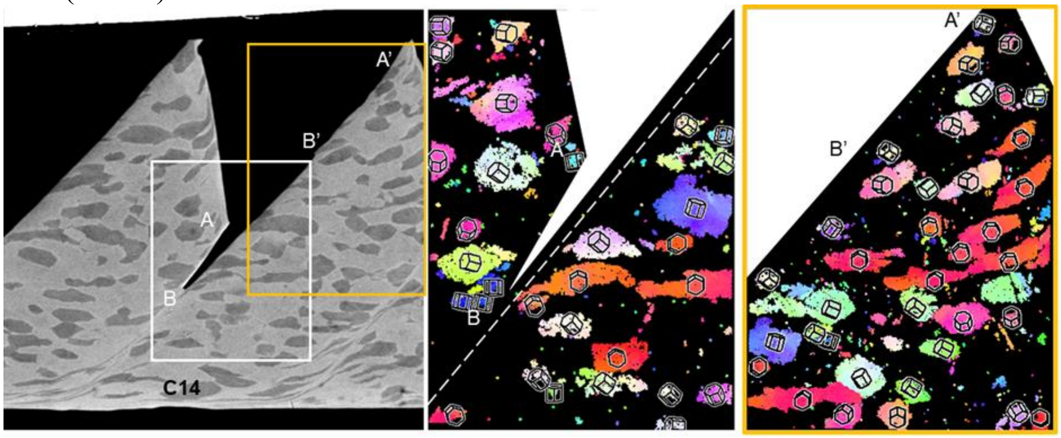

Fig 6.11 shows four examples of cracks with a strong mode I opening component in addition to the mode II shear component. In addition, the crack arrest, which makes these cracks much shorter than those long straight cracks, indicated that both the crack and shear band are responsible for the formation of segmented chips simultaneously, and the two mechanisms are competing with each other.

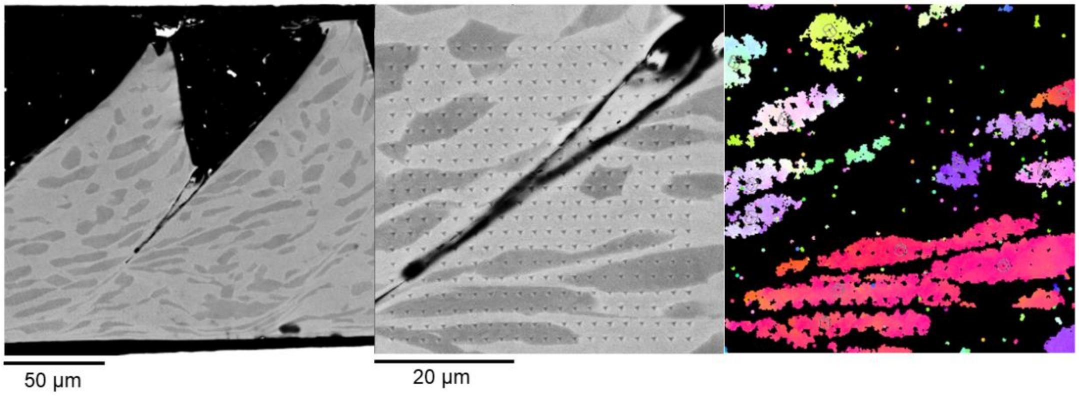

Figure 6.12 Rough-interface cracks indicate the coalescence of micro-voids.

The cracks in Fig. 6.12 show rough features that may have resulted from the growth and coalescence of micro-voids within the shear bands. Also, the two cracks branched, just like the shear band bifurcation in [52]. Shear localization precedes failure mechanisms such as voids and cracks. A well-developed shear band is often accompanied with voids and cracks within it. These defects accelerate localization and localized deformation creates fresh nucleation of micro-voids and cracks.

6.1.4 Deformation twins in 2 m/s chips

In hexagonal closed packed metals, such as magnesium, zirconium, and titanium, basal <a> and prism <a> slip are the dominant deformation mechanisms due to their low CRSS. However, the activation of these two slip systems cannot accommodate either extension or compression along c-axis [126]. In addition to the second-order <c+a> slip, twinning is another important mode to accommodate the deformation along c-axis, including $\{10\bar{1}2\} < \bar{1}011 >$ and $\{11\bar{2}1\} < \bar{1}\bar{1}26 >$ that lead to extension along c-axis, and $\{11\bar{2}2\} < 11\bar{2}\bar{3} >$ and $\{10\bar{1}1\} < \bar{1}012 >$ that give rise to contraction along c-axis [126]–[129].

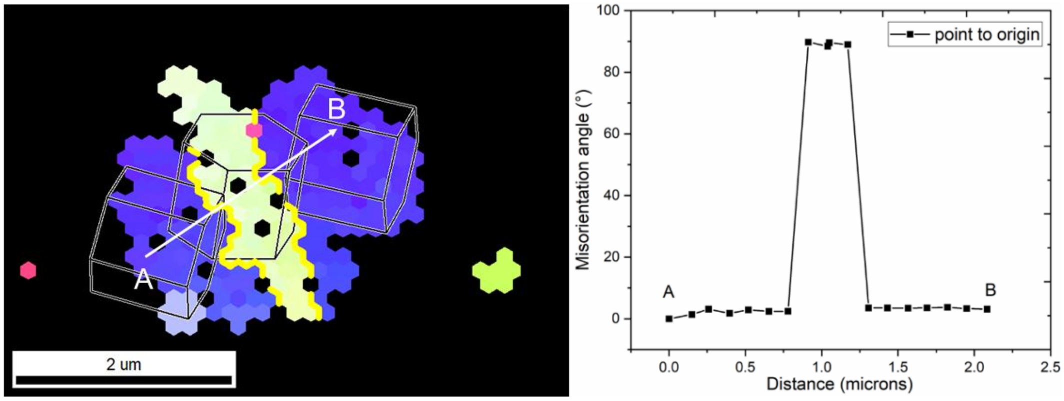

Figure 6.13 Representative T1-type twins in the chip segments exhibiting misorientation angle of ~89° (twin boundary is labeled with yellow lines).

A few twins were observed in the 2 m/s chips, which were also observed in 1 and 1.5 m/s chips. The misorientation angle between the parent and twined grains are approximately 85° and they have a common a-axis (Fig. 6.13). The twinning mode is $\{10\bar{1}2\} < \bar{1}011 >$ extension twinning. In commercially pure titanium (CP Ti), a large fraction of both extension $\{10\bar{1}2\} < \bar{1}011 >$ twins and contraction $\{11\bar{2}2\} < 11\bar{2}\bar{3} >$ twins have been observed [130]. In contrast, mechanical twining as a deformation mode is much less prevalent in α-Ti-6Al-4V alloy. It has been reported that the addition of Al is responsible for the suppression of twinning mechanisms. The accommodation of deformation along c-axis can be replaced by the activation of <c+a> slip on pyramidal planes or extra deformation in the β phase. When the Al content is higher than 5 at. %, twinning is almost fully suppressed in single crystals [131], [132]. However, there is research reporting on very small fraction of twins in Ti64 alloy at high strains and strain rates, such as cold-rolling and equal channel angular extrusion (ECAE) [128], [131], [133]. The shear strain within the segments at 2 m/s is between 0.4 and 0.65 as can be seen in Fig. 6.3, which is smaller than the theoretical homogeneous shear strain value of 1.15 from a single pass of ECAE process with a channel angle of 90° [114]. The shear strain rate of 2 m/s is calculated to be ~20000 s^{-1}. Both explain why deformation twins take place in the chips.

6.2 Chips at 1 m/s

6.2.1 Crack length, segment spacing and homogeneous shear strain distribution of 1 m/s chips

The morphology of chips cut at 1 m/s can be seen in Fig. 6.14. Compared to the 2 m/s chip, 1 m/s chip exhibited much more variations in the chip peak/valley heights, segment spacing, and crack length. For instance, a few segments in the middle look similar to those at 2 m/s and large cracks occurred at these locations (C8-C13), while the segments on the right are much less segmented and fewer cracks were observed. This observation is also reflected in the metrics shown in Fig. 6.15, where the long red bars and short blue bars are located in the middle whereas the short red bars and long blue bars are on the right.

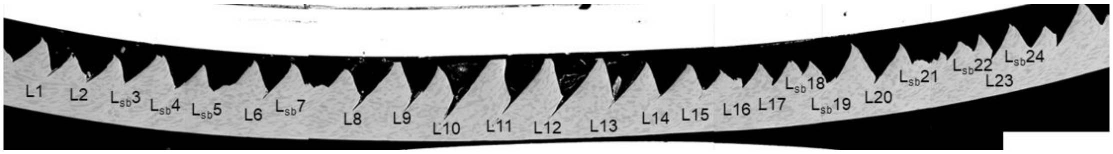

Figure 6.14 1m/s chips on which segment spacing, shear strain, and crack length are investigated.

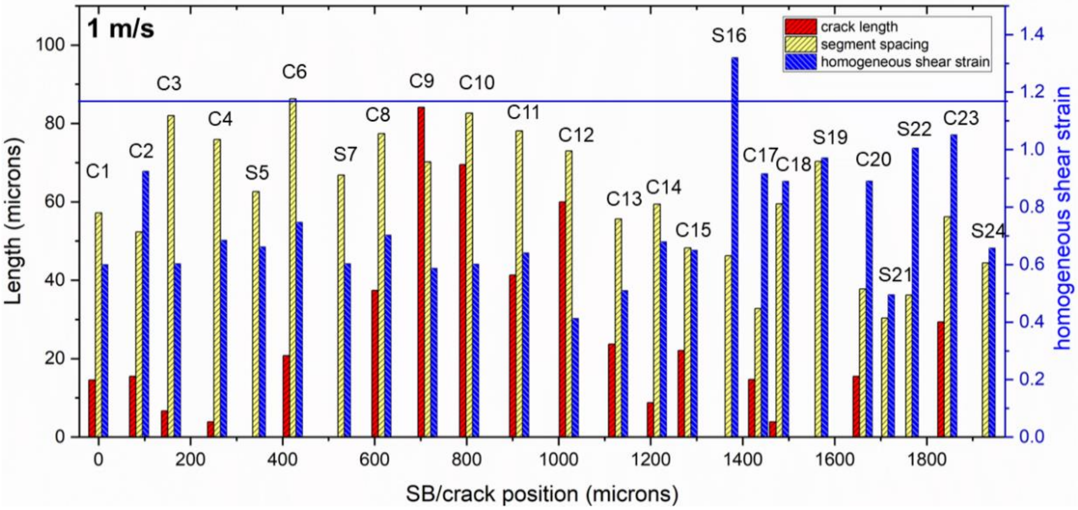

Figure 6.15 The distribution of crack length, segment spacing, and homogeneous shear strain within each segment, with respect to their actual locations at 1 m/s (the blue horizontal line indicates the theoretical shear strain value (1.15) in ECAP process).

The histogram of segment spacings show that the range of segment spacing is between 30 and 90 µm and exhibited a normal distribution (Fig. 6.16), which is smaller than those of 2 m/s chips (50-95 µm). Most of the cracks are shorter than 40 µm, while only 4 cracks have the lengths up to 85 µm. It is noteworthy that the homogeneous shear strain in the segments are between 0.4 and 1.4 at 1 m/s, which is much higher than the shear strain at 2 m/s (0.4-0.7). At the cutting speed of 1 m/s, the deformation stress is lower than at 2 m/s. As a result, more strain (deformation energy) is needed to cause temperature increase that triggers thermos-plastic instability. As indicated in Fig. 6.17, the crack length decreased with increasing shear strain, and the segment spacing shows a similar decreasing trend. Correspondingly, the segment spacing increased with increasing crack length. This phenomenon is the same as 2 m/s chips.

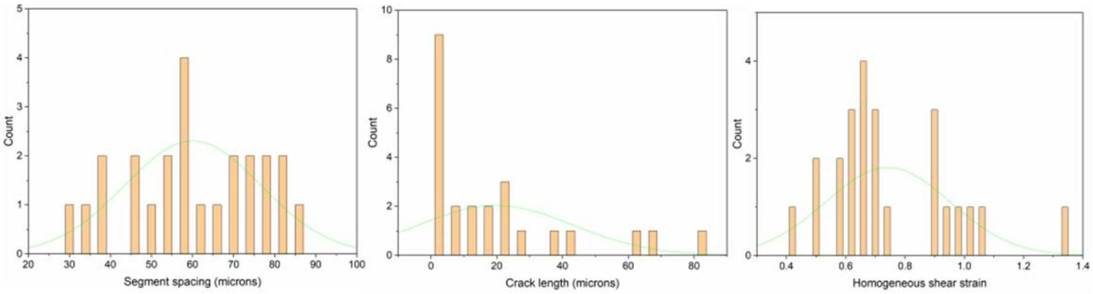

Figure 6.16 Histograms of segment spacings, crack lengths, and homogeneous shear strain within each segment.

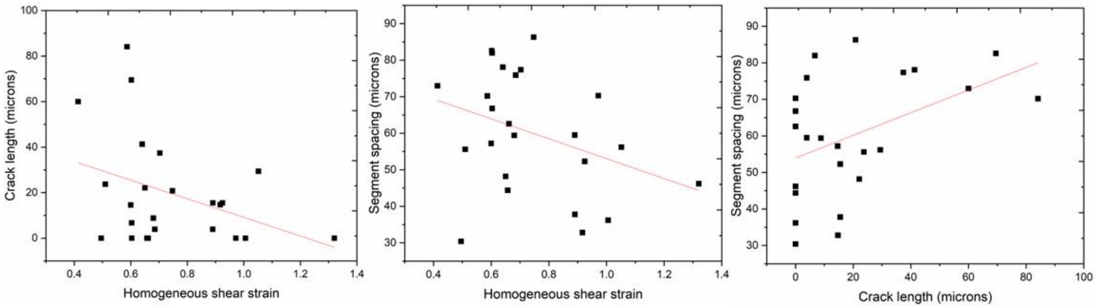

Figure 6.17 Correlation between crack length, segment spacing, and homogeneous shear strain within each segment.

6.2.2 Representative cracks and shear bands in 1 m/s chips

The cracks in Fig. 6.18 show both wide-open and long straight features, which provide evidence of both mode I and mode II propagation mechanisms activated during the propagation process. None of the α_p grains in the vicinity of the cracks have the red orientation, which depressed the formation of shear bands and promoted the cracking mechanism. In Fig. 6.20, the elongation and coalescence of the micro-voids took place within the shear band. One possibility for this phenomenon is that as higher normal stresses are encountered when a shear crack progresses downward from the free surface toward the tool tip, a continuous gross crack may gradually be converted into a discontinuous microcracked region [47]. On the other hand, Bieler et al. [134] observed that the cavity nucleation in lamellar Ti64 during upset forging process was located in boundaries with hard orientations present on one side, thus giving rise to large strain variations between neighboring colonies. Even though the stress state in upset forging is much more complicated, it is still possible that the nucleation of the micro-voids in the present study may result from the 90°-misorientation of the colonies on two sides.

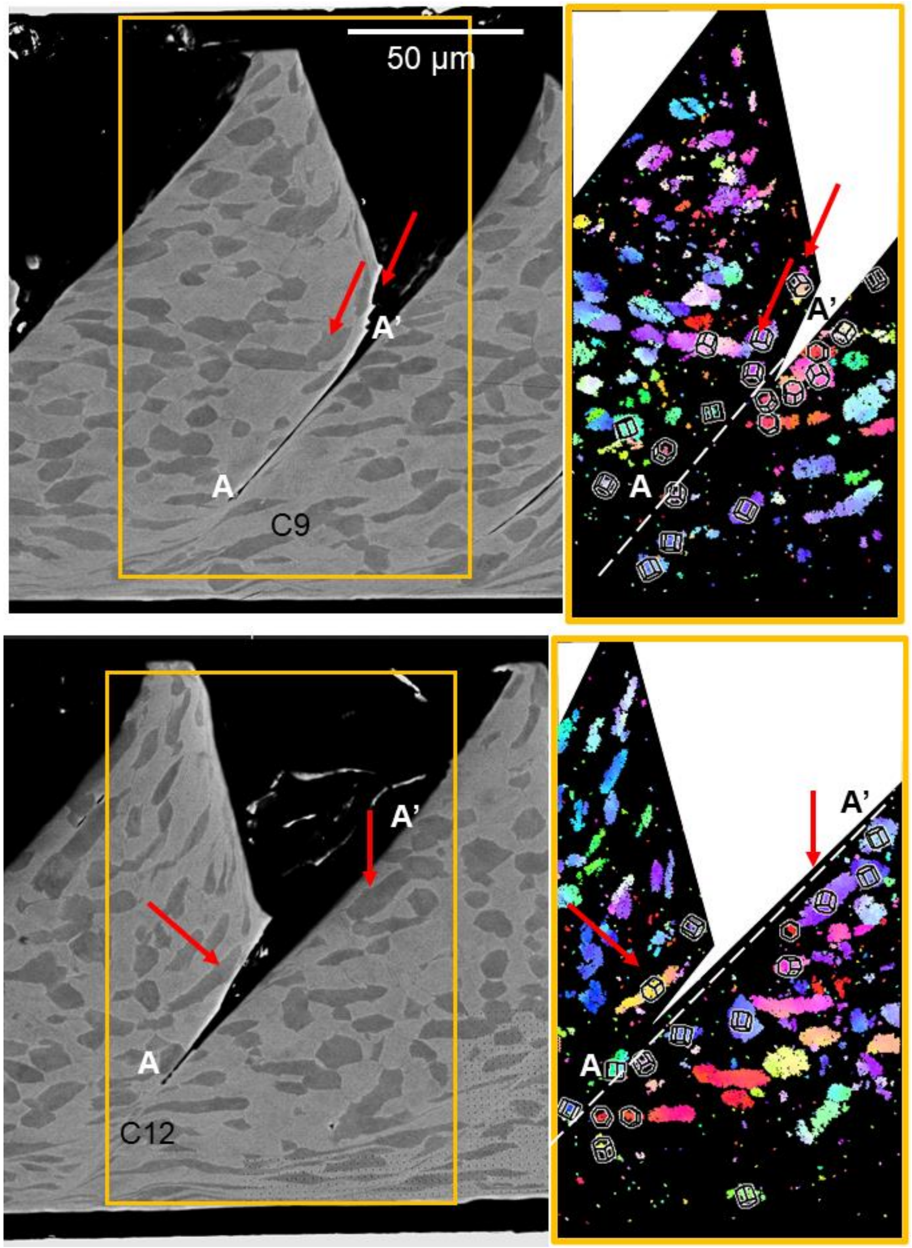

Figure 6.18 Cracks at 1 m/s are usually wide open. The arrows indicate the hard-oriented α_p grains.

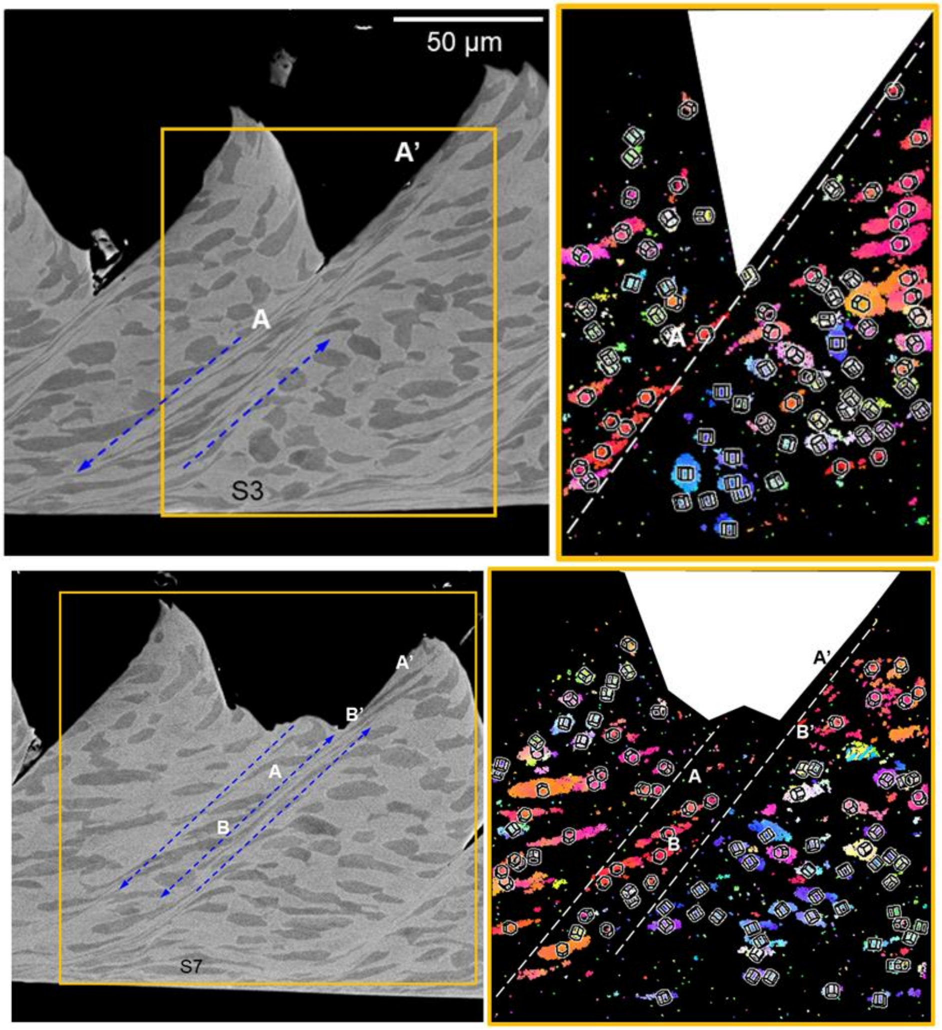

Figure 6.19 1 m/s chip segments with wide shear band regions with prism <a> favored orientations.

Compared with 2 m/s chips, α_p grains were less severely sheared in 1 m/s chips and the shear bands can be much wider, as can be seen in the PSZs in Fig. 6.19. According to the EBSD maps, the sheared α_p grains all exhibited red orientations which are favored by prism <a> slip. In S3 in Fig. 6.19, the shearing in PSZ is closely related to the SSZ. There are α_p grains in the SSZ sheared horizontally and gradually transitioning to the 45° shearing in PSZ. This observation is in agreement with the simulation result by Molinari et al [74], in which the shear bands are generated at the tool tip and propagate toward the chip free surface. However, his simulated chip morphology at 350 m/s showed no segmented features at all. Their explanation is that the shear bands did not have enough time to reach the chip free surface, which is an interesting but controversial idea.

In S3 in Fig. 6.19, the homogeneous shear strain is 0.6 and is high enough to trigger the adiabatic shear band. The localized shear strain in this shear band is estimated to be 4.38 due to a wide shear band width (15.2 μm, as shown in Fig. 6.21 (a)). In contrast, the homogeneous shear strain in S7 in Fig. 6.19 is 0.55 and the adiabatic shear band is even less localized so that the width between the two yellow arrows is much wider. The shear strain between the right two blue arrows is determined to be 1.46, which is much smaller than the localized shear strain in S3. Unlike the 2 m/s serrated chip, there is much greater variability of the shear band width in the 1 m/s, as illustrated in Fig. 6.21, where the shear band width varies from 15.2 μm to 1.3 μm. The 1.5 and 2 m/s chips show consistent shear band widths of approximately 1.5-2 μm. This observation agrees with the proposed model [135] that the shear band width is inversely proportional to the cutting speed. Using this model, the catastrophic shear strains in Fig. 6.21 are 6, 9 and 25, respectively. Using measurements of the aspect ratio of the sheared α_p grains provides catastrophic shear strain values of 17, 20, 31, which follow the same trend, but the model predicts much lower values, and a larger range. The potential crack is not considered by the model, which could also account for the shear displacement and thus the catastrophic shear strain will be smaller (in what case?). In addition, the model calculates the “average” catastrophic shear strain within the shear band, which also shows difference from the physical measurements that reflects the shear strain of specific α_p grains.

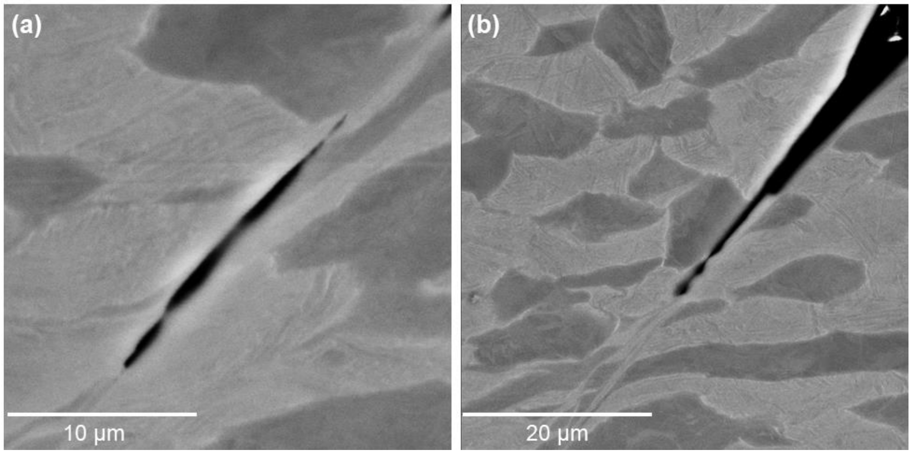

Figure 6.20 Evidence showing the elongation and coalescence of micro-voids (a) C6 ;(b) C12.

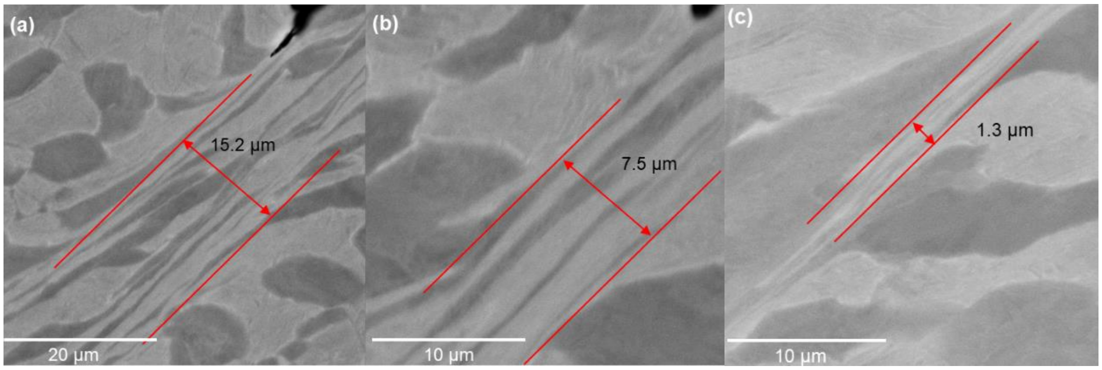

Figure 6.21 Shear band width variation (a) S3; (b) C2; (c) C18.

6.2.3 Deformation twins in 1 m/s chips

A few twins were also observed in the 1 m/s chip. The misorientation angle between the parent and twinned grains are approximately 85° and they have a common a-axis (Fig. 6.22). The twinning mode is identified to be $\{10\bar{1}2\} < \bar{1}011 >$ extension twinning.

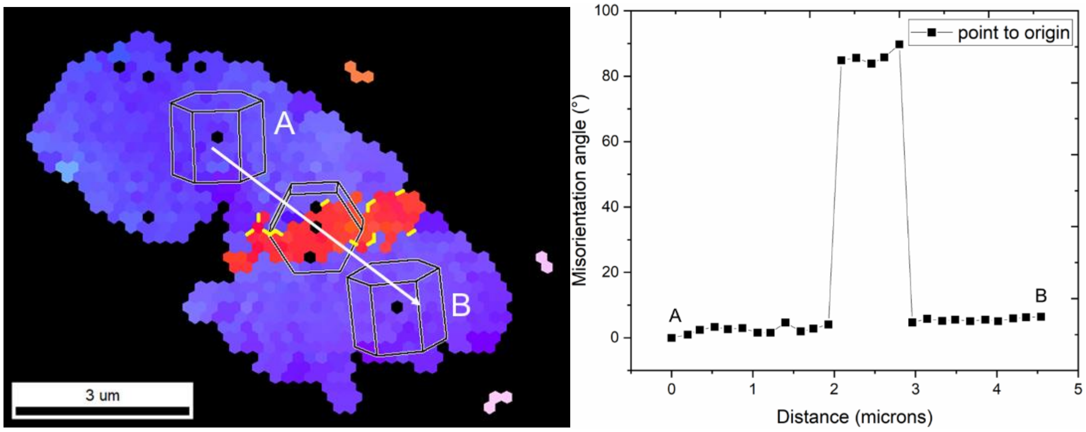

Figure 6.22 Representative T1-type twins in the chip segments exhibiting misorientation angle of ~85° (twin boundary is labeled with yellow lines).

6.3 1.5 m/s chips

6.3.1 Crack length, segment spacing and homogeneous shear strain distribution of 1.5 m/s chips

The morphology of chips cut at 1.5 m/s can be seen in Fig. 6.23. Compared to the 1 m/s chip, 1.5 m/s chip are much more uniform in the chip peak/valley heights, segment spacing, and crack length, and are a little more uniform than the 2 m/s chips as well. Another important difference is that the α_p grains are more uniformly deformed compared to the other two cutting speeds. There are no α_p grains showing extreme shear deformation, except for only a few in the vicinity of the shear bands. This conclusion can also be seen in Fig. 6.24. The homogeneous shear strain is uniformly distributed and so is the segment spacing.

From Fig. 6.25, the segment spacing is between 55 and 80 μm, similar to the 2 m/s chip. Most of the cracks are shorter than 40 μm, and only 2 cracks have the length of 60-70 μm, and are shorter than those in 2 m/s. It is noteworthy that the homogeneous shear strain in the segments is between 0.46 and 0.52, which is much smaller than the shear strain at 1 m/s (0.4-1.4) and is close to the shear strain at 2 m/s (0.4-0.7) but more homogeneously distributed. As indicated in Fig. 6.26, the crack length decreased with increasing shear strain, and the segment spacing shows a similar decreasing trend. Therefore, the segment spacing increased with increasing crack length. These parameters at all three cutting speeds show the same trend.

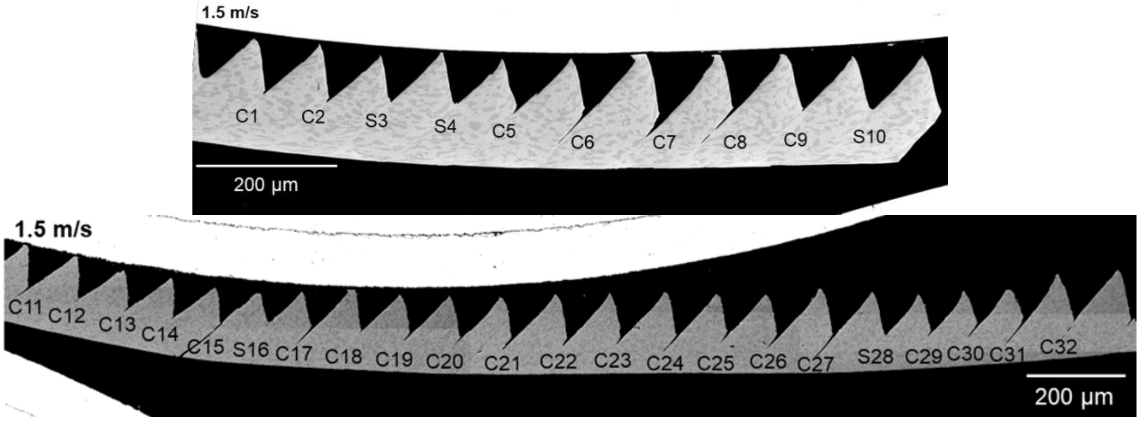

Figure 6.23 1.5 m/s chips on which segment spacing, shear strain, and crack length are investigated.

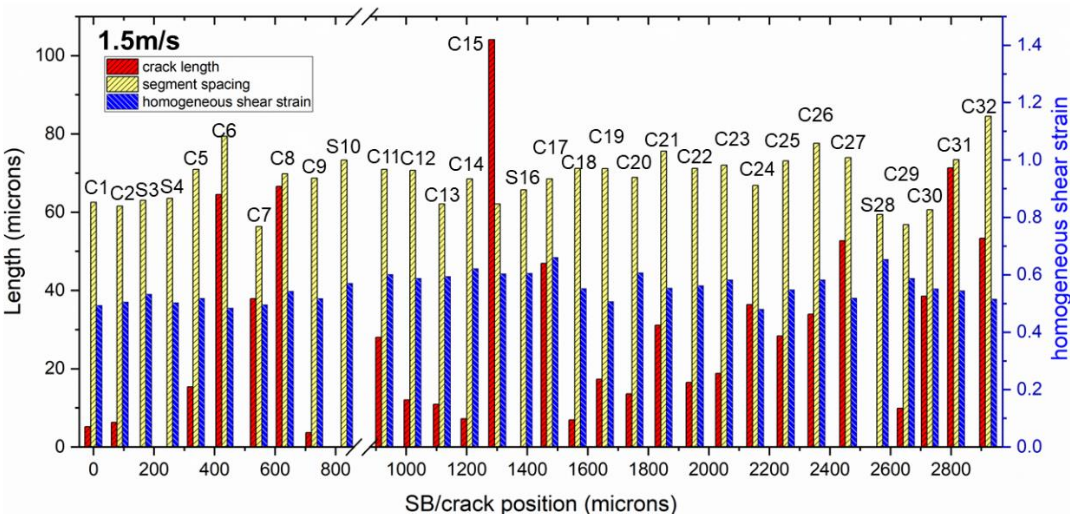

Figure 6.24 The distribution of crack length, segment spacing, and homogeneous shear strain within each segment, with respect to their actual locations at 1.5 m/s.

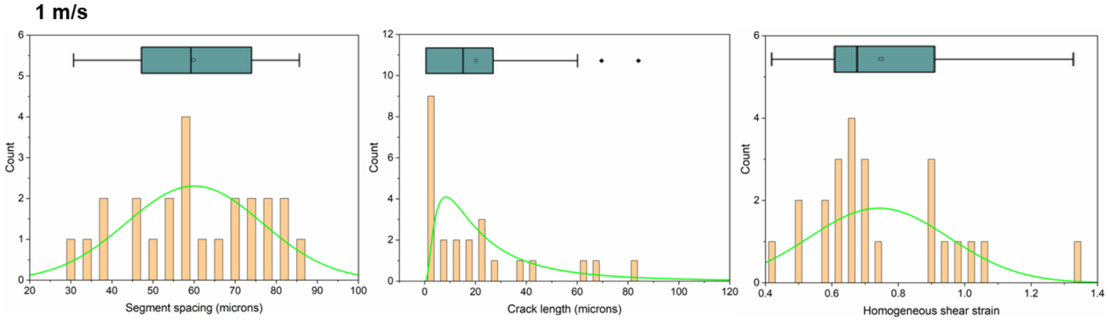

Figure 6.25 Histograms of segment spacings, crack lengths, and homogeneous shear strain within each segment.

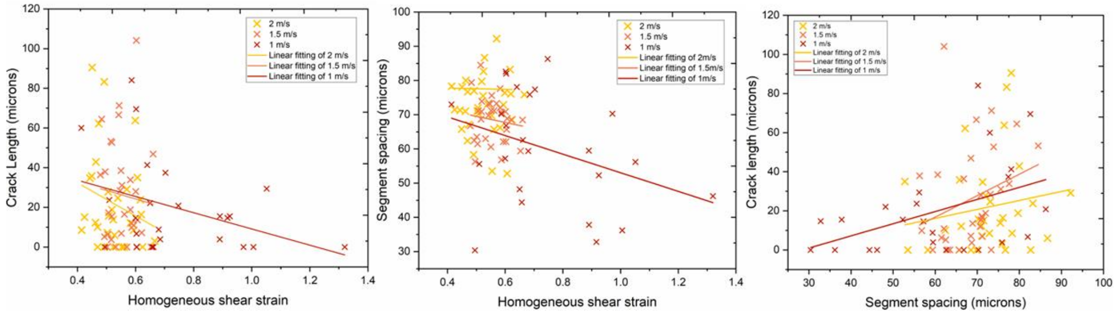

Figure 6.26 Correlation between crack length, segment spacing, and homogeneous shear strain within each segment.

6.3.2 Representative cracks and shear bands in 1.5 m/s chips

In both C6 and C8 in Fig. 6.27, there is a small crack after the arrest of the long straight crack. In the blue box shown in C6, this minor crack resulted from the elongation and coalescence of micro-voids within the shear band. The shear band is so thin that the micro-voids are small and as a result the elongation of the voids is not as pronounced. It is reasonable to infer that the small crack in C8 is also created by the coalescence of micro-voids.

Pole figures in Fig. 6.28 shows the texture evolution after cutting at three speeds (the observation directions of as-received bar and chips are consistent.). In Fig. 6.28, the as-received material has various peaks with different intensities on the (0001) pole figure, indicating the existence of a few predominant orientations. After being cut, the chips have a texture with a strong peak in the center of the (0001) pole figure, especially at 1 and 2 m/s. This means that the crystals preferentially rotated to orient the c-axis transverse to the chip flow direction as the material deforms, which can be accomplished with prism <a> slip. The difference in the 1.5 m/s chips lie in the intensity of the peaks. Maximal intensity is not in the center but located at the upper right peak.

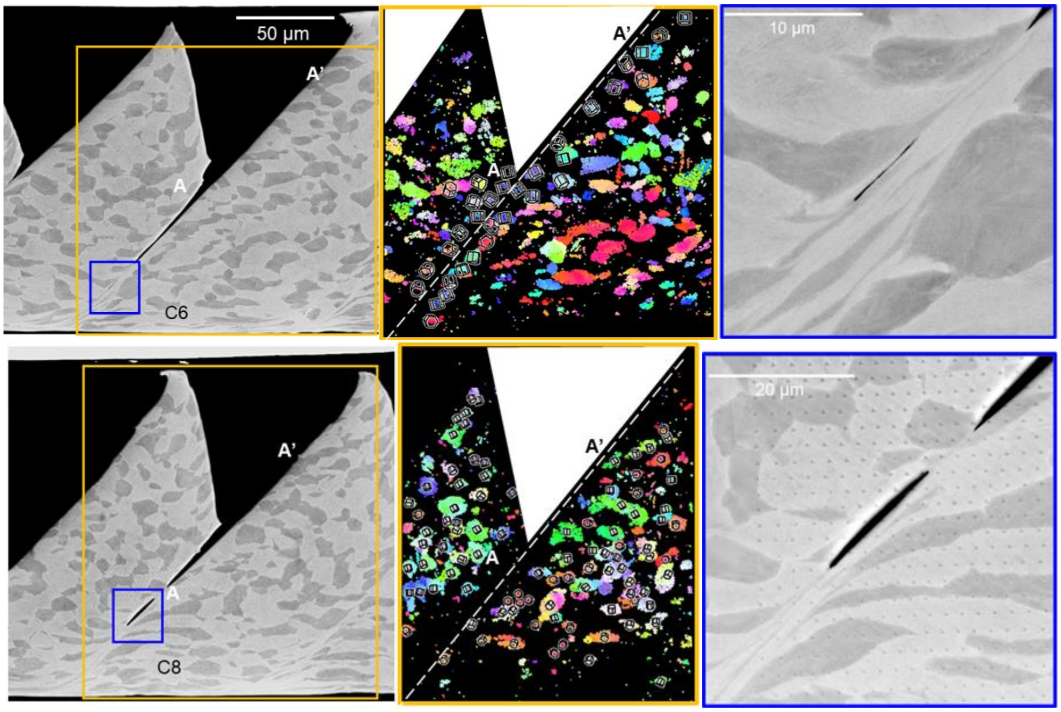

Figure 6.27 Long straight crack with small opening at the chip valley (1.5 m/s chip).

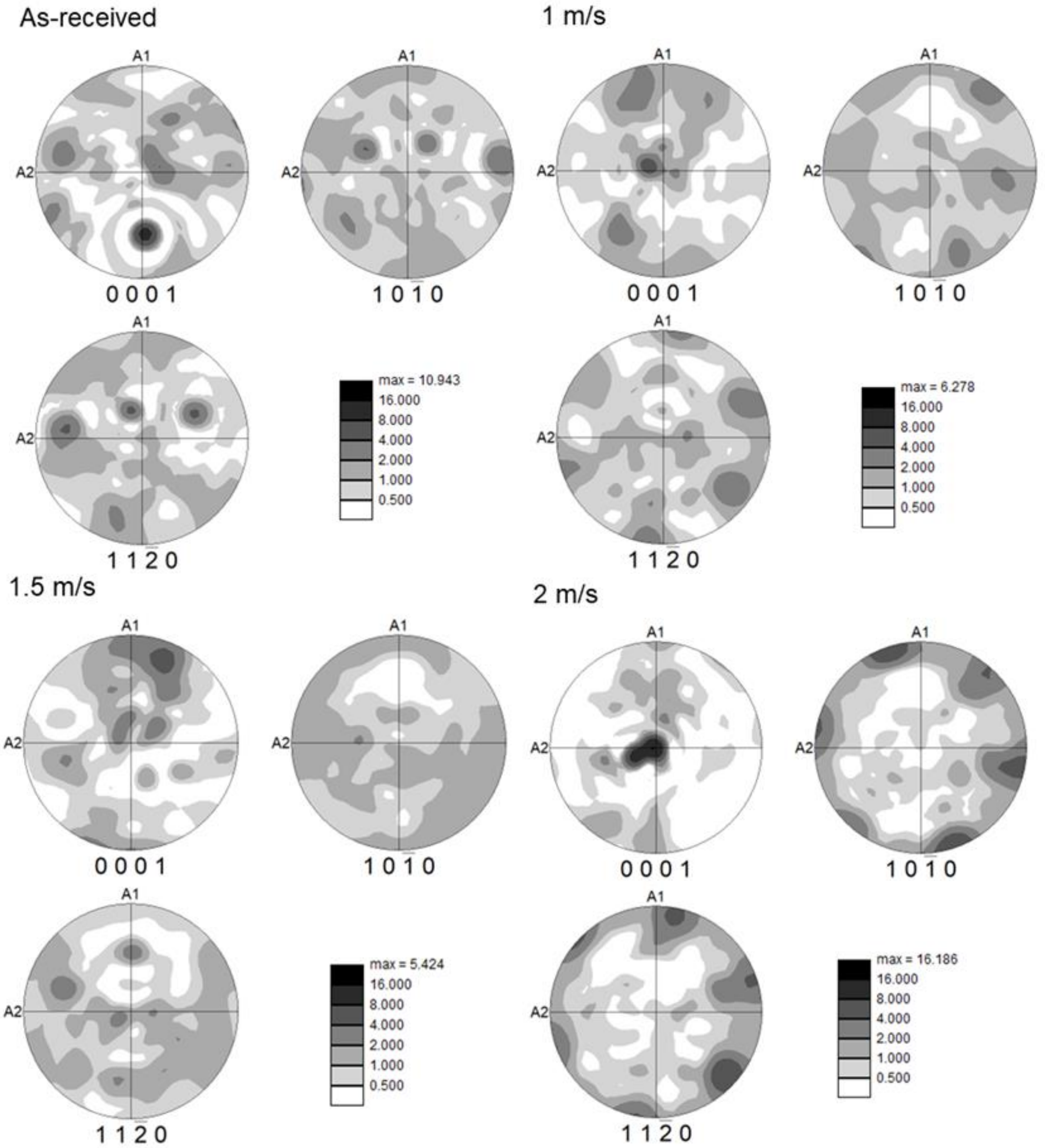

Figure 6.28 Pole figures of as-received material (radius direction) and chips (transverse direction) showing the texture evolution.

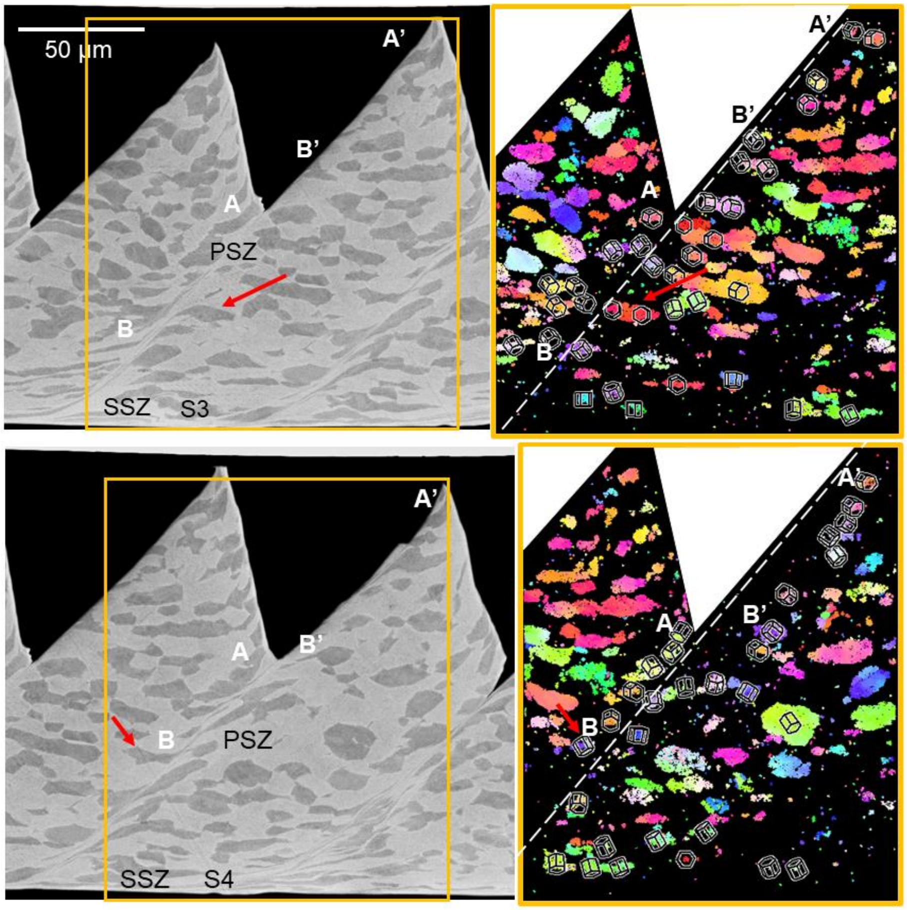

Figure 6.29 Shear bands where not much shearing in α_p is seen.

In the uncracked 1.5/s chips S3 and S4, shear bands are narrower, showing highly sheared primary α grains such as those shown in Fig. 6.29, indicating more localized shear deformation 1 and 2 m/s chips. EBSD scans show two grains that were sheared to very thin proportions, shown by arrows in S3 (a prism favored orientation) and S4 (a basal favored orientation). In both cases, the lower part of the shear band in the PSZ is highly correlated with the SSZ. From the FEM simulation, the temperature is much higher at the SSZ than in the PSZ, and the lack of cracking combined with favorable orientations for shear suggests that the PSZ was initiated by the shear taking place in the SSZ. On the other hand, the upper part of the shear band is far away enough from SSZ and thus is less associated with SSZ but more related to the orientations of its surrounding material.

6.3.3 Deformation twins in 1.5 m/s

A few twins were also observed in the 1.5 m/s chip. The misorientation angle between the parent and twined grains are approximately 85° and they have a common a-axis (Fig. 6.30). The twinning mode is identified to be $\{10\bar{1}2\} < \bar{1}011 >$ extension twinning.

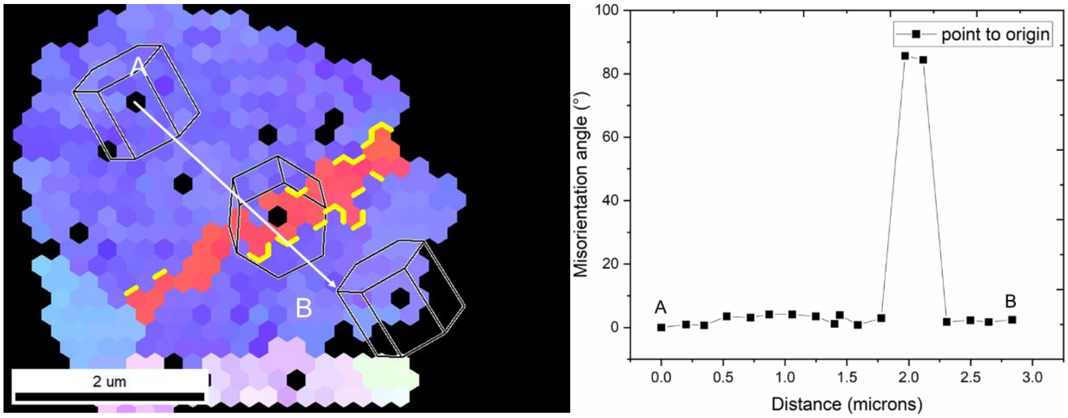

Figure 6.30 Representative T1-type twins in the chip segments exhibiting misorientation angle of ~85° (twin boundary is labeled with yellow lines).

6.4 Conclusion

1. At all three cutting speeds, the crack length decreases with increasing homogeneous shear strain in the segment, indicating that the adiabatic shear is more likely to take place with higher homogeneous shear strain and cracking and thus adiabatic shear are two competing mechanisms for the formation of segmented chips. This makes sense because the observations show that cracking usually nucleates at the subsurface of the tooth tip while the adiabatic shear always generates from the secondary shear zone due to elevated temperature from friction, both depending on the local crystal orientations. Cracks usually form when there are hard-to-cut orientations on one side (causing deformation incompatibility on two sides) or both sides, while adiabatic shear bands keep propagating when there are easy-to-cut orientations.
2. The shear band width at 1 m/s varies from 1.3 μm to 15.2 μm but barely changes at 1.5 and 2

m/s (~1.3 µm at 1.5 m/s and ~2 µm at 2 m/s). Wider shear band widths indicate less localized shear and this is consistent with the fact that calculated homogeneous shear strains at 1 m/s is between 0.4 and 1.4, which is much higher than at the other two cutting speeds, and is much more uniform at both 1.5 m/s (0.4 - 0.5) and 2 m/s (0.4 - 0.6). The shear strain calculations are believable in that the strains at 2 m/s are much lower compared with those at 1 m/s.

3. The prism <a> favored red orientation is dominant in and beneficial for the formation of adiabatic shear bands at both 1 and 2 m/s. This makes sense as prism <a> slip is the slip system with the lowest critical resolved shear stress among all the slip systems in hexagonal titanium. However, no dominant orientations have been observed from the 1.5 m/s chips.

4. $\{10\bar{1}2\} < \bar{1}011 >$ extension twinning, as a minor deformation mode, was observed at all three cutting speeds. There are only a few twins among all the locations investigated, because the deformation during cutting is large and twinning can only contribute a very small amount of deformation.

CHAPTER 7 ANNEALING TREATMENT OF STA CHIPS

The aim of annealing heat treatment on the as-received STA chips is to reduce dislocation density without modifying microstructure so that it will be easier to obtain high quality EBSD scans of the shear bands after annealing. In addition, higher temperature heat treatments provide a means to investigate the beginning of recrystallization and thus provide indirect evidence for locations with high shear strain and the nature of stored defect energy. Investigating the effect of the annealing temperature and time on microstructure change due to recovery and recrystallization provides insights about the nature of defects present in the as-formed chip.

7.1 Annealing at 500°C

From the BSE image and orientation maps, orientations within the shear band are undetectable after a 4h-anneal (Fig. 7.1) as no apparent recovery or recrystallization took place at this temperature. In Figs. 7.1 and 7.2 with 12 h-anneal, BSE images, the lamellar structure in the β_t region is still present after the annealing. The grain reference orientation deviation (GROD) map in Fig. 7.1(c) reveals the misorientation in each α_p grain where the white color indicates that the misorientation is greater than the maximum scale value of 15°.

In 1 m/s chips annealed for 12 or 16 h, in Figs. 7.2 and 7.3(a), orientations in the β_t regions away from the shear band could be indexed, but the orientations within the shear band in the 2 m/s chip are less clearly seen (Fig. 7.3(b)). In Figs. 7.2 and 7.3, there are some small orientations that are larger than single indexed points, where orientations within the shear band have a blue or cyan orientation that would favor basal <a> slip. The 500°C temperature is still too low for recovery to reveal most orientations within the β_t shear band region, and it did not cause recrystallization in a measurable way.

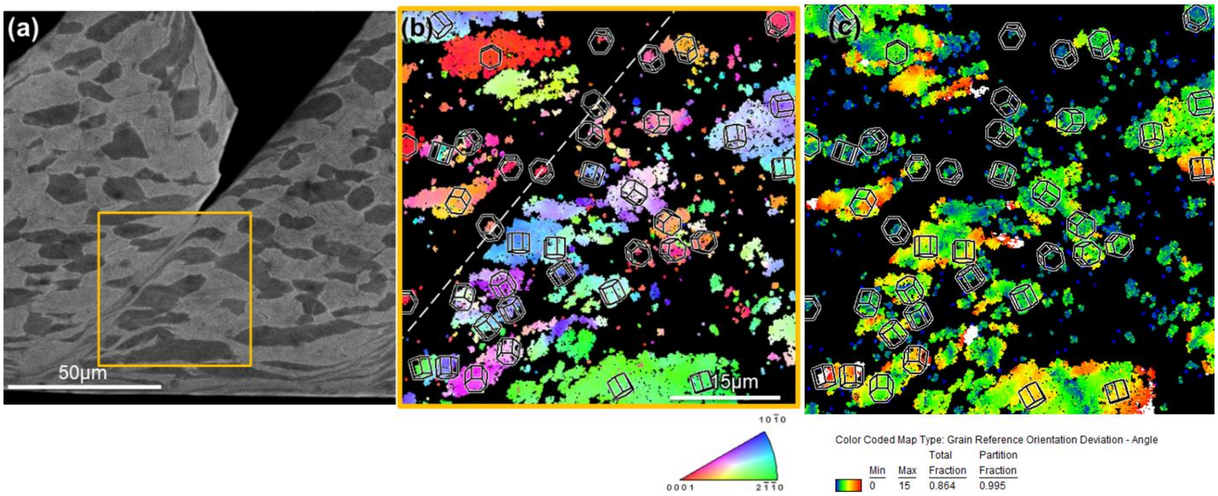

Figure 7.1 1m/s chip annealed at 500°C for 4h (a) BSE image; (b) IPF mapping in the red box in (a); (c) grain reference orientation deviation (GROD) map of (b) with a maximum misorientation of 15 °, white color indicates that the misorientation is great than 15 °. White dashed line on the IPF map indicates where the potential shear band is located.

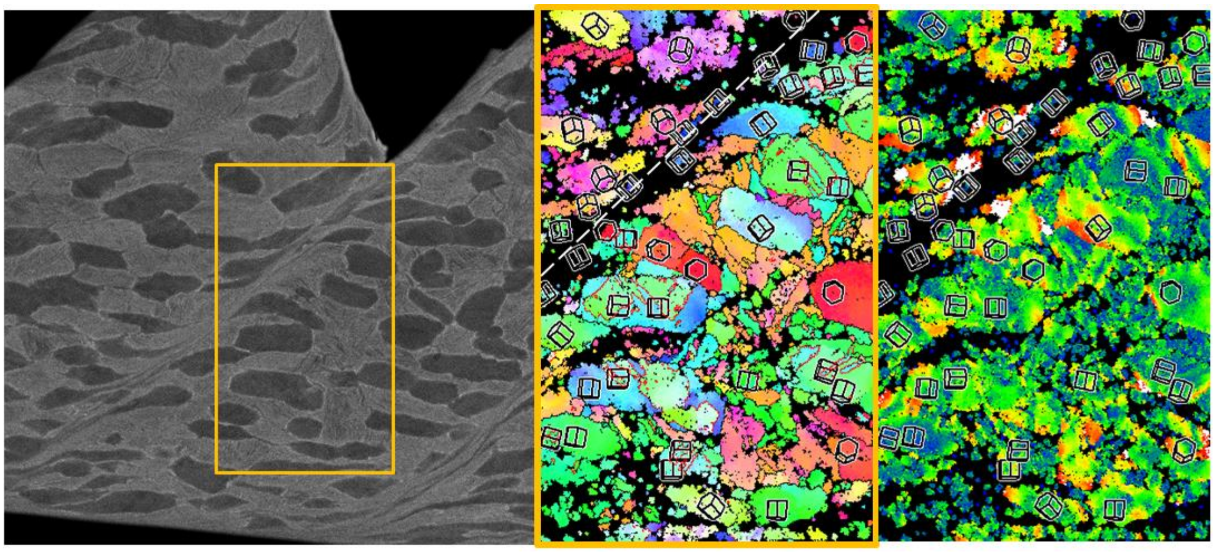

Figure 7.2 1m/s chip annealed at 500°C for 12h.

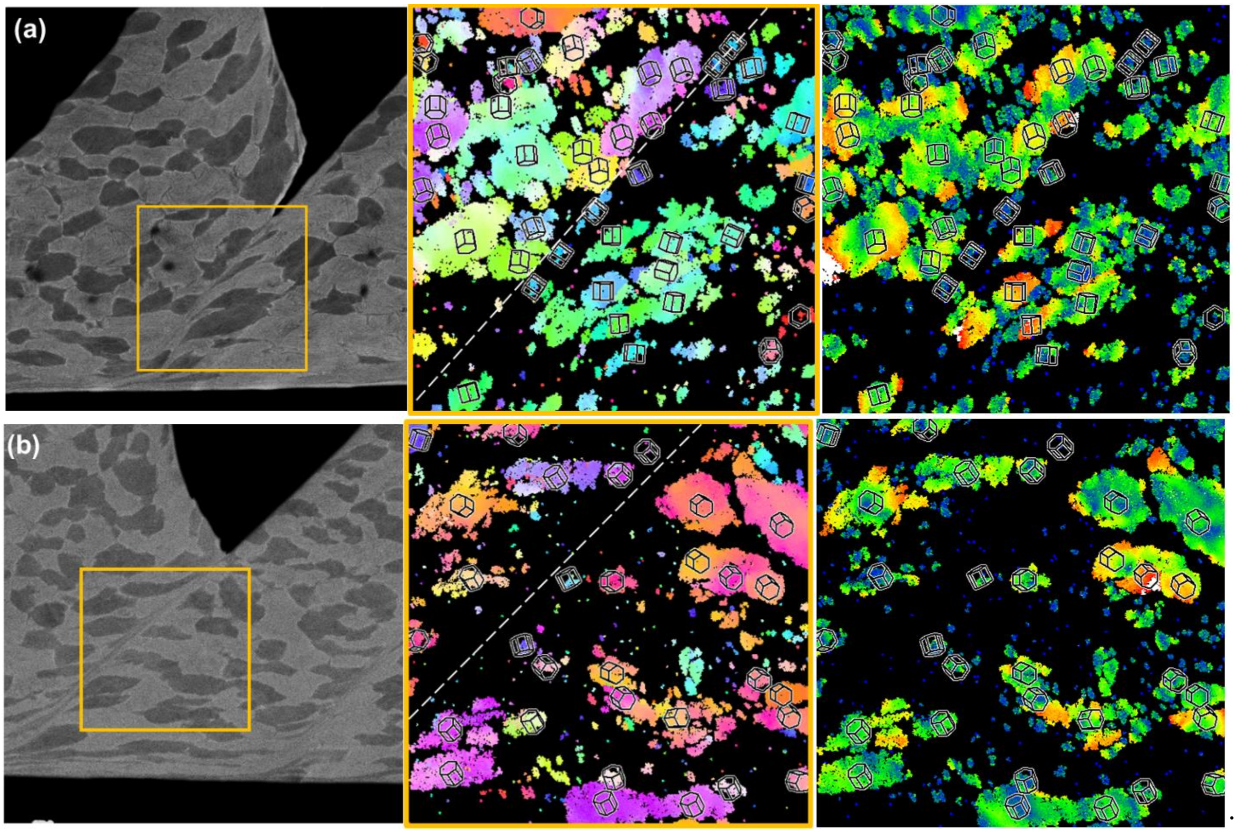

Figure 7.3 (a) 1m/s chip (b) 2m/s chip annealed at 500°C for 16 h.

7.2 Annealing at 600°C

After annealing at 600°C for 16h, orientations within the shear bands can be detected clearly in both the 1 m/s chips in Fig. 7.4 and 2 m/s chips in Fig. 7.5. All of these shear bands exhibited a similar orientation that would favor basal <a> slip (blue, cyan color). The α_p grains in the vicinity of the shear band are clearly indexed, which indicates a low dislocation density in the deformed grains. Nevertheless, the initial lamellar microstructure of the β_t region is not clearly indexed, and it is difficult to identify what took place in these areas. This 600 °C microstructure reflects sufficient temperature to generate indexible grains within most of the shear band in only 1 of the 4 cases, in Fig. 7.4(a). In the GROD maps for all four chips, there are slight misorientation gradients along the blue basal favored strip (ribbon in 3-D) within the shear band, indicating that recovery rather than recrystallization took place within the shear band. This indicates that 600°C annealing is not high enough to annihilate all of the dislocations within the shear band.

It is of great significance that there is a crystal orientation change from the red, prism <a> favored orientation to blue, basal <a> favored orientation in Fig. 7.5 (b). The orientation of this specific α_p grain would favor prism <a> slip, which is the easiest to activate due to the lowest critical resolved shear stress. However, the severely sheared portion of this same grain, composing the shear band, has an orientation favored by prism <a> and a misorientation angle of 90°, which is a possible misorientation angle of the two α variants before and after α-β-α phase transformation, which is discussed in more detail below.

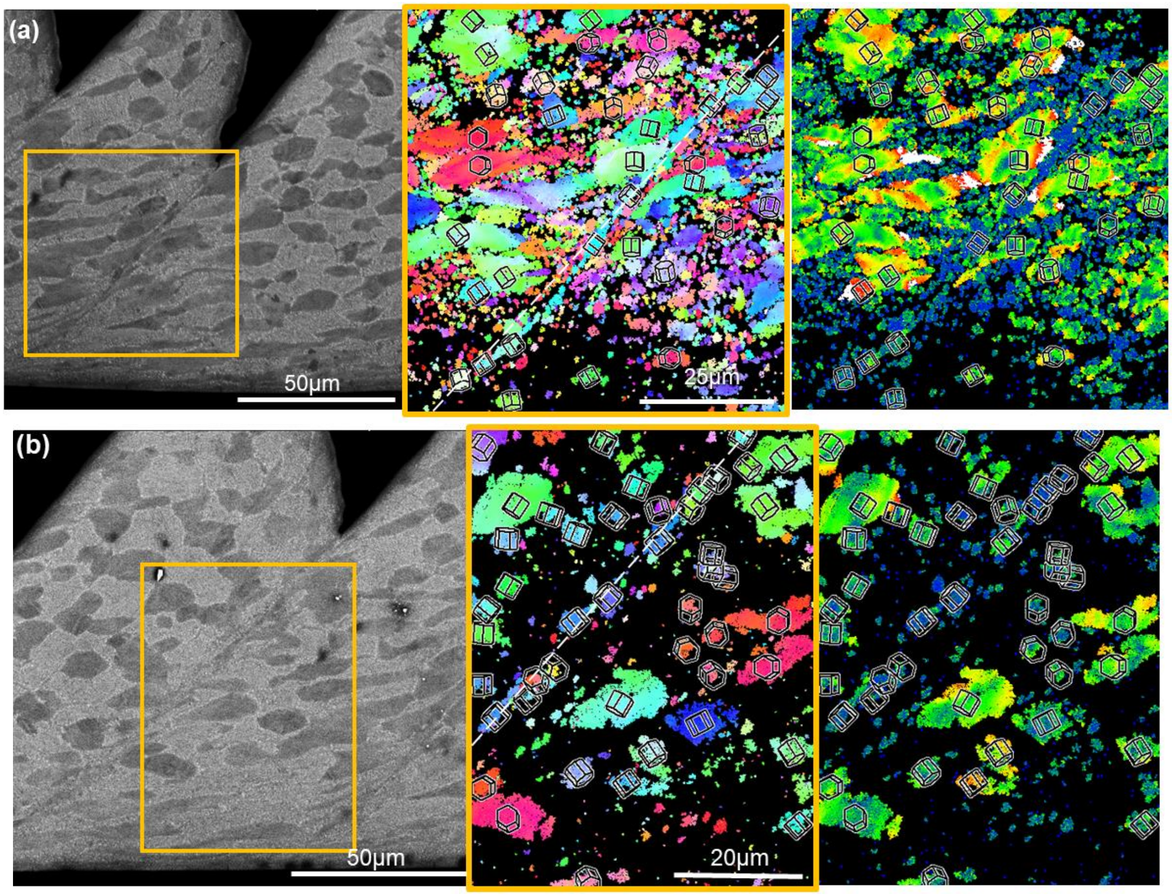

Figure 7.4 Two scans of 1m/s chip annealed at 600°C for 16h.

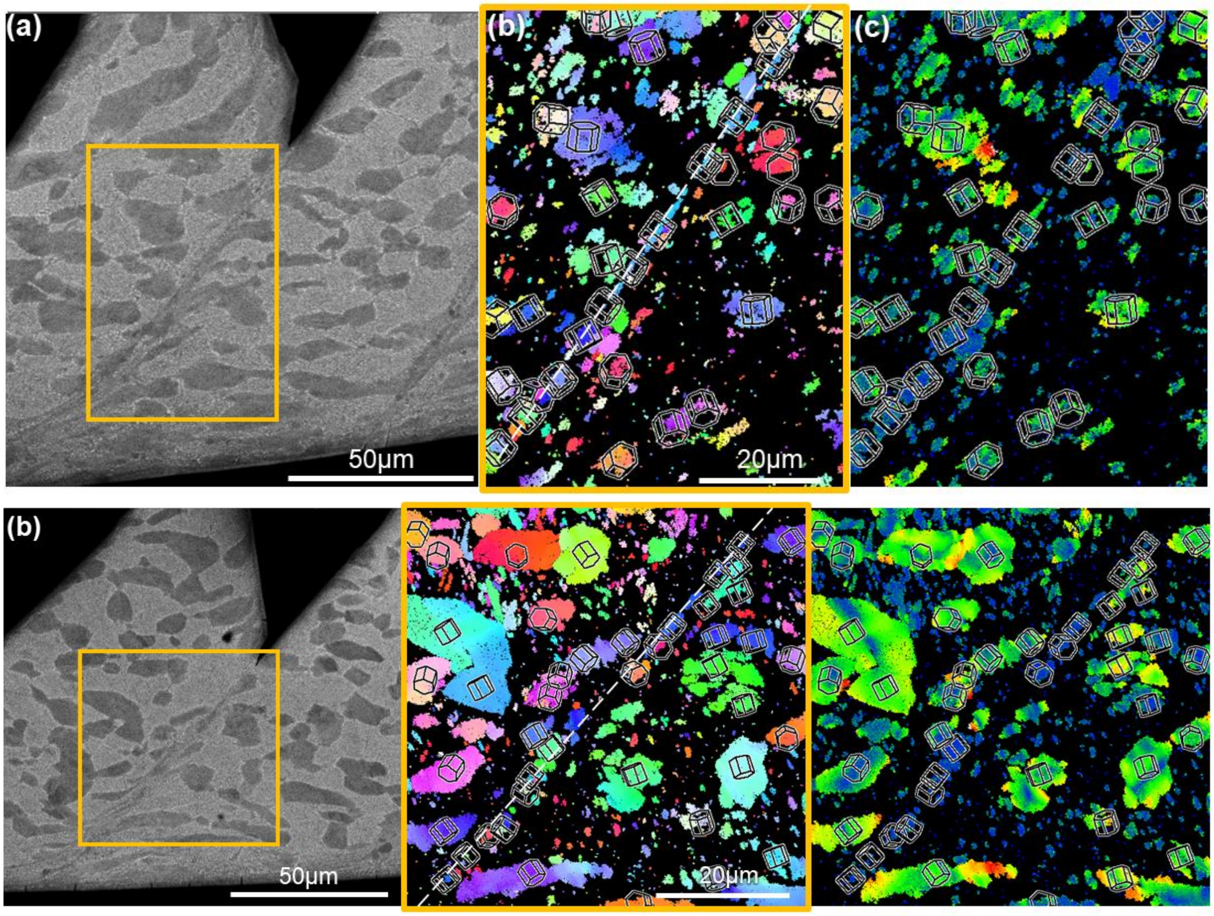

Figure 7.5 Two scans of a 2m/s chip annealed at 600°C for 16h.

7.3 Annealing at 650°C

When the annealing temperature was increased to 650 °C and annealed for 20 h (Fig. 7.6), the microstructure of the 1 m/s chip has two distinct regions. In the vicinity of the shear band (PSZ), indicated by a white arrow, there is a fine microstructure of equiaxed α grains with β on their grain boundaries, similar to the mill-annealed microstructure. In contrast, the lamellar structure can still be seen far from the shear band (indicated by the black arrow). Enlarged images of these two distinct microstructures are provided in Fig. 7.7 illustrating β lamellae in Fig. 7.7 (a) and ultra-fine recrystallized α grains in Fig. 7.7 (b). The change in microstructure reflects the different strain paths in the segments and shear bands during the cutting process. Within the segment far from the shear band, the homogeneous shear strain is much smaller than the localized shear in the shear band and thus the microstructure is not much affected by the 650 °C annealing. The highly distorted area near the shear band has enough driving force for complete recrystallization with many nucleation sites that lead to a new fine-grained microstructure.

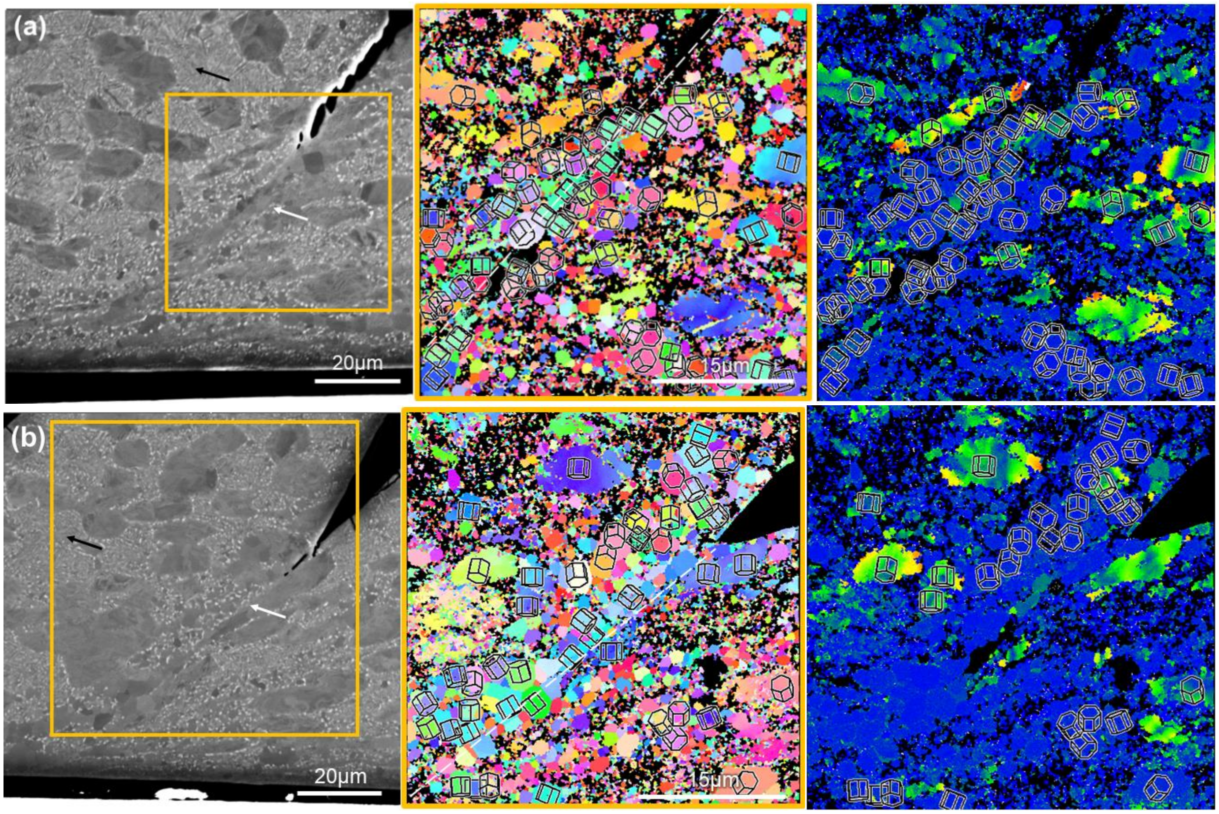

Figure 7.6 Two scans of 1m/s chip annealed at 650°C for 20h. the black arrow indicates the remaining β_t lamellar structure, and the white arrow indicates the newly formed equiaxed fine-grain structure.

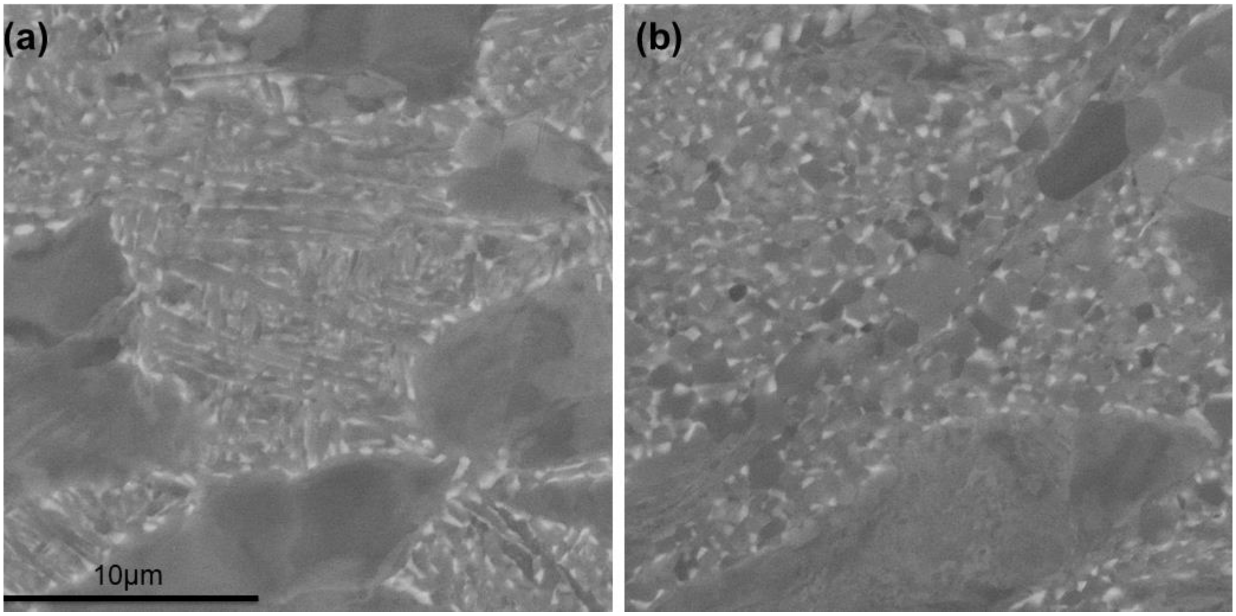

Figure 7.7 Representative images at the same magnification of (a) lamellar microstructure (black arrow in Fig. 7.6) in the segment; (b) equiaxed α grains with β on the grain boundaries (white arrow in Fig. 7.6) near the shear band.

Similar phenomena are observed in the 2 m/s chips. Annealing the 2 m/s chip for only 8 h leds to a similar microstructure as annealing the 1 m/s chip for 20 h, which suggests that the shear strain is more localized and distortion energy is higher at the cutting speed of 2 m/s. It is noteworthy that all the shear bands indexed in the annealed chips have the same blueish color and orientation that would favor basal <a> slip that was observed in the 600°C chips. In the three 1 m/s examples in Fig. 7.8, the extent of recrystallization is quite different; in the first, nearly all of the β_t is recrystallized (blue orientations in the GROD plot), but a lesser fraction is recrystallized in the other two shear band regions. There are also recrystallized grains in the SSZ in addition to those in the PSZ. The α_p grains did not recrystallize, as the orientation gradients are still present within them.

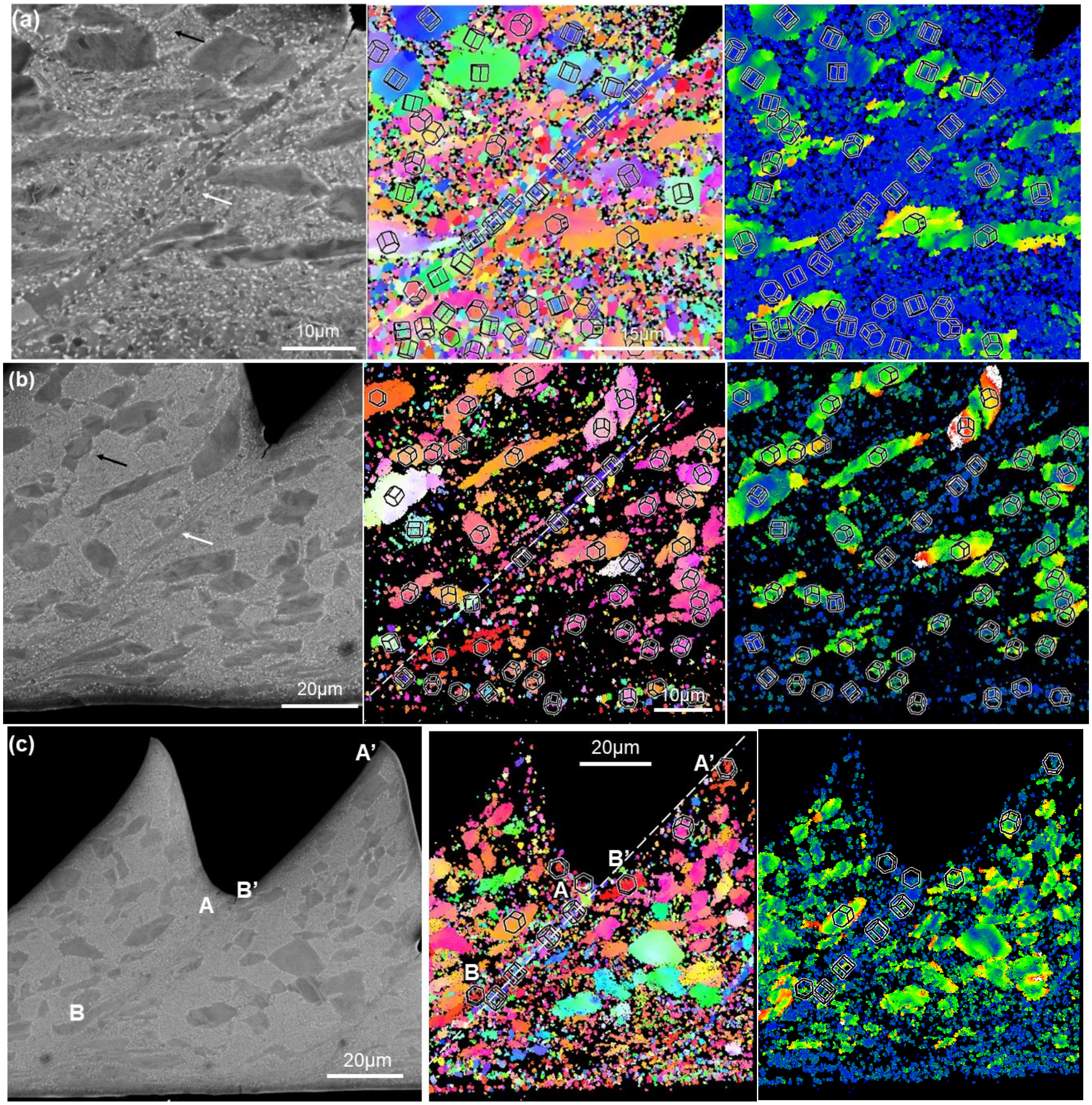

Figure 7.8 Three scans of 2m/s chip annealed at 650℃ for 8h. the black arrow indicates the remaining lamellar structure, and the white arrow indicates the newly formed structure.

7.4 Discussion

The blue basal shear band orientations show a difference from the prism <a> slip favored orientation often found in uncracked shear bands in the as-received chips. For basal <a> slip, homogeneous deformation would lead to a rotation of the c axis. In contrast, homogeneous strain due to the activation of prism <a> slip will not change the c-axis direction. The measured misorientation angle between these two orientations is close to 90°. One possible phase transformation mechanism that could account for this is that the blue orientation revealed after annealing at 600 or 650°C might be a result of the phase transformation to β during cutting.

Zhao et al. [136] carried out equal channel angle pressing (ECAP) of Ti64 samples with a shear strain of ~1.125 in each pass. Fast recrystallization was observed when annealing the sample after four passes at 620°C for only 5 mins. In addition, an increasing fraction of β phase was observed after a pulsed electric current treatment. In contrast, the shear strain in the vicinity of ASB in the present study is much larger than 4.5. The microstructure after the 650°C anneal in the present study (Fig. 7.7 (a)) is similar to the results from Zhao et al. [136]. Therefore, it is believable that the recrystallization took place when heat treated at 650 °C for 20 h and 8 h for the 1 and 2 m/s chips, respectively. The fact that many β_t regions are not indexed implies that local grain or sub-grain sizes are too small to generate a dominant Kikuchi pattern. Dynamic recrystallization (DRX) may have taken place during the cutting but the nano-scale grain from DRX in the as-cut chips is too small to be detected by EBSD [137]. If so, the grains grew to become measurable as 1-2 μm grains in Fig. 7.7 (b), but it is not clear whether this took place by static recrystallization of a DRX sub-micron grain microstructure, or if the deformed and quenched microstructure recrystallized during a static anneal.

The misorientation angle distribution of the as-received bar, is compared with regions without the ASB vicinity and only the ASB vicinity of 2 m/s chips after annealing in Fig. 7.9. Compared with the misorientation angle distribution of undeformed Ti64 and Ti64 with the tensile strain of 0.59 by Bieler et al. [138], similar peaks located at 30°, 60° and 90° that reflect the transformation from β to α, have also been observed in Fig. 7.9. In addition, the peaks at ~75° may have been caused by the large deformation during cutting, which was also observed after a hot tensile strain of 0.59 [138], a strain similar to strains between shear bands in the chips. The ASB vicinity in the annealed 2 m/s chip is similar to the as-received bar, which indicates that the α grains in the vicinity of ASB have misorientations caused by the phase transformation. This may reflect preferred misorientations from transformation that persisted during grain growth, as these misorientation have a Burgers orientation relationship.

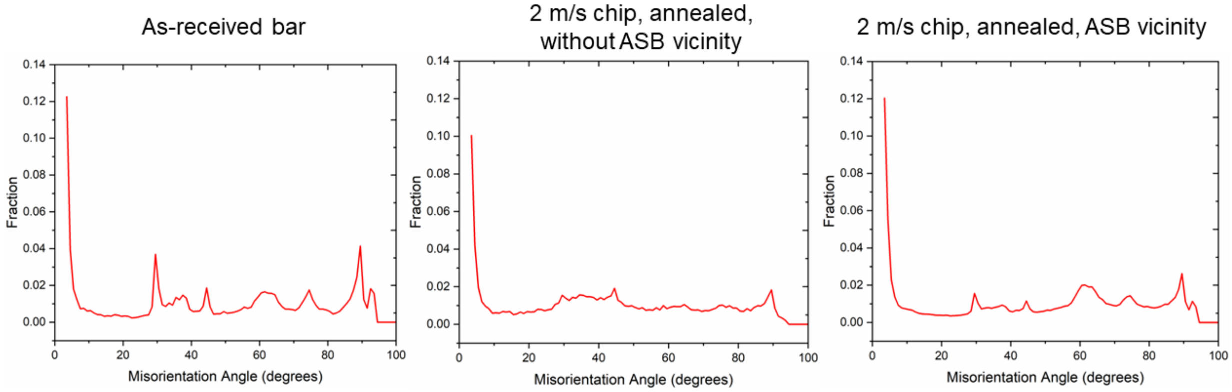

Figure 7.9 The misorientation angle of the ASB vicinity in the annealed 2 m/s chip shows a similar distribution as the as-received bar.

The pole figures of 1 and 2 m/s chips were made by merging about 15 scans so that the texture is representative. It can be seen in Fig. 7.10 that the peaks on (0001) pole figure are roughly near the center, and they have similar maximal intensities. In addition, the as-cut 1 and 2 m/s chips show similar texture except for the intensities. The strong peak near the center of the (0001) pole figure indicates that the crystals rotate toward the orientation of c-axis perpendicular to the page as they deform during the cutting.

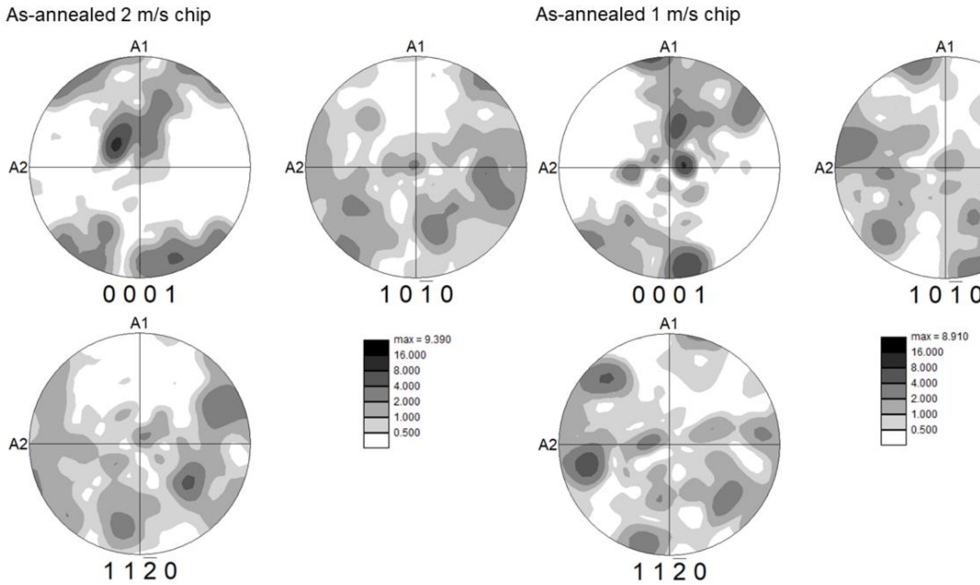

Figure 7.10 Pole figures of the 2 m/s chip (annealed at 650 ℃ for 8 h) and 1 m/s chip (annealed at 650 ℃ for 20 h).

It is noteworthy that the orientations of the ASB before and after annealing show an apparent and consistent differenec at both 1 and 2 m/s. The ASBs before annealing in Chapter 5 exhibited red color that favors prismatic <a> slip, while the ASBs after annealing in the present work have blue color that would favor basal <a> slip. Also, the blue ribbons after annealing are much narrower compared with any red shear bands that were detected before annealing. One possible explanation for the blue-ribbon orientation that favors basal slip is the β-α phase transformation.

If the β_t region transformed to β during the cutting process, it would be much softer than the hexagonal orientations in the β_t. This would facilitate and accelerate a plastic shear instability that would favor even more strain that could be accomplished by the α grain orientations. With large strain in the ASB, two two β variants that are likely to form due to large strain with the highest possible Schmid factors in the direction of shear are presented at the top of Fig. 7.11. According to the orientation relationship between α-Ti and β-Ti [139], there are 12 possible α variants that could transformed from β phase orientations. The orientations of α crystal in red boxes are consistent with the orientations detected in Fig. 7.8 (a), which have the basal plane parallel to a

$\{110\}_\beta$ plane. Compared with other possible $\{110\}_\beta$ planes, this specific orientation of α is favorably biased among all the 12 variants because the dislocation slip on the $\{110\}_\beta$ plane parallel to the shear plane resulted in lattice defects and thus preferentially favored this $\{110\}_\beta$ plane to become the basal plane of the α crystal [4]. Hence, the presence of the thin band of blue basal orientation could not have resulted as convincingly from deformation of the α phase.

The typical phase diagram of the Ti64 alloy [8], [140], [141] illustrates that the β-transus temperature is 994 °C when there is 6% Al present. However, the partition of Al and V in primary α and transformed β makes phase transformation more complicated. The phase diagram plotted in Fig. 7.12 overlays the Al and V binary phase boundaries. Assuming that there is 50% α and 50% β during the sub-transus heat treatment for the STA microstructure, then Al is an α stabilizer, and is partitioned in primary α, at a concentration of about 12wt. % Al, so the beta transus temperature is ~1080 °C. Similarly, V is a β stabilizer, and at about 8 wt. % V, the β transus is about 750 °C. The starting and finishing temperatures for a martensitic phase transformation is 780 and 650 °C, with a cooling rate larger than 20 °C/s [140]. Such a cooling rate is likely following cutting, and the temperature near ASB can reach even much higher than the predicted temperature of 750°C since the shear is more localized compared with the FE simulation (from Chapter 4). It thus is likely that the β_t regions within/near ASB transformed to β phase during the cutting and then experienced a large amount of shear deformation along the ASB direction, and finally transformed to the martensitic α' during the air cooling after being cut. This may also account for the fact that the regions near the ASB usually cannot be detected by EBSD. The α_p grains near ASB would not be able to transform to β because the transus temperature is as high as 1080 °C due to Al partitioning, and the observation that they remained intact, even though severely stretched after cutting.

When annealed at 600 or 650°C, the martensitic α’ was able to transform back to β due to the V partition in martensitic α’, because vanadium didn’t have enough time to diffuse during the air-cooling process. When withheld at 650°C for 8 hr, there was sufficient time for β to transform to α+ a small amount of β, in the form of the extremely narrow blue ribbon (compared to the wide shear band widths with red orientations), with grain growth sufficient to make the orientations visible by EBSD. In Fig. 7.8 (c), the narrow blue ribbon was still present even when the A-A’ and B-B’ pairs showed prism <a> favored soft orientations. This indicates that the β_t contributes to the adiabatic shear despite the soft α_p at 2 m/s.

While Fig. 7.12 shows one plausible path to account for the observed ribbon of basal orientations in the shear plane, other β orientations could have been present after transformation to β. The intense shear could easily have led to rotations leading to orientations similar to the two terminal orientations of β due to large strain, and consequently back transformation to a blue basal orientation, as well. The fact that there are discontinuities in the blue ribbon is consistent with variations in β grain orientations undergoing severe shear. The presence of many dislocations on (110) planes in the plane of shear provides defects that could favor formation of the basal variant of the 12 possible β-α phase variants [139].

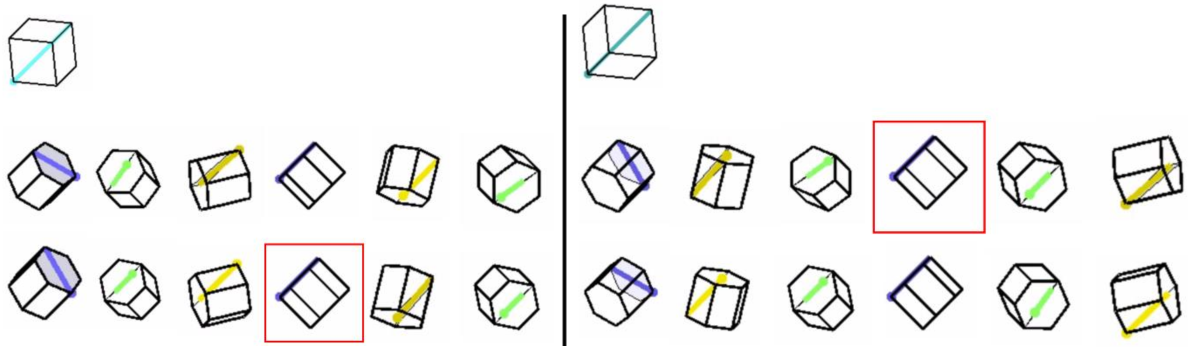

Figure 7.11 Two terminal β orientations that favor maximal shear. The red- boxed α orientations among 12 possible α variants are consistent with the α orientation detected after annealing, as shown in Fig. 7.8 (a).

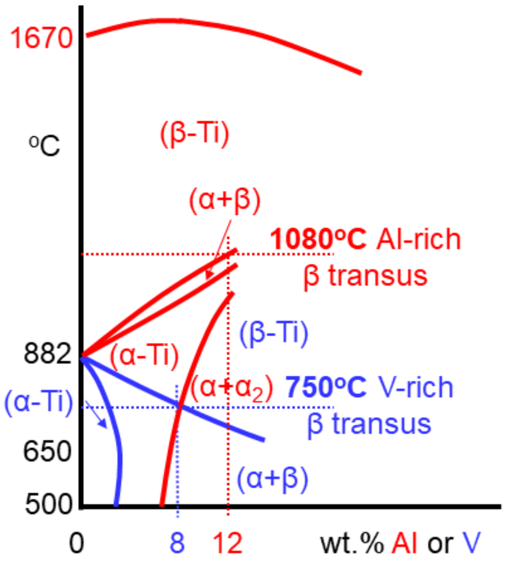

Figure 7.12 Phase diagram of titanium and the partitioned Al/V.

7.5 Conclusion

1. When annealed at 500 °C, the ASB was still invisible to EBSD, and no recrystallization was observed because the temperature is not high enough for sufficient recovery and/or recrystallization processes to grow large enough grains to generate a dominant Kikuchi pattern. At 600 °C, some parts of the ASB can be indexed but recrystallized grains were not indexable. After 650 °C annealing, both ASB and the recrystallized grains can be clearly seen and indexed by EBSD. In addition, microstructure near ASB consisted of fine equiaxed α grains with β on the grain boundaries, whereas the microstructure in the less deformed β_t segments remained lamellar and recovered sufficiently to be indexable, identifying high shear strains near the ASB, low shear strains within the segment and the gradient between them.

2. The GROD map of the shear band annealed at 650 °C has many grains with local misorientation gradients of 0 °, which indicates that the shear band has no GNDs that cause a gradient, and hence, have recrystallized. DRX may have taken place during the cutting process but the nano-scale grain from DRX in the as-cut chips is too small to be detected by EBSD. If so, the grains grew to become

measurable as 1-2 μm grains but it is not clear whether this took place by static recrystallization of a DRX sub-micron grain microstructure, or if the deformed and quenched microstructure recrystallized during a static anneal.

3. All of the narrow ribbons detected after annealing show the same blue orientation that would favor basal <a> slip, which differs by nearly 90° from the red orientation so commonly observed in uncracked (and some cracked) ASBs in as-machined chips at both cutting speeds. The blue ribbons can be best explained by a strong variant selection from transforming the β_t into the β phase above 750 °C, from which back transformation to a highly favored α with basal planes parallel to the high dislocation density β {110} planes occurs. This observation provides evidence for the $\beta_t \rightarrow \beta$ phase transformation during the cutting at 2 m/s, and accounts for the more homogeneous chip morphology at 2 m/s compared with the 1 m/s chips.

CHAPTER 8 CONCLUSIONS AND FUTURE WORK

8.1 Conclusions

This thesis demonstrates an approach to understanding the formation of segmented chips and their deformation history during turning, using EBSD, nanoindentation and annealing heat treatments. Preliminary results in Chapter 4 show that primary α exhibits high anisotropy in the hardness, and is consistently higher hardness than transformed β. Before and after cutting, the hardness of primary α generally remained unchanged, which may result from the low work hardening rate at high temperatures even under high strain rates [142]. Considering many cases, the calculated homogeneous shear strain in the segments at 1 m/s is much higher at 1 m/s than at 1.5 and 2 m/s, indicating a high strain rate sensitivity of homogeneous deformation in Ti64. Cracking originating from the surface or subsurface of the chip and the adiabatic shear generated near the tool tip are the two competing yet also complementary mechanisms for the formation of segmented chips, both depending on the local crystal orientations. Hard-to-cut orientations of primary α at tooth emergence sites will more likely lead to the nucleation of cracks. In contrast, primary α with soft orientations near the tooth emergence site is beneficial for the formation of an uncracked adiabatic shear band that is wider, and does not get as hot or unstable. Both cracks and adiabatic shear instabilities will result in a periodic load drop and hammering effect on tool. One observation of a prism <a> favored orientation resulted in a much “less localized” shear at 1 m/s and the chip morphology is more “continuous”. The Schmid factor analysis based upon many cases also indicates that orientations that favor both basal <a> and prism <a> slip are usually related to the occurrence of adiabatic shear bands without cracks, and more homogeneous deformation in and near the adiabatic shear band.

The phase diagram suggests that the transformed β half of STA microstructure to soft β can occur at temperatures above ~750°C due to partitioned vanadium. This implies that the transformed β part of the microstructure will transorm to β, deform more easily than the primary α, and then re-transform upon rapid cooling to martensitic α that cannot be indexed due to the high density of defects. This happens to a greater degree with increasing speed, and this can account for observations of increased tool damage due to tool dissolution as diffusivity is orders of magnitude faster in the β phase than the α phase. After annealing at 650 °C, static recrystallization or grain growth of dynamically recrystallized nanograins in the deformed transformed β leads to large enough grains to be indexed by EBSD, which develop preferentially in the vicinity of adiabatic shear bands. This indicates a stronger driving force to form new grains, in higher strain regions, in contrast to the lamellar β_t microstructure away from the shear band which remains intact.

While this work has clarified many aspects of deformation during turning, deformation is locally heterogeneous and very sensitive to local crystal orientations. It is still difficult to systematically understand the orientation and crystal structure evolution of the adiabatic shear band during deformation, as interpretations aided by annealing are still challenging to untangle. Nevertheless, the questions raised at the end of literature review can be answered with confidence:

1) Which mechanism is dominant when forming the segmented chips, cracking or adiabatic shearing?

In most cases, both mechanisms are activated, and pure adiabatic shearing is less common (~20%). The activation of cracking is more likely when hard-to-deform orientations are located where a tooth emerges. When most of the material has a soft orientation in the shear band volume, the lower flow stress enables adiabatic shear bands to form that do not reach a high enough temperature to transform to β phase and become unstable enough to form a shear crack.

2) How to estimate the homogeneous shear strain and the catastrophic shear strain and how

does the cutting speed affect them?

A model based on the shape of the tooth was adopted to calculate the shear strains. The homogeneous shear strain within the segment decreased significantly with increasing cutting speed due to the increasing strain rate. However, it can be seen from C12 in Fig. 6.10 that the so-called homogeneous shear strain is not homogeneous across the segment. The prsim <a> favored orientations have more deformation in the α_p than other orientations. The catastrophic shear in the shear band increased dramatically with increasing cutting speed since the shear band width generally decreased with increasing cutting speed. There is a much greater shear band width variation at 1 m/s, where the likelihood for forming cracks is lower due to a lower flow stress in the material (and hence, less adiabatic heating). The aspect ratio of the sheared α_p grains in the adiabatic shear band at three locations (Fig. 6.2) of pure adiabatic shear bands are also used and compared with the catastrophic shear strain. The catastrophic shear strains according to the model are 6, 9 and 25 while the aspect ratio measurements can be used to estimaate the catastrophic shear strain to be 17, 20 and 31. The model gives smaller values than the aspect ratio method and they they are similar in magnitude and show similar increasing trend in these cases. A possible explanation for this slight difference is that the model provides the “average” shear strain within the shear band (which consists of a few sheared α_p grains and β_t regions) while the aspect ratio measurement reflects the shear strains of the α_p grains in the center of the shear band.

3) What is the correlation between the shear strains and the two mechanisms of segmented chip formation?

The adiabatic shearing tends to take place when the homogeneous shear strain within the segment is higher while the cracking shows the opposite trend.

4) Does the microstructure and local crystal orientation influence the morphology of the

segmented chips? If so, what is the influence and what crystal orientation is beneficial for the formation of adiabatic shear?

The microstructure and local crystal orientation have significant influence on the morphology of the chips. Easy-to-cut orientations such as orientations that favor prism or basal <a> slip are beneficial for the formation of adiabatic shearing with wide ASBs and minimizing cracking. For LAM chips, the basal <a> favored orientations result in less segmented chips. For STA, adiabatic shearing propagates when the prism <a> favored orientations are present.

5) Is there direct evidence of the α → β phase transformation during cutting?

Simulations that match the material behavior of the shear band also provide a lower bound on the temperature in the shear band, indicating that temperatures exceeding 750°C are reached up to about 100 μm from the tip of the tool, which can cause transformation of β_t to β in the adiabatic shear band due to the enriched V. After annealing, consistent observation of thin basal oriented (blue) bands are present at the center of the shear band can most easily be explained by transformation of the β_t in the adiabatic shear band to β, followed by intense shearing that rotates the β orientation to a terminal orientation with $\{110\} < 111 >$ aligned with the shear plane and direction. With rapid cooling, transformation to the α’ martensite orientation with $(0001) < 2\bar{1}10 >$ aligned with the shear plane and direction in the volume that sheared preferentially as β results in a ribbon of α that becomes detectable with heat treatment. Also, the EBSD scan in Fig. 7.5 (a) shows a red, prism <a> favored α_p grain but the sheared portion of it has a blue, basal <a> favored orientation, which shows a misorientation angle of 90°. This observation provides direct evidence of the phase transformation taking place within the shear band during the machining process.

8.2 Future work

As discussed above, the formation of cracks and adiabatic shear bands should be reduced to improve the tool life. However, it is impractical to manipulate the texture of Ti64 to become what is desired for cutting. On the other hand, the present study identified the root cause for the formation of segmented chips, which is the build-up of stress and strain combined with low thermal conductivity that leads to unstable adiabatic shearing and cracking. Cryogenic machining may be a potential environmental-friendly and efficient approach to extending tool life, yet the chips will remain segmented, and the lower temperature may result in higher loads on the tool. Hence, tougher and chemically resistant tools are needed to enable faster machining or longer tool life. It will be meaningful and interesting to carry out annealing with in-situ observations to better understand how the deformed state can be understood by the outcomes of heat treatment and provide improved understanding of how particular shear bands developed.

BIBLIOGRAPHY

[1] C. Leyens and M. Peters, Eds., *Titanium and Titanium Alloys: Fundamentals and Applications*, 1st ed. Wiley, 2003. doi: 10.1002/3527602119.

[2] E. O. Ezugwu and Z. M. Wang, “Titanium alloys and their machinability—a review,” *J. Mater. Process. Technol.*, vol. 68, no. 3, pp. 262–274, Aug. 1997, doi: 10.1016/S0924-0136(96)00030-1.

[3] A. K. M. N. Amin, A. F. Ismail, and M. K. Nor Khairusshima, “Effectiveness of uncoated WC–Co and PCD inserts in end milling of titanium alloy—Ti–6Al–4V,” *J. Mater. Process. Technol.*, vol. 192–193, pp. 147–158, Oct. 2007, doi: 10.1016/j.jmatprotec.2007.04.095.

[4] L. Zeng and T. R. Bieler, “Effects of working, heat treatment, and aging on microstructural evolution and crystallographic texture of α, α′, α″ and β phases in Ti–6Al–4V wire,” *Mater. Sci. Eng. A*, vol. 392, no. 1–2, pp. 403–414, Feb. 2005, doi: 10.1016/j.msea.2004.09.072.

[5] P.-J. Arrazola, A. Garay, L.-M. Iriarte, M. Armendia, S. Marya, and F. Le Maître, “Machinability of titanium alloys (Ti6Al4V and Ti555.3),” *J. Mater. Process. Technol.*, vol. 209, no. 5, pp. 2223–2230, Mar. 2009, doi: 10.1016/j.jmatprotec.2008.06.020.

[6] P. J. Bania, “Beta titanium alloys and their role in the titanium industry,” *JOM*, vol. 46, no. 7, pp. 16–19, Jul. 1994, doi: 10.1007/BF03220742.

[7] E. O. Ezugwu, R. B. Da Silva, W. F. Sales, and A. R. Machado, “Overview of the machining of titanium alloys,” 2017.

[8] C. Leyens and M. Peters, *Titanium and titanium alloys: fundamentals and applications*. Wiley-Vch, 2003.

[9] H. Matsumoto, T. Nishihara, Y. Iwagaki, T. Shiraishi, Y. Ono, and A. Chiba, “Microstructural evolution and deformation mode under high-temperature-tensile-deformation of the Ti-6Al-4V alloy with the metastable α′ martensite starting microstructure,” *Mater. Sci. Eng. A*, vol. 661, pp. 68–78, Apr. 2016, doi: 10.1016/j.msea.2016.02.089.

[10] I. Polmear, D. StJohn, J.-F. Nie, and M. Qian, *Light Alloys: Metallurgy of the Light Metals*. Butterworth-Heinemann, 2017.

[11] S. Zhang, J. Li, H. Kou, J. Yang, G. Yang, and J. Wang, “Effects of thermal history on the microstructure evolution of Ti-6Al-4V during solidification,” *J. Mater. Process. Technol.*, vol. 227, pp. 281–287, Jan. 2016, doi: 10.1016/j.jmatprotec.2015.08.030.

[12] F. J. Gil, M. P. Ginebra, J. M. Manero, and J. A. Planell, “Formation of α-Widmanstätten structure: effects of grain size and cooling rate on the Widmanstätten morphologies and on the mechanical properties in Ti6Al4V alloy,” *J. Alloys Compd.*, vol. 329, no. 1, pp. 142–152, Nov. 2001, doi: 10.1016/S0925-8388(01)01571-7.

[13] J. Sieniawski, W. Ziaja, K. Kubiak, and M. Motyka, “Microstructure and mechanical properties of high strength two-phase titanium alloys,” *Titan. Alloys-Adv. Prop. Control*, pp. 69–80, 2013.

[14] R. P. Mulay, J. A. Moore, J. N. Florando, N. R. Barton, and M. Kumar, “Microstructure and mechanical properties of Ti–6Al–4V: Mill-annealed versus direct metal laser melted alloys,” *Mater. Sci. Eng. A*, vol. 666, pp. 43–47, Jun. 2016, doi: 10.1016/j.msea.2016.04.012.

[15] X. Liu, C. Tan, J. Zhang, F. Wang, and H. Cai, “Correlation of adiabatic shearing behavior with fracture in Ti-6Al-4V alloys with different microstructures,” *Int. J. Impact Eng.*, vol. 36, no. 9, pp. 1143–1149, Sep. 2009, doi: 10.1016/j.ijimpeng.2008.12.007.

[16] L. W. Meyer, L. Krüger, K. Sommer, T. Halle, and M. Hockauf, “Dynamic strength and failure behavior of titanium alloy Ti-6Al-4V for a variation of heat treatments,” *Mech. Time-Depend. Mater.*, vol. 12, no. 3, pp. 237–247, Sep. 2008, doi: 10.1007/s11043-008-9060-y.

[17] R. K. Nalla, J. P. Campbell, and R. O. Ritchie, “Mixed-mode, high-cycle fatigue-crack growth thresholds in Ti–6Al–4V: Role of small cracks,” *Int. J. Fatigue*, vol. 24, no. 10, pp. 1047–1062, Oct. 2002, doi: 10.1016/S0142-1123(02)00020-8.

[18] M. Armendia, A. Garay, L.-M. Iriarte, and P.-J. Arrazola, “Comparison of the machinabilities of Ti6Al4V and TIMETAL® 54M using uncoated WC–Co tools,” *J. Mater. Process. Technol.*, vol. 210, no. 2, pp. 197–203, Jan. 2010, doi: 10.1016/j.jmatprotec.2009.08.026.

[19] D. J. Schrock, D. Kang, T. R. Bieler, and P. Kwon, “Phase Dependent Tool Wear in Turning Ti-6Al-4V Using Polycrystalline Diamond and Carbide Inserts,” *J. Manuf. Sci. Eng.*, vol. 136, no. 4, p. 041018, Jun. 2014, doi: 10.1115/1.4027674.

[20] O. Hatt, P. Crawforth, and M. Jackson, “On the mechanism of tool crater wear during titanium alloy machining,” *Wear*, vol. 374–375, pp. 15–20, Mar. 2017, doi: 10.1016/j.wear.2016.12.036.

[21] C. J. Rao, D. Sreeamulu, and A. T. Mathew, “Analysis of Tool Life during Turning Operation by Determining Optimal Process Parameters,” *Procedia Eng.*, vol. 97, pp. 241–250, Jan. 2014, doi: 10.1016/j.proeng.2014.12.247.

[22] H. Liu, J. Zhang, X. Xu, and W. Zhao, “Experimental study on fracture mechanism transformation in chip segmentation of Ti-6Al-4V alloys during high-speed machining,” *J. Mater. Process. Technol.*, vol. 257, pp. 132–140, Jul. 2018, doi: 10.1016/j.jmatprotec.2018.02.040.

[23] F. Nabhani, “Wear mechanisms of ultra-hard cutting tools materials,” *J. Mater. Process. Technol.*, vol. 115, no. 3, pp. 402–412, Sep. 2001, doi: 10.1016/S0924-0136(01)00851-2.

[24] G. Li, S. Yi, S. Sun, and S. Ding, “Wear mechanisms and performance of abrasively ground polycrystalline diamond tools of different diamond grains in machining titanium alloy,” *J. Manuf. Process.*, vol. 29, pp. 320–331, Oct. 2017, doi: 10.1016/j.jmapro.2017.08.010.

[25] R. W. Maruda *et al.*, “A study on droplets sizes, their distribution and heat exchange for minimum quantity cooling lubrication (MQCL),” *Int. J. Mach. Tools Manuf.*, vol. 100, pp. 81–92, Jan. 2016, doi: 10.1016/j.ijmachtools.2015.10.008.

[26] Y. Kaynak, “Evaluation of machining performance in cryogenic machining of Inconel 718 and comparison with dry and MQL machining,” *Int J Adv Manuf Technol*, p. 15, 2014.

[27] Y. Wang *et al.*, “Experimental evaluation of the lubrication properties of the wheel/workpiece interface in minimum quantity lubrication (MQL) grinding using different types of vegetable oils,” *J. Clean. Prod.*, vol. 127, pp. 487–499, Jul. 2016, doi: 10.1016/j.jclepro.2016.03.121.

[28] M. Emami, M. H. Sadeghi, A. A. D. Sarhan, and F. Hasani, “Investigating the Minimum Quantity Lubrication in grinding of Al2O3 engineering ceramic,” *J. Clean. Prod.*, vol. 66, pp. 632–643, Mar. 2014, doi: 10.1016/j.jclepro.2013.11.018.

[29] J. Sharma and B. S. Sidhu, “Investigation of effects of dry and near dry machining on AISI D2 steel using vegetable oil,” *J. Clean. Prod.*, vol. 66, pp. 619–623, Mar. 2014, doi: 10.1016/j.jclepro.2013.11.042.

[30] M. Sarıkaya and A. Güllü, “Multi-response optimization of minimum quantity lubrication parameters using Taguchi-based grey relational analysis in turning of difficult-to-cut alloy Haynes 25,” *J. Clean. Prod.*, vol. 91, pp. 347–357, Mar. 2015, doi: 10.1016/j.jclepro.2014.12.020.

[31] F. Rabiei, A. R. Rahimi, M. J. Hadad, and M. Ashrafijou, “Performance improvement of minimum quantity lubrication (MQL) technique in surface grinding by modeling and optimization,” *J. Clean. Prod.*, vol. 86, pp. 447–460, Jan. 2015, doi: 10.1016/j.jclepro.2014.08.045.

[32] Z. G. Wang *et al.*, “Study on orthogonal turning of titanium alloys with different coolant supply strategies,” *Int. J. Adv. Manuf. Technol.*, vol. 42, no. 7–8, pp. 621–632, Jun. 2009, doi: 10.1007/s00170-008-1627-x.

[33] M. Sarıkaya and A. Güllü, “Taguchi design and response surface methodology based analysis of machining parameters in CNC turning under MQL,” *J. Clean. Prod.*, vol. 65, pp. 604–616, Feb. 2014, doi: 10.1016/j.jclepro.2013.08.040.

[34] R. Singh, “Minimum quantity lubrication turning of hard to cut materials – A review,” *Mater. Today Proc.*, vol. 37, pp. 3601–3605, Jan. 2021, doi: 10.1016/j.matpr.2020.09.769.

[35] N. N. N. Hamran, J. A. Ghani, R. Ramli, and C. H. C. Haron, “A review on recent development of minimum quantity lubrication for sustainable machining,” *J. Clean. Prod.*, vol. 268, p. 122165, Sep. 2020, doi: 10.1016/j.jclepro.2020.122165.

[36] Z. Y. Wang and K. P. Rajurkar, “Cryogenic machining of hard-to-cut materials,” *Wear*, vol. 239, no. 2, pp. 168–175, Apr. 2000, doi: 10.1016/S0043-1648(99)00361-0.

[37] A. Damir, A. Sadek, and H. Attia, "Characterization of Machinability and Environmental Impact of Cryogenic Turning of Ti-6Al-4V," *Procedia CIRP*, vol. 69, pp. 893–898, Jan. 2018, doi: 10.1016/j.procir.2017.11.070.

[38] S. Y. Hong and Y. Ding, "Cooling approaches and cutting temperatures in cryogenic machining of Ti-6Al-4V," *Int. J. Mach. Tools Manuf.*, vol. 41, no. 10, pp. 1417–1437, Aug. 2001, doi: 10.1016/S0890-6955(01)00026-8.

[39] M. Jamil *et al.*, "Influence of CO2-snow and subzero MQL on thermal aspects in the machining of Ti-6Al-4V," *Appl. Therm. Eng.*, vol. 177, p. 115480, Aug. 2020, doi: 10.1016/j.applthermaleng.2020.115480.

[40] M. I. Sadik, S. Isakson, A. Malakizadi, and L. Nyborg, "Influence of Coolant Flow Rate on Tool Life and Wear Development in Cryogenic and Wet Milling of Ti-6Al-4V," *Procedia CIRP*, vol. 46, pp. 91–94, Jan. 2016, doi: 10.1016/j.procir.2016.02.014.

[41] A. Shokrani, I. Al-Samarrai, and S. T. Newman, "Hybrid cryogenic MQL for improving tool life in machining of Ti-6Al-4V titanium alloy," *J. Manuf. Process.*, vol. 43, pp. 229–243, Jul. 2019, doi: 10.1016/j.jmapro.2019.05.006.

[42] V. Sivalingam, J. Sun, B. Yang, K. Liu, and R. Raju, "Machining performance and tool wear analysis on cryogenic treated insert during end milling of Ti-6Al-4V alloy," *J. Manuf. Process.*, vol. 36, pp. 188–196, Dec. 2018, doi: 10.1016/j.jmapro.2018.10.010.

[43] M. Calamaz, D. Coupard, M. Nouari, and F. Girot, "Numerical analysis of chip formation and shear localisation processes in machining the Ti-6Al-4V titanium alloy," *Int. J. Adv. Manuf. Technol.*, vol. 52, no. 9, pp. 887–895, Feb. 2011, doi: 10.1007/s00170-010-2789-x.

[44] H. Zhen-Bin and R. Komanduri, "On a Thermomechanical Model of Shear Instability in Machining," *CIRP Ann.*, vol. 44, no. 1, pp. 69–73, Jan. 1995, doi: 10.1016/S0007-8506(07)62277-X.

[45] A. E. Bayoumi and J. Q. Xie, "Some metallurgical aspects of chip formation in cutting Ti-6wt.%Al-4wt.%V alloy," *Mater. Sci. Eng. A*, vol. 190, no. 1, pp. 173–180, Jan. 1995, doi: 10.1016/0921-5093(94)09595-N.

[46] G. G. Ye, S. F. Xue, W. Ma, and L. H. Dai, "Onset and evolution of discontinuously segmented chip flow in ultra-high-speed cutting Ti-6Al-4V," *Int. J. Adv. Manuf. Technol.*, vol. 88, no. 1, pp. 1161–1174, Jan. 2017, doi: 10.1007/s00170-016-8847-2.

[47] A. Vyas and M. C. Shaw, "Mechanics of Saw-Tooth Chip Formation in Metal Cutting," *J. Manuf. Sci. Eng.*, vol. 121, no. 2, p. 163, 1999, doi: 10.1115/1.2831200.

[48] R. Komanduri and Z.-B. Hou, "On thermoplastic shear instability in the machining of a titanium alloy (Ti-6Al-4V)," *Metall. Mater. Trans. A*, vol. 33, no. 9, p. 2995, Sep. 2002, doi: 10.1007/s11661-002-0284-1.

[49] A. Molinari, C. Musquar, and G. Sutter, "Adiabatic shear banding in high speed machining

of Ti–6Al–4V: experiments and modeling," *Int. J. Plast.*, vol. 18, no. 4, pp. 443–459, Apr. 2002, doi: 10.1016/S0749-6419(01)00003-1.

[50] T. W. Wright and H. Ockendon, "A model for fully formed shear bands," *J. Mech. Phys. Solids*, vol. 40, no. 6, pp. 1217–1226, Aug. 1992, doi: 10.1016/0022-5096(92)90013-R.

[51] G. G. Ye, S. F. Xue, M. Q. Jiang, X. H. Tong, and L. H. Dai, "Modeling periodic adiabatic shear band evolution during high speed machining Ti-6Al-4V alloy," *Int. J. Plast.*, vol. 40, pp. 39–55, Jan. 2013, doi: 10.1016/j.ijplas.2012.07.001.

[52] Q. Xue, M. A. Meyers, and V. F. Nesterenko, "Self-organization of shear bands in titanium and Ti–6Al–4V alloy," *Acta Mater.*, vol. 50, no. 3, pp. 575–596, Feb. 2002, doi: 10.1016/S1359-6454(01)00356-1.

[53] N. He, T. C. Lee, W. S. Lau, and S. K. Chan, "Assessment of deformation of a shear localized chip in high speed machining," *J. Mater. Process. Technol.*, vol. 129, no. 1, pp. 101–104, Oct. 2002, doi: 10.1016/S0924-0136(02)00583-6.

[54] D. M. Turley, E. D. Doyle, and S. Ramalingam, "Calculation of shear strains in chip formation in titanium," *Mater. Sci. Eng.*, vol. 55, no. 1, pp. 45–48, Aug. 1982, doi: 10.1016/0025-5416(82)90082-9.

[55] M. Cotterell and G. Byrne, "Characterisation of chip formation during orthogonal cutting of titanium alloy Ti–6Al–4V," *CIRP J. Manuf. Sci. Technol.*, vol. 1, no. 2, pp. 81–85, Jan. 2008, doi: 10.1016/j.cirpj.2008.09.017.

[56] H. Zhen-Bin and R. Komanduri, "On a Thermomechanical Model of Shear Instability in Machining," *CIRP Ann.*, vol. 44, no. 1, pp. 69–73, Jan. 1995, doi: 10.1016/S0007-8506(07)62277-X.

[57] R. F. Recht, "Catastrophic Thermoplastic Shear," *J. Appl. Mech.*, vol. 31, no. 2, pp. 189–193, Jun. 1964, doi: 10.1115/1.3629585.

[58] M. Sadeghifar, R. Sedaghati, W. Jomaa, and V. Songmene, "A comprehensive review of finite element modeling of orthogonal machining process: chip formation and surface integrity predictions," *Int. J. Adv. Manuf. Technol.*, vol. 96, no. 9–12, pp. 3747–3791, Jun. 2018, doi: 10.1007/s00170-018-1759-6.

[59] J. C. Outeiro, D. Umbrello, and R. M'Saoubi, "Experimental and numerical modelling of the residual stresses induced in orthogonal cutting of AISI 316L steel," *Int. J. Mach. Tools Manuf.*, vol. 46, no. 14, pp. 1786–1794, Nov. 2006, doi: 10.1016/j.ijmachtools.2005.11.013.

[60] İ. Ucun and K. Aslantas, "Numerical simulation of orthogonal machining process using multilayer and single-layer coated tools," *Int. J. Adv. Manuf. Technol.*, vol. 54, no. 9–12, pp. 899–910, Jun. 2011, doi: 10.1007/s00170-010-3012-9.

[61] I. Al-Zkeri, J. Rech, T. Altan, H. Hamdi, and F. Valiorgue, "Optimiztion of the cutting edge geometry of coated carbide tools in dry turning of steels using a finite element analysis,"

Mach. Sci. Technol., vol. 13, no. 1, pp. 36–51, Apr. 2009, doi: 10.1080/10910340902776051.

[62] T. D. Marusich, S. Usui, and R. J. McDaniel, "Three-Dimensional Finite Element Prediction of Machining-Induced Stresses," presented at the ASME 2003 International Mechanical Engineering Congress and Exposition, American Society of Mechanical Engineers Digital Collection, May 2008, pp. 95–102. doi: 10.1115/IMECE2003-42329.

[63] B. Haddag, S. Atlati, M. Nouari, and M. Zenasni, "Analysis of the heat transfer at the tool–workpiece interface in machining: determination of heat generation and heat transfer coefficients," *Heat Mass Transf.*, vol. 51, no. 10, pp. 1355–1370, Oct. 2015, doi: 10.1007/s00231-015-1499-1.

[64] J. G. R, "A constitutive model and data for materials subjected to large strains, high strain rates, and high temperatures," *Proc 7th Inf Sympo Ballist.*, pp. 541–547, 1983.

[65] F. J. Zerilli and R. W. Armstrong, "Dislocation-mechanics-based constitutive relations for material dynamics calculations," *J. Appl. Phys.*, vol. 61, no. 5, pp. 1816–1825, Mar. 1987, doi: 10.1063/1.338024.

[66] S. T, "Flow Stress of Low Carbon Steel at High Temperature and Strain Rate (Part 1, Part 2)," *Bull Jpn. Soc Prec Eng*, vol. 17, no. 3, p. 161, 1983.

[67] P. L. B. Oxley, W. F. Hastings, and H. Ford, "Predicting the strain rate in the zone of intense shear in which the chip is formed in machining from the dynamic flow stress properties of the work material and the cutting conditions," *Proc. R. Soc. Lond. Math. Phys. Sci.*, vol. 356, no. 1686, pp. 395–410, Sep. 1977, doi: 10.1098/rspa.1977.0141.

[68] T. D. Marusich and M. Ortiz, "Modelling and simulation of high-speed machining," *Int. J. Numer. Methods Eng.*, vol. 38, no. 21, pp. 3675–3694, 1995, doi: 10.1002/nme.1620382108.

[69] W.-S. Lee and C.-F. Lin, "High-temperature deformation behaviour of Ti6Al4V alloy evaluated by high strain-rate compression tests," *J. Mater. Process. Technol.*, vol. 75, no. 1, pp. 127–136, Mar. 1998, doi: 10.1016/S0924-0136(97)00302-6.

[70] W.-S. Lee and C.-F. Lin, "Plastic deformation and fracture behaviour of Ti–6Al–4V alloy loaded with high strain rate under various temperatures," *Mater. Sci. Eng. A*, vol. 241, no. 1, pp. 48–59, Jan. 1998, doi: 10.1016/S0921-5093(97)00471-1.

[71] H. W. Meyer and D. S. Kleponis, "Modeling the high strain rate behavior of titanium undergoing ballistic impact and penetration," *Int. J. Impact Eng.*, vol. 26, no. 1, pp. 509–521, Dec. 2001, doi: 10.1016/S0734-743X(01)00107-5.

[72] S. Seo, O. Min, and H. Yang, "Constitutive equation for Ti–6Al–4V at high temperatures measured using the SHPB technique," *Int. J. Impact Eng.*, vol. 31, no. 6, pp. 735–754, Jul. 2005, doi: 10.1016/j.ijimpeng.2004.04.010.

[73] M. Sima and T. Özel, "Modified material constitutive models for serrated chip formation simulations and experimental validation in machining of titanium alloy Ti–6Al–4V," *Int. J.*

Mach. Tools Manuf., vol. 50, no. 11, pp. 943–960, Nov. 2010, doi: 10.1016/j.ijmachtools.2010.08.004.

[74] A. Molinari, X. Soldani, and M. H. Miguélez, "Adiabatic shear banding and scaling laws in chip formation with application to cutting of Ti–6Al–4V," *J. Mech. Phys. Solids*, vol. 61, no. 11, pp. 2331–2359, Nov. 2013, doi: 10.1016/j.jmps.2013.05.006.

[75] M. Calamaz, D. Coupard, and F. Girot, "A new material model for 2D numerical simulation of serrated chip formation when machining titanium alloy Ti–6Al–4V," *Int. J. Mach. Tools Manuf.*, vol. 48, no. 3, pp. 275–288, Mar. 2008, doi: 10.1016/j.ijmachtools.2007.10.014.

[76] Q. Wang, Z. Liu, B. Wang, Q. Song, and Y. Wan, "Evolutions of grain size and micro-hardness during chip formation and machined surface generation for Ti-6Al-4V in high-speed machining," *Int. J. Adv. Manuf. Technol.*, vol. 82, no. 9, pp. 1725–1736, Feb. 2016, doi: 10.1007/s00170-015-7508-1.

[77] G. Chen, L. Lu, Z. Ke, X. Qin, and C. Ren, "Influence of constitutive models on finite element simulation of chip formation in orthogonal cutting of Ti-6Al-4V alloy," *Procedia Manuf.*, vol. 33, pp. 530–537, Jan. 2019, doi: 10.1016/j.promfg.2019.04.066.

[78] M. Calamaz, D. Coupard, M. Nouari, and F. Girot, "Numerical analysis of chip formation and shear localisation processes in machining the Ti-6Al-4V titanium alloy," *Int. J. Adv. Manuf. Technol.*, vol. 52, no. 9, pp. 887–895, Feb. 2011, doi: 10.1007/s00170-010-2789-x.

[79] F. Ducobu, E. Rivière-Lorphèvre, and E. Filippi, "Numerical contribution to the comprehension of saw-toothed Ti6Al4V chip formation in orthogonal cutting," *Int. J. Mech. Sci.*, vol. 81, pp. 77–87, Apr. 2014, doi: 10.1016/j.ijmecsci.2014.02.017.

[80] S. Sun, M. Brandt, and M. S. Dargusch, "Characteristics of cutting forces and chip formation in machining of titanium alloys," *Int. J. Mach. Tools Manuf.*, vol. 49, no. 7, pp. 561–568, Jun. 2009, doi: 10.1016/j.ijmachtools.2009.02.008.

[81] J. Zang, J. Zhao, A. Li, and J. Pang, "Serrated chip formation mechanism analysis for machining of titanium alloy Ti-6Al-4V based on thermal property," *Int. J. Adv. Manuf. Technol.*, vol. 98, no. 1, pp. 119–127, Sep. 2018, doi: 10.1007/s00170-017-0451-6.

[82] G. Sutter and G. List, "Very high speed cutting of Ti–6Al–4V titanium alloy – change in morphology and mechanism of chip formation," *Int. J. Mach. Tools Manuf.*, vol. 66, pp. 37–43, Mar. 2013, doi: 10.1016/j.ijmachtools.2012.11.004.

[83] Y. Sánchez Hernández, F. J. Trujillo Vilches, C. Bermudo Gamboa, and L. Sevilla Hurtado, "Experimental Parametric Relationships for Chip Geometry in Dry Machining of the Ti6Al4V Alloy," *Materials*, vol. 11, no. 7, p. 1260, Jul. 2018, doi: 10.3390/ma11071260.

[84] D. Nguyen, D. Kang, T. Bieler, K. Park, and P. Kwon, "Microstructural impact on flank wear during turning of various Ti-6Al-4V alloys," *Wear*, vol. 384–385, pp. 72–83, Aug. 2017, doi: 10.1016/j.wear.2017.05.002.

[85] M. S. Dargusch, S. Sun, J. W. Kim, T. Li, P. Trimby, and J. Cairney, "Effect of tool wear evolution on chip formation during dry machining of Ti-6Al-4V alloy," *Int. J. Mach. Tools Manuf.*, vol. 126, pp. 13–17, Mar. 2018, doi: 10.1016/j.ijmachtools.2017.12.003.

[86] Y. Wang, B. Zou, J. Wang, Y. Wu, and C. Huang, "Effect of the progressive tool wear on surface topography and chip formation in micro-milling of Ti–6Al–4V using Ti(C7N3)-based cermet micro-mill," *Tribol. Int.*, vol. 141, p. 105900, Jan. 2020, doi: 10.1016/j.triboint.2019.105900.

[87] K. Palaniappan, M. Sundararaman, H. Murthy, R. Jeyaraam, and B. C. Rao, "Influence of workpiece texture and strain hardening on chip formation during machining of Ti–6Al–4V alloy," *Int. J. Mach. Tools Manuf.*, vol. 173, p. 103849, Feb. 2022, doi: 10.1016/j.ijmachtools.2021.103849.

[88] S. P. Timothy, "The structure of adiabatic shear bands in metals: A critical review," *Acta Metall.*, vol. 35, no. 2, pp. 301–306, Feb. 1987, doi: 10.1016/0001-6160(87)90238-0.

[89] D. Rittel and Z. G. Wang, "Thermo-mechanical aspects of adiabatic shear failure of AM50 and Ti6Al4V alloys," *Mech. Mater.*, vol. 40, no. 8, pp. 629–635, Aug. 2008, doi: 10.1016/j.mechmat.2008.03.002.

[90] B. Derby, "The dependence of grain size on stress during dynamic recrystallisation," *Acta Metall. Mater.*, vol. 39, no. 5, pp. 955–962, May 1991, doi: 10.1016/0956-7151(91)90295-C.

[91] K. Sun, X. Yu, C. Tan, H. Ma, F. Wang, and H. Cai, "Effect of microstructure on adiabatic shear band bifurcation in Ti–6Al–4V alloys under ballistic impact," *Mater. Sci. Eng. A*, vol. 595, pp. 247–256, Feb. 2014, doi: 10.1016/j.msea.2013.12.007.

[92] M. A. Meyers and H.-R. Pak, "Observation of an adiabatic shear band in titanium by high-voltage transmission electron microscopy," *Acta Metall.*, vol. 34, no. 12, pp. 2493–2499, Dec. 1986, doi: 10.1016/0001-6160(86)90152-5.

[93] H. Conrad, M. Doner, and B. De Meester, "Titanium science and technology," *Plenum Press N. Y.-Lond.*, vol. 2, p. 969, 1973.

[94] R. S. Culver, "Metallurgical effects at high strain rates," *Metall. Eff. High Strain Rates Plenum Press N. Y.*, pp. 519–523, 1973.

[95] J. Lu, R. Khawarizmi, M. Monclús, J. Molina-Aldareguia, P. Kwon, and T. R. Bieler, "Effect of cutting speed on shear band formation and chip morphology of Ti–6Al–4V alloy using nanoindentation and EBSD mapping," *Mater. Sci. Eng. A*, vol. 862, p. 144372, Jan. 2023, doi: 10.1016/j.msea.2022.144372.

[96] W. C. Oliver and G. M. Pharr, "An improved technique for determining hardness and elastic modulus using load and displacement sensing indentation experiments," *J. Mater. Res.*, vol. 7, no. 6, pp. 1564–1583, Jun. 1992, doi: 10.1557/JMR.1992.1564.

[97] R. M. Khawarizmi, J. Lu, D. S. Nguyen, T. R. Bieler, and P. Kwon, “The Effect of Ti-6Al-4V Microstructure, Cutting Speed, and Adiabatic Heating on Segmented Chip Formation and Tool Life,” *JOM*, vol. 74, no. 2, pp. 526–534, Feb. 2022, doi: 10.1007/s11837-021-05091-1.

[98] T. Obikawa and E. Usui, “Computational Machining of Titanium Alloy—Finite Element Modeling and a Few Results,” *J. Manuf. Sci. Eng.*, vol. 118, no. 2, pp. 208–215, May 1996, doi: 10.1115/1.2831013.

[99] D. Umbrello, “Finite element simulation of conventional and high speed machining of Ti6Al4V alloy,” *J. Mater. Process. Technol.*, vol. 196, no. 1, pp. 79–87, Jan. 2008, doi: 10.1016/j.jmatprotec.2007.05.007.

[100] J. Hua and R. Shivpuri, “Prediction of chip morphology and segmentation during the machining of titanium alloys,” *J. Mater. Process. Technol.*, vol. 150, no. 1, pp. 124–133, Jul. 2004, doi: 10.1016/j.jmatprotec.2004.01.028.

[101] T. Özel, M. Sima, and A. K. Srivastava, “Finite element simulation of high speed machining Ti-6Ai-4V alloy using modified material models,” in *Transactions of the North American Manufacturing Research Institution of SME 2010, NAMRI/SME*, 2010, pp. 49–56. Accessed: May 11, 2022. [Online]. Available: https://www.researchwithrutgers.com/en/publications/finite-element-simulation-of-high-speed-machining-ti-6ai-4v-alloy

[102] F. Bridier, P. Villechaise, and J. Mendez, “Analysis of the different slip systems activated by tension in a α/β titanium alloy in relation with local crystallographic orientation,” *Acta Mater.*, vol. 53, no. 3, pp. 555–567, Feb. 2005, doi: 10.1016/j.actamat.2004.09.040.

[103] Z. P. Wan, Y. E. Zhu, H. W. Liu, and Y. Tang, “Microstructure evolution of adiabatic shear bands and mechanisms of saw-tooth chip formation in machining Ti6Al4V,” *Mater. Sci. Eng. A*, vol. 531, pp. 155–163, Jan. 2012, doi: 10.1016/j.msea.2011.10.050.

[104] A. Moufki, A. Molinari, and D. Dudzinski, “Modelling of orthogonal cutting with a temperature dependent friction law,” *J. Mech. Phys. Solids*, vol. 46, no. 10, pp. 2103–2138, Oct. 1998, doi: 10.1016/S0022-5096(98)00032-5.

[105] F. Bridier, P. Villechaise, and J. Mendez, “Analysis of the different slip systems activated by tension in a α/β titanium alloy in relation with local crystallographic orientation,” *Acta Mater.*, vol. 53, no. 3, pp. 555–567, Feb. 2005, doi: 10.1016/j.actamat.2004.09.040.

[106] F. Han, B. Tang, H. Kou, J. Li, and Y. Feng, “Experiments and crystal plasticity finite element simulations of nanoindentation on Ti–6Al–4V alloy,” *Mater. Sci. Eng. A*, vol. 625, pp. 28–35, Feb. 2015, doi: 10.1016/j.msea.2014.11.090.

[107] T. B. Britton, H. Liang, F. P. E. Dunne, and A. J. Wilkinson, “The effect of crystal orientation on the indentation response of commercially pure titanium: experiments and simulations,” *Proc. R. Soc. Math. Phys. Eng. Sci.*, vol. 466, no. 2115, pp. 695–719, Mar. 2010, doi: 10.1098/rspa.2009.0455.

[108] J. Nejezchlebová *et al.*, “Elastic constants of β-Ti15Mo,” *J. Alloys Compd.*, vol. 792, pp. 960–967, Jul. 2019, doi: 10.1016/j.jallcom.2019.03.418.

[109] P. L. B. Oxley and M. C. Shaw, “Mechanics of Machining: An Analytical Approach to Assessing Machinability,” *J. Appl. Mech.*, vol. 57, p. 253, Jan. 1990, doi: 10.1115/1.2888318.

[110] B. Thimm, A. Glavas, M. Reuber, and H.-J. Christ, “Determination of chip speed and shear strain rate in primary shear zone using digital image correlation (DIC) in linear-orthogonal cutting experiments,” *J. Mater. Process. Technol.*, vol. 289, p. 116957, Mar. 2021, doi: 10.1016/j.jmatprotec.2020.116957.

[111] H. Hu, Z. Xu, W. Dou, and F. Huang, “Effects of strain rate and stress state on mechanical properties of Ti-6Al-4V alloy,” *Int. J. Impact Eng.*, vol. 145, p. 103689, Nov. 2020, doi: 10.1016/j.ijimpeng.2020.103689.

[112] T. Zhou, J. Wu, J. Che, Y. Wang, and X. Wang, “Dynamic shear characteristics of titanium alloy Ti-6Al-4V at large strain rates by the split Hopkinson pressure bar test,” *Int. J. Impact Eng.*, vol. 109, pp. 167–177, Nov. 2017, doi: 10.1016/j.ijimpeng.2017.06.007.

[113] G. Lütjering, “Influence of processing on microstructure and mechanical properties of (α+β) titanium alloys,” *Mater. Sci. Eng. A*, vol. 243, no. 1, pp. 32–45, Mar. 1998, doi: 10.1016/S0921-5093(97)00778-8.

[114] V. M. Segal, “Materials processing by simple shear,” *Mater. Sci. Eng. A*, vol. 197, no. 2, pp. 157–164, Jul. 1995, doi: 10.1016/0921-5093(95)09705-8.

[115] C. Z. Duan, M. J. Wang, J. Z. Pang, and G. H. Li, “A calculational model of shear strain and strain rate within shear band in a serrated chip formed during high speed machining,” *J. Mater. Process. Technol.*, vol. 178, no. 1, pp. 274–277, Sep. 2006, doi: 10.1016/j.jmatprotec.2006.04.008.

[116] T.-S. Jun, G. Sernicola, F. P. E. Dunne, and T. B. Britton, “Local deformation mechanisms of two-phase Ti alloy,” *Mater. Sci. Eng. A*, vol. 649, pp. 39–47, Jan. 2016, doi: 10.1016/j.msea.2015.09.016.

[117] J. Gong and A. J. Wilkinson, “Anisotropy in the plastic flow properties of single-crystal α titanium determined from micro-cantilever beams,” *Acta Mater.*, vol. 57, no. 19, pp. 5693–5705, Nov. 2009, doi: 10.1016/j.actamat.2009.07.064.

[118] S. Hémery, P. Nizou, and P. Villechaise, “In situ SEM investigation of slip transfer in Ti-6Al-4V: Effect of applied stress,” *Mater. Sci. Eng. A*, vol. 709, pp. 277–284, Jan. 2018, doi: 10.1016/j.msea.2017.10.058.

[119] D. Xia *et al.*, “Calculation of Schmid factor in Mg alloys: Influence of stress state,” *Scr. Mater.*, vol. 171, pp. 31–35, Oct. 2019, doi: 10.1016/j.scriptamat.2019.06.014.

[120] Q. Wang, R. M. Shankar, and Z. Liu, “Visco-plastic self-consistent modeling of crystallographic texture evolution related to slip systems activated during machining Ti-

6AL-4V," *J. Alloys Compd.*, vol. 853, p. 157336, Feb. 2021, doi: 10.1016/j.jallcom.2020.157336.

[121] T. R. Bieler, R. M. Trevino, and L. Zeng, "Alloys: Titanium," 2005.

[122] M. G. Glavicic, P. A. Kobryn, T. R. Bieler, and S. L. Semiatin, "A method to determine the orientation of the high-temperature beta phase from measured EBSD data for the low-temperature alpha phase in Ti-6Al-4V," *Mater. Sci. Eng. A*, vol. 346, no. 1, pp. 50–59, Apr. 2003, doi: 10.1016/S0921-5093(02)00535-X.

[123] A. Vyas and M. C. Shaw, "Mechanics of Saw-Tooth Chip Formation in Metal Cutting," *J. Manuf. Sci. Eng.*, vol. 121, no. 2, pp. 163–172, May 1999, doi: 10.1115/1.2831200.

[124] A. Chakraborty, C. Zhang, S. Balachandran, T. R. Bieler, and P. Eisenlohr, "Assessment of surface and bulk-dominated methodologies to measure critical resolved shear stresses in hexagonal materials," *Acta Mater.*, vol. 184, pp. 241–253, Feb. 2020, doi: 10.1016/j.actamat.2019.11.023.

[125] J. Lu, R. Khawarizmi, M. Monclús, J. Molina-Aldareguia, P. Kwon, and T. R. Bieler, "Effect of cutting speed on shear band formation and chip morphology of Ti–6Al–4V alloy using nanoindentation and EBSD mapping," *Mater. Sci. Eng. A*, p. 144372, Nov. 2022, doi: 10.1016/j.msea.2022.144372.

[126] M. H. Yoo, "Slip, twinning, and fracture in hexagonal close-packed metals," *Metall. Trans. A*, vol. 12, no. 3, pp. 409–418, Mar. 1981, doi: 10.1007/BF02648537.

[127] R. Alaghmandfard, D. Chalasani, A. Odeshi, and M. Mohammadi, "Activated slip and twin systems in electron beam melted Ti-6Al-4V subjected to elevated and high strain rate dynamic deformations," *Mater. Charact.*, vol. 172, p. 110866, Feb. 2021, doi: 10.1016/j.matchar.2020.110866.

[128] D. G. L. Prakash *et al.*, "Deformation twinning in Ti-6Al-4V during low strain rate deformation to moderate strains at room temperature," *Mater. Sci. Eng. A*, vol. 527, no. 21, pp. 5734–5744, Aug. 2010, doi: 10.1016/j.msea.2010.05.039.

[129] M. Preuss, J. Q. da Fonseca, V. Allen, D. G. L. Prakash, and M. R. Daymond, "Twinning in structural material with a hexagonal close-packed crystal structure," *J. Strain Anal. Eng. Des.*, vol. 45, no. 5, pp. 377–390, Jul. 2010, doi: 10.1243/03093247JSA624.

[130] Y. B. Chun, S. H. Yu, S. L. Semiatin, and S. K. Hwang, "Effect of deformation twinning on microstructure and texture evolution during cold rolling of CP-titanium," *Mater. Sci. Eng. A*, vol. 398, no. 1, pp. 209–219, May 2005, doi: 10.1016/j.msea.2005.03.019.

[131] W. Tirry, F. Coghe, S. Bouvier, M. Gasperini, L. Rabet, and D. Schryvers, "A multi-scale characterization of deformation twins in Ti6Al4V sheet material deformed by simple shear," *Mater. Sci. Eng. A*, vol. 527, no. 16, pp. 4136–4145, Jun. 2010, doi: 10.1016/j.msea.2010.03.039.

[132] F. Coghe, W. Tirry, L. Rabet, D. Schryvers, and P. Van Houtte, “Importance of twinning in static and dynamic compression of a Ti–6Al–4V titanium alloy with an equiaxed microstructure,” *Mater. Sci. Eng. A*, vol. 537, pp. 1–10, Mar. 2012, doi: 10.1016/j.msea.2011.12.047.

[133] G. G. Yapici, I. Karaman, and Z.-P. Luo, “Mechanical twinning and texture evolution in severely deformed Ti–6Al–4V at high temperatures,” *Acta Mater.*, vol. 54, no. 14, pp. 3755–3771, Aug. 2006, doi: 10.1016/j.actamat.2006.04.007.

[134] T. Bieler, R. L. Goetz, and S. L. Semiatin, “Anisotropic plasticity and cavity growth during upset forging of Ti–6Al–4V,” *Mater. Sci. Eng. A*, vol. 405, no. 1, pp. 201–213, Sep. 2005, doi: 10.1016/j.msea.2005.05.064.

[135] A. Molinari, C. Musquar, and G. Sutter, “Adiabatic shear banding in high speed machining of Ti–6Al–4V: experiments and modeling,” *Int. J. Plast.*, vol. 18, no. 4, pp. 443–459, Apr. 2002, doi: 10.1016/S0749-6419(01)00003-1.

[136] Z. Zhao, G. Wang, Y. Zhang, Y. Wang, and H. Hou, “Fast recrystallization and phase transformation in ECAP deformed Ti–6Al–4V alloy induced by pulsed electric current,” *J. Alloys Compd.*, vol. 786, pp. 733–741, May 2019, doi: 10.1016/j.jallcom.2019.01.328.

[137] X. Wang *et al.*, “Hot deformation behavior and dynamic recrystallization of melt hydrogenated Ti-6Al-4V alloy,” *J. Alloys Compd.*, vol. 728, pp. 709–718, Dec. 2017, doi: 10.1016/j.jallcom.2017.09.044.

[138] T. R. Bieler, P. D. Nicolaou, and S. L. Semiatin, “An Experimental and Theoretical Investigation of the Effect of Local Colony Orientations and Misorientation on Cavitation during Hot Working of Ti-6Al-4V,” *Metall. Mater. Trans. Phys. Metall. Mater. Sci. A*, vol. 36A, no. 1, pp. 129–140, Jan. 2005.

[139] D. Qiu, P. Zhao, R. Shi, Y. Wang, and W. Lu, “Effect of autocatalysis on variant selection of α precipitates during phase transformation in Ti-6Al-4V alloy,” *Comput. Mater. Sci.*, vol. 124, pp. 282–289, Nov. 2016, doi: 10.1016/j.commatsci.2016.07.032.

[140] S. Liu and Y. C. Shin, “Additive manufacturing of Ti6Al4V alloy: A review,” *Mater. Des.*, vol. 164, p. 107552, Feb. 2019, doi: 10.1016/j.matdes.2018.107552.

[141] A. Ducato, L. Fratini, M. La Cascia, and G. Mazzola, “An Automated Visual Inspection System for the Classification of the Phases of Ti-6Al-4V Titanium Alloy,” in *Computer Analysis of Images and Patterns*, R. Wilson, E. Hancock, A. Bors, and W. Smith, Eds., in Lecture Notes in Computer Science. Berlin, Heidelberg: Springer, 2013, pp. 362–369. doi: 10.1007/978-3-642-40246-3_45.

[142] G. Chen, C. Ren, X. Qin, and J. Li, “Temperature dependent work hardening in Ti–6Al–4V alloy over large temperature and strain rate ranges: Experiments and constitutive modeling,” *Mater. Des.*, vol. 83, pp. 598–610, Oct. 2015, doi: 10.1016/j.matdes.2015.06.048.